

**Thorium-Based Nuclear Fuel Performance Modelling with Multi-Pellet Material Fuel and Sheath Modelling Tool**

**Modélisation d'un Combustible Nucléaire Basé sur le Thorium  
par un Outil de Modélisation de Combustible à Pastilles Multiples  
et de la Gaine.**

A Thesis Submitted to the Division of Graduate Studies  
of the Royal Military College of Canada

by

**John Stuart Bell, BSc. MSc.**

In Partial Fulfillment of the Requirements for the Degree of  
Doctor of Philosophy



April 2017



© This thesis may be used within the Department of Defence but  
copyright for open publication remains the property of the author.

To my wife Sarah

## **Acknowledgements**

This work was funded under the Canada GEN-IV National Program. Funding to the Canada Gen-IV National Program was provided by Natural Resources Canada through the Office of Energy Research and Development, Atomic Energy of Canada Limited, and Natural Sciences and Engineering Research Council of Canada.

There are also many people to thank.

Thank you, Dr. Chan for providing this opportunity to study this complex and important problem.

Many thanks to members of the CNL staff: Holly Hamilton (since retired), Jeremy Pencer, Bill Richmond, Ian Lusk, Tony Williams, and Mark Floyd for their assistance and collaboration on the model.

Thank you to the members of nuclear group at RMCC both past and present. You have enriched my time during these studies. Special thanks Andrew Prudil for the excellent work he generated and his help in the development of this work.

Thanks go out to my Auntie Jean, Aunt Margie, and Brad for their willingness to read early drafts.

Lastly special thanks to my wife Sarah. It has been a long ride and I am glad you joined me in it.

## Abstract

A means of improving fuel sustainability within the nuclear power industry is to develop thorium-based fuel cycles. The Canadian Super-Critical Water cooled Reactor (SCWR) concept is using this path to achieve the sustainability requirement as part of the Gen-IV Forum. The study of Th-based fuel irradiation behaviour is less advanced than that of  $\text{UO}_2$  fuel, with the majority of studies focused on  $(\text{Th,U})\text{O}_2$ , and very limited work examining the  $(\text{Th,Pu})\text{O}_2$  fuel type proposed in the SCWR project.

The Fuel and Sheath Modelling Tool (FAST), a fuel performance model for Canadian Pressurized Heavy Water Reactor  $\text{UO}_2$  fuel, was developed at the Royal Military College of Canada (RMCC). By extending FAST's capabilities to include  $\text{ThO}_2$ ,  $(\text{Th,U})\text{O}_2$  and  $(\text{Th,Pu})\text{O}_2$  as fuel pellet materials, it seemed feasible to develop this as a tool to aid in the design and performance assessment of Th-based fuels, including the proposed SCWR  $(\text{Th,Pu})\text{O}_2$  fuel.

Development and integration of  $\text{ThO}_2$ ,  $(\text{Th,U})\text{O}_2$ , and  $(\text{Th,Pu})\text{O}_2$  models into the existing FAST model led to a new version called the Multi-Pellet Material Fuel and Sheath Modelling Tool (MPM-FAST). Model development was performed in collaboration between RMCC and Canadian Nuclear Laboratories (CNL). This work presents an outline of the MPM-FAST  $(\text{Th,U})\text{O}_2$ , and  $(\text{Th,Pu})\text{O}_2$  models. Modelling results were compared with post-irradiation

examination (PIE) data from two experimental irradiations conducted at CNL under normal operating conditions of a Canadian Pressurized Heavy Water Reactor.

Although the MPM-FAST model can be further improved, results are encouraging when compared to the PIE data. The  $\text{ThO}_2$ ,  $(\text{Th,U})\text{O}_2$ , and  $(\text{Th,Pu})\text{O}_2$  fuel performance models in MPM-FAST show a marked improvement in replicating the PIE data, as compared to the  $\text{UO}_2$  model simulating the same geometry and irradiation conditions. MPM-FAST has demonstrated that it is able to predict high fission gas release from  $(\text{Th,Pu})\text{O}_2$  and can be used to aid in the experimental design of new test irradiations. The measurement of the material properties of Th-based fuel is rare, but the development of MPM-FAST has taken the first step to collect and use the best available data and holistic approach. When further knowledge and experimental data becomes available, MPM-FAST could be used as a fuel performance modeling tool for test these new Th-based fuel types.

## Résumé

Un moyen d'améliorer la viabilité de l'industrie nucléaire est de développer des cycles de combustibles basés sur le thorium. Le concept du réacteur canadien refroidi par de l'eau surcritique utilise cette voie pour satisfaire aux exigences de viabilité comme partenaire du Forum Génération-IV. L'étude du comportement sous irradiation de combustibles basés sur le thorium est moins avancée que celle de combustibles à l' $\text{UO}_2$ , la plupart des études portant sur des mélanges de  $(\text{Th,U})\text{O}_2$  et un nombre limité de recherches sur des mélanges de  $(\text{Th,Pu})\text{O}_2$  proposés pour le projet du réacteur canadien refroidi par de l'eau surcritique.

L'outil de modélisation du combustible et de la gaine (« *Fuel and Sheath Modelling Tool (FAST)* »), est un modèle de la performance du combustible à l' $\text{UO}_2$  du réacteur canadien à eau lourde pressurisée qui a été développé au Collège militaire royal du Canada (CMRC). Il apparaît possible de développer davantage cet outil en augmentant les possibilités de « *FAST* » pour inclure le  $\text{ThO}_2$ , le  $(\text{Th,U})\text{O}_2$  et le  $(\text{Th,Pu})\text{O}_2$  comme matériaux des pastilles de combustible afin d'aider au design et à l'évaluation de la performance de combustibles basés sur le thorium, y compris le combustible au  $(\text{Th,Pu})\text{O}_2$  proposé pour le réacteur canadien refroidi par de l'eau surcritique.

Le développement et l'intégration de modèles de combustibles au  $\text{ThO}_2$ , au  $(\text{Th,U})\text{O}_2$ , et au  $(\text{Th,Pu})\text{O}_2$  dans le modèle présent "FAST" a conduit à une nouvelle version appelée « outil de modélisation de combustible à pastilles multiples et de la gaine » (« *Multi-Pellet Material Fuel and Sheath Modelling Tool (MPM-FAST)* »). Une collaboration entre le CMRC et les Laboratoires nucléaires canadiens (LNC) a permis le développement du modèle. Le présent travail décrit le « *MPM-FAST* » tel qu'appliqué à des modèles de combustibles au  $(\text{Th,U})\text{O}_2$  et au  $(\text{Th,Pu})\text{O}_2$ . Les résultats de la modélisation ont été comparés à des résultats expérimentaux provenant de données d'examen post-irradiation de deux irradiations expérimentales effectuées au LCN dans des conditions d'exploitation normales dans un réacteur canadien à eau lourde pressurisée.

Considérant que le modèle « *MPM-FAST* » peut encore être amélioré, les résultats sont encourageants à la suite d'une comparaison avec les données expérimentales des examens post-irradiation. Les modèles de la performance des combustibles au  $\text{ThO}_2$ , au  $(\text{Th,U})\text{O}_2$ , et au  $(\text{Th,Pu})\text{O}_2$  utilisant "*MPM-FAST*" montrent une nette amélioration en comparaison des données expérimentales des examens post-irradiation, lorsque l'on compare avec un modèle d'un combustible à l' $\text{UO}_2$  simulant une même géométrie et des conditions d'irradiation identiques. « *MPM-FAST* » a démontré qu'il est capable de prédire des relâchements importants de produits de fission gazeux du  $(\text{Th,Pu})\text{O}_2$  et peut être utilisé pour la conceptions de nouveaux test expérimentaux sous irradiation. Les propriétés

matérielles des combustibles basés sur le thorium sont encore peu connues, mais le développement de « *MPM-FAST* » représente un premier pas et utilise l'approche la plus disponible. Lorsque des nouvelles connaissances et des données expérimentales deviendront disponibles, le modèle pourra servir comme outil de modélisation de la performance du combustible pour des combustibles basés sur le thorium.



## Table of Contents

Acknowledgements.....	iii
Abstract.....	iv
Résumé.....	vi
List of Figures.....	xii
List of Tables .....	xvi
List of Acronyms .....	xx
List of Symbols.....	xxii
1 Introduction.....	1
2 State-of-the-Art.....	9
3 Goals and Scope of Work .....	17
4 Theory and Model Development.....	20
4.1    Geometry and Boundary Conditions.....	20
4.2    Common Equations .....	25
4.3    Sheath .....	30
4.3.1    Heat Transport .....	30
4.3.2    Deformation .....	38
4.4    Free Volume .....	43
4.4.1    Heat Transport .....	43

4.4.2	Deformation .....	49
4.5	Pellet .....	57
4.5.1	Heat Transport .....	58
4.5.2	Fission Gas.....	70
4.5.3	Deformation .....	83
5	Model Implementation.....	87
5.1	COMSOL Overview.....	87
5.2	MPM-FAST Model Components .....	92
5.3	Heat Transport .....	98
5.4	Deformation.....	101
5.5	FG Diffusion.....	103
6	Results and Discussion .....	108
6.1	Model Validation .....	108
6.1.1	(Th,U)O <sub>2</sub> Model.....	108
6.1.2	(Th,Pu)O <sub>2</sub> Model.....	124
6.2	Sensitivity Analysis .....	140
6.3	SCWR Fuel.....	151
6.4	Modelling Concerns .....	158
7	Summary and Conclusions .....	162
8	Recommendations.....	165
9	References.....	168
	Appendix A: Material properties for UO <sub>2</sub> accessible in MPM-FAST .....	177
	Appendix B : Grain Growth Kinetics Comparison.....	184
	Appendix C: Fission Gas Diffusion.....	186

Appendix D: COMSOL Report .....	191
Appendix E: Using MPM-FAST .....	335
AE.1 Input .....	337
AE.2 Post Processing .....	352

## List of Figures

Figure 1: Picture of a fuel bundle [2].....	3
Figure 2: Diagram presenting a cross section of the Canadian SCWR, with labels for: fluid flow and major reactor components [4]. ....	5
Figure 3: Cross sectional taken from the proposed 64 element fuel assembly [4].....	6
Figure 4: Fuel-cross section with overlaid boundary conditions (left) and the model geometry and mesh (right)[36].....	22
Figure 5: a) A diagram showing the geometry and labelling dimensions of a fuel pellet in an element. b) A diagram showing the geometry of the modified cylinder shape of the pellet [8]. ....	23
Figure 6: Plot displaying the temperature of the outer surface of the SWR fuel element clad [4].....	34
Figure 7: Plot of specific heat capacity of Zircaloy used within MPM-FAST [8] .....	36
Figure 8: Presents the thermal conductivity of 310 stainless steel [44].....	37
Figure 9: Linear fitting of Young's modulus data.....	39
Figure 10: Thermal strain data and fit for 310 stainless steel [44] .....	41
Figure 11: Fill gas calculation geometry, a) shows the division of the free volume regions into subdivisions, b) shows the detailed geometry of $V_4$ [8].....	51
Figure 12: Meshed geometries of pellet and sheath as outlined by parameters listed in Tables 8 and 9.....	95

Figure 13: Meshed geometry of FG diffusion model component for MPM-FAST.....	96
Figure 14: The geometries of the model components and summaries of the physical phenomena solved within each component.....	97
Figure 15: Power histories for DME-221 ThO <sub>2</sub> fueled elements, with low exit burnup ~360 MWh kgHE <sup>-1</sup> and high exit burnup ~620 MWh kgHE <sup>-1</sup> [38]. .....	110
Figure 16: Power histories for DME-221 (Th,U)O <sub>2</sub> 1.0 wt% U-235 fueled elements, with low exit burnup ~ 500 MWh kgHE <sup>-1</sup> and high exit burnup ~ 830 MWh kgHE <sup>-1</sup> [38].....	111
Figure 17: Power histories for DME-221 (Th,U)O <sub>2</sub> 1.5 wt% U-235 fueled elements, with low exit burnup >540 MWh kgHE <sup>-1</sup> and high exit burnup >900 MWh kgHE <sup>-1</sup> [3].....	112
Figure 18: Comparison of Thermal Conductivity correlations for 100% theoretically dense ceramic used in each case for 1.5% U-235 DME-221 Fuel. ....	114
Figure 19: Five power histories of OE from each bundle from BDL-422 [70]..	125
Figure 20: Unirradiated UO <sub>2</sub> thermal conductivity model compared to the unirradiated (Th,Pu)O <sub>2</sub> model.....	131
Figure 21: Centerline temperature and %FGR calculations for Case 2 simulating of the normalized ADD OE. ....	133
Figure 22: Centerline temperature and %FGR calculations for the Case 2) simulation of normalized ADF OE. ....	135
Figure 23: Centerline temperature and %FGR calculations for the Case 2) simulation of normalized ADA IE.....	136

Figure 24: Calculated centerline temperature for the three linear power cases a) 25 kW m <sup>-1</sup> b) 40 kW m <sup>-1</sup> c) 55 kW m <sup>-1</sup> presented with the uncertainty that arises in the model from the thermal conductivity correlation for the (Th,U)O <sub>2</sub> Case 2) model. ....	149
Figure 25: Calculated centerline temperature for the three linear power cases a) 25 kW m <sup>-1</sup> b) 40 kW m <sup>-1</sup> c) 55 kW m <sup>-1</sup> presented with the uncertainty that arises in the model from the thermal conductivity correlation for the (Th,Pu)O <sub>2</sub> Case 1) model. ....	150
Figure 26: Temperature of the outer clad surface for an SCWR fuel element. ..	153
Figure 27: Relative power profile based on axial location along a SCWR fuel element.....	154
Figure 28: Meshed geometry for a subsection model of the SCWR inner ring fuel element. ....	155
Figure 29: Mid-pellet radial fuel temperature profiles for subsection #1 and subsection #14, here BOL is Beginning of Life, and EOL is End of Life.....	156
Figure 30: A comparison of the modeled centreline grain diameters, using two different grain growth models.....	185
Figure 31: Default view of the MPM-FAST using the Windows version of COMSOL Multiphysics 4.4.....	337
Figure 32: Global Definitions drop menu expanded, presenting the parameter table.....	338
Figure 33: Global Definitions drop menu and Functions expanded, presenting the power history for one of the elements from BDL-422.....	347
Figure 34 Model 1, Definitions, and Variables drop menus expanded, presenting the table for Input Parameter Switches table.....	349

Figure 35: Study 1 drop menu expanded. ....	350
Figure 36: GUI during a calculation, most functions are locked, with access to the progress of the calculation available via the various tab in the left most column of the GUI. ....	351
Figure 37: Displays the GUI where the data from the calculation of the average fuel-to-sheath heat transfer coefficient. ....	353
Figure 38: Expansion of the Results drop menu with the pellet temperature profile selected. ....	355

## List of Tables

Table 1: Canadian SCWR core conceptual design parameters [4].....	6
Table 2: Dimensions from conceptual design.....	7
Table 3: Symbols used to describe pellet geometry.....	24
Table 4: Gas properties for use with the AECL model for the thermal properties of the fill gas[49].....	45
Table 5: List of models that affect deformation that are UO <sub>2</sub> based. ....	85
Table 6: Generalized coefficient terms that allow for customized ODEs and PDEs to be solved withn COMSOL .....	88
Table 7: Parameters that control time stepping in MPM-FAST.....	92
Table 8: Parameters within global domain that establish pellet and sheath geometry. ....	93
Table 9: Parameters that establish mesh distribution on the pellet and sheath model geometries.....	94
Table 10: Parameters that select the specific materials to model within MPM-FAST.....	98
Table 11: Parameters that inform the model about the composition of the mixed oxide fuel. ....	99
Table 12: Variables within model component 1 to enable a solution to heat transfer through the materials added to MPM-FAST. ....	100
Table 13: Variables within model component 1 added to allow for the deformation model to be solved.....	102



Table 14: Coefficients added to establish the ODE that solves the FG diffusion in MPM-FAST.....	103
Table 15: Parameters added for FG diffusion calculations.....	104
Table 16: Variables added to model component 1 for the FG diffusion calculation. ....	105
Table 17: Variables implemented in model component 2. ....	107
Table 18: Comparison of modelled centerline temperatures for DME-221 Elements.....	113
Table 19: Comparison of the maximum centerline temperature calculated by the (Th,U)O <sub>2</sub> models and the UO <sub>2</sub> model. ....	116
Table 20: Modeled Percent FGR for Case 1 and Case 2). ....	117
Table 21: Comparison of PIE FGR results to UO <sub>2</sub> model results.....	119
Table 22: Modeled MP sheath strain compared to PIE data.....	120
Table 23: Modeled PI sheath strain compared to PIE data. ....	121
Table 24: Comparison of the maximum calculated fuel centerline temperature for the UO <sub>2</sub> model and (Th,Pu)O <sub>2</sub> for the un-normalized power histories of BDL-422 experiment . ....	128
Table 25: Comparison of the maximum calculated fuel centerline temperature for the UO <sub>2</sub> model and (Th,Pu)O <sub>2</sub> for the normalized power histories of BDL-422 experiment. ....	129
Table 26: %FGR model results for the (Th,Pu)O <sub>2</sub> , (Case 1, Case 2), and UO <sub>2</sub> with the Un-Normalized (UN) and Normalized (N) power histories and the PIE results of BDL-422 are presented.....	132

Table 27: A comparison of the average measured mid-pellet strain to UO <sub>2</sub> , and both (Th,Pu)O <sub>2</sub> model results.....	138
Table 28: UO <sub>2</sub> and (Th,Pu)O <sub>2</sub> modelling results compared to the averaged PI measurements from BDL-422.....	139
Table 29: Design parameters for the fuel element used for sensitivity analysis.	141
Table 30: Modelling results for MP strains, PI strains, and FG volume for the base cases of the (Th,U)O <sub>2</sub> and Th,PuO <sub>2</sub> models compare to FAST's UO <sub>2</sub> results [8]. .....	144
Table 31: SA for Case 2 (Th,U)O <sub>2</sub> model.....	147
Table 32: SA for Case 1 (Th,Pu)O <sub>2</sub> model (fit to UN power histories).....	148
Table 33: Input Parameters used to generate SCWR model.....	152
Table 34: Parameters required to calculate the Heat capacity of UO <sub>2</sub> using the Fink correlation. ....	177
Table 35: IE FGR fitting for un-normalized BDL-422 power histories. ....	188
Table 36: OE FGR fitting for un-normalized BDL-422 power histories.....	188
Table 37: IE FGR fitting for normalized BDL-422 power histories. ....	189
Table 38: OE FGR fitting for normalized BDL-422 power histories. ....	190
Table 39: Parameters that establish the MPM-FAST's geometry.....	339
Table 40: Parameters that describe the initial values for various physical aspects of the fuel pellet and sheath.....	340
Table 41: Parameters that control the finite-element mesh. ....	341

Table 42: Solver control variables. ....	341
Table 43: Initial guesses or tolerance values for non-linear calculations. ....	342
Table 44: Initial values for the internal element volume displayed in Figure 5. ....	343
Table 45: Parameters to determine the initial mole fractions of fill gas, temperature and pressure. ....	344
Table 46: Energy of fission, initial values for the mass, atomic weight and atom percent of pellet materials for burnup calculation. ....	345
Table 47: Parameters that enable the model to determine the production of stable fission gas during irradiation. ....	346

## List of Acronyms

at%.....	Percent by Number of Atoms
BOL.....	Beginning of Life
CNL.....	Canadian Nuclear Laboratories
EOL.....	End of Life
FAST.....	Fuel And Sheath modelling Tool
FG.....	Fission Gas
FGR.....	Fission Gas Release
GIF.....	Generation IV International Forum
IST.....	Industry Standard Toolset
ITU.....	Institute for Trans Uranium Elements
LER.....	Linear Element Rating
MP.....	Mid-Pellet
MPM-FAST.....	Multi-Pellet Material Fuel And Sheath modelling Tool
N.....	Normalized
NOC.....	Normal Operating Conditions
NPP.....	Nuclear Power Plants
ODE.....	Ordinary Differential Equation
PDE.....	Partial Differential Equation
PHWR.....	Pressurized Heavy Water Reactor

PI.....	Pellet-to-pellet Interface
PIE.....	Post Irradiation Examination
RMCC.....	Royal Military College of Canada
SA.....	Sensitivity Analysis
SCWR.....	Super Critical Water cooled Reactor
Tecdoc.....	Technical Document
UN.....	Un-Normalized
wt%.....	Percent by Weight

## List of Symbols

Symbol	Units	Description
$P_r$	m	Pellet Radius
$P_L$	m	Pellet Length
$D_d$	m	Dish Depth
$D_r$	m	Dish Radius
$R_c$	m	Radial Chamfer
$A_c$	m	Axial Chamfer
$L_w$	m	Land Width
$P_p$	m	Initial Pellet-to-Pellet Gap
$D_{gap}$	m	Initial Pellet-to-Sheath Gap
$S_T$	m	Sheath Thickness
$r$	m	Radial Location
$T$	K	Temperature
$T_0$	K	Reference Temperature
$T_{sheath}$	K	Outside Sheath Temperature

$T_{coolant}$	K	Bulk Coolant Temperature
$T_{fuel}$	K	Temperature of Fuel's Surface
$T_{Rm}$	K	Reduced Temperature
$T_c$	K	Reference Temperature for Gas Calculation
$t$	s	Time
$\rho$	$\text{kg m}^{-3}$	Density
$\rho_{0Zr-4}$	$\text{kg m}^{-3}$	Initial Density of Zircaloy-4
$\rho_{Zr-4}$	$\text{kg m}^{-3}$	Density of Zircaloy-4
$\rho_{0310}$	$\text{kg m}^{-3}$	Initial Density of 310 Stainless Steel
$\rho_{max}$	$\text{kg m}^{-3}$	100% Theoretical Density
$\rho_U$	$\text{kg m}^{-3}$	Density of Uranium
$\rho_{UO_2}$	$\text{kg m}^{-3}$	Density of Uranium Dioxide
$k$	$\text{W m}^{-1} \text{K}^{-1}$	Thermal Conductivity
$k_f$	$\text{W m}^{-1} \text{K}^{-1}$	Thermal Conductivity of Fuel
$k_s$	$\text{W m}^{-1} \text{K}^{-1}$	Thermal Conductivity of Sheath
$k_{oxide}$	$\text{W m}^{-1} \text{K}^{-1}$	Thermal Conductivity of $\text{ZrO}_2$

$k_{Zr-4}$	$W m^{-1} K^{-1}$	Thermal Conductivity of Zircaloy-4
$k_{310}$	$W m^{-1} K^{-1}$	Thermal Conductivity of 310 Stainless Steel
$k_g$	$W m^{-1} K^{-1}$	Thermal Conductivity of Free Volume Gas
$k_{g,AECL}$	$W m^{-1} K^{-1}$	Free Volume Gas using AECL Calculation
$k_{Lucuta}$	$W m^{-1} K^{-1}$	Lucuta thermal Conductivity Model
$k_0$	$W m^{-1} K^{-1}$	Unirradiated Thermal Conductivity
$k_{0,HM}$	$W m^{-1} K^{-1}$	Unirradiated $UO_2$ Thermal Conductivity by Harding
$k_{0,AECL}$	$W m^{-1} K^{-1}$	ELESTRES Unirradiated Thermal Conductivity of $UO_2$
$k_{(Th,U)O_2}$	$W m^{-1} K^{-1}$	Effective Thermal Conductivity of (Th,U) $O_2$ Fuel
$k_{(Th,Pu)O_2}$	$W m^{-1} K^{-1}$	Effective Thermal Conductivity of (Th,Pu) $O_2$ Fuel
$k_{0,Belle}$	$W m^{-1} K^{-1}$	Unirradiated (Th,U) $O_2$ Thermal Conductivity by Belle and Berman
$k_{0,Bakker}$	$W m^{-1} K^{-1}$	Unirradiated (Th,U) $O_2$ Thermal Conductivity by Bakker et al
$X_m$	$W m^{-1} K^{-1}$	Thermal Conductivity as a Function of Temperature
$C_p$	$J kg K^{-1}$	Specific Heat Capacity
$C_{p(Th,U)O_2}$	$J kg^{-1} K^{-1}$	(Th,U) $O_2$ Heat Capacity
$C_{p(Th,Pu)O_2}$	$J kg^{-1} K^{-1}$	(Th,Pu) $O_2$ Heat Capacity



$C_{pThO_2}$	$J\ kg^{-1}\ K^{-1}$	Heat Capacity of ThO <sub>2</sub>
$C_{pPuO_2}$	$J\ kg^{-1}\ K^{-1}$	Heat Capacity of PuO <sub>2</sub>
$Q_{prod}$	$J\ m^{-3}\ s^{-1}$	Volumetric Heat Production
$F_v$	N	External Forces
$\sigma$	Pa	Stress
$\sigma_x$	Pa	Axial Component of Stress
$\sigma_y$	Pa	Axial Component of Stress
$\sigma_z$	Pa	Axial Component of Stress
$\sigma_r$	Pa	Radial Component of Stress
$\sigma_\theta$	Pa	Hoop Component of Stress
$\sigma_\phi$	Pa	Creep Stress
$\tau_{xy}$	Pa	Off Axis Component of Stress
$\tau_{xz}$	Pa	Off Axis Component of Stress
$\tau_{yz}$	Pa	Off Axis Component of Stress
$\sigma_F$	Pa	Fracture Strength of UO <sub>2</sub>
$\epsilon_{elastic}$	Unitless	Elastic Strain

$\varepsilon_x$	Unitless	Axial Component of Strain
$\varepsilon_y$	Unitless	Axial Component of Strain
$\varepsilon_z$	Unitless	Axial Component of Strain
$\gamma_{xy}$	Unitless	Off Axis Component of Strain
$\gamma_{xz}$	Unitless	Off Axis Component of Strain
$\gamma_{yz}$	Unitless	Off Axis Component of Strain
$\varepsilon_{inelastic}$	Unitless	Inelastic Strain
$\varepsilon_{total}$	Unitless	Total Strain
$\varepsilon_{thrm}$	Unitless	Thermal Strain
$\varepsilon_{thm,(Th,U)O_2}$	Unitless	Thermal Strain Correlation for (Th,U)O <sub>2</sub>
$\varepsilon_{thrm,(Th,Pu)O_2}$	Unitless	Thermal Strain Correlation for (Th,Pu)O <sub>2</sub>
$\varepsilon_r$	Unitless	Radial Component of Strain
$\varepsilon_\theta$	Unitless	Hoop Component of Strain
$\varepsilon_\phi$	Unitless	Creep Strain
$\varepsilon_{\phi,ir}$	Unitless	Creep Strain Caused by Irradiation
$\varepsilon_{vol,dens}$	Unitless	Densification Strain

$\varepsilon_{vol,SFP}$	Unitless	Strain Caused by Solid Fission Products
$\varepsilon_{vol,GFP}$	Unitless	Strain by Grain Boundary Fission Gas Bubble Swelling
$E$	Pa	Young's Modulus
$E_{Zr}$	Pa	Young's Modulus of Zircaloy-4
$E_{310}$	Pa	Young's Modulus of 310 Stainless Steel
$E_{ThO_2}$	Pa	Young's Modulus for ThO <sub>2</sub>
$\nu$	Unitless	Poisson's Ratio
$\nu_{ThO_2}$	Unitless	Poisson's Ratio for ThO <sub>2</sub>
$G$	Pa	Shear Modulus
$\alpha_p$	K <sup>-1</sup>	Thermal Expansion Coefficient
$L$	m	Initial Length of Component
$h_{film}$	W m <sup>-2</sup> K <sup>-1</sup>	Heat Transfer of Steam Film
$h_{gap,gas}$	W m <sup>-2</sup> K <sup>-1</sup>	Heat Transfer Through Free Volume Gas
$h_{gap,solid}$	W m <sup>-2</sup> K <sup>-1</sup>	Heat Transfer Through Pellet-to-Sheath Contact
$h_{gap,rad}$	W m <sup>-2</sup> K <sup>-1</sup>	Heat Transfer Through EM Waves
$t_{oxide}$	m	Thickness of ZrO <sub>2</sub> Layer

$Q_r$	$\text{W m}^{-2}$	Sheath to Coolant Heat Flux
$Q_{oxide}$	$\text{W m}^{-2}$	ZrO <sub>2</sub> Exothermic Component to Heat Flux
$\delta_{oxide}$	$\text{K}^{-1}$	ZrO <sub>2</sub> Growth Coefficient
$t_\alpha$	m	Thickness of Zircaloy Oxygen Strengthened Alpha Phase
$\delta_\alpha$	Unitless	Oxygen Strengthened Zircaloy Alpha Phase Growth Coefficient
$t_{lost}$	m	Zircaloy Lost to Sheath Thinning
$\phi_{Flux}$	$\text{m}^{-2} \text{s}^{-1}$	Fast Neutron Flux
$\phi$	$\text{m}^{-2} \text{s}^{-1}$	Local Thermal Neutron Flux
$\eta_{fast}$	Unitless	Neutrons Released per Fission
$E_f$	J	Energy Released per Fission
$d_{gap}$	m	Average Distance Between Pellet and Sheath
$R_f$	m	Surface Roughness of Pellet
$R_s$	m	Surface Roughness of Sheath
$g$	m	Effective Temperature Jump Distance
$g_m$	m	Jump Distance of Gas Mixture
$g_{0,i}$	m	Jump Distance of Gas Component

$y_i$	Unitless	Mole Fraction of Gas Component
$M_i$	kg mol <sup>-1</sup>	Molar Mass of Gas Component
$s_i$	Unitless	Empirically Derived Fitting Variable
$Y_m$	Unitless	Accounts for Gas Thermal Conductivity Changes at High Pressure
$P$	Pa	Gas Pressure
$P_{Rm}$	Pa	Reduced Pressure
$P_c$	Pa	Reference Pressure for Gas Calculations
$P_i$	Pa	Local Average Contact Pressure
$P_{est}$	Pa	Contact Pressure Estimate
$P_f$	Pa	Contact Penalty Factor
$A_{co}$	m	Axial Contact Offset
$H$	Pa	Meyer Hardness of Zircaloy-4
$\sigma_{SB}$	W m <sup>-2</sup> K <sup>-4</sup>	Stefan-Boltzmann Constant
$\varepsilon_{e,s}$	Unitless	Emissivity of the Sheath
$\varepsilon_{e,f}$	Unitless	Emissivity of the Fuel
$n_{mol}$	mol	Amount of Gas in Free Volume

$\rho_{molar}$	$\text{mol m}^{-3}$	Molar Density of the Gas
$R_{gas}$	$\text{J mol}^{-1}\text{K}^{-1}$	Gas Constant
$V$	$\text{m}^3$	Free Volume Within Fuel Element
$V_{pellet}$	$\text{m}^3$	Volume Around Pellet
$V_{1,2,3,4,5}$	$\text{m}^3$	Volumes of Subcomponents around Pellet
$V_{ends}$	$\text{m}^3$	Volume in the Element Around the End Caps
$V_{plenum}$	$\text{m}^3$	Volume of a Plenum
$F_{vf}$	Unitless	Volume Fraction Available Around Instrumentation
$n_p$	Unitless	Number of Pellets in Fuel stack
$n_{pl}$	Unitless	Number of Plena in Fuel Element
$f_{mag}$	Unitless	Proportionality Coefficient
$I_n$	-	$n^{\text{th}}$ Order Modified Bessel Function of the First Type
$K_n$	-	$n^{\text{th}}$ Order Modified Bessel Function of the Second Type
$P_{lin}$	$\text{W m}^{-1}$	Linear Power
$\beta_{flux}$	-	Flux shaping/Depression parameter
$\kappa_{flux}$	-	Flux shaping/Depression parameter

$\lambda_{flux}$	-	Flux shaping/Depression parameter
<i>PelletMat</i>	-	Logic Function
$Bu$	MWh kgHE <sup>-1</sup>	Burnup
$Bu_{avg}$	MWh kgHE <sup>-1</sup>	Average Burnup
$Bu_f$	Fission m <sup>-3</sup>	Fuel Burnup in of Fissions per Cubic Meter
$\beta_p$	at%	Burnup in Atom Percent
$M_U$	kg	Mass of Uranium in Element
$L$	m	Length of Fuel Stack
$\kappa_{1d}$	Unitless	Thermal Conductivity Dependence on Irradiation Induced Dislocations
$\kappa_{1p}$	Unitless	Thermal Conductivity Dependence on Solid Fission Product Precipitates
$\kappa_2$	Unitless	Thermal Conductivity Dependence on Porosity
$\kappa_3$	Unitless	Thermal Conductivity Dependence on the Deviation from Stoichiometry
$p$	Unitless	Porosity
$\sigma_s$	Unitless	Porosity Shape Factor
$M_{UO_2}$	Atom %	Atom % of UO <sub>2</sub> in (Th,U)O <sub>2</sub>
$A_n$	Unitless	Fitting Parameter in Thermal Conductivity Correlation

$B_n$	Unitless	Fitting Parameter in Thermal Conductivity Correlation
$C$	atoms m <sup>-3</sup>	Concentration of Fission Gas atoms within Fuel Grain
$D$	m <sup>2</sup> s <sup>-1</sup>	Effective Fission Gas Diffusion Coefficient of UO <sub>2</sub>
$D_{(Th,U)O_2}$	m <sup>2</sup> s <sup>-1</sup>	Effective Fission Gas Diffusion Coefficient of (Th,U)O <sub>2</sub>
$D_{(Th,Pu)O_2}$	m <sup>2</sup> s <sup>-1</sup>	Effective Fission Gas Diffusion Coefficient of (Th,Pu)O <sub>2</sub>
$D_0$	m <sup>2</sup> s <sup>-1</sup>	Single Fission Gas Atom Diffusion Coefficient
$D_{0,(Th,Pu)O_21}$	m <sup>2</sup> s <sup>-1</sup>	Single Fission Gas Atom Diffusion Coefficient for (Th,Pu)O <sub>2</sub>
$D_{0,(Th,Pu)O_22}$	m <sup>2</sup> s <sup>-1</sup>	
$D_{thrm}$	m <sup>2</sup> s <sup>-1</sup>	Diffusion Coefficient due to Thermally Activated Processes
$D_{irr}$	m <sup>2</sup> s <sup>-1</sup>	Diffusion Coefficient due to Irradiation Induced Vacancies
$D_{athrm}$	m <sup>2</sup> s <sup>-1</sup>	Diffusion Coefficient due to Athermal Effects
$P_{fg}$	atoms m <sup>-3</sup> s <sup>-1</sup>	Volumetric Production Rate of Fission Gas
$g_r$	m	Grain Radius
$g_d$	m	Grain Diameter
$g_{di}$	m	Initial Grain Diameter
$g_m$	m	Maximum Stable Grain Size



$g_{ir}$	m	Function of Temperature and Fission Rate Accounting Irradiation Effects on the Grain Size
$R_{fgflux}$	atoms m <sup>-2</sup> s <sup>-1</sup>	Release rate to the Grain Boundary
$R_{gb}$	atoms m <sup>-3</sup> s <sup>-1</sup>	Volumetric Release Rate
$\eta$	Unitless	Non-Dimensional Representation of Fuel Grain
$K_f$	cm <sup>3</sup> h <sup>-1</sup>	(Th,U)O <sub>2</sub> Grain Growth Fitting Coefficient
$Q$	10 <sup>3</sup> J mol <sup>-1</sup>	Vapour Activation Constant for (Th,U)O <sub>2</sub>
$k_g$	m <sup>2</sup> s <sup>-1</sup>	Grain Growth Rate
$b'$	s <sup>-1</sup>	Intragranular Resolution Rate
$g_a$	s <sup>-1</sup>	Trapping Rate
$l_f$	m	Average Distance Traveled by Fission Fragments
$\alpha_{fgb}$	Unitless	Number of Fission Gas Bubbles Nucleated
$Z_0$	m	Average Distance Between Where the Fission Took Place and the Furthest Effects of the Spike
$R_B$	m	Average Radius of Intragranular Pores
$F_{rate}$	s <sup>-1</sup>	Fission Rate
$\Omega$	m <sup>-3</sup>	Atomic Volume

$C_v^0$	$m^{-3}$	Vacancy Concentration of Unirradiated $UO_2$
$\mu$	$m^{-2}$	Sink Strength for Crystallographic Point Defects
$\nu_v$	$s^{-1}$	Vacancy Jump Frequency
$Z_n$	Unitless	Average Number of Sites Available for Recombination Around Defects
$N_{Av}$	$mol^{-1}$	Avogadro's Number
$Mm_U$	$kg\ mol^{-1}$	Molar Mass of Natural Uranium
$G_b$	$atoms\ m^{-3}$	Fission Gas on the Grain Boundary
$R_e$	$atoms\ m^{-3}\ s^{-1}$	Release Rate from the Grain Boundary to the Free Volume of the Fuel Element
$G_{bsat}$	$atoms\ m^{-3}$	Grain Boundary Saturation Condition
$P_{ext}$	Pa	Applied Hydrostatic Pressure
$\gamma_{se}$	$J\ m^{-2}$	Surface Energy of the Fission Gas Bubbles
$k_B$	$J\ K^{-1}$	Boltzmann Constant
$f_b$	Unitless	Fraction of Grain Surface Covered in Bubbles
$\theta_{fg}$	$^\circ$	Half-Angle Between Bubble Surfaces
$f(\theta_{fg})$	Unitless	Function that Accounts for the Shape of the Bubbles
$r_f$	m	Radius of Curvature of a Fission Gas Bubble

$\tau_{fg}$	s	Time Constant of Fission Gas Release
$R_{e,Tot}$	mol s <sup>-1</sup>	Total Fission Gas Atoms Released to Element
$F_{PoreR}$	Unitless	Fraction of Porosity Removed from the Fuel

## **1 Introduction**

For the last decade Canadians consumed roughly 15500 to 16500 kWh of electrical power per capita [1], with other industrialized countries having consumption rates above 5000 kWh per capita. The use of electrical power supports our daily lives by: enabling our living spaces to be a comfortable temperature, preserving food until it is convenient to eat, providing light at any time of day, and much more. With this standard of living in place in Canada and many other countries, electrical power production will continue to be an important resource, the demand of which is likely to grow globally. Certain means of power production are dependent on the combustion of fossil fuels. With the concern of CO<sub>2</sub> levels within the earth's atmosphere, the expansion of fossil fuel power production will be scrutinized in a way that is unprecedented. Within this consumer space the market share of nuclear power production will continue to be necessary, and has the opportunity to thrive.

When nuclear power is used to generate electricity, the energy from a sustained fission chain reaction is used to heat coolant (in most cases water) and generate steam (nuclear power production is the most interesting way to boil water). The steam is then used to drive a turbine. Since the fission chain reaction in a power plant's nuclear reactor fulfills the same function as fossil fuel, the

fissile material within the reactor is also described as “fuel”, with the consumption of the fuel described as burnup. There are many designs of reactors used in all the Nuclear Power Plants (NPP) around the world. Once fissile nuclear fuel is irradiated, the fission products are radioactive. Ideally during the normal operation of a reactor these fission products would not leave the reactor area minimizing unexpected radiation exposure for workers, as radiation limits are highly regulated for health and safety purposes. The primary method of achieving this is to keep the fission products from contaminating the coolant. In the current reactor designs fissile material of the fuel is formed into cylindrical ceramic pellets, ~ 1-2 cm in length (with small features formed during pelleting in order to allow the pellet to expand and thus reduce contact pressure), the stack of ceramic pellets are then encased in cylinders of a zirconium based metal alloy (conveniently named Zircaloy-4), known as cladding or sheathing, the pellet stack encased in Zircaloy-4 is referred to as a fuel element. Specifically for the Canadian designed Pressurized Heavy Water Reactors (PHWR), a fuel element is approximately 1.2 cm in diameter, fueled with natural or natural equivalent enrichment uranium dioxide, and is about 50 cm in length. 37 fuel elements are then assembled together, as a series of three concentric rings and a single central element, by welding both ends of each element to Zircaloy endplates. After the fuel is constructed in this fashion it is known as a fuel bundle and is ready to be used in the reactor. Figure 1 shows a diagram of a fuel bundle used in a Canadian

designed PHWR reactor at the Bruce Nuclear Power. Other features of the Canadian PHWR system is that the heavy water is used as moderator and coolant. With the coolant and fuel being confined to fuel channel tubes pressurized to about 10 MPa.

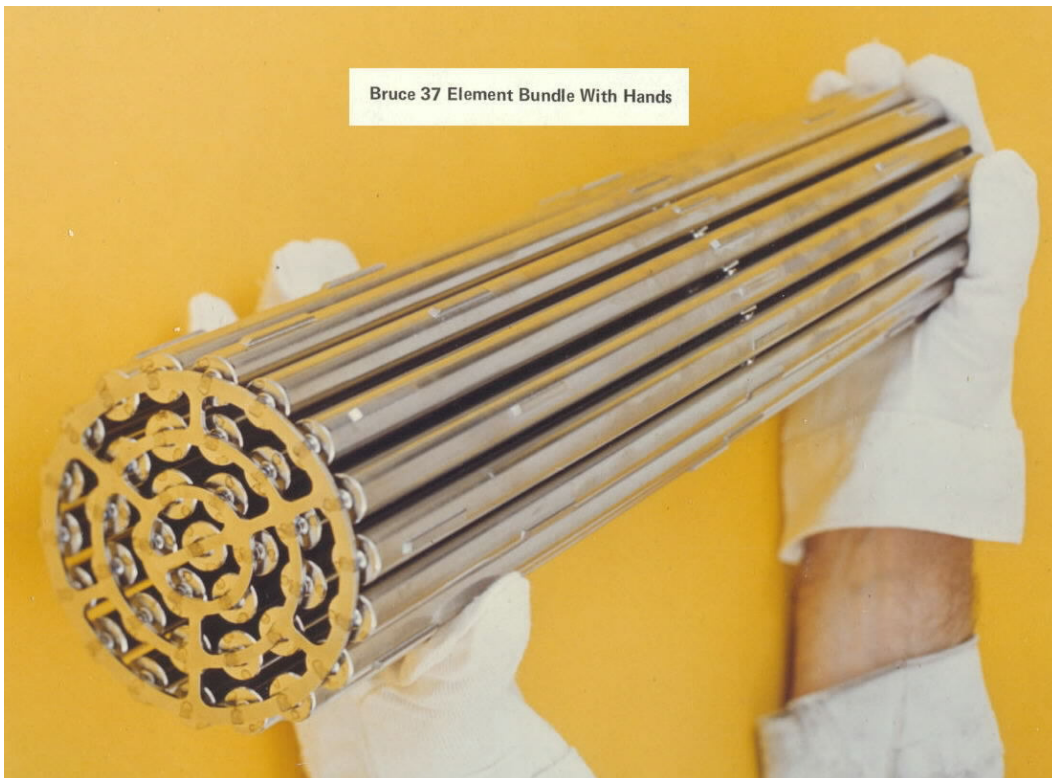


Figure 1: Picture of a fuel bundle [2].

The Generation IV International Forum (GIF) was established as an international co-operative research endeavour to direct and support the development of the next generation of NPP [3]. Nations involved with GIF agreed to pursue research that was deemed capable of providing specific improvements

over the current NPP technology. In order to address public concerns in regards to nuclear power production, the GIF reactors are to meet specific sustainability, economic, safety and reliability as well as proliferation resistant criteria that are a marked improvement over current NPP and be competitive with other power production methods.

Canada's participation in GIF is headed by Canadian Nuclear Laboratories (CNL) in conjunction with university partners, and has examined the viability of a Super Critical Water cooled Reactor (SCWR). The major features that Canada's SCWR design has in common with the PHWR type is that the fuel is contained within pressure tubes (rather than a large pressure vessel), that house 5 m long fuel assemblies, and would use deuterium as moderator. There are several major differences in the proposed reactor system, for example the coolant will be light water at 25 MPa and be between 325 to 625°C (transitioning into its supercritical state), and the clad material is required to be a corrosive resistive metal (proposed to be a variant of 310 stainless steel or Inconel 800). A major difference in fuel composition has also been proposed, it is to be composed of (Th,Pu)O<sub>2</sub> with 13 wt% Pu. The fuel was selected in the interest of reducing available plutonium (reducing proliferation risk by using up stock piled from Pu weapons programs), and to address some aspect of capital costs and sustainability with the thorium (Th is 3-4 times more abundant in the earth's crust compared to uranium). Figure 2

and Table 1 below provide further details pertaining to the Canadian's SCWR design [4]–[7].

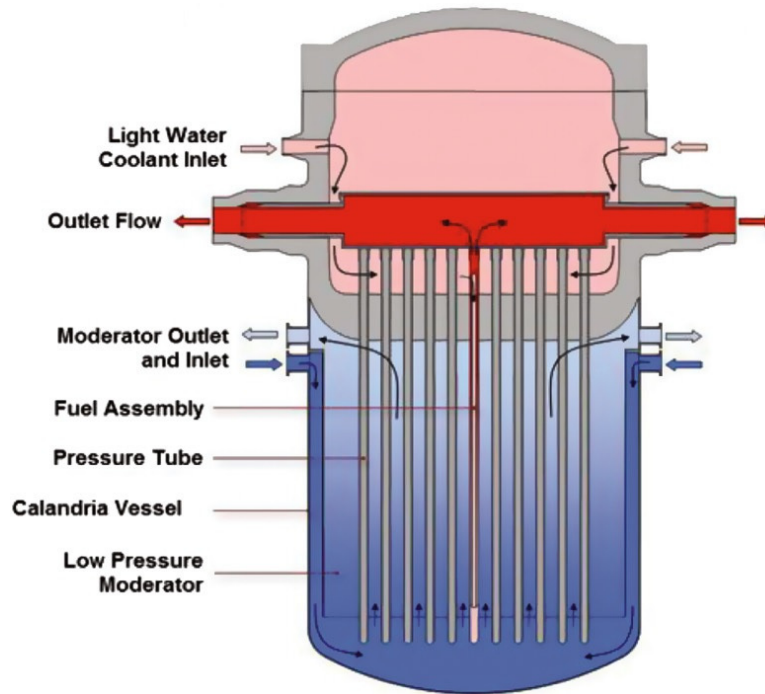


Figure 2: Diagram presenting a cross section of the Canadian SCWR, with labels for: fluid flow and major reactor components [4].

The  $(\text{Th,Pu})\text{O}_2$  fuel is held in the pressurized fuel assembly channels. As mentioned earlier, similar to other traditional fuel designs, the ceramic  $(\text{Th,Pu})\text{O}_2$  will be stacked into elements made with more corrosive resistant clad material. Once formed into an element, two rings of 32 fuel elements are then constructed into a fuel bundle placed within the assembly. Figure 3 displays a cross section of the fuel assembly and highlight the cross sectional features of the fuel bundle.



Table 1: Canadian SCWR core conceptual design parameters [4].

Parameter	Value
Thermal Power	2540 MW
Electric Power	1200 MW
Coolant Temperature	350 - 625°C
Coolant Pressure	25 - 26 MPa
Number of Fuel Channels	336
Core Radius	355 cm
Core Height	650 cm
Fuel Assembly Length	500 cm
Target Exit Burnup	40 MWd/kg

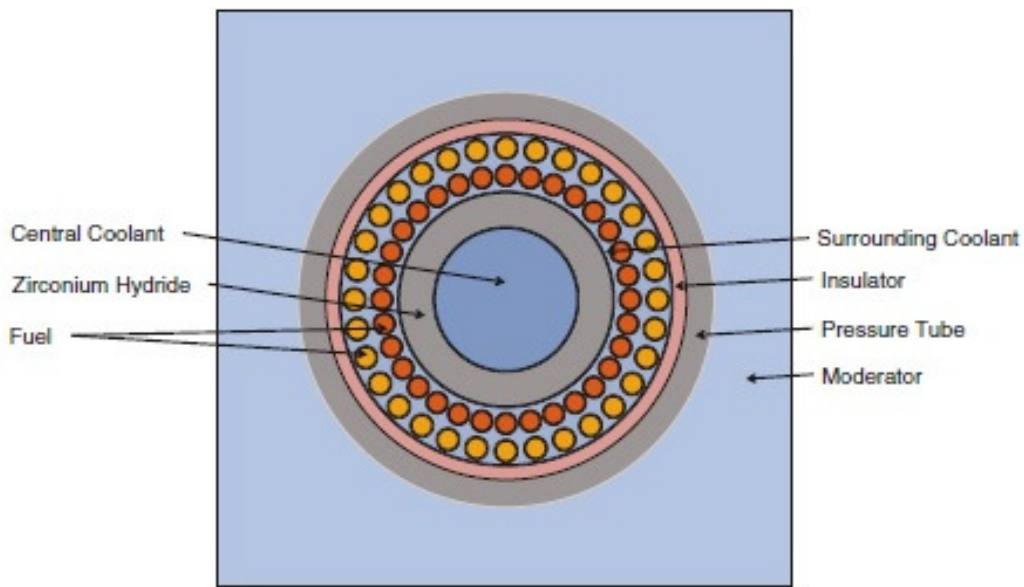


Figure 3: Cross sectional taken from the proposed 64 element fuel assembly [4].

Table 2 contains the dimensions from conceptual design for each of the fuel rings elements.

Table 2: Dimensions from conceptual design.

<b>Fuel Assembly Component</b>	<b>Parameter</b>	<b>Value</b>
Inner Fuel Ring	Number of Elements	32
	Approximate Pellet Radius	0.415 cm
	Clad Thickness	0.06 cm
	Approximate Outer Radius	0.475 cm
Outer Fuel Ring	Number of Elements	32
	Approximate Pellet Radius	0.44 cm
	Clad Thickness	0.06 cm
	Approximate Outer Radius	0.5 cm

It is desirable to begin to work out a range of viable options for the finer features of the (Th,Pu)O<sub>2</sub> fuel (such as: volume of a fission gas plenum, and pellet dimensions). Attempting to determine these fuel features solely through experimental means would be time consuming and costly. By examining what is currently known about the irradiation of Th-based nuclear fuel and developing a fuel performance model for (Th,Pu)O<sub>2</sub>, the development of a computational tool would be able to identify possible fuel designs and reduce the number of test irradiations. Another benefit of developing a Th-based fuel performance model is to enable examination of the model's limitations and determine where there is insufficient data to have a viable safety analysis model (as required for safety and licencing purposes).

Within the nuclear engineering group at the Royal Military College of Canada (RMCC), previous theses were devoted to the development of fuel performance models for the uranium dioxide ( $\text{UO}_2$ ) fueled elements used within the current fleet of Pressurized Heavy Water Reactors (PHWR) [8]–[10]. Each of these models were developed using the commercially available finite element analysis software COMSOL Multiphysics® (COMSOL is capable of calculating solutions to coupled Ordinary Differential Equations (ODEs) and Partial Differential Equations (PDEs)). The latest of these works is the Fuel And Sheath modelling Tool (FAST) [8]. Our group identified that the development of these types of models using COMSOL would enable for the testing of new material properties and prototyping of new physical phenomena models [10]. As such the opportunity to model the SCWR fuel by adding new capabilities to FAST is an ideal exercise to demonstrate this potential.

The majority of this work will outline the development of  $(\text{Th,U})\text{O}_2$  and  $(\text{Th,Pu})\text{O}_2$  fuel performance models that have been added to FAST, generating the Multi-Pellet Material Fuel And Sheath modelling Tool (MPM-FAST), and how it is implemented on COMSOL Multiphysics version 5.0.1.276. Following that, modelling results from MPM-FAST are compared to the Post Irradiation Examination (PIE) data from fuel elements of  $(\text{Th,U})\text{O}_2$ , and  $(\text{Th,Pu})\text{O}_2$  irradiation experiments conducted by CNL. Lastly an attempt to model the SCWR fuel using MPM-FAST will be presented and discussed.

## 2 State-of-the-Art

Fuel performance models calculate important parameters to assess fitness-for-service including: fuel temperature, sheath strain, pellet deformation, fission gas (FG) production, fission gas release (FGR) to the element free volume, and internal gas pressure. Many fuel performance models exist to calculate irradiation behaviour of commercial fuel. Primarily commercial reactors use a uranium based fuel cycle. For fuel elements using uranium dioxide ( $\text{UO}_2$ ) in the current Canadian PHWR fleet, ELESTRES is used for Normal Operating Conditions (NOC) and ELOCA for transient operating conditions, these codes are outlined by Chassie *et al.* [11], and Williams [12], respectively. The classification of fuel behaviour falls into two categories NOC and transient conditions. Transient fuel conditions refer to fuel behaviour that is changing rapidly over a very short time (minutes or less), under NOC the changes in fuel behaviour are slow (can be measured in days or longer). These two models are included in the Industry Standard Toolset (IST), which are a series of codes and models accepted by the Canadian Nuclear Safety Commission to be used for safety analysis. These fuel performance codes have many similarities to their internationally developed counter parts including: FRAPCON/FRAPTRAN ([13] and [14]), FALCON [15], TRANSURANUS [16], ALCYONE [17], and MOOSE/BISON [18].

Even though the utilization of thorium as a nuclear fuel has been discussed since the beginning of nuclear power production, limited work has been done to produce fuel performance models for Th-based ceramic fuel internationally. Results from irradiation tests [19] and material properties of ThO<sub>2</sub> suggest that Th-based fuel will have an overall cooler pellet centerline temperature and reduced FGR than UO<sub>2</sub> fuel type. This will provide a more efficient heat transfer from the fuel to the coolant.

Attempts at developing a fuel performance model for Th-based fuel have followed the same general process. This is to take an existing U-based fuel performance model, and modify it to make it representative of Th-based fuel irradiation. An early example on this method of model development was presented by Hastings and Notley in 1980 [20]. With data acquired from the experiments leading up to the irradiation of (Th,U)O<sub>2</sub> fuel in the Shippingport Light Water Breeding Reactor<sup>1</sup> [21], [22], Hastings and Notley altered the Canadian PHWR NOC fuel performance model ELESIM (predecessor to ELESTRES mentioned above), to predict the irradiation behaviour of (Th,U)O<sub>2</sub>. However there is no further documentation on this model.

---

<sup>1</sup> The Shippingport Light Water Breeding Reactor project aimed to study if (75% ThO<sub>2</sub> + 25% UO<sub>2</sub>) fuel could be used to fuel light water reactors. A reactor in Shippingport Pennsylvania was fueled entirely by this fuel type between 1976 – 1982. For about a decade prior to the fuel conversion a large research project was undertaken to understand the irradiation behaviour of this fuel, it included: irradiation experiments and the study of high temperature materials properties (Th,U)O<sub>2</sub>.

The next Th-based fuel performance model reported in the open literature was work done at the Idaho National Engineering and Environmental Laboratory in 2001. Loewen *et al.* outlined seven specific sub-models that were examined, and subsequently, modified the NOC model (FRAPCON) to produce a version they called FRAPCON-3Th (which accounted for ThO<sub>2</sub> and (Th,U)O<sub>2</sub> fuel properties) [23]. Within this work, a detailed comparison on the predicted thermal conductivity for UO<sub>2</sub> to various combinations of (Th,U)O<sub>2</sub> was presented. Loewen *et al.* finished reporting on their work by comparing results for several key fuel performance parameters, such as: centerline temperature, gas gap conductance, fuel growth and FGR for ThO<sub>2</sub>, 75%ThO<sub>2</sub>+25%UO<sub>2</sub> and 100% UO<sub>2</sub>.

In 2002 a group from MIT continued to work on developing a Th-based fuel performance model for FRAPCON. Long *et al.* presented work on the development of a high temperature fuel performance model [24]. Using the same data mentioned above from the Shippingport Light Water Breeding Reactor program as validation cases, they demonstrated that the Th-based version of the NOC fuel model FRAPCON was capable of replicating FGR from (Th,U)O<sub>2</sub>. One of the considerations they made was to edit the thermal conductivity model given by Belle and Berman [21], to assume the behaviour of the thermal conductivity of (Th,U)O<sub>2</sub> follows the same pattern as UO<sub>2</sub> above 2000 K. Long *et al.* made this assumption because there has not been data collected about the material

properties of (Th,U)O<sub>2</sub> at these temperatures. The second consideration that Long *et al.* made concerned altering the FG behaviour model in FRAPCON to account for the lower FGR measured from the (Th,U)O<sub>2</sub>. Heat is generated in the fuel where the neutrons are most likely to be captured by the fissile material within a pellet, which evolves over time during irradiation. In order to ensure the fuel model represents this, Long *et al.* also outlined a model to predict the radial power distribution, using coupled differential equations to represent the production and decay of important neutron capture isotopes within the fuel.

Similar work was presented by Lee *et al.* on the development of a (Th,U)O<sub>2</sub> version of Korea's Fuel Performance code INFRA-Th [25]. They implemented the change in radial power distribution as a polynomial function of fuel location and burnup. As a validation case for their (Th,U)O<sub>2</sub> model, they used INFRA-Th to replicate the irradiation history of (Th,U)O<sub>2</sub> elements from the IFA-652 Halden experiment [26]. In this experiment the fuel was instrumented, with internal element pressure gauges and thermistors constructed into the centerline of the fuel, to provide real time measurements of the element pressure and fuel centerline temperature, respectively. In addition to the Halden fuel experiment, they discuss the viability and ability of the model to represent duplex fuel pellets. The premise of duplex fuel is that there are two regions; a region of ThO<sub>2</sub>, within the center of the pellet, surrounded by an annular ring of UO<sub>2</sub>.

Long *et al.* [27] further examined the viability of other models to determine if the irradiation behavior of Th-based fuel in both NOC and transient conditions could be replicated. In this work Long *et al.* [27] examined the capabilities that were available to predict the centerline temperature and FGR of homogeneous (Th,U)O<sub>2</sub> fuel, the ThO<sub>2</sub>+UO<sub>2</sub> duplex fuel. The temperature distribution within a fuel pellet of homogeneous (Th,Pu)O<sub>2</sub> (4 wt% PuO<sub>2</sub>) was also assessed for NOC capabilities. Long *et al.* then attempted to predict the behaviour of each of these fuel types during Loss of Cooling Accident (LOCA) conditions. Long *et al.* stated that based on the scarcity of data for material properties of (Th,Pu)O<sub>2</sub> at that time, uncertainty greater than that found in the UO<sub>2</sub> calculation was expected. They came to this conclusion because at that time the latest comprehensive examination of literature by Bakker *et al.* for (Th,U)O<sub>2</sub> and (Th,Pu)O<sub>2</sub> could not provide key material properties (i.e. thermal expansion, and limited thermal conductivity data) for modelling these fuel types [28].

In the ensuing decade since this work by Long *et al.* [27], various international research programs have published their work on examining the material properties of mixed Thoria based ceramics. Specifically with India's focus to implement Th-based fuel into their current fleet of PHWRs, the study of the high temperature material behaviour, although limited, has begun. This was highlighted in the 2006 IAEA Technical Document (tecdoc) 1496 [29], and further expanded upon in the book entitled Thoria-based Nuclear Fuels published



in 2013 [30]. In addition to these works, an important set of thermal conductivity measurements in 2011 on (Th,Pu)O<sub>2</sub> were made at the Institute for Trans-Uranium Elements (ITU) in Karlsruhe, Germany. This has led to an initial correlation of the thermal conductivity behaviour of (Th,Pu)O<sub>2</sub> over an extended range of ThO<sub>2</sub> and PuO<sub>2</sub> compositions (ranging from 0 - 30 wt% PuO<sub>2</sub>) [31]. The publication of these sets of data have begun to enable the development of (Th,Pu)O<sub>2</sub> fuel performance models.

Since the publication of these data sets and material property behaviours, reports have been published on the development of fuel performance models for ceramic (Th,Pu)O<sub>2</sub> fuel pellets. There were three groups reporting on their efforts to produce a (Th,Pu)O<sub>2</sub> fuel performance model. The first was a brief report on the development of a radial power distribution sub-model to implement into TRANURANUS to enable modelling of (Th,Pu)O<sub>2</sub>. This model uses similar methods employed by Long *et al.* in 2002 with coupled differential equations except with the inclusion of Pu based capture and decay chains [32].

The second reported work on modelling (Th,Pu)O<sub>2</sub> was published by Boer *et al* [33]. Within their paper, they outlined an irradiation experiment in Belgium conducted between 2004 and 2006. Two instrumented elements fueled with (Th,Pu)O<sub>2</sub> (one with 7.9 atom % (at%) and the other 12.8 at% of metal atoms or non-oxygen atoms in the fuel) were irradiated . A fair amount of detail is given on

the fuel construction and irradiation history, including the online measurements of fuel temperature and element pressure during the fuel's residence time in the reactor. PIE data were also presented. Two main features were added within their internal lab fuel performance model MACROS in order to represent (Th,Pu)O<sub>2</sub> fuel. Modifications were made to the thermal conductivity model to ensure the unirradiated fresh fuel behaved like Cozzo *et al.* [31] measurements, as well as the radial power profile model. MACROS modelling results were compared to the in-reactor measurements of fuel centerline temperature and clad deformation PIE data. These data sets are in reasonable agreement with each other, and the model replicates the measured behaviour from the data [33].

Work done by Björk *et al.* in 2015 is the final published (Th,Pu)O<sub>2</sub> model. This was part of the Thor Energy research program on implementing Th-based fuel in the current light water reactor fleet [34],[35]. Similar to Long *et al.* in 2002 and Loewen *et al.*, Björk outlined the changes made to the current version of FRAPCON to produce FRAPCON-ThMOX. Of the three published works on modelling (Th,Pu)O<sub>2</sub>, Björk [34],[35] gave the most detail. She examined the available elastic deformation material data (Young's Modulus) for (Th,Pu)O<sub>2</sub>, thermal expansion, thermal conductivity, as well as updating the radial power profile model. Björk [35] stated that the FGR model developed by Long *et al.* was used [27]. Björk's modelling results were compared to the in-reactor measurements of the fuel centerline temperature of (Th,Pu)O<sub>2</sub> fuel containing 7.9

at% Pu metal content. The temperature calculation was within the experimental uncertainty based on the 7% uncertainty in the linear power associated with the Halden's research reactor [34]. Further modelling results are discussed in Björk's thesis [35], specifically the fuel experiment had not experienced any FGR, and that the FGR model results reflect this.

### 3 Goals and Scope of Work

The primary goal of this work was to develop NOC models of Th-based fuel, so that a design analysis tool for the SCWR fuel could be developed. As mentioned in Chapter 1, FAST is the latest UO<sub>2</sub> fuel performance model developed at the RMCC by Prudil *et al.* [36], [37], FAST has undergone proof of concept benchmarking to experiments that replicate both NOC and transient conditions for Canadian PHWR fuel [8]. FAST has demonstrated the similar capabilities of both ELESTRES and ELOCA. The other similarity that FAST shares with ELESTRES, is that finite element analysis is used to solve the fuel geometry deformation. FAST also shares the use of finite element analysis with ALCYONE, and MOOSE/BISON, as the underlying mathematical means to solve the system of equations that describe fuel behaviour [8].

When this work was started in 2012, the NOC fuel performance model FRAPCON (which has similar capabilities to ELESTRES) had been used as the basis for the development of a successful (Th,U)O<sub>2</sub> fuel model [23], [24]. Since FAST is capable of modelling the UO<sub>2</sub> fuel type, the development of a NOC (Th,U)O<sub>2</sub> model with FAST is a reasonable starting point for this work. As Long *et al.* mentioned in 2004, the feasibility of developing a (Th,Pu)O<sub>2</sub> model has another added uncertainty, because it has not been examined to the same extent as (Th,U)O<sub>2</sub> [27]. Using methods as outlined in the literature, the development of a

(Th,U)O<sub>2</sub> model from a UO<sub>2</sub> model was seen as an opportunity to learn how the new Th-models could be developed effectively. With the concern about limited (Th,Pu)O<sub>2</sub> data mentioned above, it is expected that material and irradiation effects of (Th,Pu)O<sub>2</sub> will be more similar to (Th,U)O<sub>2</sub> than UO<sub>2</sub>. Modelling assumptions could be made if (Th,Pu)O<sub>2</sub> data does not exist. In this thesis, the (Th,U)O<sub>2</sub> model is benchmarked against the PIE data from 12 elements that have been irradiated, as part of the DME-221 irradiation experiment, at CNL [38].

Once the (Th,U)O<sub>2</sub> fuel model had been benchmarked, development of the (Th,Pu)O<sub>2</sub> followed. Results obtained from the (Th,Pu)O<sub>2</sub> model will also be assessed against the PIE data from the BDL-422 irradiation experiment conducted at CNL. The goal of BDL-422 was to examine the high burnup and high power behaviour of Canadian PHWR (Th,Pu)O<sub>2</sub> fuel. For comparison the highest linear element rating and burnup were 70 kW m<sup>-1</sup> and 1100 MWh kgHe<sup>-1</sup> respectively, as compared to ~55 kW m<sup>-1</sup> and ~200 MWh kgU<sup>-1</sup> for the commercial reactor fuel [39], [40]. Björk *et al.* [34] and Boer *et al.* [33] compared their modelling results to online fuel temperature measurements; however, their irradiation experiments achieve much lower fuel temperatures and linear element rating compared to the BDL-422 fuel. For the fuel examined by Björk, the linear element rating is not reported but the maximum fuel temperature achieved is about 950°C [34]. For Boer *et al.*, a maximum temperature of 1192°C at a linear element rating of

33 kW m<sup>-1</sup> [33]. To accommodate the high temperature behaviour of the BDL-422 fuel, it is expected that modelling assumptions will need to be made for the (Th,Pu)O<sub>2</sub> model . This work will be beneficial to any subsequent (Th,Pu)O<sub>2</sub> modelling because fuel performance modelling has not been previously attempted in this temperature regime.

Once the (Th,Pu)O<sub>2</sub> model has been benchmarked against the PIE data of BDL-422, an attempt will be made to model the SCWR fuel. This will be an initial attempt to examine the proposed SCWR fuel. It will be a demonstration of the model's ability as a design analysis tool.

In summary this thesis proposes to develop fuel performance models for (Th,U)O<sub>2</sub> and (Th,Pu)O<sub>2</sub> ceramic fuel pellets. Results from these models will be compared to PIE data obtained from DME-221 and BDL-422 irradiation experiments that were previously conducted by CNL. Lastly with the data presented in Tables 1 and 2 (on pages. 6 and 7, respectively), the (Th,Pu)O<sub>2</sub> model in MPM-FAST will be used to model the behaviour of SCWR fuel during NOC.

## **4 Theory and Model Development**

MPM-FAST assumes simplified geometry and boundary conditions to approximate full element behaviour; the geometry and boundary conditions will be outlined in Section 4.1. Section 4.2 presents the differential equations that describe heat transport and deformation mechanics, which are relevant to all portions of the model's geometry. While Sections 4.3, 4.4, and 4.5 will focus on the implementation of these equations and additional physical behaviours considered within each of the three modelling regions of MPM-FAST: which are the sheath, the element free volume, and the fuel pellet, respectively.

### **4.1 Geometry and Boundary Conditions**

As mentioned in chapter 1, Canadian PHWR fuel is organized into bundles approximately 10 cm in diameter and ~50 cm in length, of concentric rings of cylindrical fuel elements (each element is ~12 mm in diameter), and are held together by welding each element to two end plates at either end of the bundle. The cylindrical design of a fuel element allows for the assumption of axial symmetry and reduces the model to two dimensions. It is further assumed that the irradiation behaviour of a single fuel pellet is representative of all the pellets within a fuel element. These assumptions lead MPM-FAST's geometry to consist

of a  $\frac{1}{2}$  pellet (that can include one or two dishes, a central hole and variation on axial and radial chamfers (see Table 3)), with the corresponding section of the sheath with azimuthal symmetry and periodic boundary conditions applied as shown in Figure 4 below. A sample of the meshed geometry is included on the right hand side of Figure 4 which was established by Prudil for FAST [8]. Control of the pellet size and geometry and the control of the meshing variables are outlined in the discussion of the input parameters within Chapter 5 and the effects of different meshing sizes are examined in the sensitivity analysis discussed in Chapter 6. How these boundary conditions are implemented is included in the description of the models within each portion of the model's geometry.

The left hand portion of Figure 4 displays the pellet and the sheath being filled with a grid. This grid represents the mesh used in the finite-element analysis. Finite element modelling takes a material of interest and divides it into small subsections called elements. The behaviour of each of these elements can be described by what occurs along the boundary of each of these elements. Where these boundaries intersect, generates what are called node points. The grid of node points is known as the mesh. At each node point in the mesh the physical and material properties are calculated as a series of polynomial approximations. A finite-element mesh acts as a piece-wise polynomial interpolation over the body of geometry of interest for the field quantities that describe the physical behaviour (see equations (1) and (2)) [41].



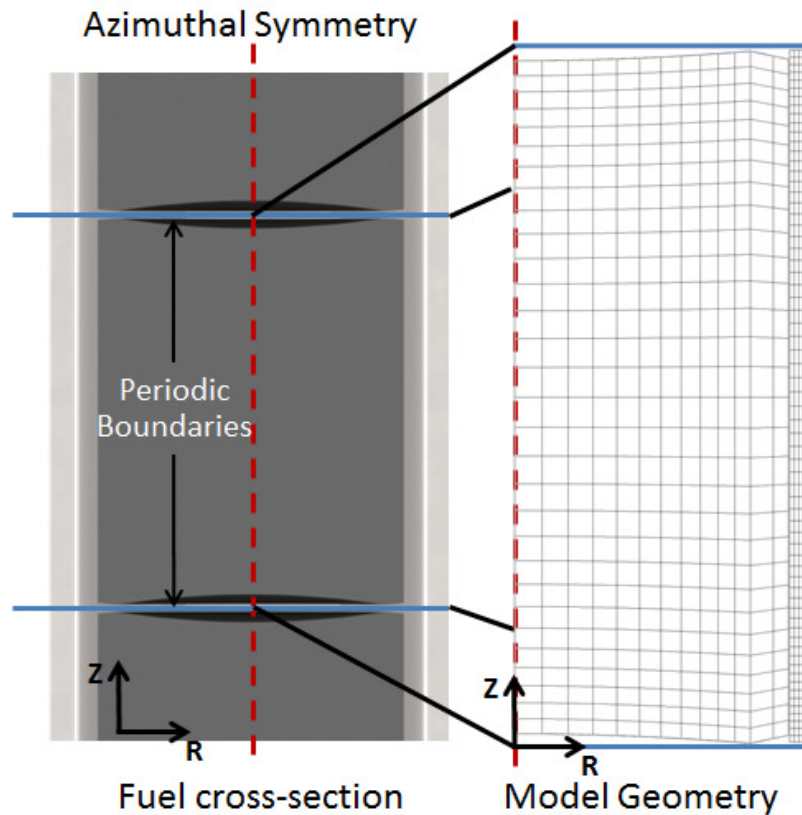


Figure 4: Fuel-cross section with overlaid boundary conditions (left) and the model geometry and mesh (right)[36].

The process of solving this set of polynomial approximations at the mesh points for the specific boundary conditions generates a set of simultaneous algebraic equations that are solved for the field quantities at the nodes. Each equation is solved at each node point and can lead to thousands of equations needing to be solved simultaneously; this lends itself to require computational

methods for solving this set of equations. Each dependent variable solved for at every mesh point generates what is known as a degree of freedom. The Degrees of Freedom (DOF) for a finite element simulation describes its size, and is a way of describing the complexity of the modelled system that is independent of the processing speed and memory requirements.

Figure 5 and Table 3 highlight the geometric features of a Canadian PHWR fuel pellet, outline the orientation of the r-z plane in the model, and lists the initial geometry input variables required to produce the geometry.

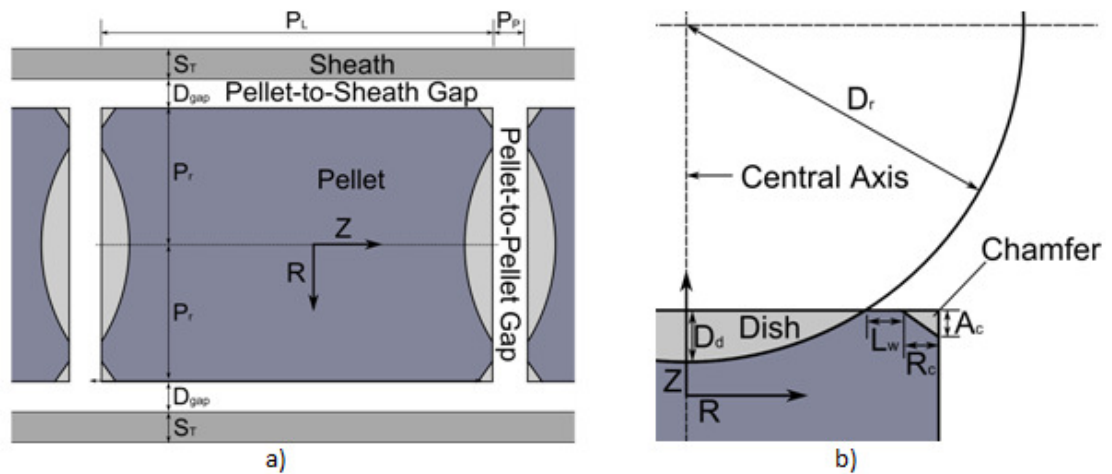


Figure 5: a) A diagram showing the geometry and labelling dimensions of a fuel pellet in an element. b) A diagram showing the geometry of the modified cylinder shape of the pellet [8].

Symbols are defined in Table 3. The dark-grey shading indicates the final pellet geometry and the light-grey indicates areas where  $\text{UO}_2$  has been removed during manufacturing. Dimensions of features exaggerated for emphasis [8].

When MPM-FAST is used to examine the SCWR fuel, further assumptions will need to be added. With the fuel element being 5 m in length and there being a substantial temperature changes in the coolant, different assumptions and simplification will be needed. These assumptions will be outlined leading into the discussion of the SCWR model in Chapter 6.

Table 3: Symbols used to describe pellet geometry

<b>Parameter</b>	<b>Symbol</b>
Pellet radius	$P_r$
Pellet length	$P_L$
Dish depth	$D_d$
Dish radius	$D_r$
Radial chamfer	$R_c$
Axial chamfer	$A_c$
Land width	$L_w$
Initial pellet-to-pellet gap	$P_p$
Initial pellet-to-sheath gap	$D_{\text{gap}}$
Sheath thickness	$S_T$

## 4.2 Common Equations

Fuel performance models attempt to predict physical behaviours that affect the temperature and deformation of nuclear fuel. Within the meshed portions of MPM-FAST's geometry (pellet and sheath), the temperature is calculated by approximating the solution to heat transport by conduction through a solid, the general differential equation is given in equation (1).

$$\rho C_p \frac{\partial T}{\partial t} = \nabla(k\nabla T) + Q_{prod} \quad (1)$$

Where,  $T$  is the temperature (K),  $t$  is time (s),  $\rho$  is the materials' density ( $\text{kg m}^{-3}$ ),  $C_p$  is the specific heat capacity of the material ( $\text{J K}^{-1}$ ),  $k$  is the thermal conductivity of the material ( $\text{W m}^{-1} \text{K}^{-1}$ ), and  $Q_{prod}$  accounts for the heat produced within the fuel, specifically within the fuel pellet ( $\text{J m}^{-3} \text{s}^{-1}$ ). Specific material properties and other physical phenomena that affect heat transport will be outlined in the subsections dealing with the pellet and sheath.

In the case of the un-meshed free volume within MPM-FAST's geometry, heat transport is handled differently. The periodic boundary conditions imposed at either end of the pellet translates to a zero heat flux boundary condition applied to those boundaries. The heat transport through the pellet-to-sheath gap is described by one dimensional steady state heat transfer. Due to the high aspect ratio (pellet-

to-sheath gap  $\ll$  pellet length) this assumption can be applied. The details of which are outlined in Section 4.4.

The second general set of equations applied to both meshed sections of MPM-FAST's geometry accounts for the deformation. Deformation due to mechanical loading, is accounted for as a pseudo-steady state equilibrium statement, the forces acting on the body,  $F_v$  in N, are stored as stress within material as stress ( $\sigma$ , (Pa)). This is given in equation (2).

$$-\nabla \cdot \sigma = F_v \quad (2)$$

Stress within the material given by Hooke's law (with the assumption that the material is isotropic, and the stress is linear-elastic) in equation (3).

$$\sigma = [C_{elastic}][\varepsilon_{elastic}] \quad (3)$$

Here  $\varepsilon_{elastic}$  (unitless) is the elastic strain vector and  $C_{elastic}$  is the stiffness matrix as shown in equation (4), but rearranged so that the strain vector is solved.

$$\begin{bmatrix} \varepsilon_x \\ \varepsilon_y \\ \varepsilon_z \\ \gamma_{xy} \\ \gamma_{xz} \\ \gamma_{yz} \end{bmatrix}_{elastic} = \begin{bmatrix} 1/E & -\nu & -\nu & 0 & 0 & 0 \\ -\nu & 1/E & -\nu & 0 & 0 & 0 \\ -\nu & -\nu & 1/E & 0 & 0 & 0 \\ 0 & 0 & 0 & 1/G & 0 & 0 \\ 0 & 0 & 0 & 0 & 1/G & 0 \\ 0 & 0 & 0 & 0 & 0 & 1/G \end{bmatrix} \begin{bmatrix} \sigma_x \\ \sigma_y \\ \sigma_z \\ \tau_{xy} \\ \tau_{xz} \\ \tau_{yz} \end{bmatrix} \quad (4)$$

The components of the stiffness matrix are dependent on the material's Young's modulus,  $E$  in Pa, Poisson's ratio,  $\nu$  that is unitless, and the Shear modulus,  $G$  in

$P_a$ , which for an isotropic material can be found using the Young's modulus and Poisson's ratio given in equation (5).

$$G = \frac{E}{2(1+\nu)} \quad (5)$$

Within the strain vector in equation (4)  $\gamma_{xy}$ ,  $\gamma_{xz}$ , and  $\gamma_{yz}$  are the off axes components of strain within the strain vector. Similarly  $\tau_{xy}$ ,  $\tau_{xz}$ , and  $\tau_{yz}$  are the off axes components of the stress. The strain tensor in equation (4) is applicable when the material is isotropic.

However there are additional sources of strains within the materials of a fuel element, such that in the model the elastic strain is found by subtracting the inelastic strain ( $\epsilon_{inelastic}$ ) from the total strain ( $\epsilon_{total}$ ) given in equation (6).

$$\epsilon_{elastic} = \epsilon_{total} - \epsilon_{inelastic} \quad (6)$$

The axial symmetry implementation in COMSOL assumes independence of the angle, and also that the azimuthal component of the displacement is identically zero. The physical components of the radial and axial displacement,  $u$  and  $w$ , are used as dependent variables for the axially symmetric geometry. These components of the strain are given in (7) below.

$$\epsilon_r = \frac{\partial u}{\partial r}, \epsilon_\phi = \frac{u}{R}, \epsilon_z = \frac{\partial w}{\partial z}, \epsilon_{rz} = \frac{1}{2} \left( \frac{\partial w}{\partial r} + \frac{\partial u}{\partial z} \right), \epsilon_{r\phi} = \epsilon_{\phi z} = 0 \quad (7)$$

Here  $u$ ,  $v$ , and  $z$  are the deformations in the axial directions of Cartesian coordinates in m;  $r$ ,  $\phi$ , and  $z$  are the axes of the cylindrical coordinate system, and  $R$  is the initial radial location within the geometry in m.

A feature that was tested in the development of the UO<sub>2</sub> portion of this model and is enabled and maintained throughout the other pellet materials is a simplified cracked pellet model. If a threshold tensile strength is exceeded in a portion of the pellet, it is assumed to have cracked (cracking is discussed further in context of pressure calculations on pg. 56, and the cracking conditions in Appendix A). It then is assumed that this specific region of the pellet is no longer capable of transferring loads circumferentially ( $\varepsilon_{\phi,elastic}=0$ )<sup>2</sup> [8].

Equations (2)-(7) apply to all meshed sections of the model geometry. For the unmeshed free volume, deformation is treated based on the deformation to the meshed pellet and sheath domains. These changes are reflected and accounted for as changes in volume for internal gas pressure calculations, and the application of contact pressure using the penalty method.

---

<sup>2</sup> At the time of the development of Th-based ceramic pellet material models, this was the formulation of pellet crack behaviour, however subsequent work has been undertaken that allows for compressive loads to occur following a crack ( $\varepsilon_{\phi,elastic} \leq 0$ ) [36]. The work presented here and in the discussion of validation (Chapter 6) uses the initial assumption of  $\varepsilon_{\phi,elastic}=0$ . The implication of this assumption is that the pellet material is no longer accounts for any hoop strain (tensile or compressive). This assumption may cause the distribution of elastic loads in compressive conditions to be re-allocated along the  $r$  and  $z$  axes. Inelastic sources of strain are dominant in fuel pellets during irradiation and this assumption has limited effect on the deformation calculation.

One of the sources of strain not caused by external forces in a fuel element will be caused by the thermal expansion of the materials, known as the thermal strain ( $\varepsilon_{thrm}$ ). Generally thermal expansion is conceived as a linear growth response to the temperature ( $T$ ) compared to a reference temperature ( $T_0$ ) at which the material is considered to have no thermal strain, and is given in equation (8).

$$\varepsilon_{thrm} = \alpha_p(T - T_0) \quad (8)$$

With  $\alpha_p$  being the thermal expansion coefficient at a constant pressure ( $K^{-1}$ ). The formulation of thermal strain in (7) is only true if  $\alpha_p$  is a constant. In its most general form  $\alpha_p$  is defined as equation (9),

$$\alpha_p = \frac{1}{L} \left( \frac{\partial L}{\partial T} \right)_p \quad (9)$$

where  $L$  is the length of the sample in the direction of axis that is measured in m. The temperature dependent behaviour of  $\alpha_p$  can be complex, this results in the temperature behaviour of the thermal strain to be reported directly as a function of temperature, instead of the form presented in equation (8). MPM-FAST uses such temperature based functions for the thermal strain (see equations (23-29) for sheath/clad materials and (116) and (117) for fuel materials).

The required material properties for both heat transport and deformation, additional models for inelastic sources of strain and the details of the models used



within the unmeshed free volume are presented in section 4.3 to 4.5. Each of these sections contains subsections that outline additional modeled behaviour based on how the phenomena are primarily coupled to either the heat transport, or deformation of the fuel.

### 4.3 Sheath

#### 4.3.1 Heat Transport

The boundary condition that allows for the unique solution of the heat transport within the model is the radial heat flux from the coolant side of the sheath to the bulk coolant. This is found by assuming that the heat is conducted through thin-film transfer. Considered within the model is the layer of  $ZrO_2$  that forms on the coolant side of the sheath. The heat flux from the sheath to the coolant is given in equation (10).

$$Q_r = \frac{(T_{sheath} - T_{coolant})}{\left(\frac{t_{oxide}}{k_{oxide}} + \frac{1}{h_{film}}\right)} - Q_{oxide} \quad (10)$$

Where  $T_{sheath}$  and  $T_{coolant}$  are the outside sheath temperature and bulk coolant temperatures, respectively (K),  $t_{oxide}$  is the thickness of the oxide layer (m),

$k_{oxide}$  is the thermal conductivity of  $ZrO_2$  ( $W\ m^{-2}\ K^{-1}$ ),  $h_{film}$  is the heat transfer coefficient of the thin film layer from the sheath to the coolant ( $W\ m^{-2}\ K^{-1}$ ) and  $Q_{oxide}$  is the heat flux from the element sheath due to the exothermic formation of  $ZrO_2$  ( $W\ m^{-2}$ ).

$T_{coolant}$  and  $h_{film}$  are required as input parameters, with  $h_{film}$  generally having a range of 38-50  $kWm^{-2}\ K^{-1}$  for CANDU fuel. The temperature dependent equation for  $k_{oxide}$  is given in (11) from the MATPRO library [14].

$$k_{oxide} = 0.835 + 1.81 \times 10^4 T \quad (11)$$

$Q_{oxide}$  is given by equation (12) below.

$$Q_{oxide} = \frac{42.426 \times 10^9}{1.56} \frac{dt_{oxide}}{dt} \quad (12)$$

MPM-FAST uses a parabolic  $ZrO_2$  growth model that is based on the one outlined by Sills [42] and Urbanic and Hendrick [43], and accounts for the surface oxide layer and the oxygen stabilized alpha phase directly below the  $ZrO_2$ .

The growth rate of the oxide phase is given in equation (13).

$$\frac{dt_{oxide}}{dt} = \frac{\delta_{oxide}^2}{2t_{oxide}} \quad (13)$$

With the temperature dependent coefficient  $\delta_{oxide}$  given by

$$\delta_{oxide} = \begin{cases} 3.60 \times 10^{-4} e^{\frac{-6793}{T}}, T \leq 1853 K \\ 1.41 \times 10^{-3} e^{\frac{-8007}{T}}, T > 1853 K \end{cases} \quad (14).$$

A similar growth rate for the oxygen stabilized alpha phase is also implemented, given in equation (15),

$$\frac{dt_{\alpha}}{dt} = \frac{\delta_{\alpha}^2}{2t_{\alpha}} \quad (15)$$

with the oxygen stabilized alpha phase growth coefficient given by (16),

$$\delta_{\alpha} = 3.90 \times 10^{-3} \exp\left(\frac{-9915}{T}\right) \quad (16).$$

Generally speaking ZrO<sub>2</sub> growth is significant only when the sheath experiences, greater temperatures than those expected during NOC. It is included because it is an important behaviour in modelling transient conditions. The intentions during the development of the UO<sub>2</sub> model, was to have the capability to model transient behaviour. A simplified model is included for the loss of sheath material structural integrity due to ZrO<sub>2</sub> and given as equation (17).  $t_{lost}$  is treated as a thinning of the fuel sheath within the structural deformation model. COMSOL allows for adaptive meshing by applying a described mesh displacement using equation (17).

$$t_{lost} = 0.641t_{oxide} \quad (17)$$

Within the context of modelling the validation cases of DME-221 and BDL-422 fuel elements, the element sheath did not experience the temperatures required to experience the loss of material. This is a model that is maintained from Prudil's development of FAST [8]. In the description the bulk coolant conditions for the SCWR fuel has an exit temperature of 650°C. If Zircaloy is placed in this temperature regime it would experience clad thinning due to  $ZrO_2$  removal as described above. When examining the SCWR fuel in this work the sheath/clad material properties will be representative of 310 stainless steel as outlined by Colton and Pencer [4] as a potential material. Colton and Pencer also present the results of thermal hydraulic analysis of the SCWR's coolant conditions that provide the outer clad temperature of the fuel elements at various points along its length from the bottom of the reactor. This data has been imported into COMSOL and is fit by piecewise cubic splines within COMSOL as displayed in Figure 6 below.

The interior sheath/clad wall boundary condition is set to the radial heat flux through the pellet-to-sheath gap which will be discussed in the free volume portion (section 4.4). Since the heat generation occurs solely within the pellet, in the sheath/clad  $Q_{prod} = 0$ , the remaining information required to solve for the heat transport are: the density, heat capacity, and the thermal conductivity of Zircaloy-4 and the 310 stainless steel.

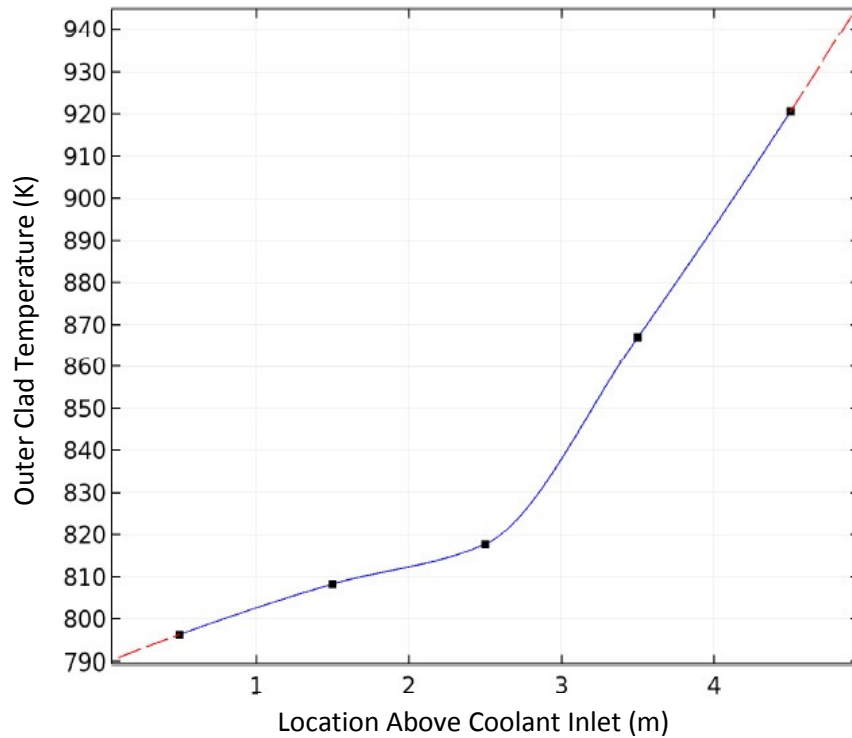


Figure 6: Plot displaying the temperature of the outer surface of the SWR fuel element clad [4].

The parameters on the left hand side of equation (1) ( $\rho$ ,  $C_p$  and  $\frac{\partial T}{\partial t}$ ) are the time dependent components of the heat conduction equation. Specifically with  $\frac{\partial T}{\partial t}$ , this term will approach zero as the length between time steps increases. This means that for NOC models where the time steps are large and the expected temperature changes are small, the time dependent components of the heat

conduction equation will have limited effect on the temperature calculation. Since the Zircaloy-4 model is a carryover from Prudil's work [8], the material properties  $\rho$  and  $C_p$  are retained from modelling transient conditions.

The density of Zircaloy-4 used in the model consists of using a reference density of Zircaloy-4 ( $\rho_{0Zr-4} = 6550 \text{ kg m}^{-3}$ ) and updating it based on the strains occurring within the sheath as given in (18) in units of  $\text{kg m}^{-3}$ .

$$\rho_{Zr-4} = \frac{6550}{(1+\varepsilon_r)(1+\varepsilon_\phi)(1+\varepsilon_z)} \quad (18)$$

Where the subscripts of  $r$ ,  $\phi$ , and  $z$  refer to the specific axial direction the strain acts in within the cylindrical coordinate system of the model's geometry. The details of the strain calculations are outlined in the deformation subsection (4.3.2).

As for the material properties for 310 stainless steel, they were found in a steel manufacturers product listing [44]. The density of 310-stainless steel at room temperature is  $\rho_{0310} = 7861 \text{ kg m}^{-3}$ , which is treated similarly as equation (18) in order to generalize the calculation.

For the Zircaloy-4 heat capacity used in MPM-FAST, data points from Brooks *et al.* [45], from the measurement of heat capacity of Zircaloy-2 are used to generate a piecewise temperature dependent function in the model (Figure 7 below) [8], [45]. The data was taken from the tabulated measurements presented

in MATPRO [14]. MATPRO also recommends the data be used for the heat capacity of Zircaloy-4. The spike that begins ~1100 K is caused by the Zircaloy-4 alpha-to-beta phase transition. For temperatures beyond the data presented in MATPRO, a constant extrapolation was used.

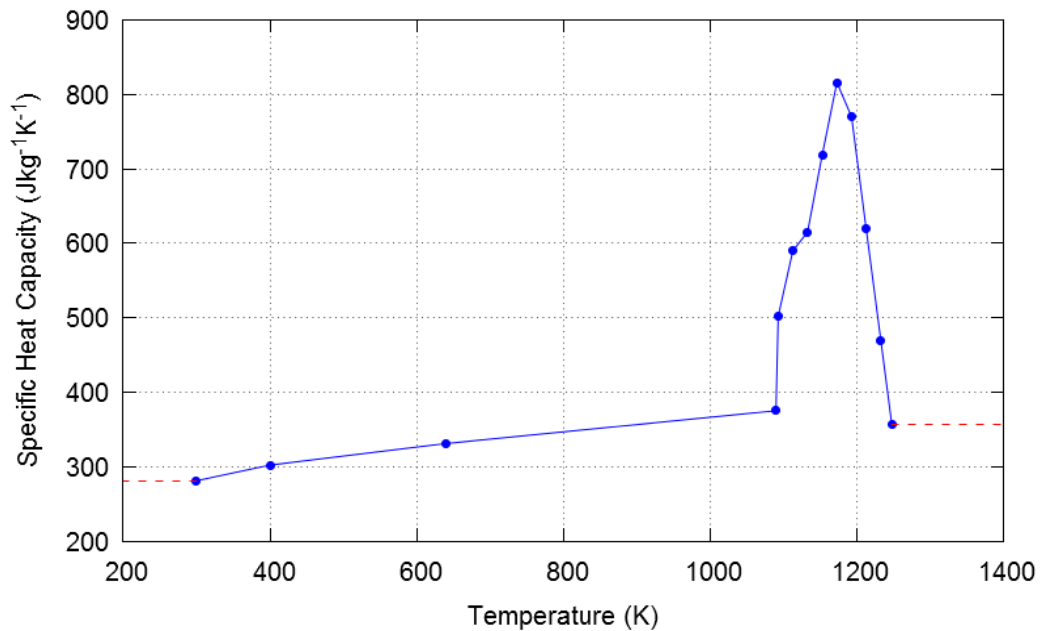


Figure 7: Plot of specific heat capacity of Zircaloy used within MPM-FAST [8]

A model of the 310 stainless steel was not added. The heat capacity model for Zircaloy-4 was maintained as the heat Capacity in the sheath/clad. Since the SCWR modelling will all be in the NOC regime, this is viewed as an acceptable assumption, due to the effect of time dependence will have on the calculation is being limited (see description on page 34).

A correlation of the thermal conductivity of Zircaloy-4 presented in the MATPRO library is used within MPM-FAST [14]. The correlation is a polynomial function of temperature ( $T < 2098$  K) and given in equation (19) in units of  $\text{W m}^{-1} \text{K}^{-1}$ .

$$k_{Zr-4} = 7.51 + 0.0209T - 1.45 \times 10^{-5}T^2 + 7.67 \times 10^{-9}T^3 \quad (19)$$

Equation (20) below was interpolated from data points provided by a steel manufactures website for 310 stainless steel and provides the thermal conductivity in  $\text{Btu ft}^{-1} \text{hr}^{-1} \text{F}^{-1}$  ( $1 \text{ Btu ft}^{-1} \text{hr}^{-1} \text{F}^{-1} = 1.731 \text{ W m}^{-2} \text{K}^{-1}$ ) [44] (see also Figure 8).

$$k_{310} = 7.1 \times 10^{-3}T + 6.8435 \quad (20)$$

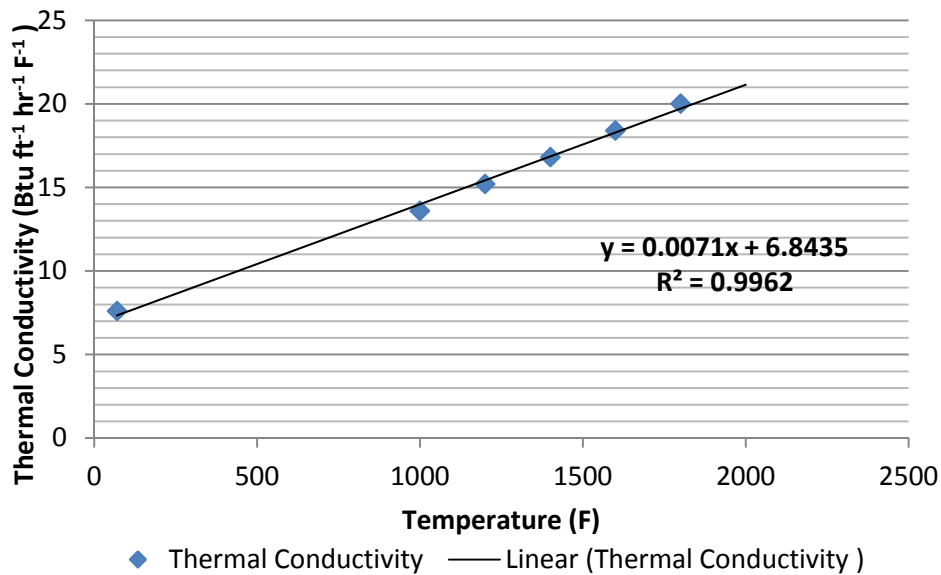


Figure 8: Presents the thermal conductivity of 310 stainless steel [44].



### 4.3.2 Deformation

The external loads ( $F_v$  in equation (2)) acting on the domain of the sheath are provided by: the coolant pressure input parameter on the outer surface of the sheath, the combination of pellet-to-sheath contact pressure, the internal element gas pressure acting on the sheath's inner surface and the axial load imposed by the expansion of the fuel stack. Details of these sub models are presented in Section 4.4. The inclusion of the periodic boundary conditions presented in Figure 4 completes the list of boundary conditions acting on the sheath required for the deformation model to be solved.

Recall that Young's modulus and Poisson's ratio are components of the stiffness matrix (equation(4)). By assuming the Zircaloy-4 within the sheath is isotropic, MPM-FAST uses the Young's modulus approximation recommended by MATPRO given by equation (21) in units of Pa [14].

$$E_{Zr} = \begin{cases} 1.088 \times 10^{11} - 5.47 \times 10^7 T, & T \leq 1090K \\ 1.017 \times 10^{11} - 4.827 \times 10^7 T, & 1090K < T \leq 1240K \\ 9.21 \times 10^{10} - 4.05 \times 10^7 T, & 1240K < T \leq 2030K \\ 1 \times 10^{10}, & T > 2030K \end{cases} \quad (21)$$

For the Young's modulus of 310 stainless steel a similar fitting process was undertaken from data reported online [44] and fitted to equation (22) in units of  $10^6$ psi (1 psi =6.89 kPa) and presented in Figure 9 below.

$$E_{310} = -0.0064T + 29.44 \quad (22)$$

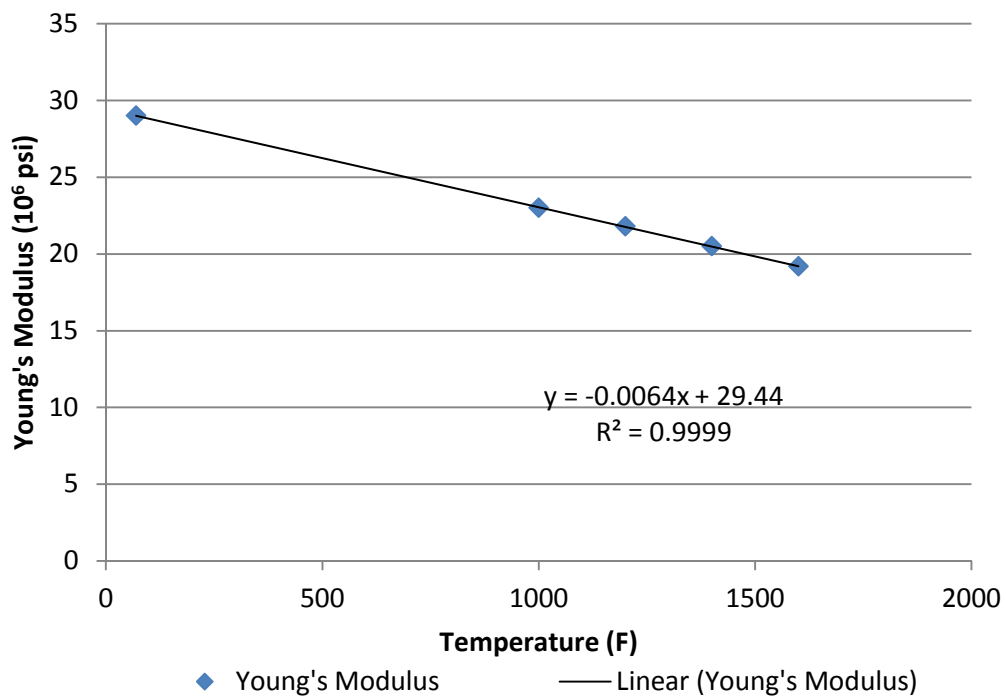


Figure 9: Linear fitting of Young's modulus data

MPM-FAST uses a Poisson's ratio value of  $\nu = 0.3$  for Zircaloy-4, while it is reported to range between 0.27-0.3 for 310 stainless steel [46] so the model maintains it as 0.3 for both materials.

Additionally, it also uses the correlations from MATPRO to calculate the thermal strains within the Zircaloy-4 of the sheath. In this case the model is an anisotropic model and includes separate correlations for the axial, radial, and hoop directions [47]. When the Zircaloy is in its alpha phase ( $273 \text{ K} \leq T \leq 1073 \text{ K}$ ), thermal strains are given by equation (23) and (24).

$$\varepsilon_{thrm,z} = -1.23 \times 10^{-3} + 4.441 \times 10^{-6}T \quad (23)$$

$$\varepsilon_{thrm,r} = \varepsilon_{thrm,\phi} = -2.0731 \times 10^{-4} + 6.721 \times 10^{-6}T \quad (24)$$

Again due to the development of this model to account for transient behaviour, the correlation for thermal strains expected within beta phase Zircaloy ( $T > 1273 \text{ K}$ ), is also included within the model as given by equations (25) and (26).

$$\varepsilon_{thrm,z} = -0.01095 + 9.7 \times 10^{-6}T \quad (25)$$

$$\varepsilon_{thrm,r} = \varepsilon_{thrm,\phi} = -9.45 \times 10^{-3} + 9.7 \times 10^{-6}T \quad (26)$$

In the temperature region  $1073 \text{ K} \leq T \leq 1273 \text{ K}$ , the strain correlation is selected to ensure continuity between the alpha and beta phase correlations, using the process by Sills to accomplish this continuity yields [42]:

$$\varepsilon_{thrm,z} = 0.01494 - 1.064 \times 10^{-5}T \quad (27)$$

$$\varepsilon_{thrm,r} = \varepsilon_{thrm,\phi} = 0.01716 - 1.12 \times 10^{-5}T \quad (28)$$

Within the 310 stainless steel the thermal expansion acts isotropically and, similar to the other physical properties discussed the thermal strain behaviour, has been fit to material data as shown in Figure 10 and presented in equation (29).

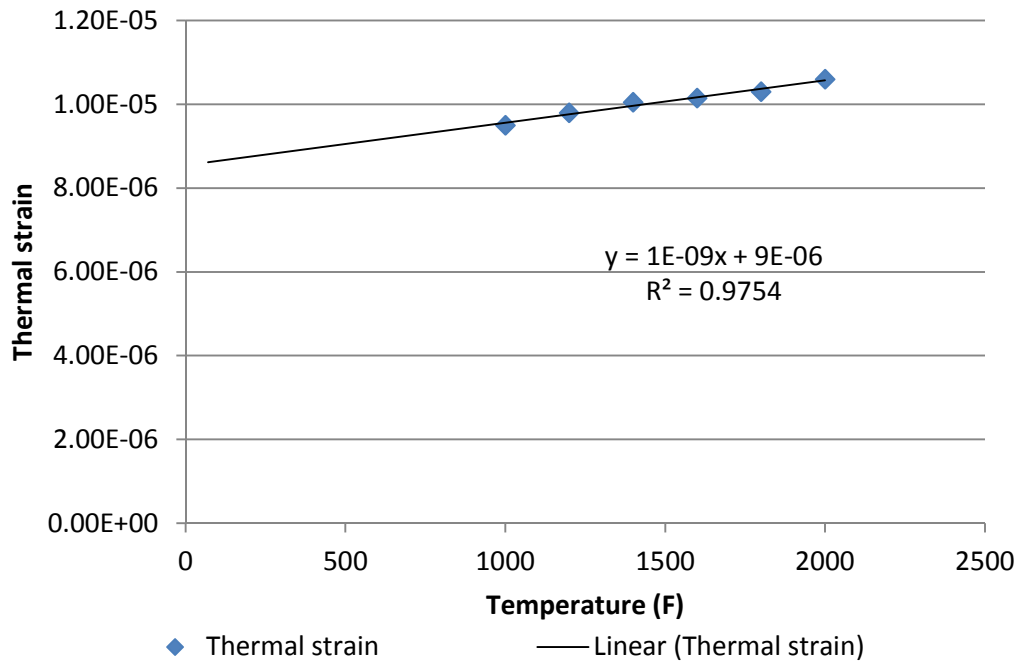


Figure 10: Thermal strain data and fit for 310 stainless steel [44]

$$\varepsilon_{thrm} = 1 \times 10^{-9}T + 9 \times 10^{-6} \quad (29)$$

Additional sources of inelastic strain accounted for in the sheath deformation model for Zircaloy are the low temperature creep strain and fast neutron irradiation creep. Creep is a time dependent plastic deformation that generally occurs at elevated temperatures. In the instance of Zircaloy-4, the

material exhibits two distinct creep strain rates, one above 700 K, and a “low temperature” creep rate that is within the temperatures experienced during NOC.

The low temperature creep strain rate is given by equation (30) [47].

$$\frac{\partial \varepsilon_{\phi}}{\partial t} = 5 \times 10^{-23} \sigma_{\phi}^2 \left( 3.47 \times 10^{-23} \frac{\sigma_{\phi}^3}{|\sigma_{\phi}|} \exp\left(\frac{-U}{T}\right) - \varepsilon_{\phi} \right) \exp\left(\frac{-U}{T}\right) \quad (30)$$

Where  $\varepsilon_{\phi}$  and  $\sigma_{\phi}$  are the creep strain and local stress in the hoop direction and  $U$  is the apparent activation energy divided by the gas constant.  $U$  as a function of temperature is given in equation (31).

$$U = 212.7 - 0.5324T + 1.17889 \times 10^{-4}T^2 + 3.3486 \times 10^{-7}T^3 \quad (31)$$

Fast neutron irradiation creep arises due to highly energetic neutrons (>1 MeV) depositing kinetic energy into lattice structure of the Zircaloy-4 when the neutrons undergo scattering by the Zircaloy. This energy then can cause interstitial and vacancy defects within the lattice structure. These types of point defects within the lattice usually arise at elevated temperatures and lead to dislocation creep in a material. The creep caused in the hoop direction, specifically by the fast neutron irradiation ( $\varepsilon_{\phi,ir}$ ), is described by the creep rate in equation (32).

$$\frac{\partial \varepsilon_{\phi,ir}}{\partial t} = \frac{2.2 \times 10^{-7} \sigma_{phi} \exp\left(\frac{-5000}{T}\right) \phi_{Flux}^{0.65}}{T^7} \quad (32)$$

Here  $\phi_{Flux}$  is the flux of neutrons ( $m^{-2} s^{-1}$ ) with kinetic energy greater than 1 MeV. A modelling assumption is made in order to estimate  $\phi_{Flux}$ , any inwardly bound neutrons moving towards the fuel can be assumed to have been moderated and have an energy of  $< 1$  MeV. This simplifies the fast portion of the flux through the sheath as being made up entirely of the neutrons released from fission given by equation (33).

$$\phi_{Flux} = \frac{\eta_{fast} P_{lin}}{2\pi P_r E_f} \quad (33)$$

Here  $\eta_{fast}$  is the number of fast neutrons released per fission (which is dependent on the isotope undergoing fission: U-233,  $\eta_{fast}=2.49$ ; U-235,  $\eta_{fast}=2.42$ ; Pu-239,  $\eta_{fast}=2.93$ .  $\eta_{fast}$  can be selected to reflect the fuel composition),  $E_f$  is the energy released per fission, which is approximately 200 MeV or  $3.204 \times 10^{-11}$  J,  $P_{lin}$  is the linear power of the fuel ( $W m^{-1}$ ), and  $P_r$  is the radius of the pellet (m).

## 4.4 Free Volume

### 4.4.1 Heat Transport

As mentioned in Section 4.2 the heat transport through the free volume in the model is accomplished by assuming the heat is transported across the pellet-to-sheath gap, and it is represented as a one-dimensional steady state heat transfer or

as if the gas in the gap has a negligible heat capacity, with the radial heat flux given by equation (34).

$$Q_r = (h_{gap,gas} + h_{gap,solid} + h_{gap,rad})(T_{fuel} - T_{sheath}) \quad (34)$$

Here  $T_{fuel}$  is the temperature of the fuel pellet surface (K),  $T_{sheath}$  is the temperature of the inner surface of the sheath (K), and the three heat transfer coefficients:  $h_{gap}$  variables refer to possible processes to transport heat through the gap,  $h_{gap,gas}$  heat transfer through the gas,  $h_{gap,solid}$  through pellet-to-sheath contact, and  $h_{gap,rad}$  through radiative heat transfer.

The first heat transfer coefficient is associated with heat transported through the fill gas and gaseous fission products that are released from the ceramic fuel ( $h_{gap,gas}$ ), and is given in equation (35) according to [48].

$$h_{gap,gas} = \frac{k_g}{1.5(R_f + R_s) + d_{gap} + g} \quad (35)$$

Here  $k_g$  is the thermal conductivity of the gas mixture ( $\text{W m}^{-1} \text{K}^{-1}$ ),  $d_{gap}$  is the average local gap distance (m),  $R_f$  and  $R_s$  are the surface roughness of the fuel and sheath, respectively (both  $\sim 0.5 \mu\text{m}$ ), that effectively increase the gap distance, and  $g$  is the effective temperature jump distance (m).

MPM-FAST's default  $k_g$  model is one developed by Sills and Peggs and used within ELESTRES [11] and used in previous models developed at RMCC

[10],[49]. The model considers the internal gas to be comprised of helium, argon, and “fission gas”. Fission gas acts as a single gas that is representative of the gaseous fission products that are released from the pellet as the fuel is being irradiated (it will be predominately xenon and krypton). Each gas’s properties used in the calculation of  $k_g$  are listed in Table 4.

Table 4: Gas properties for use with the AECL model for the thermal properties of the fill gas[49]

Gas	Molar Mass (kg mol <sup>-1</sup> )	$k_0$ (W m <sup>-2</sup> K <sup>-1</sup> )	$s$	$T_c$ (K)	$P_c$ (MPa)	$g_0$ ( $\mu\text{m}$ )
Helium	0.0040	$2.5(10^{-3})$	0.721	5.2	0.229	5.2
Argon	0.03995	$2.217(10^{-4})$	0.772	151	4.86	0.57
Fission Gas	0.1270	$4.63(10^{-5})$	0.856	281	5.86	0.26

Using the method developed by Sills and Peggs at AECL, equations 36 – 38 give the thermal conductivity of the gas ( $k_{g,AECL}$ ).

$$k_{g,AECL} = X_m(T)Y_m(P, T) \quad (36)$$

Here  $X_m(T)$  is the thermal conductivity as a function of temperature and  $Y_m(P, T)$  accounts for the change in behaviour at elevated pressures.  $X_m(T)$  is given in equation (37).

$$X_m(T) = \frac{\sum_i y_i \sqrt[3]{M_i} k_{0,i} T^{s_i}}{\sum_i y_i \sqrt[3]{M_i}} \quad (37)$$



Here the subscript  $i$  denotes the gas component,  $y_i$  is the mole fraction of the component,  $M_i$  is the molar mass of the component,  $k_{0,i}$  is the thermal conductivity of the gas at STP, and  $s_i$  is an empirically derived value for the temperature exponent to account for the species viscosity (see Table 4 above).

$Y_m$  is given in equation (38).

$$Y_m(P, T) = 1 + (0.51T_{Rm}^{-2.26})P_{Rm}^{1+2.5T_{Rm}^{-6.2}} \quad (38)$$

Here  $T_{Rm}$  (equation (39)) and  $P_{Rm}$  (40) are the reduced temperature and pressure of the gas mixture.

$$T_{Rm} = \frac{T}{\sum_i y_i T_{c,i}} \quad (39)$$

$$P_{Rm} = \frac{P}{\sum_i P_{c,i}} \quad (40)$$

The value of the temperature jump distance ( $g$ ) is also dependent on the gas mixture. The jump distance of the mixed gas ( $g_m$ ) is presented as a function of temperature and pressure in equation (41).

$$g_m(T, P) = \frac{P_c}{P} \left( \sum_i \frac{y_i}{g_{0,i} \left( \frac{T}{T_c} \right)^{s+0.5}} \right)^{-1} \quad (41)$$

Here,  $P_c$ ,  $T_c$  refer to a reference temperature and pressure (STP) respectively, and  $g_{0,i}$  is the temperature jump distance for a component gas (see Table 4).

Calculations presented in the validation data (Chapter 6) are all done using this model for the fission gas thermal conductivity<sup>3</sup>.

The next component of the heat transfer coefficient in equation (34),  $h_{gap,solid}$ , is given by equation (42).

$$h_{gap,solid} = \left( \frac{2k_f k_s}{k_f + k_s} \right) \left( \frac{1.16 \times 10^5}{H} \right) \sqrt{\frac{P_i}{d_{gap}}} \quad (42)$$

Here  $k_f$ , and  $k_s$  are the thermal conductivity of the fuel (equations 75-79) and the sheath (equation 19 or 20) at each of the surfaces,  $P_i$  is the local average contact pressure interface (Pa) (see next subsection) and  $H$  is the Meyer hardness of Zircaloy-4 (Pa) given by equation (43) over a temperature range of 298 - 877 K [14]. Due to time constraints, this model for Meyer hardness is maintained for the 310 stainless steel model.

$$H = \exp(26.034 - 0.026394T + 4.3504 \times 10^{-5}T^2 - 2.5621 \times 10^{-8}T^3) \quad (43)$$

The final component  $h_{gap,rad}$  accounts for the heat transferred through radiative heat transfer and is found by assuming it acts as grey body radiation acting between infinite parallel surfaces described using equation (44) [8].

$$h_{gap,rad} = \frac{\sigma_{SB}}{\frac{1}{\varepsilon_{e,f}} + \frac{1}{\varepsilon_{e,s}} - 1} (T_{fuel}^2 + T_{sheath}^2) (T_{fuel} + T_{sheath}) \quad (44)$$

---

<sup>3</sup> MPM-FAST also includes the option of using another method to model the gas mixtures thermal conductivity. It is a semi-empirical model using the same methodology as GAPCON-2 [50] from FRAPCON/FRAPTRAN fuel performance models and developed by Prudil as part of his PhD [8].

Here  $\sigma_{SB}$  is the Stefan-Boltzmann constant ( $5.6704 \times 10^{-6} \text{ W m}^{-2} \text{ K}^{-4}$ ),  $\varepsilon_{e,s}$  is the emissivity (how reflective/absorbing of em radiation the material is) of the sheath (unitless) and  $\varepsilon_{e,f}$  the emissivity of the fuel (unitless). This mechanism only becomes significant when there is a large fuel-to-sheath gap and the fuel temperature is high.

The emissivity of the sheath surface as given by MATPRO is presented in equations (45) and (46) [14]. The model assumes that the inner sheath surface is comprised of a  $\text{ZrO}_2$  layer. It has been found that  $\text{ZrO}_2$  emissivity is dependent on the thickness of the layer ( $t_{oxide}$ ) (equation (45)) and that it becomes temperature dependent when the sheath exceeds 1500 K (equation (46)). MPM-FAST has no model that tracks the growth of the internal sheath oxide layer. The internal sheath oxide layer is set at a constant within the model at 5  $\mu\text{m}$ . The only model for emissivity is the Zircaloy model within MPM-FAST, as it is not an applicable model when examining NOC for the SCWR fuel.

$$\varepsilon_{e,s}^{lowT} = \begin{cases} 0.325 + 0.1246 \times 10^6 t_{oxide} & t_{oxide} \leq 3.88 \times 10^{-6} m \\ 0.808642 - 50.0 t_{oxide} & t_{oxide} > 3.88 \times 10^{-6} m \end{cases} \quad (45)$$

$$\varepsilon_{e,s}^{highT} = \max\left(0.325, \varepsilon_{e,s}^{lowT} \exp\left(\frac{1500-T}{300}\right)\right) \quad (46)$$

So far MPM-FAST has implemented only the emissivity of  $\text{UO}_2$  (equation (45)). As data has not been found on the emissivity of  $(\text{Th,U})\text{O}_2$ , or

(Th,Pu)O<sub>2</sub>. Emissivity is not expected to contribute NOC model for fuel designs where the pellet and sheath come into contact. However equation (47) is used as a place holder in the calculation for both (Th,U)O<sub>2</sub> and (Th,Pu)O<sub>2</sub> fuel.

$$\varepsilon_{e,f} = 0.7856 + 1.5263 \times 10^{-5}T \quad (47)$$

#### 4.4.2 Deformation

The two models that affect the deformation in the fuel and account for the presence of the initial free volume within the fuel element are: the gas pressure calculation, and contact models to account for pellet-to-pellet and pellet-to-sheath contact.

##### Internal Gas Pressure

Calculating internal gas pressure is a complex problem, the gas temperature is non-homogenous, and the gas volume is dependent on the deformation of the pellet and the sheath. The general equation to determine the amount of gas in the element free volume,  $n_{mol}$ , in moles is given in equation (48).

$$n_{mol} = \int_V \rho_{molar} dV \quad (48)$$

Here  $\rho_{molar}$  is the molar density of the gas, and  $V$  is the volume occupied by the gas. For an ideal gas in volume  $V$ , at uniform pressure,  $P$ , and temperature,  $T$ , the ideal-gas law states:

$$PV = n_{mol}R_{gas} \quad (49).$$

$\rho_{molar}$  can then be defined by equation (50) for an ideal gas.

$$\rho_{molar} = \frac{n_{mol}}{V} = \frac{P}{R_{gas}T} \quad (50)$$

Here  $R_{gas}$  is the ideal gas constant (8.314 J mol<sup>-1</sup> K<sup>-1</sup>). For an infinitely small volume of gas the temperature can be treated as uniform, and equation (50) can be substituted into equation (48) and rearranged to solve for pressure as shown in equation (51).

$$n_{mol} = \frac{P}{R_{gas}} \int_V \frac{1}{T} dV \quad (51)$$

$$P = \frac{n_{mol}R_{gas}}{\int_V \frac{1}{T} dV}$$

As model input, any additional volume near the end caps or plena that may be inserted into the element, along with a temperature estimate of the gas is required to complete the integration in equation (51), because these regions are not explicitly modeled by MPM-FAST.

The method for subdividing the volume within the element around a pellet is presented in Figure 11 a). The volume is split into 5 simpler geometries (where  $V_{pellet} = V_1 + V_2 + V_3 + V_4 + V_5$ ).  $V_1$ - $V_3$  are straight forward to calculate, while  $V_4$  and  $V_5$  require integration. All of these initial volumes are dependent on the pellet design parameters listed in Table 3, in addition to the presence of a pellet hole (the parameter for the hole radius is  $H_r$ ), the number of dishes and chamfers are accounted for in this calculation.

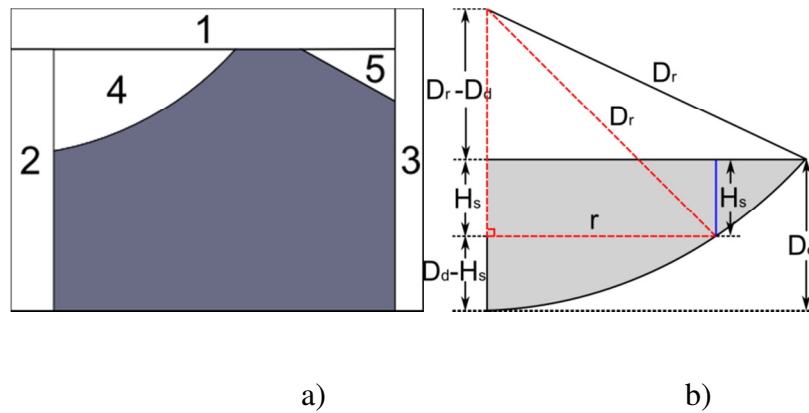


Figure 11: Fill gas calculation geometry, a) shows the division of the free volume regions into subdivisions, b) shows the detailed geometry of  $V_4$  [8].

$V_1$  is given by the volume of a cylinder as given in equation (52).

$$V_1 = \pi P_r^2 P_p \quad (52)$$

With  $P_r$  and  $P_p$  being the initial pellet radius and pellet-to-pellet gap respectively, and defined in Figure 5.

$V_2$  is also the given by the volume of a cylinder. However an additional term is added to take into account that generally the hole is present for the insertion of instrumentation, so the free volume fraction ( $F_{vf}$ ) is added to equation (53).

$$V_2 = \pi H_r^2 P_L F_{vf} \quad (53)$$

$V_3$  is a full cylindrical shell given in equation (54).

$$V_3 = \pi(P_l + P_p)(2D_{gap}P_r + D_{gap}^2) \quad (54)$$

$V_4$  is found by integrating a cylindrical shell in the radial direction given in equation (55).

$$V_4 = \int_{H_r}^{P_r - R_c - L_w} 2\pi r H_s dr \quad (55)$$

Here  $H_s$  is found using Pythagorean Theorem on the dashed triangle indicated in Figure 11 b), and given in equation (56).

$$H_s = -D_r + D_d + \sqrt{D_r^2 - r^2} \quad (56)$$

Substitution of equation (56) into (55) allows  $V_4$  to be calculated as equation (57).

$$V_4 = \pi(D_d - D_r)r^2 - \frac{2\pi}{3}(D_r^2 - r^2)^{3/2} \Big|_{H_r}^{P_r - R_c - L_w} \quad (57)$$

A similar integral is required for the volume associated with the chamfer(s), with the radial height of each of these shells given by equation (58).

$$H_c = A_c \left(1 - \frac{P_r - r}{R_c}\right) \quad (58)$$

The volume of the chamfer,  $V_5$ , is then given by the integration presented in equation (59).

$$V_5 = \int_{P_r - R_c}^{P_r} 2\pi r H_c dr = \pi A_c R_c P_r - \frac{\pi A_c R_c^3}{3} \quad (59)$$

This leads to the calculation of the initial internal element volume to be given as equation (60).

$$V_{element} = n_p V_{pellet} + V_{ends} + n_{pl} V_{plenum} \quad (60)$$

Here  $n_p$  is the number of pellets encased within the fuel element;  $V_{ends}$  is the volume in the element around the end caps,  $n_{pl}$  is the number of plena inserted into the fuel, and  $V_{plenum}$  is the volume of a single plenum.

Once the manufactured internal element free volume is found, and assuming the temperature, composition of gas, and pressure of the fill gas are



uniform, the initial amount of fill gas in the element,  $n$ , can be found using the ideal gas law as shown in equation (61).

$$n = \frac{PV}{R_{gas}T} \quad (61)$$

An additional source of volume that fill gas and fission gas can migrate to is the space that opens up in the pellet when a crack forms. Since these cracks are not explicitly modeled in MPM-FAST, the maximum volume of cracks, in the direction perpendicular to the circumferential axis is given by the integral in equation (62).

$$V_{cracked} = 2\pi \iint CrackedFlag \cdot \varepsilon_{\phi,elas} r \, dz da \quad (62)$$

Here *CrackedFlag* is a logical parameter as outlined in equation (63).

$$CrackedFlag = \begin{cases} 0, & \sigma_{\phi} < \sigma_F \\ 1, & \sigma_{\phi} \geq \sigma_F \end{cases} \quad (63)$$

Here  $\sigma_{\phi}$  is the circumferential (hoop) stress and  $\sigma_F$  is the temperature dependent fracture stress of the UO<sub>2</sub> as given in Appendix A.

With the changes in the free volume given by the deformation of both the pellet and the sheath, the initial volume and gas content enables the model to solve for the gas pressure within the fuel element as outlined in equation (51).

## Contact

Surface-to-surface contact is modeled in MPM-FAST using the penalty force method. This method is used to approximate the contact pressure between the pellet and the sheath. Pressure between two surfaces is applied as a function of separation distance (or penetration depth). Ideally the penalty function would be zero for positive separation distances and infinite for negative separation distances, as this would be the most physical representation of what occurs. This is not feasible to implement because it leads to highly oscillatory behaviour (it causes the modeled surfaces to fluctuate in and out of contact all of the time) and causes convergence issues. One method of decreasing this undesirable oscillatory behaviour is to have a smooth transition in the application of pressure between the two surfaces. The interfacial pressure,  $P_i$ , is applied on the interior surfaces of the sheath and pellet in the form given in equation (64).

$$P_i = \begin{cases} P_{est} \exp\left(\frac{P_f d_{pen}}{P_{est}}\right) & d_{pen} < 0 \\ P_{est} + P_f d_{pen} & d_{pen} \geq 0 \end{cases} \quad (64)$$

Here  $P_{est}$  is an initial estimate of the pressure in Pa,  $P_f$  is the penalty factor in Pa  $m^{-1}$ , which applies additional pressure on the surfaces if the modeled surfaces overlap each other (one boundary penetrates the other), where  $d_{pen}$  is penetration depth (how much the boundaries overlap in the local area) in m.

Initially, there is no penetration so  $d_{pen}$  is negative and the surfaces are apart enough that there is no appreciable pressure applied. As the interior wall of the sheath approaches the pellet, the pressure will approach  $P_{est}$  exponentially. Once the boundaries cross each other, additional loads are added to the surfaces linearly based on the depth of the overlap. This is to prevent the modeled sheath from passing through the pellet.  $P_{est}$  and  $P_f$  are model inputs and are adjustable to account for the conditions the model is trying to capture. Generally  $P_{est}$  should be approximately close to the coolant pressure, with the expectation that forces balance out within the model.

Pellet-to-pellet contact cannot be modeled in the same explicit manner as the pellet-to-sheath contact. Due to the periodic boundary conditions the model does not explicitly model the presence of the adjacent pellets within the fuel stack; this prevents the penalty method from being applied to this problem. The model does not calculate the pellet-to-pellet contact pressure. Once the length of the fuel stack exceeds the initial open axial space, any pellet growth beyond this is modeled as a prescribed displacement acting on the sheath. In MPM-FAST inertial effects are excluded leaving two potential sources of axial load on the sheath: first the friction between the pellets and the sheath, which the pellet-to-sheath contact model does not account for, and second the axial load if the fuel pellet stack expanded until it came into contact with the inside of the end caps. In

the manufacture of CANDU fuel elements, initial axial clearance is ensured by having the element with a fuel stack that is generally 1-3 mm shorter than the length of the sheath. The model assumes that if the pellets swell axially beyond the initial clearance that the sheath will deform to accommodate the expanded fuel because Zircaloy is significantly more malleable than the ceramic fuel.

Two potential axial boundary conditions arise if this load is going to be applied: free deformation when there is no contact, and prescribing the axial displacement to match the expanded fuel stack length. A “sticky contact” algorithm is used to prevent oscillations between the two boundary conditions and hence improve model stability. The axial contact offset,  $A_{co}$ , is used to switch conditions. The free-to-contact switch is set to enable the prescribed displacement when the pellet stack reaches the distance of  $A_{co}$  from the length of the sheath. When the stack length is shorter than  $A_{co}$ , free deformation occurs. Once the stack length is within the value of  $A_{co}$  contact loads are enabled on the axial deformation of the pellet. In the model this  $A_{co}$  is set to the 10  $\mu\text{m}$ .

#### **4.5 Pellet**

MPM-FAST has been built in such a fashion that three different material models for fuel pellets can be selected. Of these materials, the models used for  $\text{UO}_2$  were compiled and developed by Andrew Prudil [8]. Appendix A contains a

description of these models. Within this section only the work involved in adding (Th,U)O<sub>2</sub> and (Th,Pu)O<sub>2</sub> models will be discussed.

#### **4.5.1 Heat Transport**

The material properties needed to solve the heat transport equation will be presented in this section, as well as the behaviours that affects these properties during the irradiation of each pellet material.

#### **Heat Production**

Heat is produced through the fission of the unstable heavy isotopes within the fuel pellet. A simplified explanation of what occurs in the fuel is that when the fuel is in the reactor, it is exposed to a sustained neutron flux. These neutrons will interact with the atoms in the fuel pellet. Neutrons that are energetically preferential will be absorbed by fissile isotopes and lead to fission, absorbed by a fertile isotope, which will breed a new fissile atom, or scattered after a collision. Over time the composition of the fuel will begin to include the new atoms formed from fission (fission products). Neutrons that interact with these fission products will be absorbed parasitically (not lead to fission) or undergo scattering. The heat is produced when the kinetic energy of fission fragments (fission products while still ionized and highly energetic) is absorbed by the fuel matrix through collisions. Localized heat production is proportional to the localized fission rate

because fission fragments only travel ~10  $\mu\text{m}$  within the fuel matrix before stopping.

The localized fission rate (and the heat production rate) will be dependent on two major factors, the amount of fissile atoms/ability of the localized portion of the fuel to undergo fission, and the local availability of neutrons. A material's ability to undergo fission is described by its macroscopic fission cross section, which is a measure of the probability of a neutron initiating fission within the material. As mentioned above, fission is dependent on the energy spectrum of the neutrons as well as the isotopic composition of the material. The availability of neutrons in the fuel is described by the local neutron flux ( $\phi$ ). There are computational codes devoted to solving these neutron transport problems.

Within MPM-FAST the problem of accounting for the changing isotopic composition/flux shape in the fuel pellet is accomplished using the same methods employed by ELESTRES-IST for  $\text{UO}_2$  fuel. As such the method does not account for the presence of Th at any time, or any initial amounts of Pu within the fuel. This is perceived as an area in need of improvement in MPM-FAST. This method employs curve fitting results obtained from the HAMMER neutron transport code [51], to update changes in the flux shape (known as flux depression) within an analytic solution of a one group neutron diffusion model in cylindrical coordinates, with an added correction term to account for neutron

absorption near the fuel surface. This leads to the volumetric heat generation rate,  $Q_{prod}$ , to be given by equation (65).

$$Q_{prod} = f_{mag} \phi = \left( I_0(\kappa_{flux} r) + \frac{I_1(\kappa_{flux} H_r)}{K_1(\kappa_{flux} H_r)} K_0(\kappa_{flux} r) + PelletMat \beta_{flux} \exp(\lambda_{flux} (r - P_r)) \right) \quad (65)$$

Here  $f_{mag}$  is a proportionality coefficient, which ensures that the integrated volumetric heat generation is consistent with the specified linear power,  $I_n$  is the  $n^{\text{th}}$  order modified Bessel function of the first type,  $K_n$  is the  $n^{\text{th}}$  order modified Bessel function of the second type,  $r$  is the radial coordinate,  $H_r$  is the radius of the central hole,  $P_r$  is the outer radius of the pellet,  $PelletMat$  is a logic function based on the pellet material that is selected, and the parameters  $\kappa_{flux}$ ,  $\lambda_{flux}$ , and  $\beta_{flux}$  are flux shaping/depression parameters. These parameters are found by fitting the data from the HAMMER results as functions of the fuel pellet's radius, U-235 enrichment, and average fuel burnup.

$f_{mag}$  is found by equating the linear power to an average linear power for the length of a pellet, then by neglecting the fine feature of the pellet (dishes, axial gap, and chamfers), is found by integrating the volumetric heat production over the volume of the pellet, equation (66).

$$P_{lin} = 2\pi \int_{H_r}^{P_r} Q_{prod} r dr = 2\pi \int_{H_r}^{P_r} f_{mag} \phi r dr \quad (66)$$

$$f_{mag} = \frac{P_{lin}}{2\pi \int_{H_r}^{P_r} \phi r dr}$$

Here  $P_{lin}$  is the linear power in  $W m^{-1}$ , which is a required input parameter.

The function *PelletMat* in equation (65) acts as a simple on/off switch within the model to determine if  $\beta_{flux}$  term should be included within the calculation and it is outlined in equation (67) below.

$$PelletMat = \begin{cases} 1, & \text{pellet\_mat} = 1 \\ 0, & \text{pellet\_mat} \neq 1 \end{cases} \quad (67)$$

Here *pellet\_mat* is an input parameter that can be assigned an integer value between 1-3, that informs the model what fuel type the element is using (1 for  $UO_2$ , 2 for  $(Th,U)O_2$ , and 3 for  $(Th,Pu)O_2$ ). The  $\beta_{flux}$  term in  $UO_2$  fuel accounts for the presence of Pu growth in the outer region of the pellet. From works examining the flux shape within Th-based fuel, it was found that the localized power increase on the outer pellet region was not as prevalent as  $UO_2$  fuel [27], [32], [34]. This  $\beta_{flux}$  is disabled when Th-based is modelled. While within the works presented on the development of Th-based fuel performance models it has



been demonstrated that the combination of equations (65) and the second portion of (66) allows for  $Q_{prod}$  to be solved. At this time the model does not fully take into account the changes in fuel density during irradiation on the volumetric heat production.

### **Burnup**

The variable burnup is a measure of the fraction of initial heavy element atoms in fuel that have undergone (are “burned up” by) fission. Burnup is used to estimate the amount of fission products within the fuel matrix (see pellet thermal conductivity), and it is also used to briefly describe the fuel after it has undergone irradiation (i.e., exit burnup). By considering the thermal energy released by fission, burnup can also be measured as the total energy released per initial unit of heavy element. CANDU fuel burnup is typically measured in  $MWh\ kgU^{-1}$ , and can be calculated by considering the burnup rate in  $MWh\ kgU^{-1}\ s^{-1}$  using equation (68).

$$\frac{dBu}{dt} = \frac{Q_{prod}}{3.6 \times 10^9 \rho_U} = \frac{Q_{prod}}{3.6 \times 10^9 \left( \frac{238 \rho_{UO_2}}{238 + 16(2+x)} \right)} \quad (68)$$

Here  $\rho_U$  and  $\rho_{UO_2}$  are the theoretical density of uranium and uranium dioxide respectively ( $kg\ m^{-3}$ ),  $x$  is the deviation from stoichiometry of the fuel, and  $Q_{prod}$  is the volumetric heat production from equation (65). An average element burnup

rate can be found using the fuel stack length  $L$  in m and the linear power  $P_{lin}$  in  $\text{W m}^{-1}$  as given by equation (69).

$$\frac{dBu_{avg}}{dt} = \frac{P_{lin}L}{3.6 \times 10^9 M_U} \quad (69)$$

Here  $M_U$  is the initial mass of the uranium in the element in kg.

Other units used to describe burnup are, atom fraction, and  $\text{MWd tU}^{-1}$ . The approximate relationship between each of these definitions is:  $1\% \approx 225 \text{ MWh kgU}^{-1} \approx 9375 \text{ MWd tU}^{-1}$ .

Similar to the calculation of the volumetric heat production, MPM-FAST is currently using these  $\text{UO}_2$  specific models for burnup for all fuel types. Work is still required to generalize the burnup model to account for the presence of other initial heavy elements.

### Density

One of the required input variables is the initial pellet density,  $\rho_0$  ( $\text{kg m}^{-3}$ ). This property is dependent on the manufacturing conditions of fuel pellet. Density changes during irradiation are based on the strains experienced within the pellet as calculated using equation (70) (similar to equation (18)).

$$\rho = \frac{\rho_0}{(1+\varepsilon_r)(1+\varepsilon_\phi)(1+\varepsilon_z)} \quad (70)$$

Where the subscripts of r,  $\theta$ , and z refer to the specific axial directions in which the strains act within the cylindrical coordinate system of the model's geometry.

### Heat Capacity

Heat capacity (in  $\text{J kg}^{-1} \text{K}^{-1}$ ) of the fuel is modeled in MPM-FAST for  $(\text{Th,U})\text{O}_2$ , using a correlation presented by Dash *et al.* within the an IAEA Tec-Doc and given in equation (71) [29]

$$C_{p(\text{Th,U})\text{O}_2} = (66.26 + 10.91wtU) + (0.00923 - 0.00065wtU)T - (7.70 \times 10^{-5} + 6.7 \times 10^{-5}wtU)T^2 \quad (71)$$

Here  $wtU$  is the wt% of uranium within the fuel mixture and T is the fuel temperature (K). This correlation has been validated over a range of fuel mixtures of 1.9 – 90 wt % U (inputted as 0.019 – 0.9 in (71)) and temperatures of 298 – 2000 K.

$(\text{Th}_{1-y}, \text{Pu}_y)\text{O}_2$ 's heat capacity is found in MPM-FAST using equation (72) which was derived using Vegard's law and presented in Konings *et al.* [52].

$$C_{p(\text{Th,Pu})\text{O}_2} = (1 - wtPu) \cdot C_{p\text{ThO}_2} + wtPu \cdot C_{p\text{PuO}_2} \quad (72)$$

Here  $wtPu$  is the wt% of  $\text{PuO}_2$ ,  $C_{p\text{ThO}_2}$  is the heat capacity of  $\text{ThO}_2$  from Bakker *et al.* given in equation (73) [28], and  $C_{p\text{PuO}_2}$  is from Xu *et al.* and given in equation (74) [53]. The upper temperature range of the correlation is set to the melting

temperature of PuO<sub>2</sub> (2673 K).

$$C_{pThO_2} = (55.962 + 0.05126T - 3.6802 \times 10^{-5}T^2 + 9.2245 \times 10^{-9}T^3 - 5.74031 \times 10^5T^{-1}) \quad (73)$$

$$C_{pPuO_2} = \frac{347.4 \cdot 571^2 e^{\frac{571}{T}}}{T^2 [e^{571/T} - 1]^2} + 3.95 \times 10^{-4}T + \frac{3.860 \times 10^7 \cdot 1.679 \times 10^5}{R_{gas}T^2} \cdot \exp\left(\frac{(-1.965 \times 10^5)}{RT}\right) \quad (74)$$

Here  $R_{gas}$  is the ideal gas constant (8.314 J mol<sup>-1</sup> K<sup>-1</sup>).

### Thermal Conductivity

A model proposed to calculate the thermal conductivity of UO<sub>2</sub> by Lucuta,  $k_{lucuta}$ , is based on the premise that the effects of irradiation, changes in oxygen stoichiometry, and porosity on the fresh fuel's thermal conductivity ( $k_0$ ) can be accounted for by applying a series of unitless multiplicative factors given in equation (75) [54].

$$k_{Lucuta} = k_{0,HM}(T)\kappa_{1d}(\beta_p, T)\kappa_{1p}(\beta_p, T)\kappa_2(p)\kappa_3(x)\kappa_4(T) \quad (75)$$

Here  $\kappa_{1d}(\beta_p, T)$  (equation (76)) and  $\kappa_{1p}(\beta_p, T)$  (equation (77)) are UO<sub>2</sub>'s thermal conductivity dependence on irradiation induced dislocations and solid fission

product precipitates respectively,  $\kappa_2(p)$  is the dependence on the porosity of the fuel (equation (78)),  $\kappa_3(x)$  gives the dependence on the deviation from stoichiometry, where  $x$  is the deviation from stoichiometry ( $\text{UO}_{2+x}$ ), and  $\kappa_4(T)$  accounts for the dependence of radiation damage on the fuel (equation (79)). MPM-FAST sets  $\kappa_3(x)$  to one. The model does not consider fuel that is non-stoichiometric.

$$\kappa_{1d}(\beta_p, T) = \left( \frac{1.09}{\beta_p^{3.265}} + 0.0643 \sqrt{\frac{T}{\beta_p}} \right) \arctan \left( \frac{1}{\frac{1.09}{\beta_p^{3.265}} + 0.0643 \sqrt{\frac{T}{\beta_p}}} \right) \quad (76)$$

$$\kappa_{1p}(\beta_p, T) = 1 + \frac{0.019\beta_p}{(3-0.019\beta_p)(1+\exp(\frac{1200-T}{100}))} \quad (77)$$

$$\kappa_2(p) = \frac{1-p}{1+(\sigma_s-1)p} \quad (78)$$

$$\kappa_4(T) = 1 - \frac{0.2}{1+\exp(\frac{T-900}{80})} \quad (79)$$

In equation (76) and (77) the variable  $\beta_p$  is the fuel burnup in atom percent, and  $\sigma_s$  is a porosity shape factor (=1.5 for spherical pores). The porosity,  $p$ , in equation (78) is the fraction of the fuel's volume that is vacant (porous) and given by equation (80).

$$p = 1 - \frac{\rho}{\rho_{\max}} \quad (80)$$

The initial fuel porosity is a fuel design variable and is required as a model input.

Lucuta recommends using the unirradiated thermal conductivity ( $k_0$ ) correlation provided in Harding *et al.*,  $k_{0,HM}$  in equation (75) for  $UO_2$  with units of  $W\ m^{-1}\ K^{-1}$  (Appendix A displays  $k_{0,HM}$  along with other  $UO_2$  models available in MPM-FAST).

MPM-FAST uses a method for modelling the thermal conductivity of  $(Th,U)O_2$  outlined in Long *et al.* [24]. In this methodology they make the supposition that the multiplicative factors developed by Lucuta will be applicable to describe the irradiation effects on the thermal conductivity of  $(Th,U)O_2$ . Equation (81) presents the thermal conductivity of  $(Th,U)O_2$  in MPM-FAST in units of  $W\ m^{-1}\ K^{-1}$ .

$$k_{(Th,U)O_2} = k_{0,Belle}\kappa_{1p}\kappa_{1d}\kappa_2\kappa_4 \quad (81)$$

Here the various components from Lucuta given in equations (76)-(79), with  $k_{0,Belle}$  is the correlation of thermal conductivity for  $(Th,U)O_2$  presented in Belle and Berman given in equation (82) [21].

$$k_{0,Belle} = \frac{1}{A_1 + B_1 T}$$

$$A_1 = \frac{1}{46.948 - 112.072 M_{UO_2}} \quad (82)$$

$$B_1 = 1.597 \times 10^{-4} + 6.736 \times 10^{-4} M_{UO_2} - 2.155 \times 10^{-3} M_{UO_2}^2$$

Here  $M_{UO_2}$  is the mole percent of  $UO_2$  in the (Th,U) $O_2$  material (range of 0 - 30%), and the correlation was taken from data up to 2200 K.

Subsequent measurements of the thermal conductivity indicate that Belle and Berman's correlation does not reflect the change in thermal conductivity for mixtures with 10% or less  $UO_2$ . The recommended thermal conductivity correlation from literature is one given in Bakker *et al.* for thermal conductivity of (Th<sub>1-y</sub>,U<sub>y</sub>) $O_2$  at 95% theoretical density, where  $y$  is the wt% of U up to 10% ( $0 \leq y \leq 0.1$ ) and temperatures between 300-1800 K [28] (see equation (83)).

$$k_{0,Bakker} = \frac{1}{A_2 + B_2 T}$$

$$A_2 = 0.0004195 + 1.112y - 4.499y^2 \quad (83)$$

$$B_2 = 0.0002248 - 0.000917y + 0.004164y^2$$

A correction factor derived from equation (78) is applied to the Bakker correlation to make it representative of 100% dense (Th,U) $O_2$ .

For the calculation of the irradiated (Th,Pu)O<sub>2</sub> thermal conductivity, the same modelling assumption is applied. Lucuta's model is used to account for the changes in the thermal conductivity to the correlation for (Th,Pu)O<sub>2</sub>, given in equation (84) (similar assumption was made by Björk within their modelling work for (Th,Pu)O<sub>2</sub> model).

$$k_{(Th,Pu)O_2} = k_{0,Cozzo} \kappa_{1p} \kappa_{1d} \kappa_2 \kappa_4 \quad (84)$$

Here,  $k_{0,Cozzo}$  is the unirradiated thermal conductivity of (Th,Pu)O<sub>2</sub> with 5% porosity outlined in Cozzo *et al.*, and presented in equation (85)[31].

$$k_{0,Cozzo} = \frac{1}{A_3 + B_3 T}$$

$$A_3 = 0.006071 + 0.572 wtPu - 0.5937 wtPu^2 \quad (85)$$

$$B_3 = 0.00024$$

Here  $wtPu$  is the wt% of PuO<sub>2</sub> in the fuel matrix (0-100% PuO<sub>2</sub>), with the correlation being derived from a series of measurements in the temperature range of 500 K to 1600 K. A correction factor derived from equation (78) is applied to the Cozzo correlation in order for it to reflect the thermal conductivity of 100% dense (Th,Pu)O<sub>2</sub>.



### 4.5.2 Fission Gas

As discussed in the heat transport and deformation mechanics of the free volume of the element, the release of fission gas plays a significant role in the heat transfer coefficient and the gas pressure calculation. Within MPM-FAST FGR is a two-step process. The first step is solving for the concentration of fission gas within fuel grains by solving the Booth diffusion equation. The solution of the Booth equation yields the release rate of fission gas to the grain boundaries. Fission gas accumulates at the grain boundaries. The second step within the model is the determination of the boundary saturation conditions; once the boundaries become saturated by the fission gas, any fission gas that reaches the grain boundary past this point is released to the free volume of the element.

The Booth diffusion equation mentioned above treats a fuel grain as an idealized homogeneous sphere and is of the form given in equation (86) [8], [10], [55].

$$\frac{\partial C}{\partial t} = D\nabla^2 C + P_{fg} \quad (86)$$

Here  $C$  is the concentration of the fission gas atoms within the fuel grain (atoms  $\text{m}^{-3}$ ),  $D$  is the diffusion coefficient of the fission gas within the grain,  $\nabla^2$  is the Laplacian operator in spherical coordinates, and  $P_{fg}$  is the volumetric production

rate of fission gas (atoms  $\text{m}^{-3} \text{s}^{-1}$ ). The particular solution of equation (80) has to meet the initial and boundary conditions listed in equations (87) and (88).

$$C(r, t = 0) = 0 \quad (87)$$

$$C(r = g_r, t) = 0 \quad (88)$$

Here  $g_r$  is the grain radius. Since the transport of fission gas is assumed to be solely gradient driven within the fuel grain the release rate to the grain boundary is given by equation (89), as  $R_{fgflux}$  in atoms  $\text{m}^{-2} \text{s}^{-1}$ .

$$R_{fgflux}(t) = -D \left. \frac{\partial C}{\partial R} \right|_{R=g_r} \quad (89)$$

For modelling the macroscopic behaviour of gas release, the volumetric release rate  $R_{gb}$  in atoms  $\text{m}^{-3} \text{s}^{-1}$  is required, this is found by multiplying the ratio of surface area to volume of the fuel grains as shown in equation (90).

$$R_{gb}(t) = -\frac{4\pi g_r^2}{\frac{4}{3}\pi g_r^3} D \left. \frac{\partial C}{\partial R} \right|_{R=g_r} = -\frac{3}{g_r} D \left. \frac{\partial C}{\partial R} \right|_{R=g_r} \quad (90)$$

MPM-FAST uses a numerical solution to equation (90) that has shown to be in good agreement with the analytical solution of this equation derived by Kidson for  $\text{UO}_2$  fuel [8], [56]. The numerical implementation of the model is accomplished by establishing a finite element model for the grain diffusion equation. A two dimensional rectangular domain is established, with the “x-

direction” representing the radial position of the grain in the pellet, and the “y-direction” represents the radial direction in the idealized spherical grain. In order to accommodate possible grain growth, the radial coordinate within the spherical grain was transformed into a non-dimensional form presented in equation (91).

$$\eta = \frac{r}{g_r} \quad (91)$$

By substituting (91) into equation (86), the grain diffusion behaviour is now given as equation (92).

$$\eta^2 g_r^2 \frac{\partial C}{\partial t} = \frac{\partial C}{\partial \eta} \left( D \eta^2 \frac{\partial C}{\partial \eta} \right) + \eta^2 g_r^2 P_{fg} \quad (92)$$

Equation (92) can be solved by coupling the values of the average grain radius, fission gas diffusion, and fission gas production from the pellet model. These values used in the fission gas diffusion model are solved for conditions representative of the mid-length of the pellet.

With the transformation of the spherical location in the idealized grain, the concentration gradient is now given as equation (93).

$$\frac{\partial C}{\partial R} = \frac{1}{g_r} \frac{\partial C}{\partial \eta} \quad (93)$$

Substituting (93) into equation (90) provides  $R_{gb}$  in the required non-dimensional grain geometry, as equation (94).

$$R_{gb}(t) = -\frac{3}{g_r^2} D \frac{\partial C}{\partial \eta} \Big|_{\eta=1} \quad (94)$$

The volumetric production rate of fission gas,  $P_{fg}$ , in equation (86) and (92) is dependent on fission density rate ( $F_{rate}$ ) within the fuel grain. This fission density is calculated in MPM-FAST by dividing  $Q_{prod}$  by the average energy per fission ( $E_f = 200$  MeV). Leading to the  $P_{fg}$  to be found using equation (95). Further examination of the energy per fission of U-233 may need to be sought out, to determine if any differences caused by the fuel pellet materials need to be accommodated.

$$P_{fg} = y_f F_{rate} = \frac{y_f Q_{prod}}{E_f} \quad (95)$$

$P_{fg}$  in equation (95) is in units of atoms  $s^{-1}$ , where  $y_f$  is the stable fission gas yield per fission. For  $UO_2$  fuel  $y_f = 0.251$ , with the gas being composed of approximately 90% xenon and 10% krypton [8], [10]. For  $(Th,U)O_2$  and  $(Th,Pu)O_2$  fuel in MPM-FAST,  $y_f = 0.2761$ , because it was found that the fission of U-233 produced 10% more fission gas atoms per fission, with more krypton being produced (~82% xenon and 18% krypton) [21], [24].

The effective grain size in MPM-FAST is assumed to be the local average grain diameter ( $g_d = 2g_r$ ). Initial average grain radius is also one of the required input variables.  $(Th,U)O_2$  uses a grain growth model proposed initially by

McCauley [57] based on the work of Nichols [58] on UO<sub>2</sub>, for porous (Th,U)O<sub>2</sub> fuel. This work was then adapted for higher density (Th,U)O<sub>2</sub> fuel by Goldberg *et al.* [22]. Equation (96) below presents this equiaxed grain growth model.

$$g_d^3 - g_{di}^3 = K_f t \exp\left(\frac{-Q}{RT}\right) \quad (96)$$

Where  $g_{di}$  is the initial grain diameter within the ceramic fuel pellets in cm,  $t$  is time in hours,  $R$  is the universal gas constant (8.314 J mol<sup>-1</sup> K<sup>-1</sup>),  $K_f$  is a fitting coefficient with a value of 800 cm<sup>3</sup> h<sup>-1</sup> maintained from Nichols' work on UO<sub>2</sub>, and  $Q$  is the vapour activation constant for (Th,U)O<sub>2</sub>, with a value of 594×10<sup>3</sup> J mol<sup>-1</sup>. The value of  $Q$  was determined for 20-30% wt% UO<sub>2</sub>.

MPM-FAST uses a grain growth model developed for UO<sub>2</sub> Khoruzi *et al.* that is presented in equation (97) [59].

$$\frac{dg_d}{dt} = k_g \left( \frac{1}{g_d} - \frac{1}{g_m} - \frac{1}{g_{ir}} \right) \quad (97)$$

Here,  $k_g$  is the grain growth rate in m<sup>2</sup> s<sup>-1</sup>, with its value found using equation (98),  $g_m$  is the maximum stable grain size (m) as a function of temperature given in equation (99), and  $g_{ir}$  is a function of temperature and fission rate that accounts for the irradiation effects on the grain size given in equation (100).

$$k_g = 1.46 \times 10^{-8} \exp\left(\frac{-32100}{T}\right) \quad (98)$$

$$g_m = 2.23 \times 10^{-3} \exp\left(\frac{-7620}{T}\right) \quad (99)$$

$$g_{ir} = \frac{6.71 \times 10^{18} \exp\left(\frac{-5620}{T}\right)}{F_{rate} T} \quad (100)$$

A brief discussion and comparison of model results switching the different grain growth kinetics for each fuel type are presented in Appendix B.

The fission gas diffusion coefficient  $D$ , is the only remaining term from equations (86) and (92) to discuss. A complete description of the method used to determine  $D$  for  $\text{UO}_2$  fuel in MPM-FAST will be given followed by the considerations made to account for the Th-based fuel materials. The  $\text{UO}_2$  model used was developed by Morgan[10]; it was based on the work of Turnbull *et al.* from 1982, Friskney *et al.* from 1977, Turnbull *et al.* from 1977 as well as White and Tucker, from 1983[60]–[63]. The net diffusion coefficient for  $\text{UO}_2$  is given in equation (101).

$$D = \frac{D_0 b'}{b' + g_a} \quad (101)$$

Here  $b'$  is the intragranular resolution rate in  $\text{s}^{-1}$ ,  $g_a$  is the trapping rate in  $\text{s}^{-1}$ , and  $D_0$  is the single fission gas atom diffusion coefficient for a fully dense  $\text{UO}_2$  crystal. The values  $b'$  and  $g_a$  are determined using equations (102) and (103), respectively.

$$b' = 3.03\pi F_{rate} l_f (R_B + Z_0) \quad (102)$$

$$g_a = 4\pi R_B D_0 \left( \frac{1.52\alpha_{fgb}}{\pi l_f (R_B + Z_0)^2} \right) \quad (103)$$

Here  $l_f$  is the average distance travelled by a fission fragment (10  $\mu\text{m}$ ),  $\alpha_{fgb}$  is the number of fission gas bubbles nucleated by fission ( $\approx 12$ ),  $Z_0$  is the average distance between where the fission took place and the furthest effects of the path of a fission fragment are observed (1 nm), and  $R_B$  is the average radius of intragranular pores (m) given in equation (104).

$$R_B = 5 \times 10^{-10} \left( 1 + 106 \exp\left(\frac{-8702.7}{T}\right) \right) \quad (104)$$

The value of  $D_0$  for  $\text{UO}_2$  from equation (95) is found by the weighted sum of diffusion coefficients that describe the contribution of three separate mechanisms given in equation (105).

$$D_0 = D_{thrm} + 4D_{irr} + 4D_{athrm} \quad (105)$$

Here  $D_{thrm}$  is the diffusion coefficient due to thermally activated processes (dominant term  $T > 1700 \text{ K}$ ),  $D_{irr}$  is the diffusion coefficient due to irradiation induced vacancies (dominant term  $1100 \text{ K} \leq T \leq 1700 \text{ K}$ ), and  $D_{athrm}$  is the diffusion coefficient due to athermal effects (dominant  $T < 1100 \text{ K}$ ).  $D_{thrm}$ ,  $D_{irr}$ , and  $D_{athrm}$  are given in equations (106) – (108) respectively; all are in units of  $\text{m}^2 \text{ s}^{-1}$ .

$$D_{thrm} = 7.6 \times 10^{-9} \exp\left(\frac{-2.93 \times 10^5}{RT}\right) \quad (106)$$

$$D_{irr} = 10^{13} \Omega^{2/3} C_v^0 \frac{\Omega^{2/3} \mu^2 + Z_n C_v^0}{2Z_n} \sqrt{1 + \frac{2 \times 10^6 F_{rate} \Omega Z_n}{v_v (\Omega^{2/3} \mu^2 + Z_n C_v^0)}} \quad (107)$$

$$D_{athrm} = 2 \times 10^{-40} F_{rate} \quad (108)$$

$\Omega$  is the atomic volume in  $\text{m}^3$  given by equation (109).

$$\Omega = \frac{Mm_U}{\rho_{UO_2STP} N_{Av}} \quad (109)$$

$C_v^0$  is the vacancy concentration of unirradiated  $\text{UO}_2$  given by equation (110)

$$C_v^0 = \exp\left(\frac{-27780}{T}\right) \quad (110)$$

Here  $\mu \approx 10^{15} \text{m}^{-2}$  is the sink strength for crystallographic point defects (dislocations and vacancies),  $v_v = 10^{13} C_v^0$  is the vacancy jump frequency,  $Z_n \approx 100$  is the average number of sites available for recombination around defects which will inevitably recombine,  $Mm_U$  is the molar mass of natural uranium,  $\rho_{UO_2STP} = 10980 \text{kg m}^{-3}$  is the density of  $\text{UO}_2$  at STP and  $N_{Av}$  is Avogadro's number.

As this is a preliminary attempt at modelling Th-based fuels' irradiation behaviour, changing the weighting of the three components of  $D_0$  was done in MPM-FAST to replicate each fuel type's fission gas behaviour. This approach



was taken, as at this point in time there is limited data available on fission gas diffusion behaviour in Th-based fuel, limiting the ability to derive a model of the fission gas diffusion in thorium. For (Th,U)O<sub>2</sub> fuel the change in the fission gas diffusion behaviour is scaled by a factor of 0.1 applied to the effective diffusion coefficient (equation (101)) as outlined in equation (111).

$$D_{(Th,U)O_2} = 0.1D \quad (111)$$

The movement of gaseous ions within Th-based fluorite grain structures has not been as thoroughly studied as U-based diffusion. Early measurements of oxygen diffusion within grains of ThO<sub>2</sub> were reported by Matzke [64] in comparison with UO<sub>2</sub>. It was reported that O diffusion in ThO<sub>2</sub> was markedly reduced compared to UO<sub>2</sub> [64]. It was found in CNL irradiation experiments that the observed FGR from Th-based fuels is significantly less than that observed in UO<sub>2</sub> fuel [38], [19]. During the irradiation test of a defected (Th,U)O<sub>2</sub> fuel element, online monitoring of the <sup>133</sup>Xe released was found to be 1 to 2 orders of magnitude less than that of UO<sub>2</sub> fuel. The ingress of coolant into a defected element leads to fuel oxidation in UO<sub>2</sub>, which affects the thermal conductivity and microstructure and leads to an increase in FGR. ThO<sub>2</sub> is resistant to steam oxidation, contributing to the retention of fission gas; however, it is uncertain what effect this has for defected Th-based fuel. Some reactions may alter the release rate of <sup>133</sup>Xe; however, in post-irradiation annealing tests on thoria-uranium

fuel (35% ThO<sub>2</sub>, 65% UO<sub>2</sub>) by Kim *et al.* [65], it was found that the diffusion of <sup>133</sup>Xe in poly-crystalline (Th,U)O<sub>2</sub> was approximately an order of magnitude less than that of UO<sub>2</sub>. These findings provided the rationale for selecting the 0.1 scaling factor for the (Th,U)O<sub>2</sub> fission gas diffusion model used. Aside from these measurements, previous models by Long *et al.* for (Th,U)O<sub>2</sub> light water reactor fuel also applied the assumption of a scaling factor of 0.1 to the high temperature portion of the fission gas diffusion coefficient [24]. A second model developed by Lee *et al.* [25] for (Th,U)O<sub>2</sub> fuel also considered the work of Kim *et al.*[65] mentioned above when examining their fission gas release model, [25] . This establishes a precedent in terms of approximating the fission gas diffusion of (Th,U)O<sub>2</sub> be one tenth that of UO<sub>2</sub>. These models have also demonstrated an ability to provide fission gas release calculations comparable to measurements of irradiations from a wide range of (Th,U)O<sub>2</sub> compositions.

MPM-FAST treats the (Th,Pu)O<sub>2</sub> fission gas diffusion by altering the individual weightings to the components of  $D_0$  from equation (105), producing a single atom diffusion coefficient specifically for (Th,Pu)O<sub>2</sub>. Two variations of  $D_{0,(Th,Pu)O_2}$  were generated by fitting the FGR based on the irradiation history from the BDL-422 experiment given in equation (112).

$$D_{0,(Th,Pu)O_2 1} = 1.74D_{thrm} + 0.25D_{irr} + 0.25D_{athrm} \quad (112)$$

$$D_{0,(Th,Pu)O_2 2} = 1.415D_{thrm} + 0.1604D_{irr} + 0.1604D_{athrm}$$

A description of the fitting process will be described in detail after the experiment is described in the Chapter 6 Results and Discussion as well as Appendix C, which contains a listing of the various steps taken in the fitting processes.

With the total fission gas diffusion behaviour in (Th,Pu)O<sub>2</sub>,  $D_{(Th,Pu)O_2}$ , is given by equation (113).

$$D_{(Th,Pu)O_2} = \frac{D_{0,(Th,Pu)O_2} b'}{b' + g_a} \quad (113)$$

The term  $g_a$  in the denominator of equation (113), is given in (103).

This outlines all that is required to calculate the fission gas transport to the grain boundary. The second step in the release model is to determine the boundary saturation conditions and the amount of fission gas that has been released from the boundary. Once the fission gas is released from the grain it becomes trapped in intergranular bubbles on the grain boundaries. The fission gas on the grain boundary,  $G_b$ , in atoms m<sup>-3</sup> can be described by equation (114).

$$\frac{\partial G_b}{\partial t} = R_{gb} - R_e \quad (114)$$

Here  $R_{gb}$  is given in equation (90) and  $R_e$  is the release rate from the grain boundary to the free volume of the fuel element. Within MPM-FAST the release of fission gas to the free volume of the element is modeled as the inter-linkage of intergranular bubbles at the grain boundaries producing a path to the fuel's surface through the intergranular porosity and cracks. Initially gas collects on the grain surface as isolated bubbles. The bubbles grow until they reach the point where they touch and interlink, termed grain boundary saturation. The model assumes that only the fission gas that exceeds the grain boundary saturation conditions gets released. Effectively this would physically mean that fission gas bubbles are isolated when the grain boundary is saturated, and the paths to the fuel surface only open up when excessive gas is available. As the bubbles form at the interface between grains they are lenticular in shape rather than spherical. The grain boundary saturation conditions used in MPM-FAST were derived in White and Tucker [63] and are given in equations (115) and (116).

$$G_{bsat} = \frac{4r_f f(\theta_{fg}) f_b}{3k_B T \sin^2(\theta_{fg})} \left( P_{ext} + \frac{2\gamma_{se}}{r_f} \right) \left( \frac{3}{g_r} \right) \quad (115)$$

$$f(\theta_{fg}) = 1 - 1.5 \cos(\theta_{fg}) + 0.5 \cos^3(\theta_{fg}) \quad (116)$$

Here,  $r_f = 5 \times 10^{-7}$  m is the radius of curvature of a fission gas bubble,  $f(\theta_{fg})$  is a function that accounts for the shape of the bubbles,  $\theta_{fg} = 50^\circ$  is the half-angle between bubble surfaces,  $f_b = 0.5$  is the fraction of the grain surface covered in

bubbles when interlinkage occurs,  $k_B=1.3806 \times 10^{-23}$  J K<sup>-1</sup> is the Boltzmann constant,  $T$  is the temperature in K,  $P_{ext}$  is the externally applied hydrostatic pressure in Pa,  $\gamma_{se}=0.626$  J m<sup>-2</sup> is the surface energy of the bubbles, and  $g_r$  is the radius of the grains in m. Substituting these values into (115), the boundary saturation conditions can be described by equation (117).

$$G_{bsat} = \frac{2.0811 \times 10^{16}}{\tau g_r} (P_{ext} + 2.504 \times 10^6) \quad (117)$$

This version of MPM-FAST assumes  $P_{ext}=0$ . This assumption is consistent with other models examining fission gas release behaviour, and is considered to be conservative because the exclusion of hydrostatic pressure minimizes the amount of fission gas that can be stored on the grain boundary [8], [10], [66]. With knowledge of the grain boundary saturation conditions, the grain-boundary-to element release rate for a small volume is given by equation (118).

$$R_e = \begin{cases} \frac{G_b - G_{bsat}}{\tau_{fg}} & G_b \geq G_{bsat} \\ 0 & G_b < G_{bsat} \end{cases} \quad (118)$$

Here  $\tau_{fg}$  is the time constant of fission gas release. It is to be thought of as the time required for the fission gas that is over saturating the boundary to be completely released if the release rate remains constant. In NOC analysis, fission gas release is considered to be instantaneous; however, in transient analysis, it is considered to be on a time scale large enough for its release to be ignored.

Essentially this time constant dependence is included to enable the model to extend to both types of analysis. It is also somewhat arbitrary. As such, it is a model input parameter, recommended to be between the order of minutes to days, and set to 18 hours for the work presented in Chapter 6.

Using this model, the release rate of fission gas to the free element of the volume can be found by integrating (118) over the volume of the fuel, as given in equation (119) in units of mole per second.

$$R_{e,Tot} = \frac{1}{N_{Av}} \int_V R_e dV \quad (119)$$

### 4.5.3 Deformation

#### Elastic Deformation

For the Th-based ceramic fuel, MPM-FAST uses the Young's modulus and Poisson's ratio for ThO<sub>2</sub> (equations (120) and (121)), to date no data has been found on what these parameters are for either (Th,U)O<sub>2</sub> or (Th,Pu)O<sub>2</sub> [21].

$$E_{ThO_2} = E_{ThO_2,273} p \left( 1.023 - 1.405 \times 10^{-4} T e^{\frac{-181}{T}} \right) \quad (120)$$

$$\nu_{ThO_2} = 0.28 \quad (121)$$

In equation (120),  $E_{ThO_2,273}$  is the young's modulus of ThO<sub>2</sub> at 273 K with a value of 249.1 GPa. Equation (120) was validated up to 1500 K. The fuel can exceed this temperature during irradiation, again it is also the only model currently available.

### Thermal Expansion

$\varepsilon_{thm,(Th,U)O_2}$ , the thermal strain correlation for (Th,U)O<sub>2</sub> is given in equation (122) and derived by Bakker *et al.*[28].

$$\varepsilon_{thm,(Th,U)O_2} = \begin{cases} -0.179 - 0.087wtUO_2 + (5.097 + 4.705wtUO_2) \times 10^{-4}T + \\ (3.732 - 4.002wtUO_2) \times 10^{-7}T^2 + (-7.594 + 11.98wtUO_2) \times 10^{-11}T^3 \\ -0.179 - 0.149wtUO_2 + (5.097 + 6.693wtUO_2) \times 10^{-4}T + \\ (3.732 - 4.002wtUO_2) \times 10^{-7}T^2 + (-7.594 + 19.784wtUO_2) \times 10^{-11}T^3 \end{cases} \quad (122)$$

Here the first component is valid over the temperature range of  $273 \text{ K} \leq T < 923 \text{ K}$ , the second component over the range of  $923 \text{ K} \leq T < 2000 \text{ K}$ , and wtUO<sub>2</sub> is the weight percent of UO<sub>2</sub> in the fuel over the range  $0 \leq wtUO_2 \leq 0.1$  (0.1 = 10%).

$\varepsilon_{thrm,(Th,Pu)O_2}$ , thermal strain for (Th,Pu)O<sub>2</sub> is given by the correlation in equation (123) [29].

$$\begin{aligned} \varepsilon_{thrm,(Th,Pu)O_2} = & -0.179 - 0.049wtPu + (5.079 + 225wtPu) \\ & \times 10^{-4}T + (3.732 - 2.257wtPu) \times 10^{-7}T^2 \\ & + (-7.594 + 12.454wtPu) \times 10^{-11}T^3 \end{aligned} \quad (123)$$

There are other sources of inelastic deformation accounted for in FAST that are maintained in MPM-FAST but use the UO<sub>2</sub> models that are available. Table 5 (below) lists these phenomena along with their referenced source, again the implementation of these models is discussed in Prudil's work [8]. Again further details are available in Appendix A for these models.

Table 5: List of models that affect deformation that are UO<sub>2</sub> based.

<b>Physical Phenomena</b>	<b>Sources and Notes</b>
Pellet Densification	Adapted in Prudil's work [8] from an empirical correlation for CANDU fuel presented by Hastings and Evans [67]
Solid Fission Product Swelling	Burnup dependent function discussed in Olander [68]
Swelling from Grain Boundary Fission Gas Bubbles	MATPRO correlation from Luscher and Geelhood [10] altered by Prudil [8] to account for differences in fission gas release models
Pellet Fracturing	A pellet cracking model is implemented in FAST and uses the fracture strength of UO <sub>2</sub> given in MATPRO [14]

It should be noted that the fracture strength for ThO<sub>2</sub> is presented in Matzke at room temperature [69]. In Matzke's work [69] the ThO<sub>2</sub> measurements



of fracture surface energy and measurements of  $\text{UO}_2$  are presented, however  $\text{UO}_2$  measurements were taken at temperatures above room temperature. The  $\text{ThO}_2$  fracture surface energy can be anywhere from a factor of 2.5 to 12.5 times greater than  $\text{UO}_2$ , however with the temperature differences between the measurements and unknown effects of porosity Matzke felt it was not tenable to make a direct comparison. The fracture model for  $\text{UO}_2$  was maintained due to the limited understanding of the fracture strength at operational temperatures. In general, the sensitivity of the solution to the fracture stress is small, as a result of the high elastic moduli leading to relatively small elastic strains compared to inelastic strains.

## 5 Model Implementation

As discussed in the previous chapter, many of the physical phenomena within fuel performance models are described by PDEs and ODEs. These models have been implemented using the finite element analysis software COMSOL Multiphysics®, to provide numerical solutions to the coupled sets of equations needed to determine the irradiation behavior of nuclear fuel. The complete details of how MPM-FAST is implemented in COMSOL are presented in Appendix D. The focus of this chapter is to show how the models for (Th,U)O<sub>2</sub> and (Th,Pu)O<sub>2</sub> are developed with UO<sub>2</sub> as a starting point. This chapter will describe a brief overview of COMSOL in (5.1), followed by outlining the components in MPM-FAST (5.2), and the implementation of the Th-based models for each of the different phenomena models: Heat Transport (5.3), Deformation (5.4), and FG diffusion (5.5).

### 5.1 COMSOL Overview

Within COMSOL there are built in ODE and PDE equations that solve many common reoccurring physical phenomena of interest in physics and engineering. Examples of these equations used within MPM-FAST are heat transport in solids through conduction (equation 1) and solid mechanics that accounts for pellet and sheath deformation. Another feature of COMSOL is that it

contains the frame work to solve custom ODEs and PDEs by implementing generalized coefficient forms, as presented in equations (124) and (125) below respectively.

$$e \frac{\partial^2 u}{\partial t^2} + d_a \frac{\partial u}{\partial t} = f \quad (124)$$

$$e \frac{\partial^2 u}{\partial t^2} + d_a \frac{\partial u}{\partial t} + \nabla \cdot (-c \nabla u - \alpha u + \gamma) + \beta \cdot \nabla u + a_c u = f \quad (125)$$

Here  $u$  represents the dependent variable the user is solving for within the equation. The remaining terms are listed in Table 6 below.

Table 6: Generalized coefficient terms that allow for customized ODEs and PDEs to be solved withn COMSOL

Symbol	Description
$e$	mass coefficient
$d_a$	damping coefficient or mass coefficient
$c$	diffusion coefficient
$\alpha$	conservative flux convection coefficient
$\beta$	convection coefficient
$\gamma$	conservative flux source term
$a_c$	absorption coefficient
$f$	source term

The various forms of ODEs and PDEs that the user wishes to solve are applied to the geometry that represents the physical system, within a model component. A model component will contain a series of individually defined

equations that are to be solved. With the required boundary and initial conditions, the geometry of the system; is defined and meshed. The information required by the user to input into COMSOL is organized into different types of variables and operators. Several are outlined below to aide in explaining the model implementation.

*Parameters* are global values that are independent of position or time and can be applied to all model components. Parameters are constant; they are evaluated once at the start of a model run and are not updated with a model step. They are defined as numerical constants or the result of mathematical operation of numerical constants. Generally they are used to define geometries, establish solver settings, and define mesh sizing. An additional use of parameters, allow COMSOL to perform consecutive model runs. These consecutive runs are known as parameter sweeps and are defined by providing COMSOL with a series of differing parameter values that are to be investigated.

*Variables* are defined within each model component or as global values. They can have time or positional dependence and may be defined as functions of other variables, parameters or dependent variables. Variables can be defined on any type of geometry within COMSOL (points, boundaries, surfaces, volumes). They are only evaluated if it is required to

calculate a dependent variable, and are updated with each time step.

Variables can be passed between different model components through the use of coupling operators.

*Coupling Operators* are used to evaluate variables on a subset of the geometry within a model component. These operators can act as a way of finding a specific value or mathematical function on the variable in that specific region of the geometry. Some operators available in COMSOL are: maximum value, minimum value, average value, integration, as well as general extrusion. These operators allow for a refined analysis of the model results in the region they are applied to and allow for the mapping of a variable from one model component to another.

*Functions* are mathematical expressions or data handling instructions that require one or more inputs to produce an output. For example there are functions that act as conditional operators `min()`, `max()`, and `if()` statements, as well as the `nojac()` function which removes the expression in the brackets from the Jacobian matrix to reduce the complexity of the system of equations. Functions can also be defined by the user. By providing look up table data, COMSOL is capable of generating, piecewise fitting or interpolation to produce a function. This is often used to define power

histories, material properties, or complex boundary conditions (see Figure 3 in Chapter 4).

*Dependent Variables* are the solutions to the PDEs and ODEs that COMSOL is solving. Similar to the variables, these are updated with each time step and are tested for convergence. They may also be defined globally or on any geometry type (point, edge, surface or volume).

All variables and functions can be assigned units using square brackets following its expression value. All units are converted into SI internally. Unit analysis acts as a means of checking for input errors. COMSOL will highlight an expression with yellow text in the event of a mismatch. However COMSOL will perform the calculation regardless of the presence of such a mismatch.

COMSOL has an array of nonlinear-solvers that enable the user to select settings that best match the system of equations that are being examined. There are multiple types of iterative and direct solvers to select from. MPM-FAST uses a direct solver algorithm called PARADISO. The time dependent model solver is controlled semi-automatically by an Implicit Differential-Algebraic (IDA) solver. This solver type attempts to take the maximum time step possible while satisfying the tolerance settings. COMSOL allows the user to define a damping factor to control the maximum time step and reduce the relative change in moving onto the next step size.

MPM-FAST establishes smaller maximum time steps when initiating the model. This allows for the model to better handle the rapid change in the dependent variables as the thermal expansion occurs in the pellet. Table 7 below lists the parameters that establish the step sizes and periods. A maximum time step is also established outside of the initial time step intervals. COMSOL will take intermediate smaller time steps if the convergence criteria are not met.

Table 7: Parameters that control time stepping in MPM-FAST.

Parameter	Value
timestep_range1_start	0.1[s]
timestep_range1_size	0.1[s]
timestep_range1_end	5[s]
timestep_range2_start	5[s]
timestep_range2_size	1[s]
timestep_range2_end	6[s]

MPM-FAST contains ~13000 DOF (dependent on mesh density) per run and when solved on a computer containing an Intel Xeon CPU dual processor that runs at 2.93 GHz and 96 GB RAM, a run required 10 minutes and 5 seconds.

## 5.2 MPM-FAST Model Components

There are two model components within MPM-FAST. The first component is dedicated to heat transport (equation (1)) and deformation (equations (2)-(9)) for the fuel pellet and sheath, as well as the overall gas release (equations (111) & (112)). The second component is devoted to the calculation of

the fission gas concentration within the fuel grains (equation (80)) and the grain boundary fission gas accumulation rate (equation(90)). Table 8 below outlines the parameters used to generate the geometry used within component 1.

Table 8: Parameters within global domain that establish pellet and sheath geometry.

Input Parameter	Description	Sample Value
pellet_radius	Radius of fuel pellet ( $P_r$ )	13.438[mm]/2
radial_chamfer	Length of the pellet chamfer in the radial direction ( $R_c$ ).	0.827[mm]
axial_chamfer	Length of the pellet chamfer in the axial direction ( $A_c$ )	0.176[mm]
land_width	Size of the land width ( $L_w$ ).	0.0 [mm]
dish_depth	Depth of the pellet dish ( $D_d$ )	0.27 [mm]
dish_radius	Radius of the dish sphere. Calculated from the pellet radius, radial chamfer and landwidth ( $D_r$ )	$(dish\_depth^2+(pellet\_radius-land\_width-radial\_chamfer)^2)/(2*dish\_depth)$
pellet_length	Axial length of pellet ( $P_l$ )	18.52 [mm]
num_pellets	Number of pellets in fuel element	26
pellet_sheath_gap	Radial size of the pellet-to-sheath clearance	0.08/2 [mm]
pellet_pellet_gap	Axial clearance between pellets measured land-to-land	2.29[mm]/num_pellets
sheath_internal_radius	Internal radius of the fuel sheath	pellet_radius+pellet_sheath_gap
sheath_thickness	Radial thickness of the fuel sheath ( $S_T$ )	0.405 [mm]
num_dishes	Number of dished surfaces per pellet. (1 is top only, 2 is top and bottom)	2
num_chamfers	Number of chamfered edges per pellet (1 is top only, 2 is top and bottom)	2

The equations, which the finite-element analysis is solving, are approximated at nodes within a mesh. Table 9 outlines the parameters which



control the distribution of nodes along the specific boundaries of the pellet and sheath geometries.

Table 9: Parameters that establish mesh distribution on the pellet and sheath model geometries.

Parameter	Sample Value
mesh_nodes_pellet_dish	11
mesh_nodes_pellet_chamfer	3
mesh_nodes_pellet_axial	30
mesh_nodes_sheath_radial	4
mesh_nodes_sheath_axial	44

Using the listed sample values from Tables 8 and 9, the geometry of the fuel and sheath, the first model component produces the meshed geometry presented in Figure 12 below. MPM-FAST treats this geometry in cylindrical coordinates. The axis of rotation is along the left most boundary of the pellet; periodic boundary conditions are applied along the top and bottom of the geometry, and the coolant temperature and pressure conditions acting along the right most boundary of the sheath allow the model to find a unique solution to the heat transfer and deformation equations. First order elements are used for the majority of equations solved for within this component, with the exception of deformation, which uses second order elements.

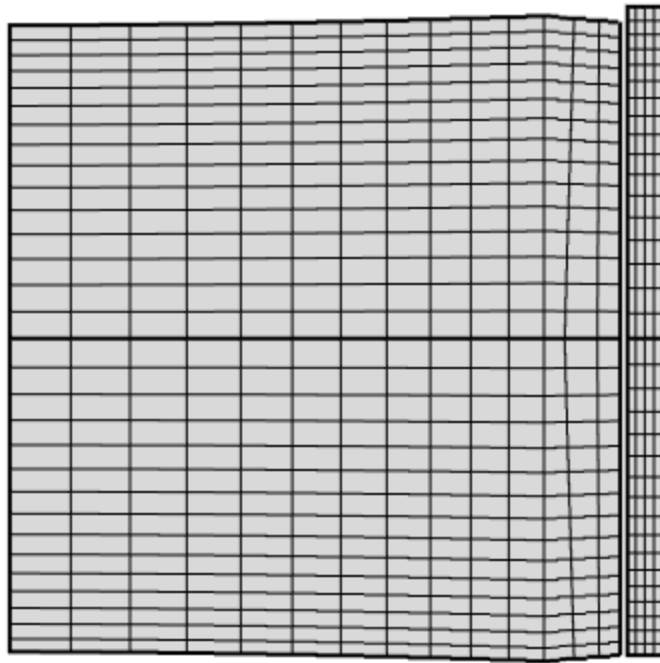


Figure 12: Meshed geometries of pellet and sheath as outlined by parameters listed in Tables 8 and 9.

As mentioned above, there is a second model component within MPM-FAST. Its geometry is a simple rectangle that has a width (length along x-axis) of the pellet's radius and height (length along y axis) of 1. Unlike the previous modelling geometry, where it is representative of the physical construction of fuel, this rectangular geometry is a mathematical construct that acts to represent the diffusion behavior of the FG through spherical grains from the center of the fuel pellet ( $x=0$ ), out to the pellet's outer cylindrical surface ( $x=\text{pellet\_radius}$ ). The y-axis acts as the radial location within a grain,  $y=0$  is the center of the grain,  $y=1$  is the grain sphere's boundary, a grain radius from the center. The meshed

geometry of this model component is presented in Figure 13 below. Mesh distribution along the y-axis is controlled by establishing the number of nodes (20) and setting the ratio of the minimum divided by the maximum to be  $10^{-3}$ . Since the boundary condition has the fission gas concentration set to 0 at the grain boundary, a steep gradient is anticipated, requiring a fine mesh in this region. The x-axis mesh distribution is equal to  $\text{mesh\_nodes\_pellet\_dish} + \text{mesh\_nodes\_pellet\_chamfer}$ .

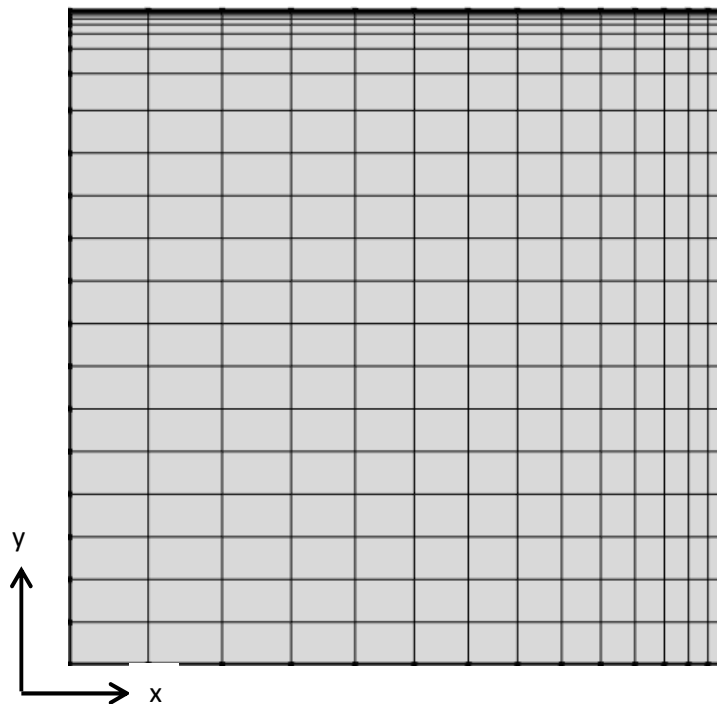


Figure 13: Meshed geometry of FG diffusion model component for MPM-FAST.

Figure 14 below summarizes the equations solved within each model component and highlights the modelling results from each component that

couples them. The full details of how this is accomplished are outlined by Prudil [8] in his work on the development of the UO<sub>2</sub> fuel performance model FAST.

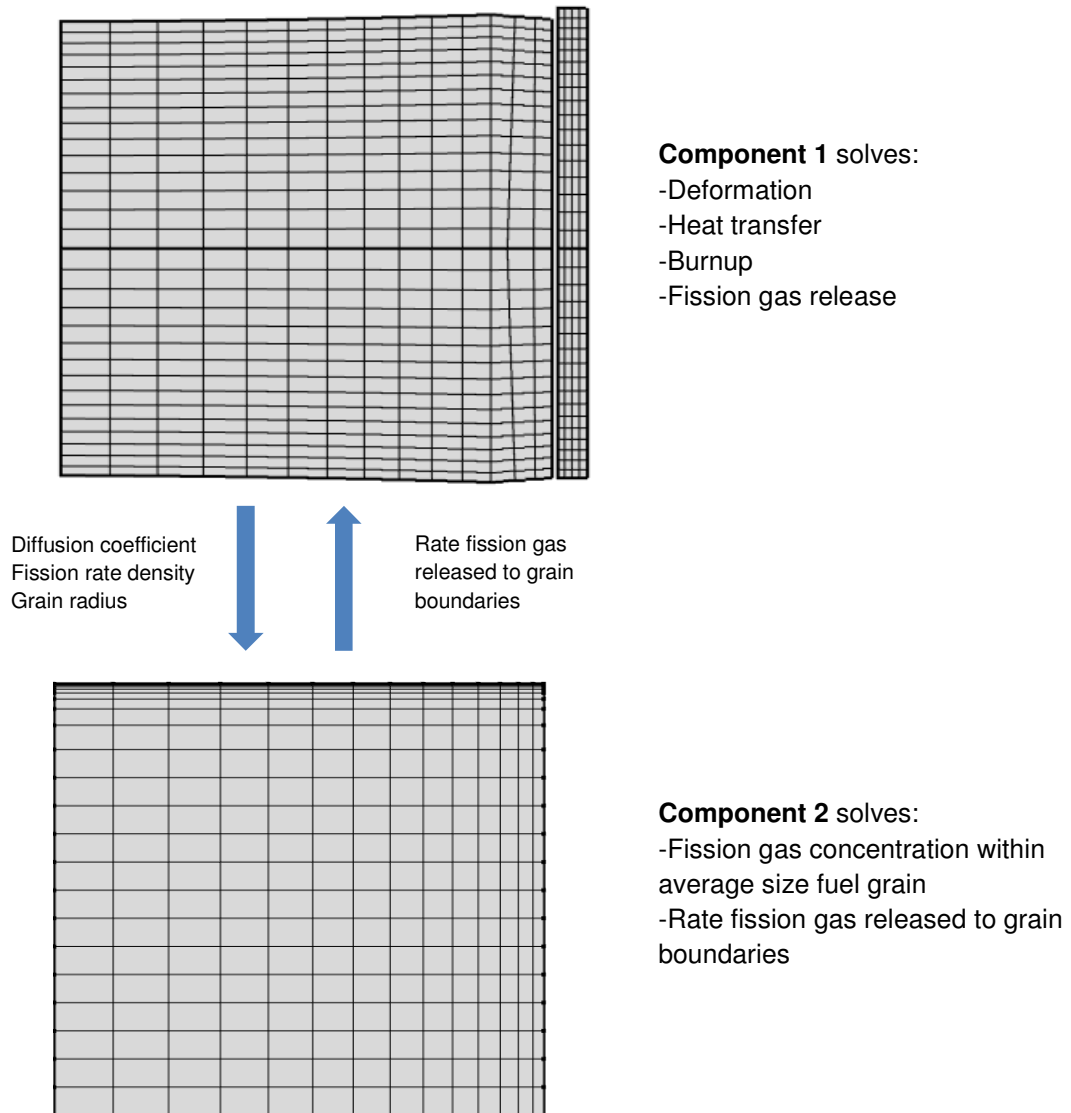


Figure 14: The geometries of the model components and summaries of the physical phenomena solved within each component.

### 5.3 Heat Transport

Implementing the heat transport for Th-based fuel and adding 310 stainless steel models into MPM-FAST comprised of: adding the material properties required to solve the heat conduction in a solid as variables available for model component 1, and enable a MPM-FAST user to select what materials to model. Table 10 contains the Parameters added to select the materials to model.

Table 10: Parameters that select the specific materials to model within MPM-FAST.

Parameter	Values	Comments
pellet_mat	1,2,3	Each value selects a ceramic material for the pellet: 1=UO <sub>2</sub> , 2=(Th,U)O <sub>2</sub> , 3=(Th,Pu)O <sub>2</sub>
sheath_mat	1,2	Each value selects a metal for the clad/sheath: 1=Zircaloy-4, 2=310 Stainless Steel

Further parameters added to enable the modelling of thorium mixed oxide fuel are displayed in Table 11 below. These parameters act as the input for the amount of either uranium or plutonium mixed with the thorium as a weight percent. The weight percent is converted to an atom percent for (Th,U)O<sub>2</sub> or (Th,Pu)O<sub>2</sub>, as it is a necessary input in the material properties correlations.

Table 11: Parameters that inform the model about the composition of the mixed oxide fuel.

Parameter	Sample Value	Comments
wPer_U	0.015	Weight percent of either Uranium or Plutonium in ceramic fuel. Expressed as a decimal (i.e. 10%=0.1)
M_HEU	235.321[g/mol]	Molar mass of heavily enriched uranium.
M_Th	232.038 [g/mol]	Molar mass of thorium.
M_O	15.999[g/mol]	Molar mass oxygen
M_m	$wPer\_U * M\_HEU + (1 - wPer\_U) * M\_Th$	Molar mass of metal atoms in fuel matrix
M_mO2	$M\_m + 2 * M\_O$	Molar mass of (Th,U)O <sub>2</sub>

Lastly, Table 12 contains the variables established in model component 1 that provide the material properties correlations added to make MPM-FAST capable of solving for the heat conduction equations for (Th,U)O<sub>2</sub>, (Th,Pu)O<sub>2</sub> and the 310 stainless steel (equation (1)).

Table 12: Variables within model component 1 to enable a solution to heat transfer through the materials added to MPM-FAST.

Variable	Expression	Comments
k_pellet	$(\text{if}(\text{pellet\_mat}==1, k_{\text{UO2}}, 0) + \text{if}(\text{pellet\_mat}==2, k_{\text{ThUO2}}, 0) + \text{if}(\text{pellet\_mat}==3, k_{\text{ThPuO2}}, 0))$	Series of if statements controlled by value of pellet_mat selects appropriate thermal conductivity
kappa1d_Lucuta	$(1.09/\text{burnup\_p}^3.265 + 0.0643 * \sqrt{T[1/K]/\text{burnup\_p}}) * \text{atan}(1/(1.09/\text{burnup\_p}^3.265 + 0.0643 * \sqrt{T[1/K]/\text{burnup\_p}}))$	Implementation of the Lucuta factors that affect thermal conductivity of fuel (equations 70-73)
kappa1p_Lucuta	$1 + 0.019 * \text{burnup\_p} / (3 - 0.019 * \text{burnup\_p}) / (1 + \exp(12 - T[1/K]/100))$	
kappa2_Lucuta	$(1 - \text{pore\_fraction}) / (1 + 0.5 * \text{pore\_fraction})$	
kappa4_Lucuta	$1 - 0.2 / (1 + \exp((T[1/K] - 900)/80))$	
k_ThUO2_FRAPCON3	$k_{\text{ThUO2\_FRAPCON3}}$	
k_ThUO2_BelleBer	$k0_{\text{ThUO2\_BelleBer}} * \text{kappa1d\_Lucuta} * \text{kappa1p\_Lucuta} * \text{kappa2\_Lucuta} * \text{kappa4\_Lucuta}$	
A_ThU	$1 / (46.948 - 112.072 * M_{\text{per\_U}})$	Unirradiated thermal conductivity of (Th,U)O <sub>2</sub> from Belle and Berman, Equation (76)
M_per_U	$M_{\text{HEU}} * w_{\text{Per\_U}} / M_{\text{mO2}}$	
k_Bakker_ThU	$((1 / (\text{bakker\_a} + \text{bakker\_b} [1/K] * T)) / 0.926829) [W/(m * K)]$	
bakker_a	$0.0004195 + 1.112 * w_{\text{Per\_U}} - 4.499 * w_{\text{Per\_U}}^2$	
bakker_b	$(0.0002248 - 0.000917 * w_{\text{Per\_U}} + 0.004164 * w_{\text{Per\_U}}^2)$	
k_bakker_luc	$k_{\text{Bakker\_ThU}} * \text{kappa1d\_Lucuta} * \text{kappa1p\_Lucuta} * \text{kappa2\_Lucuta} * \text{kappa4\_Lucuta}$	
k_ThPuO2	$k0_{\text{ThPuO2\_cozzo}} * \text{kappa1d\_Lucuta} * \text{kappa1p\_Lucuta} * \text{kappa2\_Lucuta} * \text{kappa4\_Lucuta}$	
k0_ThPuO2_cozzo	$(1 / (A_{\text{ThPu}} + 0.00024 [1/K] * T)) [W/(m * K)] / 0.926829268$	Unirradiated thermal conductivity of (Th,Pu)O <sub>2</sub> from Cozzo <i>et al.</i> , Equation (77)
A_ThPu	$0.006071 + 0.572 * w_{\text{Per\_U}} - 0.5937 * w_{\text{Per\_U}}^2$	
Cp_pellet	$\text{if}(\text{pellet\_mat}==1, cp_{\text{UO2}}, 0) + \text{if}(\text{pellet\_mat}==2, cp_{\text{ThUO2}}, 0) + \text{if}(\text{pellet\_mat}==3, cp_{\text{ThPuO2}}, 0)$	Series of if statements

	ellet_mat==3,cp_ThPuO2,0)	controlled by value of pellet_mat selects appropriate heat capacity
cp_ThUO2	$(10.087-2.891*10^{-4}[1/K]*T-6.354*10^{-7}*wPer\_U+5.111*10^{-6}*wPer\_U^2)[J/kg/K]$	Equation (65)
cp_ThO2	$(55.9620+51.2579e-3[1/K]*T-36.8022e-6[1/K^2]*T^2+9.22542e-9[1/K^3]*T^3-5.7403e5[K^2]/T^2)[J/kg/K]$	Equation (67)
cp_PuO2	$(347.4*(571[K])^2*exp(571[K]/T)/T^2/(exp(571[K]/T)-1)^2+3.95e-4[1/K]*T+3.86e7*1.967e5[J*K]/8.31447[J/K]/T^2*exp(-1.965e5[J]/8.31447[J/K]/T))[J/kg/K]$	Equation (68)
cp_ThPuO2	$(1-wPer\_U)*cp\_ThO2+wPer\_U*cp\_PuO2$	Equation (66)
K_Zir	if(sheath_mat==1,k_Zir_1,0)+if(sheath_mat==2,thermal_conductivity_310,0)	Series of if statements controlled by value of sheath_mat selects appropriate thermal conductivity
thermal_conductivity_310	$(0.0071[degF^{-1}]*T+6.8435)[BTU/h/degF*ft^{-1}]$	Equation (20)
density_310	nojac(0.284[lb*in^{-3}])	Chapter 4 page 38

## 5.4 Deformation

Recall equations (2)-(7) that outline the solid mechanics calculations required to find the deformation of the fuel geometry. Listed below in Table 13 are the material properties of the 310 stainless steel, (Th,U)O<sub>2</sub>, and (Th,Pu)O<sub>2</sub> that enable MPM-FAST to calculate the deformation.



Table 13: Variables within model component 1 added to allow for the deformation model to be solved.

Variables	Expression	Comments
thermal_expansion_310	$(0.001[\text{degF}^{-1}]*T+8.5452)*10^{-6}$	Equation (29)
youngs_modulus_310	$(-0.0064[\text{degF}^{-1}]*T+24.99)*10^6[\text{psi}]$	Equation (22)
pellet_poisson_ratio	$\text{if}(\text{pellet\_mat}==1,\text{poisson\_ratio\_UO2},0)+\text{if}(\text{pellet\_mat}==2,\text{poisson\_ratio\_ThO2},0)+\text{if}(\text{pellet\_mat}==3,\text{poisson\_ratio\_ThO2},0)$	Series of if statements controlled by value of pellet_mat selects appropriate Poisson's ratio
poisson_ratio_ThO2	0.28	Equation (115)
Youngs_pellet	$\text{if}(\text{pellet\_mat}==1,E_{\text{UO2}},0)+\text{if}(\text{pellet\_mat}==2,E_{\text{ThO2}},0)+\text{if}(\text{pellet\_mat}==3,E_{\text{ThO2}},0)$	Series of if statements controlled by value of pellet_mat selects appropriate Young's Modulus
E_ThO2	$249.1[\text{GPa}]*(1-2.21*(1-\rho_{\text{UO2}}/\rho_{\text{UO2\_theory}}))*(1.023-1.405e-4[1/\text{K}]*T*\exp(-181[\text{K}/T]))$	Equation (114)
Thermal_Strain	$(\text{if}(\text{pellet\_mat}==1,\text{thermal\_strain\_UO2},0)+\text{if}(\text{pellet\_mat}==2,\text{thermal\_strain\_ThUO2},0)+\text{if}(\text{pellet\_mat}==3,\text{thermal\_strain\_ThPuO2},0))$	Series of if statements controlled by value of pellet_mat selects appropriate thermal strain correlation
thermal_strain_ThUO2	$((273[\text{K}]<T<923[\text{K}])*(-0.179-w_{\text{Per\_U}}*0.087+(5.097*10^{-4}+w_{\text{Per\_U}}*4.705*10^{-4})[1/\text{K}]*T+(3.732*10^{-7}-w_{\text{Per\_U}}*4.002*10^{-7})[1/\text{K}^2]*T^2-(7.594*10^{-11}-w_{\text{Per\_U}}*11.98*10^{-11})[1/\text{K}^3]*T^3)+(923[\text{K}]<T)*(-0.179-w_{\text{Per\_U}}*0.149+(5.097*10^{-4}+w_{\text{Per\_U}}*6.693*10^{-4})[1/\text{K}]*T+(3.732*10^{-7}-w_{\text{Per\_U}}*4.002*10^{-7})[1/\text{K}^2]*T^2-(7.594*10^{-11}-w_{\text{Per\_U}}*11.98*10^{-11})[1/\text{K}^3]*T^3))/100$	Equation (116)
thermal_strain_ThPuO2	$(-0.179-0.049*w_{\text{Per\_U}}+(5.079e-4+2.51e-4*w_{\text{Per\_U}})[1/\text{K}]*T+(3.732e-7+2.506e-7*w_{\text{Per\_U}})[1/\text{K}^2]*T^2+(-7.594e-11+12.454e-11*w_{\text{Per\_U}})[1/\text{K}^3]*T^3)/100$	Equation (117)

## 5.5 FG Diffusion

The Booth diffusion equation for FG, in an idealized spherical fuel grain (equation (86)), is implemented in COMSOL using a general coefficient form ODE module within the second modelling component of MPM-FAST. Table 14 presents the expressions that are used to enable COMSOL to implement this calculation.

Table 14: Coefficients added to establish the ODE that solves the FG diffusion in MPM-FAST.

Symbol	Expression
$d_a$	$(y[1/m])^2 * \text{mod1.pellet\_mid}((\text{UO2\_grain\_radius}[1/m])^2)$
$c$	$\begin{pmatrix} 0 & 0 \\ 0 & (y[1/m])^2 * \text{mod1.pellet\_mid}(\text{fg\_diff\_coeff}) \end{pmatrix}$
$f$	$(y[1/m])^2 * \text{fg\_percent\_yield} * \text{mod1.pellet\_mid}((\text{UO2\_grain\_radius}[1/m])^2 * \text{fission\_rate\_density})$

$\text{mod1.pellet\_mid}()$  is a custom operator that maps the variable behavior listed in brackets from the center of the fuel pellet to its outer radius at the pellet mid plane along its length. This operator and several others used within MPM-FAST are given detailed descriptions within Prudil's work on the  $\text{UO}_2$  model development [8].

Parameters that affect the FG diffusion calculation have been added to MPM-FAST, so that they are available globally and allow for them to be accessed as part of a parameter sweep if necessary. Table 15 presents these parameters.

Table 15: Parameters added for FG diffusion calculations.

Parameter	Value	Comments
w_thrm	1.415	Weighting factor applied to thermal component of FG Diffusion of (Th,Pu)O <sub>2</sub>
w_irr	0.1604	Weighting factor applied to irradiation component of FG Diffusion of (Th,Pu)O <sub>2</sub>
w_athrm	0.1604	Weighting factor applied to athermal component of FG Diffusion of (Th,Pu)O <sub>2</sub>
Percent_fission_ga s_yield_Th	0.2761	Chapter 4 following equation (89)

The models that calculate the microstructural grain growth and the variables that calculate the FG diffusion in the fuel are within model component 1 because of their fuel temperature dependence. Table 16 summarizes the variables that edit these calculations to account for the particular fuel type being examined within MPM-FAST.

Table 16: Variables added to model component 1 for the FG diffusion calculation.

Variable	Expression	Comments
UO2_grain_growth_rate	$\text{if}(\text{pellet\_mat}==1, \text{UO2\_grain\_growth\_rate\_1}, 0) + \text{if}(\text{pellet\_mat}==2, \text{ThO2\_grain\_growth\_rate}, 0) + \text{if}(\text{pellet\_mat}==3, \text{UO2\_grain\_growth\_rate\_1}, 0)$	Series of if statements controlled by value of pellet_mat selects appropriate grain growth rate
ThO2_grain_growth_rate	$(\text{Th\_Growth\_rate\_constant} * \exp(-167700[\text{cal}]/T/8.31447[\text{J}/\text{K}])) / (\text{UO2\_grain\_diameter})^2$	Equation (90)
Th_Growth_rate_constant	800[cm <sup>3</sup> /h]	Pg 34 of chapter 4
fg_diff_coeff	$\text{if}(\text{pellet\_mat}==1, \text{UO2\_fg\_diff}, 0) + \text{if}(\text{pellet\_mat}==2, \text{ThO2\_fg\_diff}, 0) + \text{if}(\text{pellet\_mat}==3, \text{D\_exp\_new}, 0)$	Series of if statements controlled by value of pellet_mat selects appropriate FG diffusion coefficient
UO2_fg_diff	$.1818e-4[\text{m}^2/\text{s}] * (.76e-9 * \exp(-35225.44283[\text{K}]/T) + .5451144545e-8 * \exp(-27780[\text{K}]/T) * (.1090228909e-3 + 100 * \exp(-27780[\text{K}]/T))) * ((1 + .7199569632e-33 * \text{fission\_rate\_density}[\text{m}^3 * \text{s}] / \exp(-27780[\text{K}]/T) / (.1090228909e-3 + 100 * \exp(-27780[\text{K}]/T))^2)^{(1/2)} - 1) + .2e-39 * \text{fission\_rate\_density}[\text{m}^3 * \text{s}] * \text{fission\_rate\_density}[\text{m}^3 * \text{s}] * \pi * (.15e-8 + .530e-7 * \exp(-8702.7[\text{K}]/T))^2 / (24320000.00 * (.5e-9 + .530e-7 * \exp(-8702.7[\text{K}]/T)) * (.76e-9 * \exp(-35225.44283[\text{K}]/T) + .2180457818e-7 * \exp(-27780[\text{K}]/T) * (.1090228909e-3 + 100 * \exp(-27780[\text{K}]/T))) * ((1 + .7199569632e-33 * \text{fission\_rate\_density}[\text{m}^3 * \text{s}] / \exp(-27780[\text{K}]/T) / (.1090228909e-3 + 100 * \exp(-27780[\text{K}]/T))^2)^{(1/2)} - 1) + .8e-39 * \text{fission\_rate\_density}[\text{m}^3 * \text{s}] / (.15e-8 + .530e-7 * \exp(-8702.7[\text{K}]/T))^2 + .1818e-4 * \text{fission\_rate\_density}[\text{m}^3 * \text{s}] * \pi * (.15e-8 + .530e-7 * \exp(-8702.7[\text{K}]/T))^2)$	Numerical value found by Prudil for Equation (95) for UO <sub>2</sub>

ThO2_fg_diff	$0.1 * \text{UO2\_fg\_diff}$	Equation (105)
D_exp_new	$(\text{D}_0\_morgan * b\_prime2) / (b\_prime2 + g\_a4)$	Generalized Equation(95)
g_a4	$2.432000000 * 10^7 [m^{-2}] * (5. * 10^{(-10)} + 5.30 * 10^{(-8)} * \exp(-8702.7 [K]/T)) * \text{D}_0\_morgan / (1.5 * 10^{(-9)} + 5.30 * 10^{(-8)} * \exp(-8702.7 [K]/T))^2$	Equation (97)
b_prime2	$0.1818e-4 [1/s] * \text{fission\_rate\_density} [m^3 * s] * \pi * (1.5 * 10^{(-9)} + 5.30 * 10^{(-8)} * \exp(-8702.7 [K]/T))^2$	Equation (96) Experimental single atom FG diffusion
D_0_morgan	$w\_thrm * \text{D\_thrm\_test} + w\_irr * \text{D\_irr\_test} + w\_athrm * \text{D\_athrm\_test}$	coefficient to test various weighting factors. Generalized Equation (106)
D_thrm_test	$7.6 * 10^{(-10)} [m^2/s] * \exp(-35225.44283 [K]/T)$	Equation (100)
D_irr_test	$5.451144545 * 10^{(-9)} [m^2/s] * \exp(-27780 [K]/T) * (0.1090228909e-3 + 100 * \exp(-27780 [K]/T)) * (\text{sqrt}(1 + 7.199569632 * 10^{(-34)} * \text{fission\_rate\_density} [m^3 * s]) / (\exp(-27780 [K]/T) * (0.1090228909e-3 + 100 * \exp(-27780 [K]/T))^2) - 1)$	Equation (101)
D_athrm_test	$2. * 10^{(-40)} [m^2/s] * \text{fission\_rate\_density} [m^3 * s]$	Equation (102)

With the difference in FG yield per fission between Th-based fuel and UO<sub>2</sub>, it was necessary to enable MPM-FAST to select the appropriate value. Table 17 displays the variable and expression established in model component 2 that accomplishes this.

Table 17: Variables implemented in model component 2.

Variables	Expression	Comments
fg_percent_yield	if(pellet_mat==1,Percent_fission_gas_yield_UO2,0)+if(pellet_mat==2,Percent_fission_gas_yield_Th,0)+if(pellet_mat==3,Percent_fission_gas_yield_Th,0)	Series of if statements controlled by value of pellet_mat selects appropriate FG yield percentage

## 6 Results and Discussion

The main focus of this chapter will be to present and discuss the results that the model produces. Specifically, the proof of concept validation cases (sections 6.1.1 and 6.1.2), sensitivity analysis (6.2), and the results of NOC SCWR fuel model will be discussed (Section 6.3). To finish the chapter the limitations of the model will be discussed.

### 6.1 Model Validation

Validation exercises for the (Th,U)O<sub>2</sub> and (Th,Pu)O<sub>2</sub> consist of demonstrating how capable MPM-FAST is of replicating the results of fuel irradiations that have occurred. The (Th,U)O<sub>2</sub> model validation consists of comparing PIE data from twelve fuel elements from the irradiation experiment DME-221. Similarly, the (Th,Pu)O<sub>2</sub> model validation is attempted through the comparison of PIE data from five bundles irradiated during the BDL-422 experiment.

#### 6.1.1 (Th,U)O<sub>2</sub> Model

Two variations of the (Th,U)O<sub>2</sub> MPM-FAST model were examined: Case 1) uses Belle and Berman's thermal conductivity correlation [21] (equation 76) and Case 2) uses the thermal conductivity presented by Bakker *et al.* [28]

(equation (77)). The model predictions from Case 1) and Case 2) will be compared to PIE measurements of FGR and end-of-life sheath strain data from DME-221.

DME-221 is an experimental fuel irradiation test conducted by CNL [38]. DME is short hand for “demountable element”; this refers to how the experimental fuel is inserted into the U1 and U2 test loops of the National Research Universal (NRU) reactor. The experimental fuel is fabricated as elements that can be inserted into or removed (demounted) from the outer ring of a fuel bundle assembly. In the case of DME-221, the bundle has the same geometry as a 37-element Canadian PHWR fuel bundle, with the 18 elements in the outer ring available to house demountable elements, and the centre element removed to allow the bundle to be irradiated on a fuel string in the NRU loops. Six variations of experimental fuel were fabricated for DME-221: three different fuel compositions ( $\text{ThO}_2$ ,  $(\text{Th,U})\text{O}_2$  with 1.0 wt.%  $^{235}\text{U}$  and  $(\text{Th,U})\text{O}_2$  with 1.5 wt.%  $^{235}\text{U}$ ) having two different pellet geometries, one set of pellets has a length-to-diameter (L/D) pellet ratio of  $\sim 1.3$  and the other set has a reduced L/D ratio of  $\sim 0.7$ . The initial average grain size of the fuel was reported as 6 - 8  $\mu\text{m}$ , as well as initial densities of  $\geq 95\%$  theoretical density [38]. The experiment is ongoing, with twelve elements having undergone PIE and the three remaining elements to undergo further irradiation. The twelve elements that have undergone PIE were removed from the outer element ring on two separate occasions, leading to



elements being either a “low” or “high” exit burnup case. Figures 15 – 19 are reproduced with permission from Corbett [38] and display two power histories for each fuel composition that are representative of the low and high exit burnup cases for DME-221.

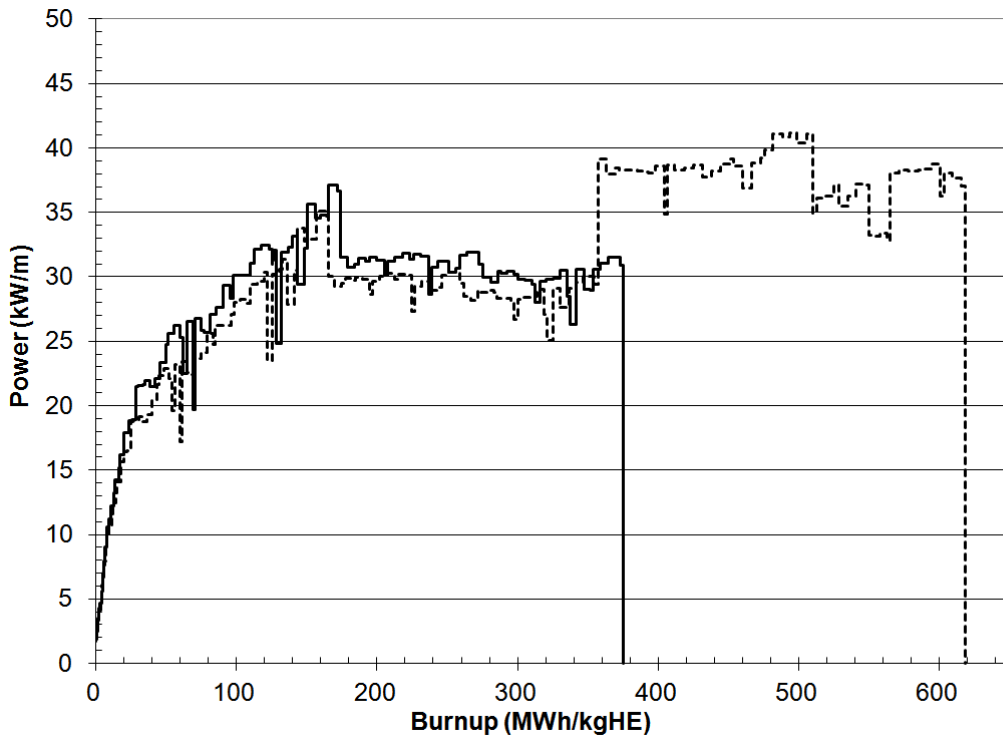


Figure 15: Power histories for DME-221 ThO<sub>2</sub> fueled elements, with low exit burnup ~360 MWh kgHE<sup>-1</sup> and high exit burnup ~620 MWh kgHE<sup>-1</sup>[38].

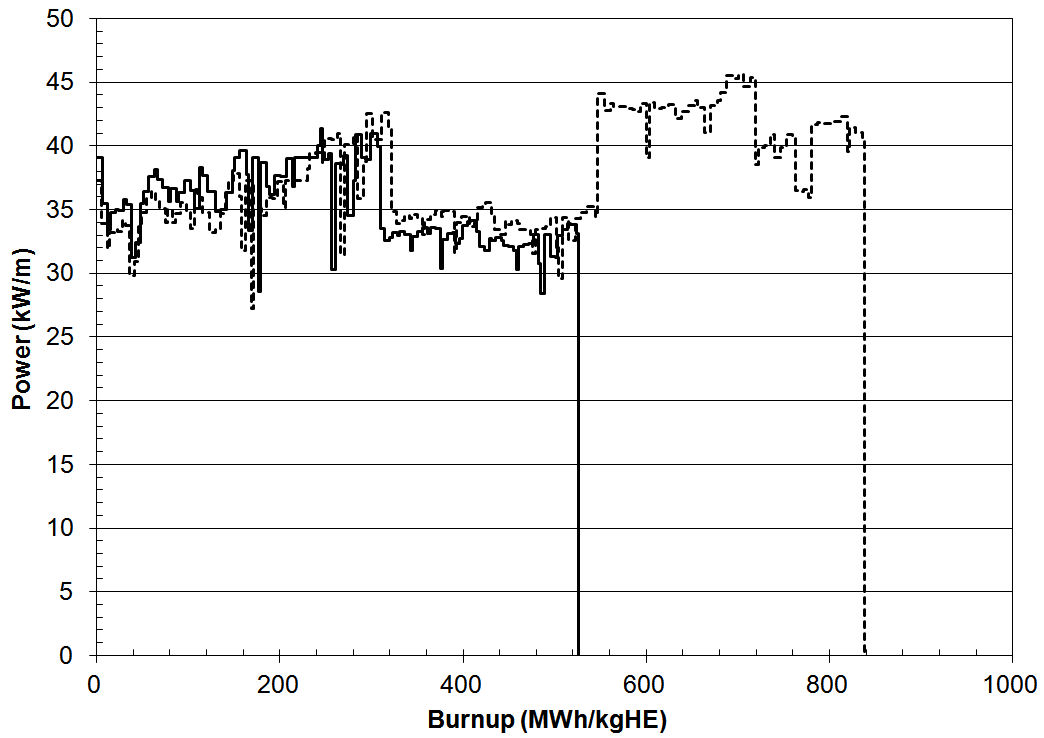


Figure 16: Power histories for DME-221 (Th,U)O<sub>2</sub> 1.0 wt% U-235 fueled elements, with low exit burnup ~ 500 MWh kgHE<sup>-1</sup> and high exit burnup ~ 830 MWh kgHE<sup>-1</sup> [38].

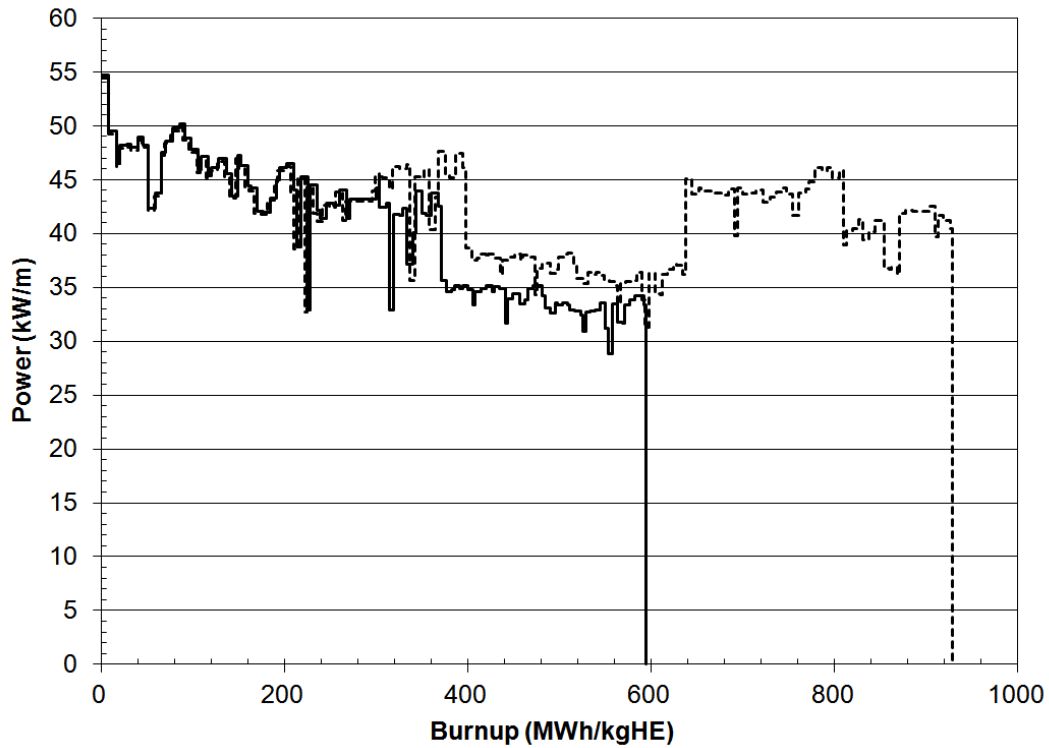


Figure 17: Power histories for DME-221 (Th,U)O<sub>2</sub> 1.5 wt% U-235 fueled elements, with low exit burnup >540 MWh kgHE<sup>-1</sup> and high exit burnup >900 MWh kgHE<sup>-1</sup> [3].

The maximum modeled centerline temperature, FGR, and plastic sheath strain are presented below.

### 6.1.1.1 Centerline Temperature

Table 18 displays a comparison of the highest achieved centerline temperatures (calculated) between Case 1) and Case 2) for each DME-221 element.

Table 18: Comparison of modelled centerline temperatures for DME-221 Elements.

% U-235	Burnup (MWh kgHE <sup>-1</sup> )	Modeled Max. Temp. DME-221 Fuel (K)		Magnitude of Temperature Difference (K)
		Case 1)	Case 2)	
<b>0</b>	<b>361</b>	1144	1244	100
<b>0</b>	<b>619</b>	1317	1460	143
<b>0</b>	<b>375*</b>	1174	1281	107
<b>0</b>	<b>618*</b>	1344	1520	176
<b>1</b>	<b>499</b>	1261	1421	160
<b>1</b>	<b>525*</b>	1315	1411	96
<b>1</b>	<b>839*</b>	1611	1820	209
<b>1.5</b>	<b>929</b>	1698	1860	162
<b>1.5</b>	<b>549</b>	1592	1860	268
<b>1.5</b>	<b>593*</b>	1592	1731	139
<b>1.5</b>	<b>914*</b>	1669	1831	162
<b>1.5</b>	<b>903*</b>	1653	1804	151

\* Fueled with “short” pellets (L/D = 0.7)

Centerline temperature results from Case 1) are consistently lower than those modeled in Case 2). With higher uranium content, the difference in temperature is greater. This temperature difference arises because the Bakker *et al.*[28] model predicts lower thermal conductivity values for Case 2) models compared to the Belle and Berman model [21] (used in Case 1)). Figure 18 displays the conductivity curves from both models for the 1.5% U-235 fuel (assuming 100% theoretical density fuel, porosity is accounted for via Lucuta factor [54]). Consensus within the literature is in favour of using the Bakker correlation [28] over the Belle and Berman correlation [21], due to later

measurements displaying larger degradation in thermal conductivity with uranium content than predicted by Belle and Berman [21], [29], [52].

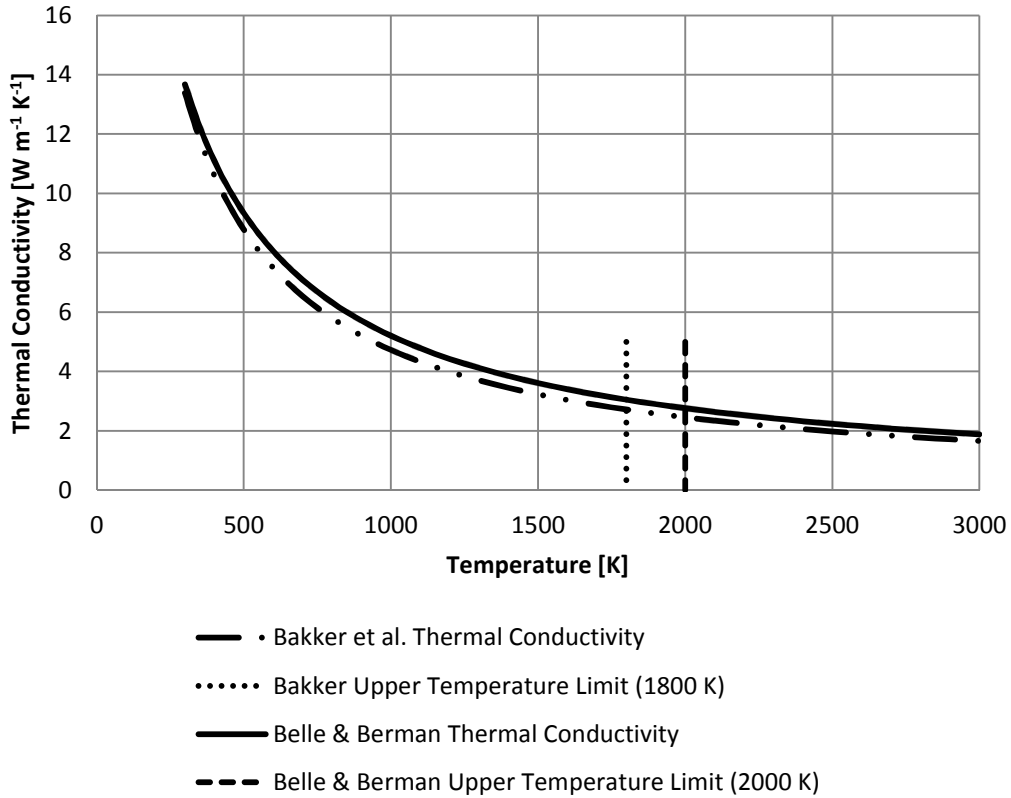


Figure 18: Comparison of Thermal Conductivity correlations for 100% theoretically dense ceramic used in each case for 1.5% U-235 DME-221 Fuel.

In Figure 18, the vertical lines indicate the uppermost validation temperature for each of the models. It should be noted that many of the high burnup elements in Case 2) exceed the maximum temperature for which the Bakker *et al.*[28] conductivity correlation was developed. This leads to additional

uncertainty in the temperature behaviour for these cases because it is not known if extrapolating the Bakker correlation [28] is representative in this regime.

As mentioned previously, within the open literature, the expectation is that the Belle and Berman model [21] will over-predict thermal conductivity, and lead to an under-prediction of the fuel temperature. Based on this, it is suspected that the modelling results for Case 1) fuel temperatures are low. At this time, this suspected behaviour cannot be confirmed because DME-221 is not an instrumented fuel test; thus, there are no fuel temperature measurements to validate the modelling results against.

Corbett *et al.* reports that limited grain growth occurred in the central region of the 1.5 wt% U-235 elements [38]. Case 1) and Case 2) uses the grain growth model outlined by Goldberg *et al.* and is presented in equation (25) [22]. For both sets of results and for all compositions of fuel, the results show no grain growth.

For a comparison of the difference in fuel performance between the Th-based fuel and UO<sub>2</sub>; Table 19 displays the results of the Th-based models given in Table 18 in the middle two columns, and the left-most column displays the maximum temperature calculated using the UO<sub>2</sub> model, using the same element geometry and power histories from DME-221.

Table 19: Comparison of the maximum centerline temperature calculated by the (Th,U)O<sub>2</sub> models and the UO<sub>2</sub> model.

% U-235	Burnup (MWh kgHE <sup>-1</sup> )	Modeled Max. Temp. of Fuel (K)		
		Case 1)	Case 2)	UO <sub>2</sub>
0	361	1144	1244	1314
0	619	1317	1460	1680
0	375*	1174	1281	1537
0	618*	1344	1520	1792
1	499	1261	1421	1455
1	525*	1315	1411	1554
1	839*	1611	1820	3127
1.5	929	1698	1860	2487
1.5	549	1592	1860	2921
1.5	593*	1592	1731	1950
1.5	914*	1669	1831	2396
1.5	903*	1653	1804	2386

\* Fueled with “short” pellets (L/D = 0.7)

The Th-based fuel model using either the Belle and Berman correlation or the Bakker *et al.* thermal conductivity correlation, consistently predict lower centerline temperatures than the UO<sub>2</sub> model. This temperature difference is most pronounced in the high burnup cases.

### 6.1.1.2 Fission Gas Release

Table 20 compares the modeled FGR for Case 1) and Case 2) to measured data [38].

Table 20: Modeled Percent FGR for Case 1 and Case 2).

U-235 (%)	Burnup (MWh kgHE <sup>-1</sup> )	Modeled % FGR		Measured % FGR Range
		Case 1)	Case 2)	
0	361	0	0	
0	619	0.2	1.0	0.05-0.1
0	375*	0	0	
0	618*	0.4	1.6	
1	499	0	0	
1	525*	<0.1	<0.1	0.06-1.2
1	839*	2.4	4.3	
1.5	929	3.3	5.0	
1.5	549	0.1	1.1	
1.5	593*	0.2	0.5	0.08-2.8
1.5	914*	2.9	4.3	
1.5	903*	2.5	3.7	

\* Fueled with “short” pellets (L/D = 0.7)

In the validation of UO<sub>2</sub> FAST, it was found that the model tended to over-predict FGR for elements with relatively low measured FGR [7]. With this model behaviour in mind, Case 1) reasonably replicates the natural thoria (0% U-235) with the model over-predicting the upper bound of measurement range (0.1% compared to 0.4%), as seen in Table 20. By contrast for Case 2, the two simulations with predicted gas release exceeded the measured gas releases by at least a factor of 10 for the same irradiation history. Comparing all the low burnup (< 600 MWh kgHE<sup>-1</sup>) results for both Case 1) and 2), a similar trend that Case 2 predictions are generally 2-10 times larger than Case 1) predictions is observed.



As expected, the higher burnup cases predict greater fission gas release. For burnups  $> 900 \text{ MWh kgHE}^{-1}$ , with 1.5% U-235 enriched fuel elements, Case 1) models the FGR within the measured range with the exception of the 929 MWh  $\text{kgHE}^{-1}$  exit burnup element, which exceeded the measurement range by a relatively small value (modeled 3.3% in comparison to the 2.8% measurement). For Case 2 the model exceeded the upper measurement range of the measured data in all three elements. For the 929 MWh  $\text{kgHE}^{-1}$  exit burnup element, Case 2 predicts 5.0% FGR that is almost twice the measured FGR. Although the Case 2 results for the low burnup fuel elements (containing 1.5% U-235) were within the measured data range, none of them reflect the lower bound of the measurement range.

With both models using the fission gas diffusion behaviour assumption outlined in equation (111), the Case 1 model better replicates the FGR behaviour of DME-221 fuels. As discussed earlier, it is suspected that the Case 1 model will predict lower fuel temperature than Case 2) because of its use of the Belle and Berman thermal conductivity correlation [21]. If it is found that the temperature behaviour of Case 2) models are more physically representative of the fuel temperature, it would suggest that further study of the FG diffusion behaviour is required to simultaneously produce more realistic fuel temperatures as well as FGR. These changes could include further reductions to the fission gas diffusion coefficient (directly or by modifying the activation energy or athermal terms), or

higher grain boundary bubble contact angle or saturation coverage to increase grain boundary retention.

Results as presented here recommend that the Case 1) model is to be used, as it is better at reproducing the FGR behaviour of the DME-221 experiment.

The FGR prediction for the Th-based fuel is improved using the MPM-FAST model being developed. As illustrated in Table 21, the FGR calculated by the UO<sub>2</sub> model is over-predicting the measured values by a large margin [38].

Table 21: Comparison of PIE FGR results to UO<sub>2</sub> model results.

<b>% U-235</b>	<b>Burnup (MWh kgHE<sup>-1</sup>)</b>	<b>Modeled % FGR</b>	<b>Measured % FGR Range</b>
<b>0</b>	<b>361</b>	0.5	
<b>0</b>	<b>619</b>	15.1	0.05-0.1
<b>0</b>	<b>375*</b>	5.0	
<b>0</b>	<b>618*</b>	18.1	
<b>1</b>	<b>499</b>	5.0	0.06-1.2
<b>1</b>	<b>525*</b>	6.3	
<b>1</b>	<b>839*</b>	36.6	
<b>1.5</b>	<b>929</b>	22.3	0.08-2.8
<b>1.5</b>	<b>549</b>	21.4	
<b>1.5</b>	<b>593*</b>	10.3	
<b>1.5</b>	<b>914*</b>	21.1	
<b>1.5</b>	<b>903*</b>	20.1	

\* Fueled with “short” pellets (L/D = 0.7)

Both Table 19 and Table 21 highlight the advantages of Th-based fuels over conventional  $\text{UO}_2$  fuels; the lower temperatures and fission gas release lead to better fuel performance for the same power history.

### 6.1.1.3 Deformation

Modelling results for the sheath strain at the mid-pellet (MP) region and at the pellet-interface (PI) are presented in Table 22 and Table 23, respectively, along with the PIE measurements from DME-221[38].

Table 22: Modeled MP sheath strain compared to PIE data.

% U-235	Burnup (MWh kgHE <sup>-1</sup> )	Modeled MP Strain (%)		Measured Range MP Strain (%)
		Case 1)	Case 2)	
0	361	-0.2	-0.1	
0	619	0.08	0.2	
0	375*	-0.2	-0.1	-0.3 - 0.0
0	618*	0.07	0.2	
1	499	-0.03	-0.2	
1	525*	-0.04	0.02	-0.4 – 0.0
1	839*	0.4	0.6	
1.5	929	0.8	1.0	
1.5	549	0.1	0.4	
1.5	593*	0.1	0.2	-0.2 – 0.1
1.5	914*	0.6	0.8	
1.5	903*	0.6	0.7	

\* Fueled with “short” pellets (L/D = 0.7)

Table 23: Modeled PI sheath strain compared to PIE data.

% U-235	Burnup (MWh kgHE <sup>-1</sup> )	Modeled PI Strain (%)		Measured Range PI Strain (%)
		Case 1)	Case 2)	
0	361	-0.1	0.02	
0	619	0.2	0.4	
0	375*	-0.1	0.04	-0.1 - 0.2
0	618*	0.2	0.4	
1	499	0.1	-0.2	
1	525*	0.1	0.2	-0.1 – 0.3
1	839*	0.7	0.9	
1.5	929	1.1	1.4	
1.5	549	0.3	0.6	
1.5	593*	0.3	0.5	0.0 – 0.4
1.5	914*	0.9	1.2	
1.5	903*	0.8	1.1	

\* Fueled with “short” pellets (L/D = 0.7)

For the natural thoria pellets, when the maximum fuel temperature is below 1300 K, both the MP and PI deformation fall within the measurement range. With a burnup of up to 620 MWh kgHE<sup>-1</sup> modeled under Case 1 conditions, where the fuel temperature does not exceed 1350 K, the deformation calculations agree with the experimentally measured range. For fuel containing 1.0 wt% U-235, the models that exceed 1400 K begin to exceed the upper bound of DME-221 results. For fuel centerline temperatures above 1450 K, fuel elements deform outside the measured range. Similarly, a fuel temperature of 1650 K appears to be the limit for the 1.5 wt% U-235 fuel. There appears to be a

systematic high temperature limit for each of the fuel compositions beyond which the model begins to over predict the end-of-life element strains. It is difficult to identify the exact cause. A significant number of the models for plastic deformation within the Th-based fuel pellet were adopted from the UO<sub>2</sub> model. An example of this is the gaseous swelling strain, since the model is highly dependent on temperature (leading to the observed temperature dependence) and that the fission gas behavior in ThO<sub>2</sub> is significantly reduced compared to UO<sub>2</sub>. This could lead to an over-prediction of sheath strain. The Th-based fuel pellet model does not account for creep and axial cracking; the same approach as FAST's UO<sub>2</sub> fuel pellet model. These may be contributing to the discrepancy in the observed deformation results. The results are encouraging as a first attempt to model sheath strains in comparison to limited PIE results.

Previous (Th,U)O<sub>2</sub> models by Long *et al.*[8] and Lee *et al.*[9] elected to use the thermal conductivity model presented by Belle and Berman and were able to produce comparable modelling results to the FGR measurements of irradiated (Th,U)O<sub>2</sub> fuel for light water reactors. Similarly from the Case 1 results presented above, MPM-FAST reaffirms that using similar assumptions for fission gas diffusion and thermal conductivity, FGR behaviour can be replicated. Case 2 models that use the Bakker *et al.* [28] thermal conductivity were included to indicate that despite the availability of physically representative models of FGR, the understanding of high temperature behaviour of the thermal conductivity

continues to evolve, and further examination of high temperature FGR may be required. From Table 20 for Case 2, the model's ability to replicate FGR is limited to the temperature range of the Bakker thermal conductivity correlation. It is currently recommended that the Belle and Berman thermal conductivity model be used for fuel temperature calculations because it has been correlated over a larger temperature range.

Fewer deformation modelling results are in agreement to the end-of-life measurements of DME-221 compared to the FGR results. It should be noted that the models by Long *et al.* [8] and Lee *et al.* [9] do not discuss fuel deformation. The applicability of the deformation model in MPM-FAST appears to be limited to low temperature fuel: ~1350 K for ThO<sub>2</sub>, ~1450K for the 1 %wt U-235, and ~1650K for the 1.5 wt% U-235 fuel. However, it is a step forward in the development of (Th,U)O<sub>2</sub> fuel performance models with similar capabilities to those expected in a UO<sub>2</sub> model. The current over-prediction of fuel swelling (and consequently sheath strain) may function as bounding estimates for experiment design (at least in the moderate temperature regime).

### 6.1.2 (Th,Pu)O<sub>2</sub> Model

The MPM-FAST (Th,Pu)O<sub>2</sub> model validation exercise was to attempt to replicate the irradiation behaviour of BDL- 422. BDL- 422 was a fuel irradiation experiment that was undertaken to demonstrate the ability of (Th,Pu)O<sub>2</sub> bundles to operate to high burnups (>1000 MWh kgHE<sup>-1</sup>) [39], [40], [70]. Six bundles were irradiated in test loops of the NRU reactor. Each bundle was fueled exclusively with (Th,Pu)O<sub>2</sub> with 1.53 wt% Pu. In order to avoid potential over pressurization caused by fission gas release, the outer ring elements were fabricated with plena at both ends of each element. The BDL-422 fuel pellets had an average initial grain size of 3 - 4 μm and an average initial pellet density of 9.469 g cm<sup>-3</sup>. The six BDL-422 bundles were labelled ADA – ADF. A selection of outer ring elements (OE) and an additional element from the intermediate bundle ring (IE) were chosen for PIE from ADA, ADC, ADD, ADE and ADF [39], [40], [70]. The fuel pellets from BDL-422 are considered to have sub-optimal microstructure. For commercial fuel, grain size tolerance is set between 5 - 7 μm. Additional concerns with the microstructure arose when ceramographic, and alpha radiograph images taken of unirradiated pellet materials found that the structure contained granules, and non-uniform regions of Pu concentration [71]. Despite BDL-422 fuel's microstructure being below commercial fuel standards, the fuel exhibited less FGR compared to UO<sub>2</sub> for burnups up to ~ 900 MWh

kgHE<sup>-1</sup> (1-5% FGR). For the fuel with burnup > 1000 MWh kgHE<sup>-1</sup> the FGR increased to 20-30%. An underlying assumption of most fuel performance models is that the pellet material is homogeneous. It is not clear how applicable this assumption is when applied to the BDL-422 fuel.

Figure 19 below displays the power histories for BDL-422 OEs as presented by Floyd [70].

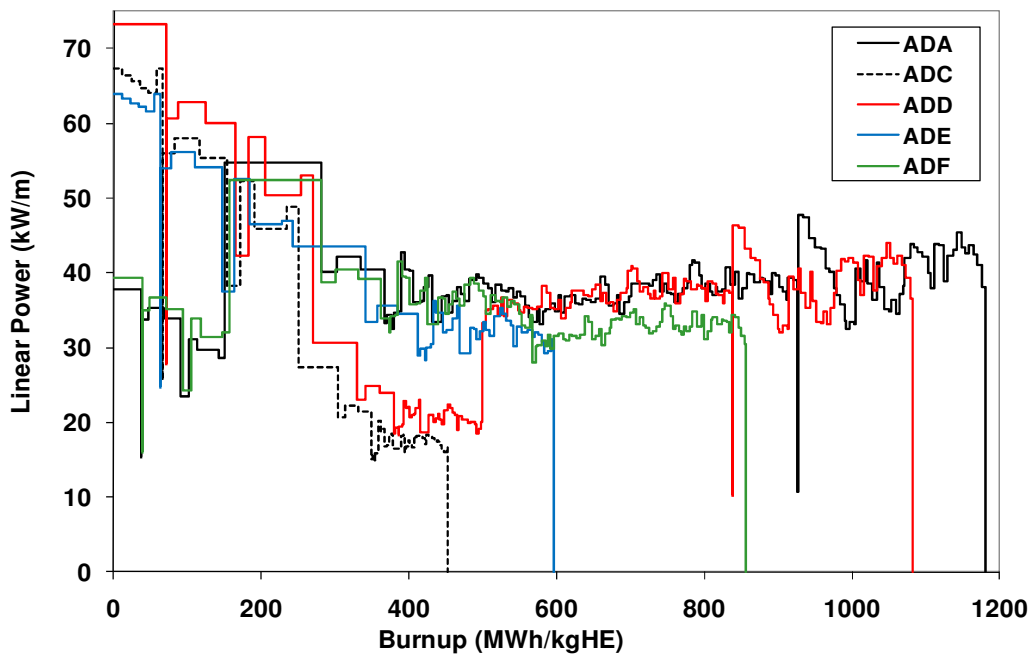


Figure 19: Five power histories of OE from each bundle from BDL-422 [70].

As experimental fuels are being irradiated, a calculation of the linear power and burnup of the fuel is produced. Once the irradiation goal of the fuel is



obtained, one of the measurements taken of the fuel is to determine empirically the fuel's burnup. For the BDL-422 fuel this was done by measuring the amount of lanthanum produced during the irradiation. The power histories in Figure 19 have been normalized to match these exit burnup measurements for each element. It was found that the measured exit burnup varied as much as 10% greater than the as-calculated power histories for the BDL-422 fuel. The process of normalizing the power history calculation in this way is to try to eliminate systematic bias within the power histories. By scaling the as-calculated power history of the experimental fuel to the burnup measurement, systematic bias error is accounted for; however, there is still a  $\pm 6\%$  random error associated with a normalized power history [72]. In between the random error and the effect of the systematic bias a 10% lower burnup in the BDL-422 fuel is feasible.

Recall that in Chapter 4, in the FG diffusion for  $(\text{Th,Pu})\text{O}_2$  (equation (112)), two sets of weighting variables were generated for the single fission gas atom diffusion coefficient. The potential difference of a 10% increase in linear power leads the simulation of BDL-422 fuel to calculate elevated fuel temperatures. With the temperature dependence associated with the different mechanisms that allow FG to diffuse, in order to elucidate the generalized FG behaviour, the uncertainty of the fuel temperature must be accounted for. As such, the expectation is that FG diffusion behaviour is bounded by these two sets of weighting factors for the single fission gas atom diffusion.

The weighting factors presented in equation (112) were found by fitting the FGR model to the PIE results from the intermediate elements from BDL-422, while testing various weighting factors within the single fission gas diffusion coefficient for the components that dominate below 1700 K ( $D_{athrm}$ , and  $D_{irr}$ ). A subsequent fitting optimization was taken to determine an appropriate weighting factor for the high temperature diffusion behaviour ( $D_{thrm}$ ). The FGR from the OE from bundle ADA, ADC, and ADD were selected to fit the high temperature behaviour. As shown in Figure 19, these bundles experienced the highest power rating (and subsequently the highest FGR) in the experiment. It was deemed that by focusing on replicating the high release cases the model would be conservative. The selection of weighting factors was aided by using non-linear, least squares optimization software. The fitting steps and further details on the process are outlined in Appendix C.

### **6.1.3.1 Centerline Temperature**

Recall that in equation (112) that two iterations of the single fission gas atom diffusion coefficient were presented,  $D_{0,(Th,Pu)O_21}$  having been fit to the as-calculated or “un-normalized” BDL-422 power histories, and  $D_{0,(Th,Pu)O_22}$ , having been fit to the normalized power histories. Both series of results will be presented as individual cases, Case 1 for un-normalized power histories and Case 2 for the normalized power histories. Table 24 (below) contains a comparison of

the maximum calculated centerline temperature of UO<sub>2</sub> fuel in the same configuration as the BDL-422 fuel to the (Th,Pu)O<sub>2</sub> model using  $D_{0,(Th,Pu)O_21}$  (Case 1).

Table 24: Comparison of the maximum calculated fuel centerline temperature for the UO<sub>2</sub> model and (Th,Pu)O<sub>2</sub> for the un-normalized power histories of BDL-422 experiment .

Bundle	Modelled Max. Fuel Temp. [K]		Temperature Difference[K]
	UO <sub>2</sub>	Case 1	
Outer Elements			
ADA	1953	2989*	-1036
ADC	2394	2572	-178
ADD	2468	2687	-219
ADE	2156	2246	-90
ADF	1887	1869	18
Intermediate Elements			
ADA	1364	1354	10
ADC	1047	1046	1
ADD	1578	1549	29
ADE	1223	1218	5
ADF	1358	1348	10

\*Non-physical temperature behaviour

For the temperature calculations for power histories normalized to the lanthanide measurements and using the fitted behaviour of  $D_{0,(Th,Pu)O_22}$  (Case 2), results are displayed in Table 25.

Table 25: Comparison of the maximum calculated fuel centerline temperature for the UO<sub>2</sub> model and (Th,Pu)O<sub>2</sub> for the normalized power histories of BDL-422 experiment.

Bundle	Max Linear Power [KW m <sup>-1</sup> ]	Burnup [MWh kgHE <sup>-1</sup> ]	Modelled Max. Fuel Temp. [K]		Temperature Difference[K]
			UO <sub>2</sub>	Case 2	
Outer Elements					
ADA	54	1181	3416*	3102*	314
ADC	67	451	2488	2606	-118
ADD	73	1082	3156*	2961*	195
ADE	64	597	2384	2446	-62
ADF	52	856	1980	2017	-37
Intermediate Elements					
ADA	27	718	1364	1456	-92
ADC	22	288	1047	1052	-5
ADD	45	665	1578	1640	-62
ADE	32	308	1223	1280	-57
ADF	39	531	1358	1413	-55

\*Non-physical temperature behaviour

It is expected that Th-based fuel will experience lower fuel temperatures than UO<sub>2</sub>. Predicted temperatures for the outer fuel elements from BDL-422 fuel with un-normalized power histories excluding ADF all have higher temperature than UO<sub>2</sub> irradiated in the same conditions. The intermediate elements and the outer elements from ADF in Case 1 have modelled temperature results that meet the expectation of reduced fuel temperatures.

The calculated outer element temperature and for Case 1 simulations of OE ADA as well as ADA and ADD from Case 2, find fuel temperatures that reach approximately the melting temperature of ThO<sub>2</sub>. Since there was no

evidence of fuel melting or the columnar grain growth from the PIE this indicates that for these instances the model is producing non-physical temperature behaviour.

Table 25 compares Case 2 using the normalized power histories for BDL-422 to UO<sub>2</sub>. The models predicts that the temperature difference between the UO<sub>2</sub> and the (Th,Pu)O<sub>2</sub> will be within ~ 120K. The fuel that experienced non-physical behaviour will be discussed further after the FGR results are presented.

In order to determine if the temperatures calculated by these models are physical, the thermal conductivity correlation needs to be examined. Figure 20 presents the unirradiated thermal conductivity for BDL-422 fuel as predicted by the Cozzo correlation [31] altered for 100% dense ceramic, in comparison to the unirradiated UO<sub>2</sub> thermal conductivity predicted by the ELESTRES fuel code for the same temperature range [8] .

With the Cozzo correlation [31] adjusted to account for 100% dense ceramic fuel, the temperature predicted by the model will likely fall in line with the expectation that the Th-based fuel will have lower centerline temperatures until the fuel reaches ~1850 K. The fuel temperature results for Case 1 reflect this behaviour; however this is not reflected in the normalized power histories in Case 2. The temperature difference between these simulations below 1850 K, found the UO<sub>2</sub> model and those found in Case 2 were all within 100 K of each other. The

sensitivity analysis in section 6.2, shows that this temperature difference is within the uncertainty of the fuel temperature calculation of the (Th,Pu)O<sub>2</sub> model.

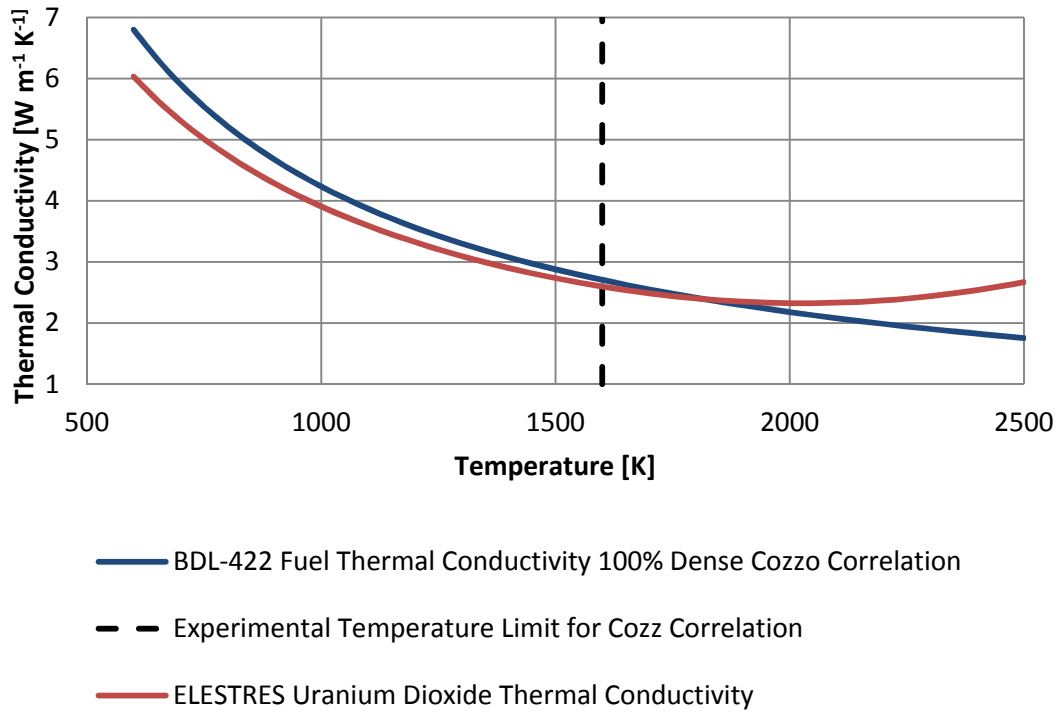


Figure 20: Unirradiated UO<sub>2</sub> thermal conductivity model compared to the unirradiated (Th,Pu)O<sub>2</sub> model.

### 6.1.3.2 Fission Gas Release

Results from the UO<sub>2</sub> and (Th,Pu)O<sub>2</sub> Case 1) and Case 2) models for %FGR are compared to the FGR data from BDL-422, as shown in Table 26.

Table 26: %FGR model results for the (Th,Pu)O<sub>2</sub>, (Case 1, Case 2), and UO<sub>2</sub> with the Un-Normalized (UN) and Normalized (N) power histories and the PIE results of BDL-422 are presented.

Bundle	Max Linear Power [kW m <sup>-1</sup> ]	Burnup [MWh kgHE <sup>-1</sup> ]	Modelled %FGR				Measured %FGR
			UN-UO <sub>2</sub>	N-UO <sub>2</sub>	Case 1	Case 2	
Outer Elements							
ADA	54	1181	27.7	43	29.7	29	26.2 -32.8
ADC	67	451	3.6	34.4	4.1	4	5.3
ADD	73	1082	26.3	40.9	20.5	25.7	19.6 - 26.9
ADE	64	597	8.5	11.9	4.4	5.8	1.2
ADF	52	856	19.4	20.8	10.2	10.6	2.8
Intermediate Elements							
ADA	27	718	11.4	11.4	1	1.1	1
ADC	22	288	0	0	0	0	0.3
ADD	45	665	10	10	0.5	0.4	0.5
ADE	32	308	0.3	0.3	0	0	0.1
ADF	39	531	4.9	4.9	0	0	0.2

As discussed above, the weighting factors for equation (112) were determined by attempting to fit the fission gas diffusion behavior to the intermediate element FGR results for the lower temperature region, followed by fitting the FGR of ADA ADC and ADD to determine the weighing coefficient for  $D_{thrm}$ . This has led to the model being capable of replicating FGR for the OE ADA, ADC, and ADD. Additionally both versions of the (Th,Pu)O<sub>2</sub> model (Case 1 and Case 2) are also in reasonable agreement with the IE measurements of FGR. (Th,Pu)O<sub>2</sub> models are a substantial improvement over the UO<sub>2</sub> model.

Recall that both the normalized ADA and ADD Case 2) (Table 25) and Case 1) (Table 24) ADA simulations produced non-physical maximum fuel

temperatures. To examine and understand this behaviour, Case 2 ADD OE FGR and fuel temperature over its irradiation is presented in Figure 21 below.

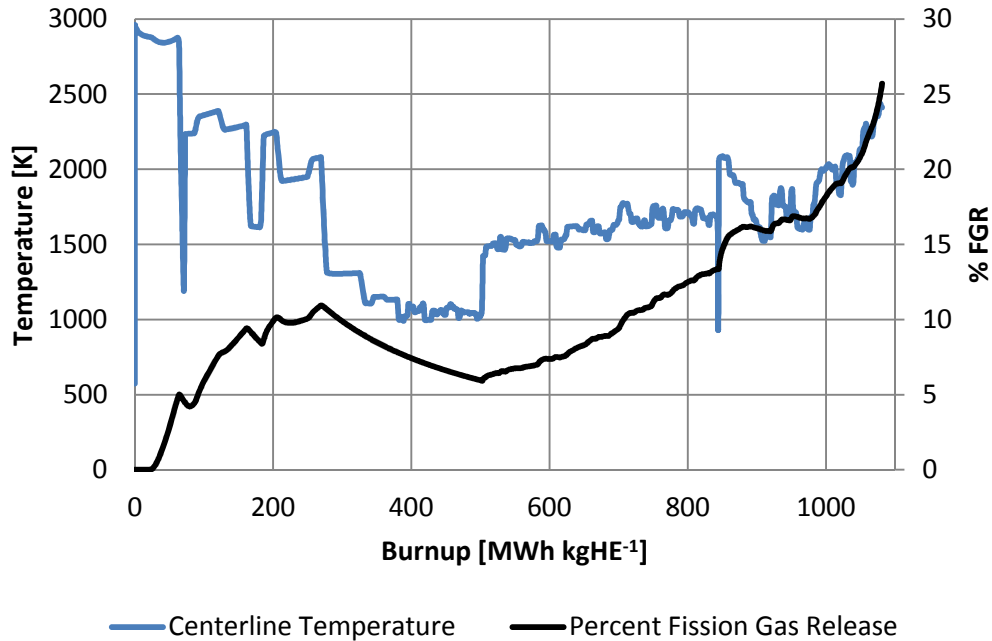


Figure 21: Centerline temperature and %FGR calculations for Case 2 simulating of the normalized ADD OE.

ADD achieves its maximum temperature at the beginning of its irradiation when it experiences a linear power of  $73 \text{ kW m}^{-1}$ , however there are several features in Figure 21 that are of interest. It can be seen that after the fuel reaches  $\sim 250 \text{ MWh kgHE}^{-1}$  burnup, the centerline temperature drops below 1500 K. In the region from  $\sim 250$  to  $500 \text{ MWh kgHE}^{-1}$  when the fuel stays below 1500 K no further FG is released to the free volume of the element (as indicated with the decreasing %FGR, because the FG is staying within the pellet). FGR begins to



increase again when the fuel centerline temperature rises above 1500 K (approximately 500 MWh kgHE<sup>-1</sup>). The next feature of interest occurs shortly after 800 MWh kgHE<sup>-1</sup>, there is a brief dip in temperature and then a sudden ramp up. This is caused by a power ramp, and the model captures a spike in FG release. It can be seen in Figure 19 that ADA and ADD experience a power ramp late in their irradiation, followed by relatively constant power levels. The model predicts an increase in centerline temperature as it approaches its exit burnup.

Each feature in Figure 21 highlights aspects of how the modelling assumptions affect the prediction of high fission gas release for OE ADD. When the fuel temperature is below 1500 K, FGR ceases. When the fuel temperature exceeds 1500 K, FGR is prevalent. Lastly there is the increasing FGR rate and temperature as the fuel approaches end-of-life. From Figure 20 it can be seen that the model for thermal conductivity decreases with temperature. This will cause the (Th,Pu)O<sub>2</sub> model to predict an increase in fuel temperature, because the fuel is less efficient at transferring heat out of the pellet. The increase in fuel temperature will cause the FG diffusion and release to increase. As described in Chapter 4 this feedback loop further degrades the ability of heat to be transferred out of the fuel, hence the centerline temperature and FGR are increasing continuously.

Figure 22 presents a similar plot for the normalized ADF OE simulation and Figure 23 for the normalized ADA IE simulation. These simulations maintain fuel temperatures averaging 1500 K (ADF OE) and below 1500 K (ADA IE).

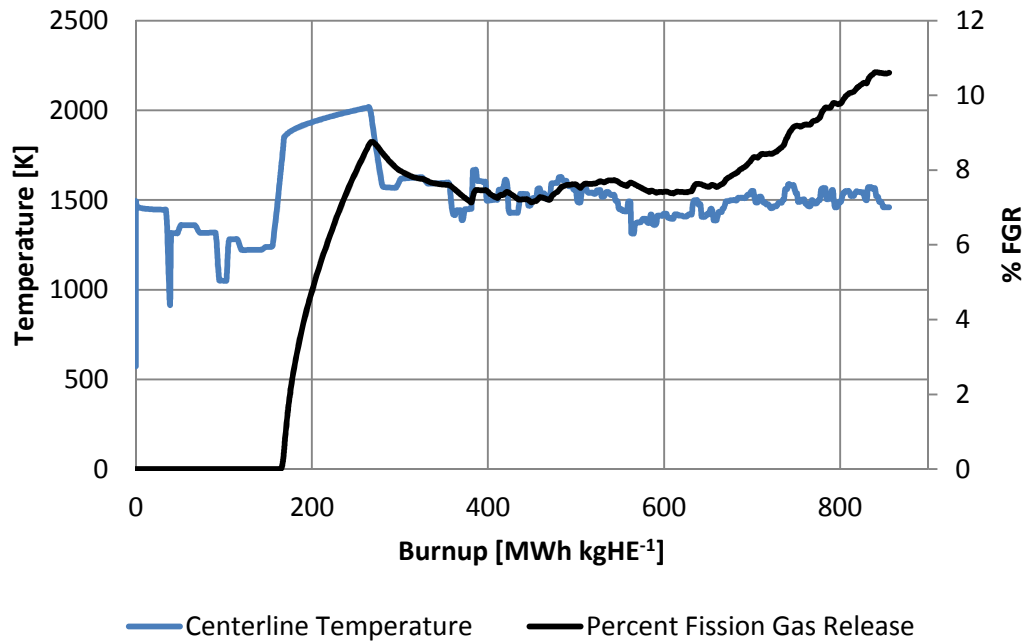


Figure 22: Centerline temperature and %FGR calculations for the Case 2 simulation of normalized ADF OE.

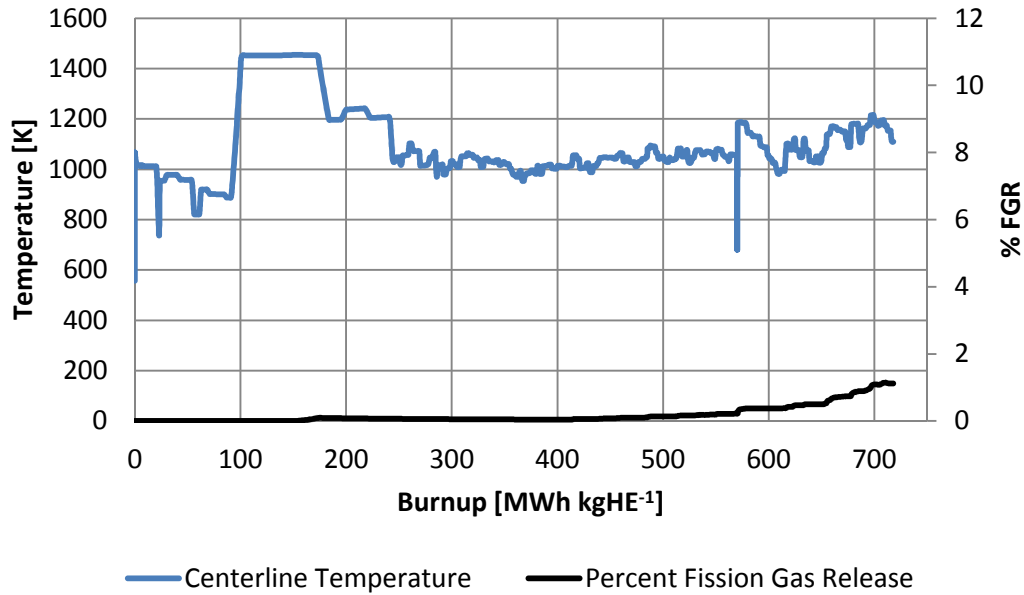


Figure 23: Centerline temperature and %FGR calculations for the Case 2 simulation of normalized ADA IE.

The difference in FGR shown between Figures 22 and 23 highlights the modelling assumptions that are limiting its ability to reflect the behaviour for all BDL-422 FGR data. The measurement of FGR for ADF OE is 2.8%, whereas either Case 1 or Case 2 versions of the (Th,Pu)O<sub>2</sub> model calculate about 10% FGR. In Figure 22 FGR does not occur until a power ramp around ~150 MWh kgHE<sup>-1</sup>. Then FGR increases to about 8%. There is a period from ~250 MWh kgHE<sup>-1</sup> to ~375 MWh kgHE<sup>-1</sup> where the model is not releasing FG to the free volume of the element and the model temperature is sustained around 1500 K. This is followed by a section that plateaus at around 8% until ~650 MWh

$\text{kgHE}^{-1}$ , this indicates that the FG is sufficiently mobile to saturate the grain boundaries and is similar to ADD (Figure 21) when fuel temperature exceeds 1500 K. Beyond  $650 \text{ MWh kgHE}^{-1}$ , the FGR acts almost linearly indicating that all FG that reaches the grain boundaries is being released at this point. This is in contrast to the ADA IE simulation shown in Figure 23 where there was not significant FGR until the last third of its power history when burnup reaches  $\sim 500 \text{ MWh kgHE}^{-1}$ .

Both Case 1 and Case 2 models over predicted the FGR of ADE OE and ADF OE substantially. These models are calculating high FG mobility with centerline fuel temperatures around 1500 K; hence the models are over predicting FG diffusion in this temperature range. The modelling assumptions were made in an attempt to match the high release measurements of ADA and ADD OE, and not suitable for the elements that experienced higher temperatures but lower FGR.

Factors that contribute to the uncertainty in the FGR results are: the behaviour of the thermal conductivity model discussed earlier (see non-physical behaviour in Tables 24 and 25), the various microstructural features of the fuel (small grain sizes, granular, and inhomogeneous Pu content) and the assumption that fuel microstructure is uniform. Inhomogeneous distribution of Pu and granular microstructure will lead to localized high temperature regions, which would contribute to an increase in FGR that the model is unable to replicate. Both

Case 1 and Case 2 versions of the (Th,Pu)O<sub>2</sub> model are capable of replicating the lower temperature FGR.

### 6.1.3.3 Deformation

Tables 27 and 28 present the modelling result for MP and PI strain in comparison to the averaged MP and PI measurements from BDL-422.

Table 27: A comparison of the average measured mid-pellet strain to UO<sub>2</sub>, and both (Th,Pu)O<sub>2</sub> model results.

Bundle	Max Linear Power [KW m <sup>-1</sup> ]	Burnup [MWh kgHE <sup>-1</sup> ]	Modelled MP (%)		Average MP Strain (%)	
			N- UO <sub>2</sub>	Case 1		Case 2
<b>Outer Elements</b>						
ADA	54	1181	4.3	1.88	1.90	0.41
ADC	67	451	0.4	0.32	0.34	1.1
ADD	73	1082	4.2	1.13	1.74	0.34
ADE	64	597	0.6	0.30	0.52	0.35
ADF	52	856	0.3	0.07	0.16	0.05
<b>Intermediate Elements</b>						
ADA	27	718	-0.01	-0.20	-0.11	-0.23
ADC	22	288	-0.28	-0.34	-0.34	-0.36
ADD	45	665	-0.04	-0.21	-0.11	-0.22
ADE	32	308	-0.23	-0.30	-0.29	-0.32
ADF	39	531	-0.14	-0.24	-0.24	-0.27

Table 28: UO<sub>2</sub> and (Th,Pu)O<sub>2</sub> modelling results compared to the averaged PI measurements from BDL-422.

Bundle	Max Linear Power [KW m <sup>-1</sup> ]	Burnup [MWh kgHE <sup>-1</sup> ]	Modelled PI (%)			Average PI Strain (%)
			N-UO <sub>2</sub>	Case 1	Case 2	
<b>Outer Elements</b>						
<b>ADA</b>	<b>54</b>	<b>1181</b>	4.4	1.89	1.92	0.53
<b>ADC</b>	<b>67</b>	<b>451</b>	1.0	0.88	0.91	1.7
<b>ADD</b>	<b>73</b>	<b>1082</b>	4.2	1.84	2.64	0.93
<b>ADE</b>	<b>64</b>	<b>597</b>	1.2	0.71	1.10	0.82
<b>ADF</b>	<b>52</b>	<b>856</b>	0.4	0.16	0.29	0.14
<b>Intermediate Elements</b>						
<b>ADA</b>	<b>27</b>	<b>718</b>	0.00	-0.18	-0.11	-0.21
<b>ADC</b>	<b>22</b>	<b>288</b>	-0.28	-0.34	-0.34	-0.36
<b>ADD</b>	<b>45</b>	<b>665</b>	0.00	-0.17	-0.10	-0.195
<b>ADE</b>	<b>32</b>	<b>308</b>	-0.23	-0.30	-0.29	-0.32
<b>ADF</b>	<b>39</b>	<b>531</b>	-0.14	-0.24	-0.24	-0.269

Tables 27 and 28 indicate that the UO<sub>2</sub> model does not replicate the end-of-life strain measurements from BDL-422. Both Case 1 and Case 2 over predict the MP and PI strains for ADA and ADD OE elements, because the models over predict the fuel temperature. In general, both versions of the (Th,Pu)O<sub>2</sub> model calculate the end-of-life strain much closer to the averaged measurements than the UO<sub>2</sub> model. The (Th,Pu)O<sub>2</sub> model appears to be in better agreement with the PIE measurement than those predicted by (Th,U)O<sub>2</sub> for the DME-221 fuel, with the un-normalized power histories being in better agreement than those from the

normalized elements. The work presented by Boer *et al.* also demonstrated that their (Th,Pu)O<sub>2</sub> fuel performance model was able to replicate the end-of-life profilometry measurements of their experimental fuel [16]. The results from the simulation of ADE and ADF OE cases demonstrate that the deformation model is effective for elements where centerline fuel temperatures approach 2200 K.

There are several concerns about the model's abilities. These concerns arise from the limitations of the un-irradiated thermal conductivity correlation that is limited to 1600 K. The FGR model has also been fitted to the extreme cases from BDL-422. For OE from ADE and ADF, the model over predicts the FGR by about a factor of 4 (this experiences temperatures greater than 1500 K for extended periods). The MPM-FAST (Th,Pu)O<sub>2</sub> models developed in this work are much more capable of replicating the FGR and end-of-life strain for BDL-422 fuel than the FAST-UO<sub>2</sub> model. In addition to this, no other (Th,Pu)O<sub>2</sub> model in literature has replicated high power and high FGR cases similar to BDL-422 fuel.

## **6.2 Sensitivity Analysis**

In Prudil's work [8] on FAST, 26 separate parameters were tested while conducting his sensitivity analysis of the UO<sub>2</sub> fuel model, to determine the effect they had on the model's ability to calculate MP strain, PI strain, and FG volume released. Prudil examined these behaviours for three base cases that maintained a

constant linear power ( $25 \text{ kW m}^{-1}$ ,  $40 \text{ kW m}^{-1}$ , and  $55 \text{ kW m}^{-1}$ ) until each simulation had achieved  $200 \text{ MWh kgU}^{-1}$  burnup. Additionally the parameters of the fuel element geometry used for these cases are recorded in Table 29 below.

Table 29: Design parameters for the fuel element used for sensitivity analysis.

Pellets per element	Stack Axial Clearance (mm)	Diametral Clearance (mm)	Outer Diameter (mm)	Dish Depth (mm)	Axial Chamfer (mm)	Radial Chamfer (mm)	Land Width (mm)	Pellet Length (mm)	Sheath Thickness (mm)	Initial Grain Size ( $\mu\text{m}$ )	Initial Density ( $\text{kg m}^{-3}$ )
26	2.29	0.08	14.33	0.236	0.176	0.827	0.00	18.52	0.405	11.6	10690

The 26 parameters Prudil examined [8] were categorized into three groups: 1) input parameters, 2) material properties, and 3) solver/numerical technique parameters. A model run was performed for each of the parameters' upper and lower values, with a single parameter being altered per run.

The set of input parameters that were examined in the sensitivity analysis consisted of: the linear power, exit burnup, coolant temperature, sheath-to-coolant heat transfer coefficient, initial pellet-to-sheath gap size, axial gap between pellets, pellet radius, sheath thickness, dish depth, fuel grain size, initial pellet density, element end/plenum volume, and the inclusion of 10% Ar as part of the initial element fill gas. It was found that any change to an input parameter that leads to systemic increase or decrease of fuel temperature can have a significant



effect on the FGR volume (which is most of the inputs listed). As the fuel temperature can cause positive feedback, increased temperature releases more FG and decreasing the thermal conductivity through the pellet-to-sheath gap. As for the prediction of the sheath strains, these results show little dependence on these variables, and was found to be most sensitive to initial pellet-to-sheath gap and changes to the linear power.

Within the examination of the sensitivity of the model to the uncertainty of material parameters the following properties underwent analysis: pellet cracking model disabled, fission gas release time constant,  $\text{UO}_2$  thermal conductivity,  $\text{UO}_2$  thermal expansion strain, fission gas diffusion coefficient, fission gas grain boundary saturation concentration, Zircaloy thermal conductivity, Zircaloy Young's modulus, and Zircaloy thermal expansion strain.

At low power conditions the fission gas release results are only sensitive to the boundary saturation condition. At the higher power the fission gas release is sensitive to changes in, saturation conditions, diffusion coefficients, and  $\text{UO}_2$  thermal conductivity. For the modeled mid-pellet and pellet-to-pellet sheath strains the greatest change in the results were caused when: the pellet cracking was disabled (making the pellet more compressive), thermal expansion strain of the pellet, and thermal conductivity of the pellet (both affect how much the pellet will deform).

The final sets of parameters examined for model sensitivity were solver parameters, which include: mesh density, solver dampening factor, maximum time step, contact pressure estimate, contact penalty factor, and the increase of both the contact pressure estimate and penalty factor simultaneously by a factor of 5. It was found that generally, variations in these parameters had little effect on the calculation of fission gas release and sheath strain. Indicating that these base values of mesh size, time stepping, and solver settings allow the model to be convergent [8].

Since MPM-FAST is built over the framework of the FAST's UO<sub>2</sub> and Zircaloy-4 model, this means that only the parameters that have been added for the Th-based fuel need to be examined in this sensitivity analysis. Table 30 shows the differences in the modelling results between the Th-based models using equivalent initial fissile material as natural U, compared to the UO<sub>2</sub> base cases used by Prudil [8].

Table 30: Modelling results for MP strains, PI strains, and FG volume for the base cases of the (Th,U)O<sub>2</sub> and Th,PuO<sub>2</sub> models compare to FAST's UO<sub>2</sub> results [8].

Fuel Type	Liner Power [kW m <sup>-1</sup> ]	MP Strain [%]	PI Strain [%]	FG Volume [mL]
UO <sub>2</sub>	25	-0.24	-0.22	0
	40	-0.11	-0.04	2.1
	55	0.71	1.37	23.1
(Th,U)O <sub>2</sub> Case 1)	25	-0.65	-0.62	0
	40	-0.37	-0.22	0
	55	-0.07	0.09	0
(Th,U)O <sub>2</sub> Case 2)	25	-0.62	-0.57	0
	40	-0.30	-0.14	0
	55	0.01	0.31	0.4
(Th,Pu)O <sub>2</sub> Case 1)	25	-0.66	-0.64	0
	40	-0.56	-0.50	0.1
	55	-0.11	0.09	19.0
(Th,Pu)O <sub>2</sub> Case 2)	25	-0.66	-0.64	0
	40	-0.54	-0.50	0.02
	55	-0.11	0.09	17.9

Overall the Th-based fuel models exhibit end-of-life strains that are more compressive and have lower FG volume released to the free volume of the element under these irradiation conditions in comparison with the UO<sub>2</sub> model. These results are in line with the other observed model behaviours as discussed in the validation sections.

Six parameters were selected for the sensitivity analysis (SA). They are specific to the Th-based fuel's material models (thermal conductivity, thermal expansion, and fission gas diffusion). The input parameters linear power, exit burnup, and initial grain size, directly affect the pellet materials' thermal

conductivity and FGR models are also examined. These six parameters are examined within the (Th,U)O<sub>2</sub> model using the Bakker thermal conductivity [28] (Case 2), and the (Th,Pu)O<sub>2</sub> model using the UN power histories (Case 1). These cases were selected because results presented in Table 30 shows that these cases are more sensitive to the irradiation conditions and the uncertainty within them will be bounded by their behaviour. The results are presented separately in Tables 31 & 32. The changes in modelling results, as well as the percentage change are reported.

### 6.2.1 (Th,U)O<sub>2</sub>

Table 31 presents the sensitivity analysis for the model that uses the Bakker *et al.* conductivity model (Case 2). The parameter that has the largest effect on all three results is the thermal conductivity, specifically when it is reduced by 20%. This causes ~4 mL more FG to be released and the end of life sheath strains becoming more tensile for the MP and PI strains for 40 and 55 kW m<sup>-1</sup>. The order in which the parameters that affected FGR of the 55 kW m<sup>-1</sup> the most are: FG diffusion (-0.35 to +0.86 mL), linear power (-0.32 to +0.56 mL), grain size (-0.1 to 0.19 mL), burnup ( $\pm$ 0.12 mL), and lastly the thermal expansion (-0.02 mL). As for the strain results: grain size and FG diffusion have no effect, linear power has a limited effect, while the thermal expansion has the largest effect after thermal conductivity.

### 6.2.2 (Th,Pu)O<sub>2</sub>

The sensitivity analysis results for the (Th,Pu)O<sub>2</sub> Case 1 are presented in Table 32. Similar to the (Th,U)O<sub>2</sub> model the parameter with the largest effect on all the modelling results is the thermal conductivity. For the FGR at 55 kW m<sup>-1</sup>, the permutations in thermal conductivity cause ~13 mL of FG volume difference from the base case. For the 40 kW m<sup>-1</sup> with the reduced thermal conductivity (TC), the calculated volume increased by almost 10 mL. The reduced thermal conductivity also causes the greatest change in the end-of-life strain calculations (more tensile than any other cases). The list of parameters and their relative sensitivities on the FGR, and strain calculations follows the same order as listed for the (Th,U)O<sub>2</sub> fuel model.

Table 31: SA for Case 2 (Th,U)O<sub>2</sub> model.

	Parameter Variation	LER	MP Sheath Strain (%)	Change	% Change	PI Sheath Strain (%)	Change	% Change	FG Vol. (mL)	Change	% Change
Baseline Cases		25	-0.62			-0.57			0.00		
		40	-0.30			-0.14			0.00		
		55	0.01			0.31			0.38		
Linear Power	-5%	25	-0.65	-0.03	-4.7	-0.61	-0.05	8	0.00	0.00	0
		40	-0.34	-0.04	-13	-0.20	-0.06	41	0.00	0.00	0
		55	-0.03	-0.04	-312	0.18	-0.13	-42	0.06	-0.32	-84
	+5%	25	-0.60	0.02	4	-0.53	0.04	6	0.00	0.00	0
		40	-0.25	0.05	16	-0.10	0.04	31	0.00	0.00	0
		55	0.13	0.12	974	0.50	0.19	62	0.94	0.56	150
Burnup	-5%	25	-0.62	0.00	0	-0.57	0.00	0	0.00	0.00	0
		40	-0.31	0.00	0	-0.15	0.01	-2.5	0.00	0.00	0
		55	0.01	0.00	0	0.30	-0.01	-1.9	0.26	-0.12	-31
	+5%	25	-0.62	0.00	0	-0.56	0.00	0	0.00	0.00	0
		40	-0.30	0.01	1.8	-0.14	0.00	0	0.00	0.00	0
		55	0.01	0.00	0	0.32	0.01	2.6	0.50	0.12	33
Initial Grain Size (μm)	-1	25	-0.62	0.00	0	-0.57	0.00	0	0.00	0.00	0
		40	-0.30	0.00	0	-0.14	0.00	0	0.00	0.00	0
		55	0.01	0.00	0	0.31	0.00	0	0.56	0.19	50
	+1	25	-0.62	0.00	0	-0.57	0.00	0	0.00	0.00	0
		40	-0.30	0.00	0	-0.14	0.00	0	0.00	0.00	0
		55	0.01	0.00	0	0.31	0.00	0	0.27	-0.10	-27
Fuel TC	+20%	25	-0.51	0.11	18	-0.40	0.17	29	0.00	0.00	0
		40	-0.11	0.19	64	0.06	0.20	139	0.00	0.00	0
		55	1.05	1.03	8300	1.78	1.47	474	4.49	4.11	1095
	-20%	25	-0.69	-0.07	-11	-0.68	-0.11	-19	0.00	0.00	0
		40	-0.42	-0.11	-38	-0.29	-0.15	-105	0.00	0.00	0
		55	-0.14	-0.16	-1300	0.02	-0.29	-94	0.00	-0.38	-100
Thermal Expansion strain	-10%	25	-0.66	0.04	-6.8	-0.62	-0.05	-9	0.00	0.00	0
		40	-0.38	-0.08	-25	-0.23	-0.09	-64	0.00	0.00	0
		55	-0.05	-0.06	-490	0.15	-0.16	-52	0.36	-0.02	-4.2
	+10%	25	-0.58	0.04	6.8	-0.52	0.05	9	0.00	0.00	0
		40	-0.23	0.07	25	-0.06	0.08	57	0.00	0.00	0
		55	0.11	0.10	804	0.44	0.13	42	0.37	-0.01	-2
Fission Gas Diffusion	x0.5	25	-0.62	0.00	0	-0.57	0.00	0	0.00	0.00	0
		40	-0.30	0.00	0	-0.14	0.00	0	0.00	0.00	0
		55	0.02	0.00	0	0.32	0.02	4.9	0.03	-0.35	-92
	X2	25	-0.62	0.00	0	-0.57	0.00	0	0.00	0.00	0
		40	-0.30	0.00	0	-0.14	0.00	0	0.00	0.00	0
		55	0.01	0.00	0	0.31	0.00	0	1.23	0.86	228

Table 32: SA for Case 1 (Th,Pu)O<sub>2</sub> model (fit to UN power histories).

	Parameter Variation	LER	MP Sheath Strain (%)	Change	% Change	PI Sheath Strain (%)	Change	% Change	FG Vol. (mL)	Change	% Change
Baseline Cases		25	-0.66			-0.64			0.0		
		40	-0.56			-0.51			0.1		
		55	-0.11			0.09			19.0		
Linear Power	-5%	25	-0.67	0.0	-0.9	-0.65	-0.01	-1.2	0.0	0	0
		40	-0.58	-0.02	-3.3	-0.53	-0.03	-5.3	0.0	0	0
		55	-0.22	-0.1	-100	-0.09	-0.18	-191	15.2	-3.8	-20
	+5%	25	-0.66	0.0	1.0	-0.64	0.01	1.26	0.0	0	00
		40	-0.54	0.0	4.0	-0.47	0.03	6.5	0.7	0.6	511
		55	0.02	0.1	118	0.41	0.32	338	22.2	3.3	17
Burnup	-5%	25	-0.66	0.0	-0.5	-0.65	0	0	0.0	0	0
		40	-0.56	0.0	-0.5	-0.51	0	0	0.0	0	0
		55	-0.12	0.0	-6.9	0.07	-0.02	-24	17.0	-2	-10
	+5%	25	-0.66	0.0	0.6	-0.64	0	0	0.0	0	0
		40	-0.55	0.0	0.7	-0.50	0	0	0.2	0.1	73
		55	-0.10	0.0	4.2	0.12	0.02	25	21.0	2.1	11
Initial Grain Size (µm)	-1	25	-0.66	0.0	0	-0.64	0	0	0.0	0	0
		40	-0.56	0.0	0	-0.51	0	0	0.1	0	0
		55	-0.11	0.0	0	0.10	0.01	7.3	20.5	1.5	7.9
	+1	25	-0.66	0.0	0	-0.64	0	0	0.0	0	0
		40	-0.56	0.0	0	-0.51	0	0	0.1	-0.02	-17
		55	-0.11	0.0	0	0.09	-0.01	-5.8	17.7	-1.3	-6.6
Fuel TC	-20%	25	-0.63	0.0	4.4	-0.61	0.04	5.9	0.0	0	0
		40	-0.36	0.2	35	-0.23	0.28	55	9.7	9.6	8900
		55	0.72	0.8	762	1.44	1.35	1430	32.1	13.2	69.5
	+20%	25	-0.68	-0.02	-2.6	-0.67	-0.02	-3.4	0.0	0	0
		40	-0.61	-0.05	-8.8	-0.58	-0.07	-14	0.0	-0.1	-100
		55	-0.43	-0.3	-294	-0.32	-0.42	-440	5.3	-13.7	-72
Thermal Expansion strain	-10%	25	-0.70	-0.04	-5.8	-0.69	-0.07	-6.7	0.0	0	0
		40	-0.61	-0.1	-9.4	-0.57	0.06	-12	0.1	0.003	2.8
		55	-0.14	0.03	-32	0.03	0.08	-73	19.5	0.5	2.8
	+10%	25	-0.62	0.03	-5.8	-0.60	0.04	6.7	0.0	0	0
		40	-0.51	0.1	-9.4	-0.45	0.06	12	0.1	-0.01	-9.4
		55	-0.10	0.01	-7.5	0.17	0.08	81	18.5	-0.45	-2.3
Fission Gas Diffusion	x0.5	25	-0.66	0.0	0.0	-0.64	0.00	0	0.0	0	0
		40	-0.56	0.0	0	-0.50	0.00	0	0.0	0	0
		55	-0.12	0.0	0	0.06	-0.03	-33	12.6	-6.3	-33
	X2	25	-0.66	0.0	0	-0.64	0.00	0	0.0	0	0
		40	-0.56	0.0	0	-0.51	0.00	0	0.7	0.6	530
		55	-0.10	0.0	0	0.13	0.03	36	25.7	6.7	35

Based on the results of the sensitivity analysis, a comparison of the center line fuel temperature of the (Th,U)O<sub>2</sub> and (Th,Pu)O<sub>2</sub> base cases will be compared to the centerline temperature of the cases that examine the upper and lower bounds of the thermal conductivity. Figures 24 and 25 display the Case 2) (Th,U)O<sub>2</sub> and Case 1) (Th,Pu)O<sub>2</sub> centerline temperature model results, respectively.

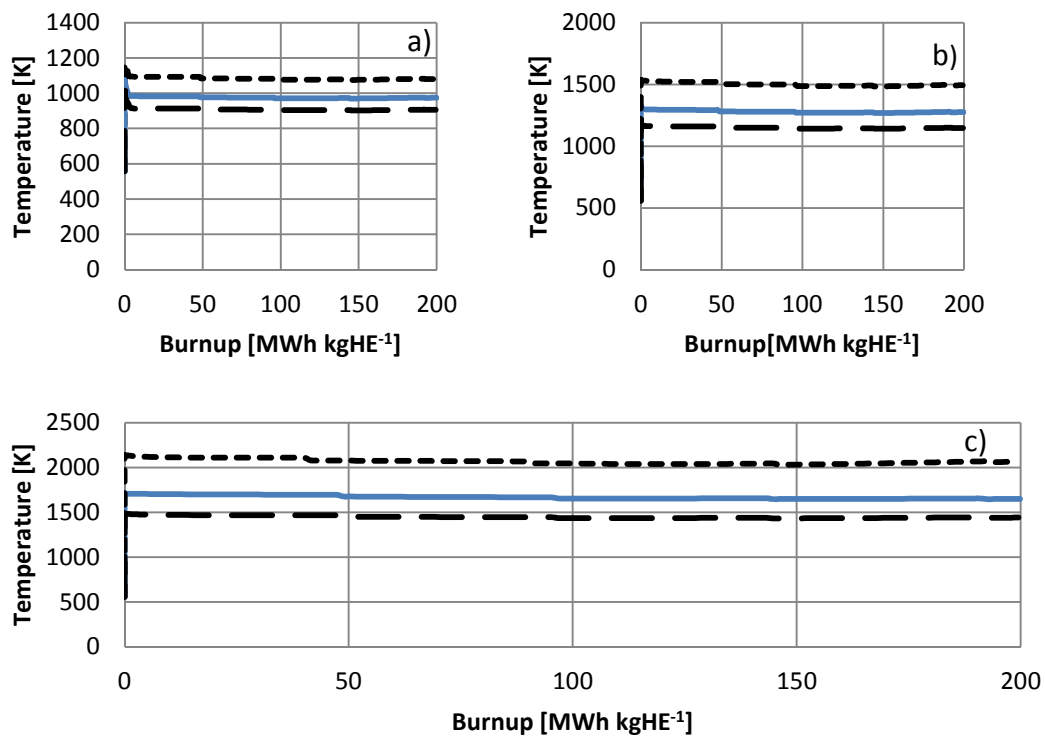


Figure 24: Calculated centerline temperature for the three linear power cases a) 25 kW m<sup>-1</sup> b) 40 kW m<sup>-1</sup> c) 55 kW m<sup>-1</sup> presented with the uncertainty that arises in the model from the thermal conductivity correlation for the (Th,U)O<sub>2</sub> Case 2) model.



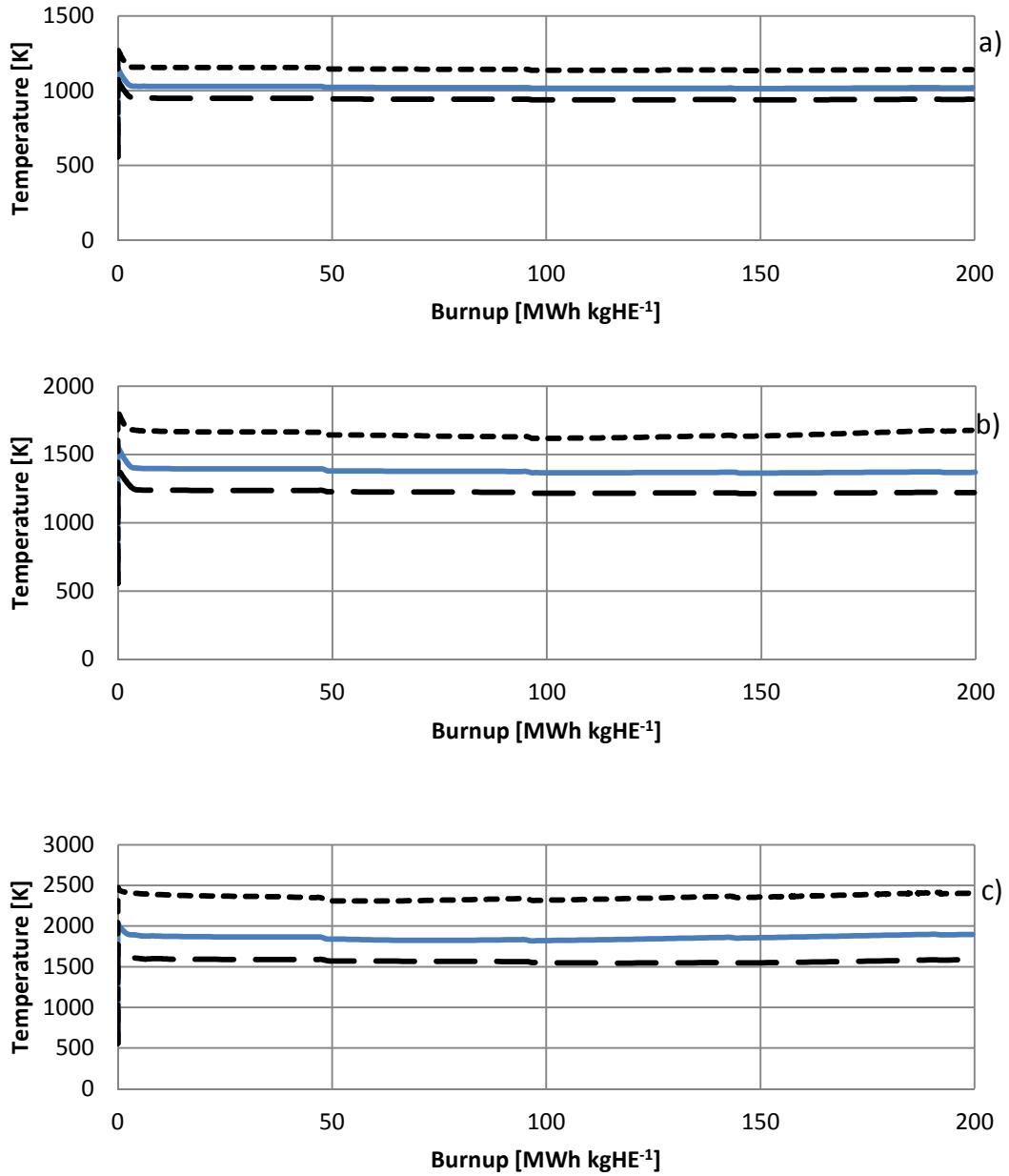


Figure 25: Calculated centerline temperature for the three linear power cases a) 25 kW m<sup>-1</sup> b) 40 kW m<sup>-1</sup> c) 55 kW m<sup>-1</sup> presented with the uncertainty that arises in the model from the thermal conductivity correlation for the (Th,Pu)O<sub>2</sub> Case 1) model.

Figures 24 and 25 demonstrate that the uncertainty within the temperature calculations of both the (Th,U)O<sub>2</sub> and (Th,Pu)O<sub>2</sub> increases with temperature. This is seen in the behaviour of the upper bounds of the 55 kW m<sup>-1</sup> cases, where the change in the temperature between the upper bounds and the base case is more pronounced than the lower bounds. In both (Th,U)O<sub>2</sub> and (Th,Pu)O<sub>2</sub> for 25 kW m<sup>-1</sup> cases, the temperature uncertainty range is about 150 K from the lower bounds to the upper bounds. For the 40 kW m<sup>-1</sup> cases, this ranges extends to about 300 K and 400 K for (Th,U)O<sub>2</sub> and (Th,Pu)O<sub>2</sub> respectively. These ranges extend further on to about 600 K and 800 K for the 55 kW m<sup>-1</sup> cases of (Th,U)O<sub>2</sub> and (Th,Pu)O<sub>2</sub> respectively.

### **6.3 SCWR Fuel**

To move forward in determining if MPM-FAST is capable of modelling the SCWR fuel, an attempt to model a fuel element from SCWR's inner ring was undertaken. A version of MPM-FAST that included heat transport, grain growth, fission gas transport in the fuel grains and the heat transfer through the gas gap was used. The fission gas release, elastic and plastic deformation models were disabled. As mentioned above there are several material properties within the (Th,Pu)O<sub>2</sub> model that have a limited upper temperature to which they have been correlated. The primary concern is the thermal conductivity model. Since fuel temperature is the primary driver of many fuel behaviours, any results that exceed

this temperature for extended periods of time will have an un-quantifiable uncertainty.

Table 33 lists the input parameters used to generate the geometry and model conditions for calculating the fuel temperature of a fuel element from a SCWR's inner ring.

Table 33: Input Parameters used to generate SCWR model.

<b>Parameter</b>	<b>Value</b>
pellet_length	1 [cm]
pellet_radius	0.44 [cm]
sheath_thickness	0.06 [cm]
linear_power_parameter	34 [kW m <sup>-1</sup> ]
burnup_max	960 [MWh kgHE <sup>-1</sup> ]
pore_fraction_initial	0.03
initial_grain_size	7 [μm]
v0_ends	2 [L]
mf0_He	1
num_pellets	25
pellet_mat	3
sheath_mat	2
coolant_pressure	25 [MPa]
P_gas_calc	10 [MPa]
P_contact	15 [MPa]
d_gap	1.5 [μm]

The model was set to examine the behaviour of a 25 cm subsection of an element. The model treats them as separate sub elements, and the general assumptions used to model PHWR fuel still apply. With the deformation model being disabled, contact pressure, gas pressure and the gap distance between the pellet and the clad are included as input parameters. A full version of MPM-FAST

was used to determine that the contact pressure and gas pressure as 15 MPa, and 10 MPa, respectively, to counteract the 25 MPa coolant pressure acting on the clad during NOC.  $960 \text{ MWh kgHE}^{-1}$  (equivalent to  $40 \text{ MWd kgHE}^{-1}$ ) and  $34 \text{ kW m}^{-1}$  are the estimated SCWR burnup and linear power that maintain the upper power limit below  $40 \text{ kW m}^{-1}$ . The parameters pellet\_mat and sheath\_mat are set so that the model will use the (Th,Pu)O<sub>2</sub> model and 310 stainless steel material correlations for the heat conduction calculations.

Figures 26 and 27 display the outer clad temperature and axial power variations applied to the various sub regions of the SCWR fuel element against the data points from Colton *et al.* [4], and Pencer *et al.* [7], for the clad temperature and power profile, respectively.

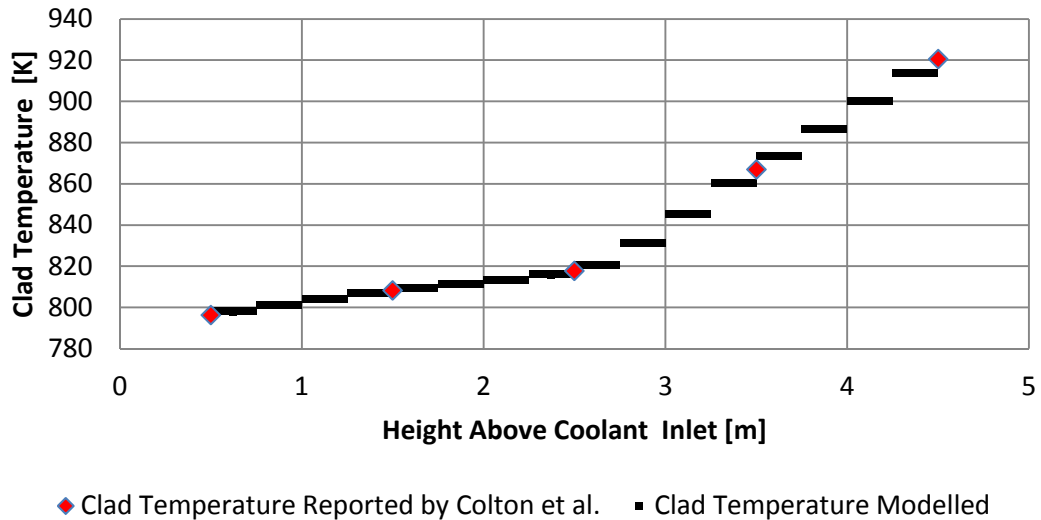


Figure 26: Temperature of the outer clad surface for an SCWR fuel element.

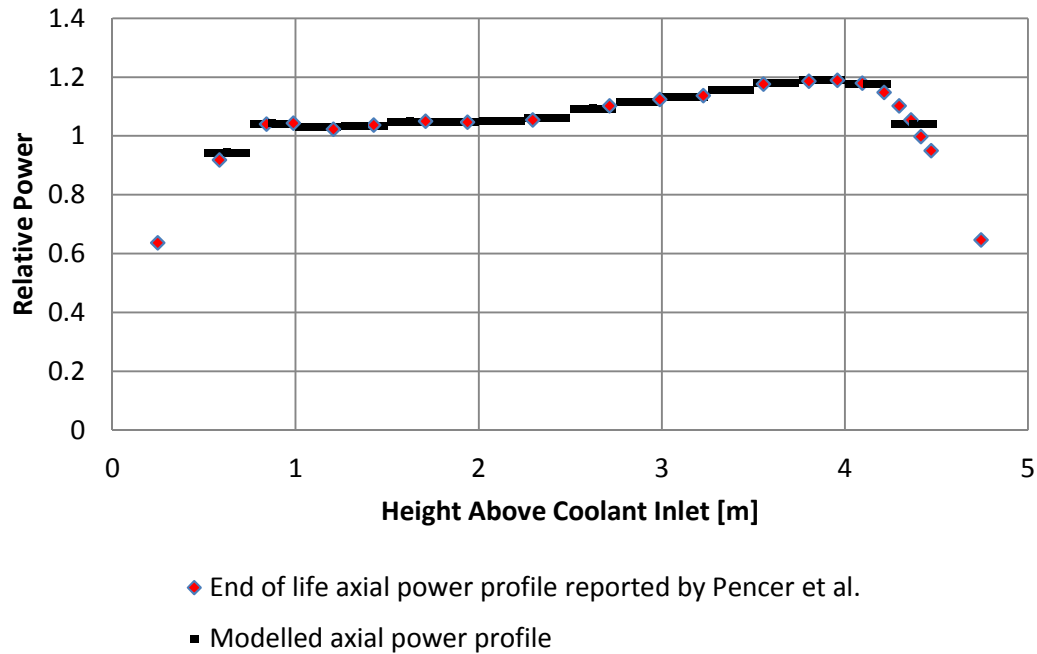


Figure 27: Relative power profile based on axial location along a SCWR fuel element.

Each 25 cm long subsection was assigned a case index number between 1-16 based on the height above the coolant inlet. Based on Figures 26 and 27, the subsection of the fuel that will experience the lowest fuel temperature will be subsection #1 and the highest will be subsection #14. Subsection #14 has a relative axial power of approximately 1.19 compared to subsection #16 which is about 1.03. This difference in relative power leads subsection #14 to experience the highest fuel temperature. With the deformation model disabled, the fine features such as the pellet dishes, and chamfers are made redundant. This simplifies the examined geometry to a rectangle representing the fuel pellet and

subsection of the clad. Figure 28 below displays the meshed geometry for a subsection.

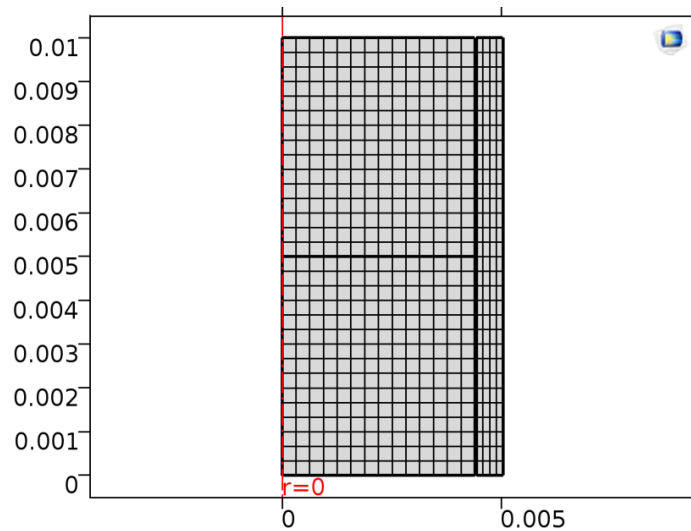


Figure 28: Meshed geometry for a subsection model of the SCWR inner ring fuel element.

Figure 29 displays the radial fuel temperature profiles for these subsections. The dark blue line and the dark green line in Figure 29 represent the beginning and end of irradiation temperatures for subsection #1 respectively. Similarly the red line and light blue line represent the beginning and end of irradiation temperatures for subsection #14 respectively.

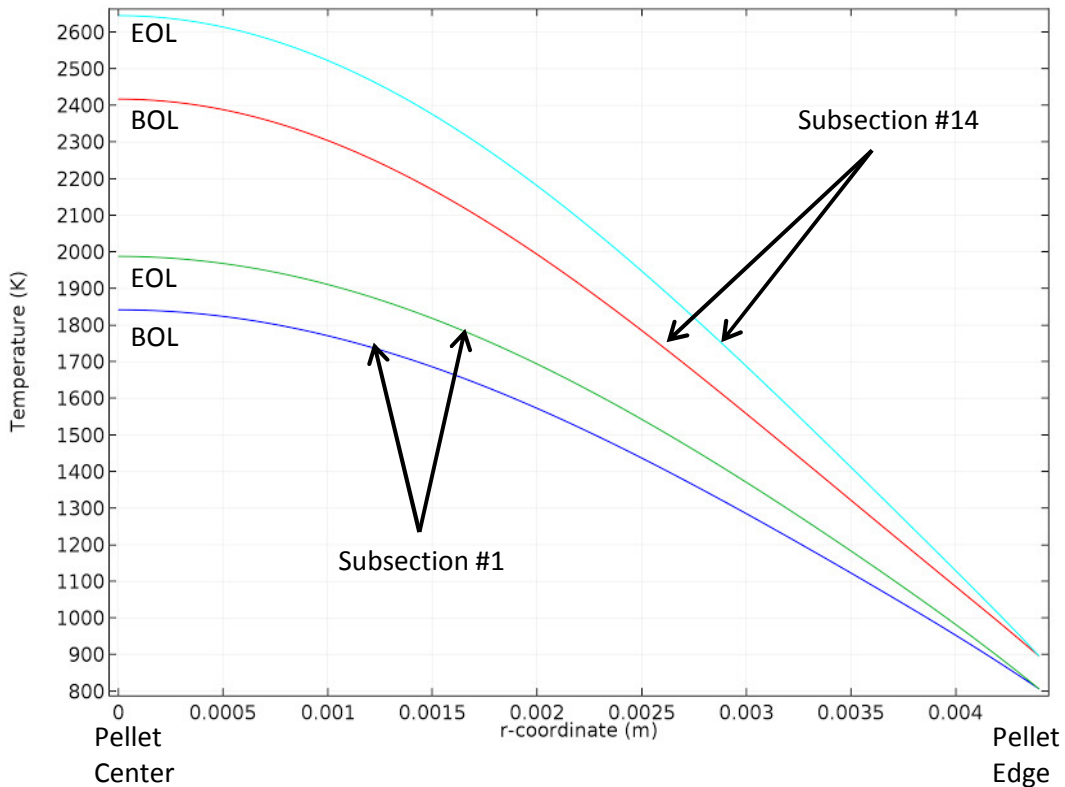


Figure 29: Mid-pellet radial fuel temperature profiles for subsection #1 and subsection #14, here BOL is Beginning of Life, and EOL is End of Life.

An element from the inner fuel ring was selected to use as the test case because it is the smaller diameter, and it will experience lower fuel temperatures in general, when compared to an outer ring element. It can be observed from Figure 29 that in subsection #1, at the beginning of the irradiation between the center of the fuel until ~1.9 mm, the fuel temperature is greater than 1600 K and by the end of the irradiation this region expands to ~2.4 mm. Similarly, for subsection 14 this region varies between ~2.9 mm and ~3.2 mm. This exercise demonstrates that a majority of the SCWR fuel will have an unquantifiable

uncertainty in deformation modelling because of the knowledge gaps in (Th,Pu)O<sub>2</sub> material properties.

Even though the deformation modelling has been disabled, it should also be noted that the fuel experiences temperatures beyond 2000 K and is outside the validation of the thermal expansion models. Other modelling assumptions that are currently disabled such as the FGR will also be affected in this temperature regime, leading to further limitations in developing a fully validated model.

Based on the known limitations of the thermal physical behaviour of (Th,Pu)O<sub>2</sub>, and the findings of this simplified heat conduction model for the SCWR fuel element, it is not recommended that MPM-FAST be used to determine the physical strains and therefore, deformation within the SCWR fuel. Further knowledge will need to be gained from the measurement of various thermal mechanical properties at high temperatures. MPM-FAST has demonstrated that it is capable of providing burnup dependent behaviour of the fuel, which is likely on the conservative side due to the behaviour of the Cozzo thermal conductivity model above 1600 K [31]. The work presented here can lead to a conservative estimate of the FG volume and help inform the selection of plenum designs.



## 6.4 Modelling Concerns

In Chapter 4 all of the modelling assumptions are outlined. The following section will highlight perceived limitations or concerns about assumptions in MPM-FAST. These limitations are presented below.

- The heat transfer through the gas in the fuel-to-sheath gap uses the AECL fission gas parameters, which are based on the FG released from natural  $\text{UO}_2$ , these values may not be representative of the fissioning of primarily U-233.
- $\text{UO}_2$  emissivity, densification, and fission product swelling, are used for all fuel types.
- Only  $\text{ThO}_2$  values for Young's modulus and Poisson's ratio are available and these values are used for the  $(\text{Th,U})\text{O}_2$  and  $(\text{Th,Pu})\text{O}_2$  models.
- Heat generation, burnup, and flux shaping/depression models are all based on the  $\text{UO}_2$  model, and do not fully represent  $(\text{Th,U})\text{O}_2$  and  $(\text{Th,Pu})\text{O}_2$  behaviour.
- Fission gas diffusion coefficient for  $(\text{Th,U})\text{O}_2$  has limited basis for the assumptions that have been made, and the  $(\text{Th,Pu})\text{O}_2$  model has been generated based solely on the BDL-422 data.
- Material properties correlations for Th-based ceramics are limited by their temperature ranges.

The greatest limitations within MPM-FAST's modelling capabilities arise due to the current correlations for the material properties of the ceramic mixed oxide fuels. Models that calculate fuel temperature beyond the ranges the material properties have been validated will need to be examined in order to determine if the modelling results are suitable. The user of the model will need to be aware of when and how these limitations arise and take them into account, while analyzing the model results. For example, the unirradiated thermal conductivity correlation for (Th,Pu)O<sub>2</sub> predicts the thermal conductivity will continue to decrease with temperatures greater than 1600 K; this would lead to the assumption that MPM-FAST would over predict the temperature of (Th,Pu)O<sub>2</sub> fuel at temperatures greater than 1600 K. Similar considerations will also have to be made in examining the deformation behaviour of (Th,U)O<sub>2</sub> and (Th,Pu)O<sub>2</sub> pellets because of the MPM-FAST's dependence on using ThO<sub>2</sub> properties for elastic strain calculations. The solution to this set of limitations will be the development of material properties over the entire range of fuel temperatures up to fuel melting. This is far beyond the scope of this work.

In Chapter 4 it is noted that the UO<sub>2</sub> models for emissivity, densification, and fission product swelling are used to represent this behaviour for all fuel types in MPM-FAST. Since emissivity only contributes substantially to the heat transfer within the fuel-to-sheath gap when the gap is large, it is not a dominant factor in Canadian PHWR type fuel at NOC. As for the densification, and fission product

swelling models, no models for these behaviours have been found in the literature. It is assumed, since these are neutron irradiation interaction behaviours and the result of fission products being produced, that these behaviours will be equivalent in Th-based ceramic fuel. The only means of removing this dependence will be to develop models specifically for these fuel types.

Other physical phenomena currently being represented by  $\text{UO}_2$  models are the heat generation, burnup, and flux shaping/depression models. Work by Long *et al.* [24], Bjork [34], and Seidl *et al.* [32] have all demonstrated that flux depression models can be developed for Th-based fuel.

Appendix C focuses on the modelling assumptions made to the fission gas diffusion behaviour models to replicate the fission gas behaviour exhibited by BDL-422. As mentioned above there is limited experimental evidence to support the  $(\text{Th,U})\text{O}_2$  assumptions, whereas the model for  $(\text{Th,Pu})\text{O}_2$  has been developed on assumptions made in an attempt to replicate the BDL-422 behaviour. The limited experimental basis on which these models have been developed is a concern; it is uncertain how applicable they will be to differing initial fuel compositions. It is also uncertain if the modelling assumptions made to account for the high gas release is applicable to all temperature ranges, and what the effects of BDL-422's less than ideal grain structures are. However, by implementing the model in COMSOL these models are easily updated.

The last modelling concern listed above is MPM-FAST's use of the AECL fission gas parameters for the internal element pressure calculation. As mentioned above these parameters have been generated for fission gas that is the result of the fission of unenriched  $\text{UO}_2$  fuel. The Xe to Kr ratio of the fission gas from a Th-based fuel may differ enough to question the validity of using this model. The framework has been established in MPM-FAST to switch to the FRAPCON/FRAPTRAN gas mixture model. The advantage of the FRAPCON/FRAPTRAN formulation is that it deals with detailed gas mixtures; using this model will enable an analysis on the changes in Xe to Kr ratio due, to the use of Th-based fuel and determine if there is substantial effect on the thermal conductivity in the gas gap.

## 7 Summary and Conclusions

MPM-FAST has been developed to provide a modelling tool capable of examining the irradiation behaviour of Th-based mixed oxide fuels under normal operating conditions. Similar to previous work on the development of mixed oxide models, MPM-FAST was developed as an extension of the UO<sub>2</sub> fuel performance model FAST. The highly coupled and complex system of ODEs and PDEs that enable the calculation of fuel behaviour has been implemented using the finite element analysis software COMSOL Multiphysics®.

The (Th,U)O<sub>2</sub> model within MPM-FAST has undergone a proof of concept validation exercise. Using manufacturing data and irradiation histories from the DME-221 irradiation experiment, MPM-FAST was used to simulate the irradiation conditions the fuel experienced, with the calculated results compared to the post irradiation examination measurements. Two versions of the model were examined using different thermal conductivity correlations of (Th,U)O<sub>2</sub>. The comparison of the model results demonstrated that one case was in good agreement with the FGR measurements from DME-221 and because of this, the version based on the Belle and Berman thermal conductivity model should be used at this time. Comparison between the end of life sheath strain measurements and the model results demonstrated that both versions of the model over predicted the strain but tended to be in better agreement if the fuel experienced lower

overall temperature during its irradiation, while still being an improvement over using the  $\text{UO}_2$  model as a test case.

The  $(\text{Th,Pu})\text{O}_2$  model was used to calculate the irradiation behaviour of the BDL-422 experiment to determine if it is physically representative. Unlike other irradiation experiments on  $(\text{Th,Pu})\text{O}_2$ , BDL-422 achieved higher linear powers and experienced greater fission gas release. MPM-FAST is the first fuel performance model that is capable of replicating this fission gas release behaviour, as well as the low power fission gas release behaviour. MPM-FAST results for end-of-life sheath strain are also in good agreement with the BDL-422 data when the fuel temperature does not exceed 1600 K.

Preliminary models of the SCWR fuel design were attempted using the  $(\text{Th,Pu})\text{O}_2$  model in MPM-FAST. It demonstrated that the SCWR fuel will achieve temperatures above the limitations of the current models for the thermal physical behaviours and indicate that MPM-FAST is not suitable to approximate the deformation behaviour of the SCWR fuel at this time. It is possible to use MPM-FAST to approximate the volume of fission gas release, and it can be used to generate information about the size of plenum required in the SCWR fuel elements.

For the base cases that are representative of the normal operating condition in Canadian PHWR fuel, the Th-based fuel models predict lower fission

gas release and end of life strain for Th-based fuel. The Th-based fuel performance models in MPM-FAST can be seen as a good platform to aid in the design of irradiation experiments and test out new thermal physical property models within the context of fuel performance modelling.

## 8 Recommendations

Presented below are recommendations to be considered as future work that are feasible with the current state of knowledge. It is categorized into two types of work: 1) improving the current Th-based models, 2) adding further functionality to MPM-FAST.

### *Improving Th-based models*

1. Further examination may be required of the FGR of the (Th,U)O<sub>2</sub> Bakker *et al.* [28] thermal conductivity model. The simulation of DME-211 using this version of the model over predicted the fission gas release of higher powered cases from DME-221 indicating that the current fission gas diffusion assumptions do not match this temperature behaviour and may need to be re-examined.
2. The assumptions made in the flux depression of Th-based fuel in MPM-FAST can be improved. It is recommended that the examples from literature that demonstrate that implementing a 1-D radial representation of the fuel pellet to find neutron capture, can calculate the flux shape within a pellet be replicated [24], [35]. Aside from implementing these methods for the Th-based fuel, it can also be applied to UO<sub>2</sub> fuel as well



similar to how TRANSURANUS calculates the flux shape in a pellet [16], [32]. This is a more fundamental and flexible approach than relying on the look up table method that was inherited from ELESTRES.

3. Further validation cases can be attempted for both the (Th,U)O<sub>2</sub> and (Th,Pu)O<sub>2</sub> models. One of the concerns with the (Th,U)O<sub>2</sub> and (Th,Pu)O<sub>2</sub> models are the limited data on which the FG diffusion assumptions are made. Especially the (Th,Pu)O<sub>2</sub> model which is based solely on the behaviour of BDL-422 fuel. The work by Long *et al.* for (Th,U)O<sub>2</sub> [24], as well as the work by Björk *et al.* [34], [35] and Boer *et al.* [33] provide enough construction and irradiation data that these cases may be simulated. This would determine if the FG diffusion assumptions are applicable to a wider variety of fuel compositions, and could provide a means of determining if further study of this behaviour is required.

*Adding further functionality to MPM-FAST*

4. (U,Pu)O<sub>2</sub> Mixed OXide (MOX) fuel has been studied more thoroughly than Th-based fuel as it has been irradiated in commercial reactors. Similar methods to develop the Th-based fuel models presented in this

work can be applied to create an equivalent model in MPM-FAST for MOX fuel.

## 9 References

- [1] “Electric power consumption (kWh per capita) | Data.” [Online]. Available: <http://data.worldbank.org/indicator/EG.USE.ELEC.KH.PC?end=2013&locations=CA&start=1960&view=chart&year=2013>. [Accessed: 09-Dec-2016].
  
- [2] “CANDU Fuel bundle picture.” Apr-2011.
  
- [3] “GIF Portal - Home - Public.” [Online]. Available: [https://www.gen-4.org/gif/jcms/c\\_9260/public](https://www.gen-4.org/gif/jcms/c_9260/public). [Accessed: 07-Apr-2016].
  
- [4] A. Colton and J. Pencer, “A solid moderator physics assessment for the canadian scwr,” *CNL Nucl. Rev.*, pp. 1–8, Jul. 2016.
  
- [5] M. Yetisir, W. Diamond, L. K. H. Leung, D. Martin, and R. Duffer, “Conceptual Mechanical Design for a Pressure-Tube Type Supercritical Water-Cooled Reactor,” presented at the 5th International Symposium on Super Critical Water Cooled Reactors, Vancouver, British Columbia, Canada, 2011.
  
- [6] M. H. McDonald *et al.*, “Pre-Conceptual Fuel Design Concepts for Canadian Super Critical Water-Cooled Reactor,” presented at the 5th International Symposium on Super Critical Water Cooled Reactors, Vancouver, British Columbia, Canada, 2011.
  
- [7] J. Pencer, M. Edwards, and N. Onder, “AXIAL AND RADIAL GRADED ENRICHMENT OPTIONS FOR THE CANADIAN SCWR,” in *CCSC-2012*, Xi’an, China, 2012.
  
- [8] A. Prudil, “FAST: A Fuel And Sheath Modeling Tool for CANDU Reactor Fuel,” Doctoral, Royal Military College of Canada, Kingston, Ontario, Canada, 2013.

- [9] K. Shaheen, "A Mechanistic Code for Intact and Defective Nuclear Fuel Element Performance," Doctoral, Royal Military College of Canada, Kingston, Ontario, Canada, 2011.
- [10] D. Morgan, "A Thermomechanical Model of CANDU Fuel," Masters, Royal Military College of Canada, Kingston, Ontario, Canada, 2007.
- [11] G. G. Chassie, K. S. Sim, B. Wong, and G. Papayiannis, "ELESTRES code Upgrades," presented at the 9th International Conference on CANDU Fuel, Bellville, Ontario, Canada, 2005.
- [12] A. F. Williams, "The ELOCA Fuel Modelling Code: Past, Present and Future," presented at the 9th International Conference on CANDU Fuel, Bellville, Ontario, Canada, 2005.
- [13] K. J. Geelhood, W. G. Luscher, and C. E. Beyer, "FRAPCON-3.4: A Computer Code for the Calculation of Steady-State, Thermal-Mechanical Behavior of Oxide Fuel Rods for High Burnup (NUREG/CR-7022, Volume 1, PNNL-19418, Volume 1)," PNNL, (NUREG/CR-7022, Volume 1, PNNL-19418, Volume 1), 2011.
- [14] W. G. Luscher and K. J. Geelhood, "Material Property Correlations: Comparisons between FRAPCON-3.4, FRAPTRAN 1.4, and MATPRO," PNNL, NUREG/CR-7024, Mar. 2011.
- [15] W. Lyon, R. Montgomery, A. Zangari, D. Sunderland, Y. Rashid, and R. Dunham, "Fuel Performance Analysis Capability in FALCON," EPRI, EPRI, 000000000001002866, Dec. 2002.
- [16] K. Lassmann, "TRANSURANUS: a fuel rod analysis code ready for use," *J. Nucl. Mater.*, vol. 188, pp. 295–302, Jun. 1992.
- [17] B. Baurens, J. Sercombe, C. Riglet-Martial, L. Desgranges, L. Trotignon, and P. Maugis, "3D thermo-chemical–mechanical simulation of power

- ramps with ALCYONE fuel code,” *J. Nucl. Mater.*, vol. 452, no. 1–3, pp. 578–594, Sep. 2014.
- [18] C. Newman, G. Hansen, and D. Gaston, “Three dimensional coupled simulation of thermomechanics, heat, and oxygen diffusion in nuclear fuel rods,” *J. Nucl. Mater.*, vol. 392, no. 1, pp. 6–15, Jul. 2009.
- [19] S. J. Livingstone and M. R. Floyd, “Thoria Irradiation and Post-Irradiation Examination Experience at AECL,” presented at the 12th International Conference on CANDU Fuel, 2013.
- [20] I. J. Hastings and M. J. F. Notley, “Fission Gas Release From Thori-Based Fuels: Comparison With Model Predictions,” Montreal, Quebec, Canada, Conference Proceedings from the Canadian Nuclear Society’s 1st Annual Conference AECL-6983, Jun. 1980.
- [21] J. Belle and R. M. Berman, “Thorium dioxide: properties and nuclear applications,” USDOE Assistant Secretary for Nuclear Energy, DOE/NE--0060, 1984.
- [22] I. Goldberg, L. A. Waldman, J. F. Giovengo, and W. R. Campbell, “Fission Gas Release and Grain Growth in ThO<sub>2</sub>-UO<sub>2</sub> Fuel Irradiated at High Temperature,” Bettis Atomic Lab., Pittsburgh, PA, Technical Report, Addendum WAPDTM-1350, Jul. 1979.
- [23] E. P. Loewen, R. D. Wilson, J. K. Hohorst, and A. S. Kumar, “Preliminary FRAPCON-3Th Steady-State Fuel Analysis of ThO<sub>2</sub> and UO<sub>2</sub> Fuel Mixtures,” *Nucl. Technol.*, vol. 136, no. 3, pp. 261–277, Dec. 2001.
- [24] Y. Long, Y. Yuan, M. S. Kazimi, R. G. Ballinger, and E. E. Pilat, “A Fission Gas Release Model for High-Burnup LWR ThO<sub>2</sub>-UO<sub>2</sub> Fuel,” *Nucl. Technol.*, vol. 138, no. 3, pp. 260–272, Jun. 2002.

- [25] C. B. Lee, Y. S. Yang, Y. M. Kim, D. H. Kim, and Y. H. Jung, "Irradiation Behavior of Thoria-Urania Fuel in a PWR," *Nucl. Technol.*, vol. 147, no. 1, pp. 140–148, Jul. 2004.
- [26] R. Calabrese, F. Vettrano, and T. Tverberg, "Under irradiation issues of the CSZ-based inert matrix fuels from IFA-652 Halden experiment," *Prog. Nucl. Energy*, vol. 52, no. 4, pp. 352–358, May 2010.
- [27] Y. Long *et al.*, "The Behavior of ThO<sub>2</sub>-Based Fuel Rods During Normal Operation and Transient Events in LWRs," *Nucl. Technol.*, vol. 147, no. 1, pp. 120–139, Jul. 2004.
- [28] K. Bakker, E. H. P. Cordfunke, R. J. M. Konings, and R. P. C. Schram, "Critical evaluation of the thermal properties of ThO<sub>2</sub> and Th<sub>1-y</sub>U<sub>y</sub>O<sub>2</sub> and a survey of the literature data on Th<sub>1-y</sub>Pu<sub>y</sub>O<sub>2</sub>," *J. Nucl. Mater.*, vol. 250, no. 1, pp. 1–12, Nov. 1997.
- [29] IAEA, "Thermophysical Properties Database of Materials for Light Water Reactors and Heavy Water Reactors," 2006.
- [30] D. Das and S. R. Bharadwaj, Eds., *Thoria-based Nuclear Fuels: Thermophysical and Thermodynamic Properties, Fabrication, Reprocessing, and Waste Management*. London: Springer, 2013.
- [31] C. Cozzo, D. Staicu, J. Somers, A. Fernandez, and R. J. M. Konings, "Thermal diffusivity and conductivity of thorium–plutonium mixed oxides," *J. Nucl. Mater.*, vol. 416, no. 1–2, pp. 135–141, Sep. 2011.
- [32] M. Seidl, P. Van Uffelen, A. Schubert, S. Brèmier, and P. Poeml, "TRANSURANUS Burn-up Extension for (Th,Pu)O<sub>2</sub> Type Fuel In light Water Reactors," presented at the Top Fuel 2015, Zurich, Switzerland, 2015, pp. 20–29.

- [33] B. Boer *et al.*, “Irradiation performance of (Th,Pu)O<sub>2</sub> fuel under Pressurized Water Reactor conditions,” *J. Nucl. Mater.*, vol. 471, pp. 97–109, Apr. 2016.
- [34] K. Insulander Björk and L. Kekkonen, “Thermal–mechanical performance modeling of thorium–plutonium oxide fuel and comparison with on-line irradiation data,” *J. Nucl. Mater.*, vol. 467, Part 2, pp. 876–885, Dec. 2015.
- [35] K. I. Björk, “Thorium Fuels for Light Water Reactors Steps towards commercialization,” Chalmers Reproservice, Göteborg, Sweden, 2015.
- [36] A. Prudil, B. J. Lewis, P. K. Chan, and J. J. Baschuk, “Development and testing of the FAST fuel performance code: Normal operating conditions (Part 1),” *Nucl. Eng. Des.*, vol. 282, pp. 158–168, Feb. 2015.
- [37] A. Prudil, B. J. Lewis, P. K. Chan, J. J. Baschuk, and D. Wowk, “Development and testing of the FAST fuel performance code: Transient conditions (Part 2),” *Nucl. Eng. Des.*, vol. 282, pp. 169–177, Feb. 2015.
- [38] S. Corbett, M. R. Floyd, S. J. Livingstone, H. Hamilton, and N. F. Harrison, “DME-221 Thoria Fuel: Fabrication, Irradiation Testing, and Post-Irradiation Examination,” presented at the 12th International Conference on CANDU Fuel, Kingston, Ontario, Canada, 2013.
- [39] M. Karam, F. C. Dimayauga, and J. Montin, “Fission Gas Release of (Th, Pu)O<sub>2</sub> CANDU Fuel,” in *Proceedings of the 10th International Conference on CANDU Fuel*, Ottawa, Ontario, Canada, 2008.
- [40] M. Karam, F. C. Dimayauga, and J. Montin, “Post-Irradiation Examination of CANDU Fuel Bundles Fuelled With (Th,Pu)O<sub>2</sub>,” in *Proceedings of the 11th International Conference on CANDU Fuel*, Niagara Falls, Ontario, Canada, 2010.
- [41] “Wiley: Finite Element Modeling for Stress Analysis - Robert D. Cook.” [Online]. Available:

<http://www.wiley.com/WileyCDA/WileyTitle/productCd-0471107743.html>.  
[Accessed: 27-Feb-2017].

- [42] H. E. Sills, "ELOCA: Fuel element behaviour during high-temperature transients," Atomic Energy of Canada Limited, Chalk River Nuclear Laboratories, AECL-6357.
- [43] V. F. Urbanic and T. R. Heidrick, "High-temperature oxidation of zircaloy-2 and zircaloy-4 in steam," *J. Nucl. Mater.*, vol. 75, no. 2, pp. 251–261, Aug. 1978.
- [44] "310 - Rolled Alloys, Inc." [Online]. Available: <http://www.rolledalloys.ca/alloys/stainless-steels/310/en/>. [Accessed: 17-Oct-2016].
- [45] C. R. Brooks and E. E. Stansbury, "The specific heat of zircaloy-2 from 50 to 700/dg C," *J. Nucl. Mater.*, vol. 18, no. 2, pp. 233–234, Feb. 1966.
- [46] "eFunda: Properties of Stainless Steel AISI Type 310." [Online]. Available: [http://www.efunda.com/materials/alloys/stainless\\_steels/show\\_stainless.cfm?ID=AISI\\_Type\\_310&show\\_prop=all&Page\\_Title=AISI%20Type%20310](http://www.efunda.com/materials/alloys/stainless_steels/show_stainless.cfm?ID=AISI_Type_310&show_prop=all&Page_Title=AISI%20Type%20310). [Accessed: 24-Feb-2017].
- [47] D. L. Hagrman and G. A. (comps ) Reymann, "Matpro-Version 11: A Handbook of Materials Properties for Use in the Analysis of Light Water Reactor Fuel Rod Behavior," Idaho National Engineering Lab., Idaho Falls (USA), NUREG/CR-0497; TREE-1280, Feb. 1979.
- [48] F. . Campbell, L. R. Bourque, R. DesHaies, H. Sills, and M. J. F. Notley, "In-Reactor Measurements of Fuel-to-Sheath Heat Transfer Coefficients between UO<sub>2</sub> and Stainless Steel," Atomic Energy of Canada Limited, Chalk River, Ontario, AECL-5400, May 1977.



- [49] H. E. Sills and I. D. Peggs, "Fuel to Sheath Heat Transfer Coefficient," Atomic Energy of Canada Limited, Chalk River Nuclear Laboratories.
- [50] C. E. Beyer, C. R. Hann, D. D. Lanning, F. E. Panisko, and L. J. Parchen, "GAPCON-THERMAL-2: A computer program for calculating the thermal behavior of an oxide fuel rod," *Other Information: Orig. Receipt Date: 30-JUN-76*, 01-Nov-1975. [Online]. Available: <https://digital.library.unt.edu/ark:/67531/metadc872628/m1/135/>. [Accessed: 25-Feb-2017].
- [51] J. E. Suich and H. C. Honeck, "The Hammer System: Heterogeneous Analysis by Multigroup Methods of Exponentials and Reactors.," Du Pont de Nemours (E. I.) and Co., Aiken, S. C. Savannah River Lab., DP--1064, Jan. 1967.
- [52] R. Konings, *Comprehensive Nuclear Materials*. Elsevier, 2012.
- [53] IAEA, "Thermophysical Properties of Materials for Water Cooled Reactors," 1997.
- [54] P. G. Lucuta, H. Matzke, and I. J. Hastings, "A pragmatic approach to modelling thermal conductivity of irradiated UO<sub>2</sub> fuel: Review and recommendations," *J. Nucl. Mater.*, vol. 232, no. 2–3, pp. 166–180, Sep. 1996.
- [55] A. H. Booth, "A Method of Calculating Fission Gas Release from UO<sub>2</sub> Fuel and its Application to the X-2-f Loop Test." Atomic Energy of Canada Limited - 469, Sep-1957.
- [56] G. V. Kidson, "A generalized analysis of the cumulative diffusional release of fission product gases from an 'Equivalent Sphere' of UO<sub>2</sub>," *J. Nucl. Mater.*, vol. 88, no. 2, pp. 299–308, Feb. 1980.

- [57] J. E. McCauley, "Observations on the Irradiation Behavior of a Zircaloy-4 Clad Rod Containing Low Density ThO<sub>2</sub> - 5.3 w/o UO<sub>2</sub> Pellets (LWBR Development Program)," Bettis Atomic Lab., Pittsburgh, PA, Technical Report WAPD-TM-664, Dec. 1969.
- [58] F. A. Nichols, "Further Comments on the Theory of Grain Growth in Porous Compacts," *J. Am. Ceram. Soc.*, vol. 51, no. 8, pp. 468–468, Aug. 1968.
- [59] O. V. Khoruzhii, S. Y. Kourtchatov, and V. V. Likhanskii, "New model of equiaxed grain growth in irradiated UO<sub>2</sub>," *J. Nucl. Mater.*, vol. 265, no. 1–2, pp. 112–116, Feb. 1999.
- [60] J. A. Turnbull, C. A. Friskney, J. R. Findlay, F. A. Johnson, and A. J. Walter, "The diffusion coefficients of gaseous and volatile species during the irradiation of uranium dioxide," *J. Nucl. Mater.*, vol. 107, no. 2–3, pp. 168–184, Jun. 1982.
- [61] C. A. Friskney, J. A. Turnbull, F. A. Johnson, A. J. Walter, and J. R. Findlay, "The characteristics of fission gas release from monocrystalline uranium dioxide during irradiation," *J. Nucl. Mater.*, vol. 68, no. 2, pp. 186–192, Oct. 1977.
- [62] J. A. Turnbull, C. A. Friskney, F. A. Johnson, A. J. Walter, and J. R. Findlay, "The release of radioactive gases from uranium dioxide during irradiation," *J. Nucl. Mater.*, vol. 67, no. 3, pp. 301–306, Aug. 1977.
- [63] R. J. White and M. O. Tucker, "A new fission-gas release model," *J. Nucl. Mater.*, vol. 118, no. 1, pp. 1–38, Aug. 1983.
- [64] H. Matzke, "Diffusion in Ceramic Oxide Systems," in *Proceedings of a symposium on fission-product behavior in ceramic oxide fuel held at the 87th Annual Meeting of the American Ceramic Society, Cincinnati, Ohio, 1985*, vol. 17.

- [65] H. Kim *et al.*, “Xenon Diffusivity in Thoria-Urania Fuel,” *Nucl. Technol.*, vol. 147, no. 1, pp. 149–156, Jul. 2004.
- [66] M. Maldován, A. Denis, and R. Piotrkowski, “Simulation of isothermal fission gas release: An analytical solution,” *Nucl. Eng. Des.*, vol. 187, no. 3, pp. 327–337, Mar. 1999.
- [67] I. J. Hastings and L. E. Evans, “Densification Algorithm for Irradiated UO<sub>2</sub> Fuel,” *J. Am. Ceram. Soc.*, vol. 62, no. 3–4, pp. 217–218, Mar. 1979.
- [68] D. R. Olander, “Fundamental Aspects of Nuclear Reactor Fuel Elements,” California Univ., Berkeley (USA). Dept. of Nuclear Engineering, TID-26711-P1, Jan. 1976.
- [69] H. Matzke, “Hertzian indentation of thorium dioxide, ThO<sub>2</sub>,” *J. Mater. Sci.*, vol. 15, no. 3, pp. 739–746, 1980.
- [70] M. R. Floyd, “Advanced Fuel Cycle Development at Chalk River Laboratories,” in *Proceedings of the International Conference on the Future of Heavy Water Reactors*, Ottawa, Ontario, Canada, 2011.
- [71] M. R. Floyd *et al.*, “PROGRESS IN THE DEVELOPMENT OF THORIA FUEL SCIENCE & TECHNOLOGY,” presented at the 13th International Conference on CANDU Fuel, Kingston, Ontario, Canada, 2016.
- [72] M. R. Floyd, “Normalization of powerhistories from NRU fuel,” 16-Mar-2017.
- [73] M. H. A. Piro, “OPTIMA: A General Non-linear Least Squares Solver User Manual,” User Manual, Apr. 2014.

## Appendix A: Material properties for UO<sub>2</sub> accessible in MPM-FAST

The materials models that are available in MPM-FAST to calculate UO<sub>2</sub> irradiation behaviour are presented below. For the full details of this model please seek out Prudil's thesis [8].

### Heat Capacity

Heat Capacity for UO<sub>2</sub> fuel using a correlation developed by Fink for a temperature range between 298.15 – 3120 K is given in equation (126).

$$C_p = C_1 \left(\frac{\theta}{T}\right) \exp\left(\frac{\theta}{T}\right) \left(\exp\left(\frac{\theta}{T}\right) - 1\right)^{-2} + 2C_2 T + C_3 E_a \exp\left(\frac{-E_a}{T}\right) T^{-2} \quad (126)$$

Here,  $\theta$  is the Einstein temperature of UO<sub>2</sub>,  $E_a$  is the electron activation energy of UO<sub>2</sub> divided by the Boltzmann constant, and the parameters  $C_{1-3}$  are fitting coefficients. All of these values are given in Table 34 below.

Table 34: Parameters required to calculate the Heat capacity of UO<sub>2</sub> using the Fink correlation.

Parameter	Value	Units
$C_1$	302.27	J kg <sup>-1</sup> K <sup>-1</sup>
$C_2$	8.463x10 <sup>-3</sup>	J kg <sup>-1</sup> K <sup>-2</sup>
$C_3$	8.741x10 <sup>7</sup>	J kg <sup>-1</sup>
$\theta$	548.68	K
$E_a$	18531.7	K

## Thermal Conductivity

The unirradiated thermal conductivity models available for UO<sub>2</sub> are Harding's as discussed in context of equation (74) in Chapter 4 presented in equation (127).

$$k_{0,HM}(T) = \frac{1}{0.0375 + 2.165 \times 10^{-4}T} + \frac{2.165 \times 10^{-4}}{T^2} \exp\left(-\frac{16361}{T}\right) \quad (127)$$

The second UO<sub>2</sub> model available in MPM-FAST is the model used within ELESTRES and ELOCA codes and is given in equation (125) [12]

$$k_{ELESTRES} = k_{0,AECL}(T) \kappa_{1d}(\beta_p, T) \kappa_{1p}(\beta_p, T) \kappa_{2p}(p, T) \quad (128)$$

Here  $k_{0,AECL}$  is the unirradiated thermal conductivity of fully dense UO<sub>2</sub>,  $\kappa_{1d}(\beta_p, T)$  and  $\kappa_{1p}(\beta_p, T)$  are given in (75) and (76) respectively and  $\kappa_{2p}(p, T)$  is a modified porosity correction factor given in equation (129).

$$\kappa_{2p} = 1.0 - (2.05 - 5.0 \times 10^{-4}T)p \quad (129)$$

$k_{0,AECL}(T)$  is similar to  $k_{0,HM}(T)$ ; however it was altered to match thermal conductivity tests in natural enrichment UO<sub>2</sub> fuel, and accounts for radiation damage that does not anneal at low temperatures by introducing a low temperature cut-off ( $T_{CO} = \max(T, 727 \text{ K})$ ), thus rendering  $\kappa_4$  from the Lucuta

model unnecessary.  $k_{0,AECL}(T)$  is presented in equation (130), giving the thermal conductivity in units of  $\text{W m}^{-1} \text{K}^{-1}$ .

$$k_{0,AECL}(T) = \frac{1}{0.030771 + 2.25 \times 10^{-4} T_{co}} + \frac{9.28 \times 10^9}{T_{co}^2} \exp\left(-\frac{18295.09}{T_{co}}\right) \quad (130)$$

The AECL thermal conductivity model is the default model used in MPM-FAST for  $\text{UO}_2$  fuel. As it takes editing a portion of the model to switch from one method to the next and not the input parameters, the details of the third method (which is the one outlined in MATPRO) are not included.

### **Fission Gas Production**

For  $\text{UO}_2$  fuel the fission gas yield  $y_f = 0.251$ , with the gas being composed of approximately 90% xenon and 10% krypton [8], [10]

### **Elastic Deformation**

The material properties of  $\text{UO}_2$  required to fill the stiffness matrix,  $C_{\text{elastic}}$  in equation (3),  $E_{\text{UO}_2}$  and  $\nu_{\text{UO}_2}$  are given in equations (131) and (132) respectively [14].

$$E_{\text{UO}_2} = 2.33 \times 10^{11} (1 - 2.752p)(1 - 1.0915 \times 10^{-4}T) \quad (131)$$

$$\nu_{\text{UO}_2} = 0.316 \quad (132)$$

In equation (131),  $p$  is the porosity from equation (78), and  $T$  is the temperature of the fuel, equation (132) has only been validated to 1600 K. CANDU  $\text{UO}_2$  fuel

centerline temperatures regularly exceed this value however it is currently the only model available.

## Deformation

The thermal strain correlation used in MPM-FAST for UO<sub>2</sub>, is given in equation (133) [14].

$$\varepsilon_{thrm} = -3.0 \times 10^{-3} + 1.0 \times 10^{-5}T + 4 \times 10^{-2} \exp\left(\frac{-5.0 \times 10^3}{T}\right) \quad (133)$$

(133) has been validated up to UO<sub>2</sub> melting temperature, with the reference temperature of  $\varepsilon_{thrm} = 0$  set to 300 K.

Other sources of strain considered in the UO<sub>2</sub> model within MPM-FAST are fuel densification due to irradiation and the fission product swelling. Similar correlations for Th-based ceramic pellets have not been found in the literature, and currently the UO<sub>2</sub> correlations are used in (Th,U)O<sub>2</sub> and (Th,Pu)O<sub>2</sub> models.

Fuel densification is caused by continued sintering of UO<sub>2</sub> after it is within the reactor, this leads to a decrease in volume. The densification strain,  $\varepsilon_{vol,dens}$ , is given in equation (134).

$$\varepsilon_{vol,dens} = \frac{\Delta V_{dens}}{V_0} = \frac{-p_0 F_{PoreR}}{1-p_0(1-F_{PoreR})} \quad (134)$$

Here  $p_0$  is the initial porosity of the fuel which is a model input parameter, and  $F_{PoreR}$  is the fraction of the porosity removed from the fuel. The model used in MPM-FAST was adapted from an empirical correlation for  $F_{PoreR}$  at constant power conditions given in equation (135).

$$F_{PoreR} = 0.6 - 0.6\exp(-b_d T^3(1 - \exp(-c_d Bu))) \quad (135)$$

Here  $b_d$  and  $c_d$  are empirical constants equal to  $8.67 \times 10^{-10} \text{ K}^{-3}$  and  $2.867 \times 10^{-2} \text{ kg MWh}^{-1}$ ,  $T$  is the local fuel temperature in Kelvin and  $Bu$  is the burnup of the fuel in  $\text{MW h kgU}^{-1}$ . The model was developed by examining CANDU fuel with up to 7% initial porosity. The model predicts an upper limit to the pore fraction that can be removed to be 60%. In the form presented in (135) the model could allow for the non-physical growth of porosity if the fuel temperature dropped. This is prevented within MPM-FAST by implementing the pore reduction model as a rate given in equation (136).

$$\frac{dF_{PoreR}}{dt} = c_d(0.6 - F_{PoreR}) \max\left(\ln\left(1 - \frac{F_{PoreR}}{0.6}\right) + b_d T^3, 0\right) \frac{dBu}{dt} \quad (136)$$

Fission product swelling of the fuel is considered to have two sources: the first is the inclusion of the solid fission products within the fuel matrix; the second is the strain due to the gaseous fission products migrating to the grain boundaries. MPM-FAST uses the volumetric strain caused by solid fission products,  $\epsilon_{vol,SFP}$ , given in equation (137) [68].



$$\varepsilon_{vol,SFP} = \frac{0.0032}{225} Bu \quad (137)$$

Here  $Bu$  is burnup in units of MWh kgHE<sup>-1</sup>.

MPM-FAST uses a model presented in MATPRO to account for the swelling caused by the presence of fission gas bubbles on the grain boundaries,  $\varepsilon_{vol,GFP}$ , and is given in equation (138) [14].

$$\frac{d(\varepsilon_{vol,GFP})}{dt} = 8.8 \times 10^{-56} (2800 - T)^{11.73} \exp(-0.0162(2800 - T) - 8.0 \times 10^{-27} Bu_f) \frac{dBu_f}{dt} \quad (138)$$

Here  $Bu_f$  is the fuel burnup measured by number of fissions per cubic meter. The conversion of  $Bu$  to  $Bu_f$  is found using the unit conversion shown in equation (139).

$$Bu_f = Bu \left( \frac{3600 \times 10^6 \rho_u}{E_f} \right) \quad (139)$$

The burnup rate is obtained by taking the partial derivative of (136), as shown in equation (140).

$$\frac{\delta Bu_f}{\delta t} = \frac{\delta Bu}{\delta t} \left( \frac{3600 \times 10^6 \rho_u}{E_f} \right) \quad (140)$$

In MATPRO upper and lower temperature bounds of 2000 and 1000 K are applied to this correlation, based on a rough estimate of when fission gas bubbles

will form on the grain boundaries and if they are collecting the released fission gas. In MPM-FAST the high temperature cut off is replaced by a dependence on the grain boundary saturation conditions outlined in equation (118) [8].

As discussed in Chapter 4, special consideration is given to the elastic deformation of the pellet when a crack is believed to have developed in the pellet. The model assumes that the pellet is no longer able to sustain strains in the hoop direction ( $\varepsilon_{\theta,elastic}=0$ ) within that subsection of the pellet. This change in the elastic deformation model is initiated when the fracture strength of  $UO_2$  is exceeded. The MATPRO recommended correlation for the fracture strength of  $UO_2$ ,  $\sigma_F$ , is given in equation (141) with units of Pa [14].

$$\sigma_F = 1.7 \times 10^8 \sqrt{(1 - 2.62p)} (10^6 g_r)^{0.047} \exp\left(-\frac{191.2}{T}\right) \quad (141)$$

The initiation of the cracked elastic deformation model is limited to when the pellet temperature is below 1000 K. Any deformation that occurs above this temperature is considered to be plastic deformation in the pellet.

## Appendix B: Grain Growth Kinetics Comparison

As mentioned in Chapter 4, the ceramic  $\text{UO}_2$  grain growth model applied to the  $(\text{Th,Pu})\text{O}_2$  fuel behaviour. Karam *et al.* report that the average grain diameter at the center of the fuel pellets from OE ADC, ADE, and ADF was approximately 10  $\mu\text{m}$ . These three elements were simulated using the grain growth model for Th-based fuel proposed by Goldberg *et al* (see equation (90))[22], and the  $\text{UO}_2$  grain growth model by Khoruzii *et al.* [59]. The calculated average grain diameter for these three elements are shown in Figure 30 below. All three results using the Khoruzii model are in better agreement with the PIE measurements.

Of the three power histories ADC experiences the highest linear power (67  $\text{kW m}^{-1}$ ) while ADF's maximum linear power is significantly lower (52  $\text{kW m}^{-1}$ ). This indicates that the temperature at which the Goldberg model begins to generate appreciable grain growth is higher than those achieved in the model of the element from ADF, and also demonstrates that it is not physically representative of BDL-422 fuel since the PIE results show there is grain growth. In the case of the modelled element from ADC, the grain growth from the Goldberg model exceeds the PIE results ( $\sim 32 \mu\text{m}$  compared to  $\sim 10 \mu\text{m}$ ). The grain growth model developed for  $\text{UO}_2$  is currently recommended for the use of modelling  $(\text{Th,Pu})\text{O}_2$ . It is unknown if the growth rate in equation (92) is entirely

accurate, however the end result is more representative than the Goldberg model. Additionally from the results of modelling ADC, the inclusion of the  $g_m$  and  $g_{ir}$  are apparently beneficial by limiting grain growth and lead this model to be more physically representative.

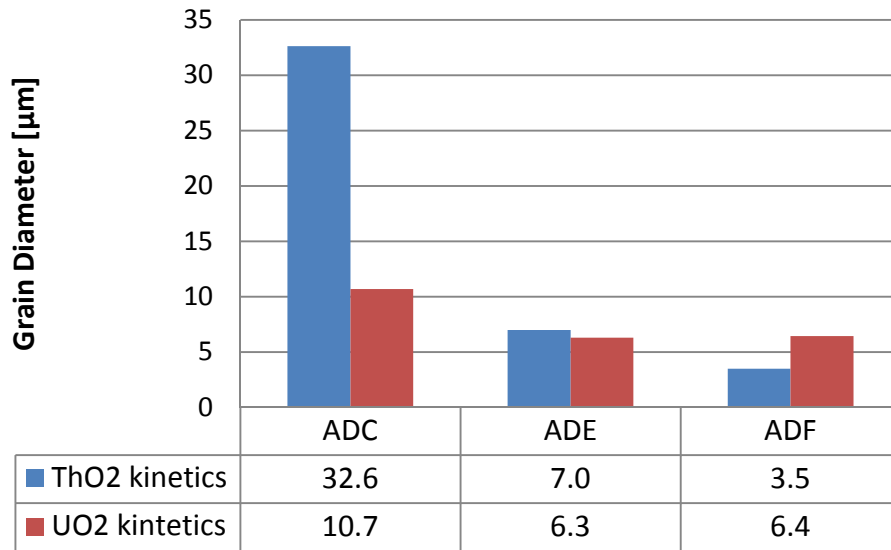


Figure 30: A comparison of the modeled centreline grain diameters, using two different grain growth models.

## Appendix C: Fission Gas Diffusion

The weighting factors presented in equation (112) were found by fitting the FGR model to the PIE results from BDL-422, while testing various weighting factors within the single fission gas diffusion coefficient. This was done by using non-linear, least squares optimization software. The optimization tool used was OPTIMA, a generalized standalone least squares software developed by M. Piro [73]. The method of least squares reduces to minimizing an objective function given in equation (139).

$$S(x, \beta) = \frac{1}{2} \sum_{i=1}^m (r_i(x_i, \beta))^2 \quad (139)$$

Here  $r_i(x_i, \beta)$  is the residual of the  $i$ th term given by equation (140).

$$r_i(x_i, \beta) = q_i - f(x_i, \beta) \quad (140)$$

Here  $x_i$  and  $q_i$  are the  $m$  independent and dependent variables of the empirical data, respectively,  $\beta$  is the vector of the unknown parameters,  $f$  is the functional model to be fitted and  $S(x, \beta)$  is the objective function to be minimized.

OPTIMA uses iterative Levenberg-Marquardt algorithms to minimize  $S(x, \beta)$  for non-linear functions. The optimization problem is required to meet the criteria that the number of empirical data measurements ( $q$  through  $q_m$ ) be greater than the number of components in the vector of unknown components  $\beta$ . Additional

requirements to enable the software to work are; two sets of initial estimates of  $\beta$  and resulting  $f(x_i, \beta)$  to initiate the iterative cycle, and providing two parameters that adjust the step size and behaviour of the Levenberg-Marquardt algorithms to reduce the number of iterations to converge.

In the case of fitting the FGR behaviour of BDL-422, our dependent variable data ( $y_i$ ) are the end-of-life FG measurements from BDL-422,  $\beta$  are the values of the weighting factors ( $w_{irr}$ , and  $w_{athrm}$  from chapter 5), and  $f(x_i, \beta)$  is the calculated FGR provided by MPM-FAST. As discussed in Chapter 6, the FGR dataset was segmented into: FGR from IE that experienced maximum fuel temperatures less 1700 K, and FGR from the OE of ADA, ADC, and ADD. The dataset of IE FGR being used to determine the weighting factors for  $D_{irr}$  and  $D_{athrm}$ , while the OE of ADA, ADC, and ADD data was used to find the weighting factor for  $D_{thrm}$ . Table 35 below presents the values of  $w_{irr}$ , and  $w_{athrm}$  and the MPM-FAST FGR model results during iterative process for the IE un-normalized power histories.

Table 35: IE FGR fitting for un-normalized BDL-422 power histories.

Iteration	w_irr	w_athrm	ADA	ADC	ADD	ADE	ADF
1	1	1	9.9	0	8.7	0.002	3.19
2	0.1	0.1	0.01	0	0	0	0
3	0.104	0.104	0.02	0	0	0	0
4	0.109	0.109	0.03	0	0	0	0
5	0.131	0.131	0.09	0	0.02	0	0
6	0.18	0.18	0.29	0	0.14	0	0
7	0.22	0.22	0.63	0	0.3	0	0
8	0.23	0.23	0.74	0	0.37	0	0
9	0.24	0.24	0.86	0	0.43	0	0
10	0.241	0.241	0.88	0	0.44	0	0
11	0.245	0.245	0.92	0	0.46	0	0
12	0.248	0.248	0.93	0	0.48	0	0
13	0.25	0.25	0.97	0	0.49	0	0
Measured	-	-	1	0.3	0.5	0.1	0.2

Table 36 contains the iterations taken to fit w\_thrm for the un-normalized BDL-422 power histories of OE ADA, ADD, ADC.

Table 36: OE FGR fitting for un-normalized BDL-422 power histories.

Iteration	w_thrm	ADA	ADC	ADD
1	1.25	23.5	3.6	18.7
2	1.5	26.0	3.7	19.2
3	1.61	27.9	3.8	20.2
4	1.641	28.6	3.9	20.3
5	1.66	28.5	3.9	20.3
6	1.72	29.6	4	20.5
7	1.74	29.7	4.1	20.5
Measured	-	26.2 -32.8	5.3	19.6 - 26.9

Table 37 presents the steps taken to fit w\_irr and w\_athrm for the normalized power histories of IE from BDL-422.

Table 37: IE FGR fitting for normalized BDL-422 power histories.

Iteration	w_irr	w_athrm	ADA	ADC	ADD	ADE	ADF
1	0.25	0.25	2.8	0	1.3	0	0.1
2	0.2	0.2	1.7	0	0.68	0	0.01
3	0.198	0.198	1.7	0	0.67	0	0.02
4	0.192	0.192	1.6	0	0.61	0	0.02
5	0.182	0.182	1.4	0	0.52	0	0.01
6	0.174	0.174	1.3	0	0.46	0	0.01
7	0.167	0.167	1.2	0	0.41	0	0.009
8	0.163	0.163	1.1	0	0.38	0	0.008
9	0.1619	0.1619	1.1	0	0.37	0	0.008
10	0.1614	0.1614	1.1	0	0.37	0	0.008
11	0.1602	0.1602	1.1	0	0.36	0	0.008
12	0.1599	0.1599	1.1	0	0.36	0	0.008
13	0.1594	0.1594	1.1	0	0.36	0	0.008
14	0.1622	0.1622	1.1	0	0.37	0	0.008
15	0.1619	0.1619	1.1	0	0.37	0	0.008
16	0.1604	0.1604	1.1	0	0.36	0	0.008
Measured	-	-	1	0.3	0.5	0.1	0.2

Table 38 contains the iterations taken to fit w\_thrm for the normalized BDL-422 power histories of OE ADA, ADD, and ADC.



Table 38: OE FGR fitting for normalized BDL-422 power histories.

Iteration	w_thrm	ADA	ADC	ADD
1	1.1	22.3	3.8	22.6
2	1.15	22.9	3.9	23
3	1.17	22.9	3.9	23
4	1.171	23.1	3.9	23
5	1.175	23.1	3.9	23.2
6	1.2	23.3	3.9	23.3
7	1.32	26.1	4	24.4
8	1.35	26.7	4	25
9	1.37	27.6	4	25
10	1.38	27.9	4	25
11	1.41	29	4	25.5
12	1.42	29	4.1	25.7
13	1.415	29	4	25.7
Measured	-	26.2 -32.8	5.3	19.6 - 26.9

Unfortunately there are very few irradiation tests of (Th,Pu)O<sub>2</sub> discussed in open literature, and the literature review has as of yet to find diffusion data on any gas within grains of (Th,Pu)O<sub>2</sub>. The only justification for the selection of these weighting factors is that it fits the FGR data from BDL-422. Th-based ceramics have a higher melting temperature than UO<sub>2</sub> which would indicate that more energy is required to break apart the solid structure of this fuel type. It is reasonable to assume that producing interstitial defects that enable fission gas diffusion within a Th-based fuel grain would similarly require more energy. For the low temperature dependent terms in equation (112), that are less than 1, there is only a mild reassurance that this set of weighting factors reaffirms this assumption.

## Appendix D: COMSOL Report

### Global Definitions

Parameters 1

Parameters

Name	Expression	Value	Description
pellet_radius	13.48[mm]/2	0.00674 m	
radial_chamfer	0.827[mm]	8.27E-4 m	
axial_chamfer	0.176[mm]	1.76E-4 m	
land_width	0.0[mm]	0 m	
dish_depth	0.27[mm]	2.7E-4 m	
pellet_length	18.52[mm]	0.01852 m	
pellet_sheath_gap	0.080[mm]/2	4E-5 m	
pellet_pellet_gap	2.29[mm]/27	8.4815E-5 m	
pellet_hole_radius	0[mm]	0 m	
pellet_hole_free_vol_fraction	0	0	
v0_ends	232.17[mm^3]	2.3217E-7 m <sup>3</sup>	
v0_total	(v0_gap + v0_disk + v0_chamfer*num_chamfers + v0_dish*num_dishes)*num_pellets + v0_ends + v0_plenum + v0_C_insert	4.1842E-6 m <sup>3</sup>	
sheath_thickness	0.405[mm]	4.05E-4 m	thickness of the sheath in radial direction
mf0_He	1	1	mole fraction of He in fill gas
mf0_Ne	0	0	mole fraction of Ne in the fill gas

Name	Expression	Value	Description
mf0_Ar	0	0	mole fraction of Ar in the fill gas
mf0_Kr	0	0	mole fraction of Kr in the fill gas
mf0_Xe	0	0	mole fraction of Xe in the fill gas
mf0_N2	0	0	mole fraction of N2 in the fill gas
mf0_O2	0	0	mole fraction of O2 in the fill gas
linear_power_parm	55[kW/m]	55000 W/m	
coolant_pressure_parm	9.98e6[Pa]	9.98E6 Pa	
coolant_temperature_parm	557[K]	557 K	
sheath_coolant_ht_coef_parm	50[kW/m^2/K]	50000 W/(m <sup>2</sup> ·K)	
gas_pressure_forced_parm	0	0	
T_ends_parm	-140[K]	-140 K	ends/plenum temp parm
t_max	1e9[s]	1E9 s	
burnup_max	200	200	
UO2_pore_fraction_initial	1 - 10.65/10.98	0.030055	rho/rho_theoretical_max
UO2_roughness	1[um]	1E-6 m	surface roughness of unirradiated UO2
Zir_roughness	0.5[um]	5E-7 m	surface roughness of unirradiated zir
s_dev	0	0	stoichiometric deviation of the fuel
U235_percent	1.5	1.5	enrichment percent
num_pellets	26	26	
UO2_grain_diameter_int	11.6[um]	1.16E-5 m	

Name	Expression	Value	Description
dish_radius	$(\text{dish\_depth}^2 + (\text{pellet\_radius} - \text{land\_width} - \text{radial\_chamfer})^2) / (2 * \text{dish\_depth})$	0.064882 m	
sheath_internal_radius	$\text{pellet\_radius} + \text{pellet\_sheath\_gap}$	0.00678 m	
RMS_surf_roughness	$\sqrt{(\text{UO2\_roughness}^2 + \text{Zir\_roughness}^2) / 2}$	7.9057E-7 m	the RMS value of the pellet to sheath surface roughness
v0_gap	$\pi * (\text{pellet\_length} + \text{pellet\_pellet\_gap}) * (\text{sheath\_internal\_radius}^2 - \text{pellet\_radius}^2)$	3.1609E-8 m <sup>3</sup>	
v0_chamfer	$\text{axial\_chamfer} * \pi * \text{radial\_chamfer} * (\text{pellet\_radius} - \text{axial\_chamfer} / 3)$	3.0551E-9 m <sup>3</sup>	
v0_disk	$\pi * \text{pellet\_pellet\_gap} * \text{pellet\_radius}^2$	1.2104E-8 m <sup>3</sup>	
v0_dish	$\pi * (\text{dish\_depth} - \text{dish\_radius}) * ((\text{pellet\_radius} - \text{radial\_chamfer} - \text{land\_width})^2 - \text{pellet\_hole\_radius}^2) - 2 * \pi / 3 * ((\text{dish\_radius}^2 - (\text{pellet\_radius} - \text{radial\_chamfer} - \text{land\_width})^2)^{3/2} - (\text{dish\_radius}^2 - (\text{pellet\_hole\_radius})^2)^{3/2})$	1.4839E-8 m <sup>3</sup>	
v0_pellet_hole	$\pi * \text{pellet\_hole\_radius}^2 * \text{pellet\_length} * \text{pellet\_hole\_free\_vol\_fraction}$	0 m <sup>3</sup>	
v0_pellet	$\text{v0\_gap} + \text{v0\_chamfer} * \text{num\_chamfers} + \text{v0\_disk} + \text{v0\_dish} * \text{num\_dishes} +$	7.9501E-8 m <sup>3</sup>	

Name	Expression	Value	Description
	v0_pellet_hole		
P0_fill	1[atm]	1.0133E5 Pa	initial fill gas pressure
T0_fill	293.15[K]	293.15 K	initial fill gas temperature
m0_gas_element	$P0\_fill*v0\_total/8.314[J/mol/K]/T0\_fill$	1.7395E-4 mol	number of moles of fill gas
T_geom_ref	293.15[K]	293.15 K	
energy_per_fission	200[MeV]	3.2044E-11 J	
rho_UO2_theory	10980[kg/m^3]	10980 kg/m <sup>3</sup>	MATPRO/SCDAP
pellet_solid_volume	$(\pi*(\text{pellet\_radius}^2 - \text{pellet\_hole\_radius}^2)*\text{pellet\_length} - \text{num\_dishes}*v0\_dish - \text{num\_dishes}*v0\_chamfer)$	2.6073E-6 m <sup>3</sup>	
mass_UO2_pellet	$\text{rho\_UO2\_theory}*(1 - \text{UO2\_pore\_fraction\_initial})*(\pi*(\text{pellet\_radius}^2 - \text{pellet\_hole\_radius}^2)*\text{pellet\_length} - \text{num\_dishes}*v0\_dish - \text{num\_dishes}*v0\_chamfer)$	0.027768 kg	
mass_U_pellet	$\text{mass\_UO2\_pellet}*238/(238 + (2 + s\_dev)*16)$	0.024477 kg	
sheath_length_initial	$(\text{pellet\_length} + \text{pellet\_pellet\_gap})*\text{num\_pellets\_model}$	0.018605 m	
missing_vol_ratio	$(v0\_disk + v0\_dish*\text{num\_dishes} + v0\_chamfer*\text{num\_chamfers} + v0\_pellet\_hole*\text{pellet\_hole\_free\_vol\_fraction})/v0\_pellet\_cylinder$	0.018037	fraction of pellet missing due to gap, dishing and chamfering
v0_pellet_cylinder	$\pi*(\text{pellet\_radius}^2 - \text{pellet\_hole\_radius}^2)*\text{pellet\_hole\_free\_vol\_fraction}$	2.6552E-6 m <sup>3</sup>	

Name	Expression	Value	Description
	*(pellet_length + pellet_pellet_gap)		
num_neutron_per_fission	2.42	2.42	Approximate number of neutrons released per fission U232=2.49,U235=2.42, Pu239=2.93 (Gladstone and Sesonske pg 107)
num_dishes	2	2	
num_chamfers	2	2	
mesh_nodes_pellet_dish	11	11	
mesh_nodes_pellet_chamfer	1	1	
mesh_nodes_pellet_axial	30	30	
mesh_nodes_sheath_radial	4	4	
mesh_nodes_sheath_axial	44	44	
timestep_range1_start	0.5[s]	0.5 s	
timestep_range1_size	0.5[s]	0.5 s	
timestep_range1_end	1[s]	1 s	
timestep_range2_start	2[s]	2 s	
timestep_range2_size	1[s]	1 s	
timestep_range2_end	3[s]	3 s	
timestep_range3_start	4[s]	4 s	
timestep_range3_size	1[s]	1 s	
timestep_range3_end	5[s]	5 s	
timestep_range4_start	6[s]	6 s	
timestep_range4_size	1[s]	1 s	
timestep_range4_end	7[s]	7 s	
max_time_step	36*3600	1.296E5	

Name	Expression	Value	Description
solver_initial_damping_factor	1/2^3	0.125	
solver_damping_growth_rate	2	2	
fg_release_damping_constant	18*3600[s]	64800 s	
contact_penalty_factor	1e13[Pa/m]	1E13 N/m <sup>3</sup>	
contact_pressure_est	15[MPa]	1.5E7 Pa	
contact_error_tol	1e7[Pa]	1E7 Pa	
peripheral_tc_location	7.35[mm]	0.00735 m	
peripheral_tc_raadius	0.65[mm]	6.5E-4 m	
cracked_model_flag	1	1	
gas_pressure_set_time	9e99[s]	9E99 s	
gas_pressure_set_value	1[Pa]	1 Pa	
case_index_number	0	0	
UO2_add_TC	0	0	
UO2_mul_Texp	1	1	
UO2_mul_FGDiff	1	1	
UO2_mul_FGGBSat	1	1	
Zir_add_TC	0	0	
Zir_add_YoungsM	0	0	
Zir_mul_Texp	1	1	
num_pellets_model	1	1	
axial_contact_pressure_est	100[MPa]	1E8 Pa	
axial_contact_penalty_factor	1e14[Pa/m]	1E14 N/m <sup>3</sup>	
axial_contact_offset_dist	1e-5[m]	1E-5 m	
pellet_pellet_gap_model	pellet_pellet_gap/10*0	0 m	
periodic_bc_flag	1	1	

Name	Expression	Value	Description
fg_Pext_param	0	0	
pellet_axial_constraint_location_lag	1	1	
thermal_to_fission_power_ratio	0.925	0.925	
burnup_avg_flag	0	0	
transient_start	387972[s]	3.8797E5 s	
power_missing_vol_flag	0	0	0 = dont increase power, 1 use missing vol fraction, 2 use numerical flux int
M_HEU	235.3213[g/mol]	0.23532 kg/mol	
M_Th	232.0380504[g/mol]	0.23204 kg/mol	
M_O	15.999[g/mol]	0.015999 kg/mol	
M_m	$wPer_U * M_{HEU} + (1 - wPer_U) * M_{Th}$	0.23209 kg/mol	
wPer_U	0.0163	0.0163	
M_mO2	$M_m + 2 * M_O$	0.26409 kg/mol	
v0_plenum	1885[mm^3]	1.885E-6 m <sup>3</sup>	
v0_C_insert	0	0	
pellet_mat	3	3	
Percent_fission_gas_yield_UO2	0.251	0.251	
Percent_fission_gas_yield_Th	0.251*1.1	0.2761	
Xe_to_Kr_UO2	9/10	0.9	
Xe_to_Kr_Th	9/11	0.81818	
w_thrm	1.415	1.415	Weighting factor applied to thermal



Name	Expression	Value	Description
			component of FG Diffusion of (Th,Pu)O2
w_irr	0.1604	0.1604	Weighting factor applied to irradiation component of FG Diffusion of (Th,Pu)O2
w_atrm	0.1604	0.1604	Weighting factor applied to athermal component of FG Diffusion of (Th,Pu)O2
case_index	NaN	NaN	
sheath_mat	1	1	

## Component 1

Date Feb 20, 2014 10:37:58 AM

### Component settings

Unit system SI  
Geometry shape order automatic

### Geometry 1

Units  
Length unit m  
Angular unit deg

### Geometry statistics

Description	Value
Space dimension	2

Description	Value
-------------	-------

Number of domains 3

Number of boundaries 13

Number of vertices 12

Rectangle 1 (r1)

Position

Description	Value
-------------	-------

Position {pellet\_hole\_radius, 0}

Layers

Size

Description	Value
-------------	-------

Width pellet\_radius - pellet\_hole\_radius

Height pellet\_length

Circle 1 (c1)

Position

Description	Value
-------------	-------

Position {0, pellet\_length + dish\_radius - dish\_depth}

Layers

Size and shape

Description	Value
-------------	-------

Radius dish\_radius

If 2 (if2)

Condition

Description	Value
Condition	num_dishes==2

Circle 2 (c2)

Position

Description	Value
Position	{0, -dish_radius + dish_depth}

Layers

Size and shape

Description	Value
Radius	dish_radius

Polygon 1 (pol1)

Object type

Description	Value
Type	Solid

Coordinates

Description	Value
r	{0.0053105, 0.0061005, 0.0061005}
z	{0.01609, 0.01595, 0.01637}

If 1 (if1)

Condition

Description	Value
Condition	num_chamfers==2

Polygon 2 (pol2)

Object type

Description	Value
Type	Solid

Coordinates

Description	Value
r	{0.0053105, 0.0061005, 0.0061005}
z	{0, 1.4000000000000001E-4, -1.4000000000000001E-4}

Point 1 (pt1)

Point

Description	Value
Point coordinate	{pellet_radius - radial_chamfer, 0}

Polygon 3 (pol3)

Object type

Description	Value
Type	Solid

Coordinates

Description	Value
-------------	-------

Description	Value
r	{0, 0.0061005}
z	0.008045

Array 1 (arr1)

Settings

Description	Value
Size	{1, num_pellets_model}
Full size	{1, num_pellets_model}
Displacement	{0, pellet_length + pellet_pellet_gap_model}

If 4 (if4)

Condition

Description	Value
Condition	num_pellets_model>1

Rectangle 4 (r4)

Position

Description	Value
Position	{pellet_hole_radius, pellet_length/2}

Layers

Size

Description	Value
Width	pellet_radius - pellet_hole_radius - radial_chamfer
Height	(pellet_length + pellet_pellet_gap_model)*(num_pellets_model - 1)

Difference 2 (dif2)

Settings

Description	Value
Keep input objects	On

Polygon 4 (pol4)

Object type

Description	Value
Type	Solid

Coordinates

Description	Value
r	0
z	{0.008045, 0.008045}

Rectangle 2 (r2)

Position

Description	Value
Position	{sheath_internal_radius, 0}

Layers

Size

Description	Value
Width	sheath_thickness
Height	(pellet_length + pellet_pellet_gap)*num_pellets_model

If 3 (if3)

Condition

Description	Value
Condition	pellet_hole_radius>0

Rectangle 3 (r3)

Position

Description	Value
Position	{0, (dish_depth - dish_radius + sqrt(dish_radius^2 - pellet_hole_radius^2))*(num_dishes - 1)}

Layers

Size

Description	Value
Width	pellet_hole_radius
Height	pellet_length*num_pellets_model + pellet_pellet_gap_model*(num_pellets_model - 1) - num_dishes*(dish_depth - dish_radius + sqrt(dish_radius^2 - pellet_hole_radius^2))

Materials

Zircaloy

Selection

Geometric entity level Domain

Selection Domain 3

Material parameters

Name	Value	Unit
------	-------	------

Name	Value	Unit
Young's modulus	youngs_modulus_Zir	Pa
Poisson's ratio	poissons_ratio_Zir	1
Density	rho_Zir	kg/m <sup>3</sup>

#### Basic Settings

Description	Value
Young's modulus	youngs_modulus_Zir
Poisson's ratio	poissons_ratio_Zir
Heat capacity at constant pressure	cp_Zir
Thermal conductivity	{{k_Zir, 0, 0}, {0, k_Zir, 0}, {0, 0, k_Zir}}
Density	rho_Zir

#### UO2

##### Selection

Geometric entity level Domain

Selection Domains 1–2

##### Material parameters

Name	Value	Unit
Poisson's ratio	0.28	1
Density	rho_UO2	kg/m <sup>3</sup>
Young's modulus	youngs_modulus_UO2	Pa

#### Basic Settings

Description	Value
-------------	-------



Description	Value
Thermal conductivity	{{k_pellet, 0, 0}, {0, k_pellet, 0}, {0, 0, k_pellet}}
Poisson's ratio	0.28
Heat capacity at constant pressure	Cp_pellet
Density	rho_UO2
Young's modulus	youngs_modulus_UO2

Solid Mechanics

Used products

COMSOL Multiphysics

Structural Mechanics Module

Selection

Geometric entity level Domain

Selection Domains 1–3

Equations

$$\mathbf{0} = \nabla \cdot \mathbf{F} \mathbf{S} + \mathbf{F} \mathbf{v}, \quad \mathbf{F} = \mathbf{I} + \nabla \mathbf{u}$$

Settings

Description	Value
Displacement field	Quadratic
Compute boundary fluxes	Off
Value type when using splitting of complex variables	Real
Typical wave speed for perfectly matched layers	solid.cp

Variables

Name	Expression	Unit	Selection
solid.R	R	m	Domains 1–3
solid.Z	Z	m	Domains 1–3
solid.r	r	m	Domains 1–3
solid.z	z	m	Domains 1–3
solid.nR	nR	1	Boundary 3
solid.nPHI	0	1	Boundary 3
solid.nZ	nZ	1	Boundary 3
solid.nR	dnR	1	Boundaries 1–2, 4–13
solid.nPHI	0	1	Boundaries 1–2, 4–13
solid.nZ	dnZ	1	Boundaries 1–2, 4–13
solid.nr	nr	1	Boundary 3
solid.nphi	0	1	Boundary 3
solid.nz	nz	1	Boundary 3
solid.nr	dnr	1	Boundaries 1–2, 4–13
solid.nphi	0	1	Boundaries 1–2, 4–13
solid.nz	dnz	1	Boundaries 1–2, 4–13
solid.nRmesh	root.nRmesh	1	Boundary 3
solid.nPHImesh	0	1	Boundary 3
solid.nZmesh	root.nZmesh	1	Boundary 3
solid.nRmesh	root.dnRmesh	1	Boundaries 1–2, 4–13

Name	Expression	Unit	Selection
solid.nPHImesh	0	1	Boundaries 1-2, 4-13
solid.nZmesh	root.dnZmesh	1	Boundaries 1-2, 4-13
solid.nrmesh	root.nrmesh	1	Boundary 3
solid.nphimesh	0	1	Boundary 3
solid.nzmesh	root.nzmesh	1	Boundary 3
solid.nrmesh	root.dnrmesh	1	Boundaries 1-2, 4-13
solid.nphimesh	0	1	Boundaries 1-2, 4-13
solid.nzmesh	root.dnzmesh	1	Boundaries 1-2, 4-13
solid.refpntr	0	m	Global
solid.refpntphi	0	m	Global
solid.refpntz	0	m	Global
solid.cref	solid.cp	m/s	Domains 1-3
rt	d(r,TIME)	m/s	Global
phit	0	m/s	Global
zt	d(z,TIME)	m/s	Global

Linear Elastic Material 1

Selection

Geometric entity level    Domain

Selection                    No domains

Equations

$$\mathbf{0} = \nabla \cdot \mathbf{S} + \mathbf{F}_v$$

$$\mathbf{S} = \mathbf{S}_{ad} + \mathbf{C} : \boldsymbol{\epsilon}_{el}, \quad \boldsymbol{\epsilon}_{el} = \boldsymbol{\epsilon} - \boldsymbol{\epsilon}_{inel}$$

$$\mathbf{S}_{ad} = \mathbf{S}_0 + \mathbf{S}_{ext} + \mathbf{S}_q$$

$$\boldsymbol{\epsilon}_{inel} = \boldsymbol{\epsilon}_0 + \boldsymbol{\epsilon}_{th} + \boldsymbol{\epsilon}_{hs} + \boldsymbol{\epsilon}_{pl} + \boldsymbol{\epsilon}_{cr}$$

$$\boldsymbol{\epsilon} = \frac{1}{2} [(\nabla \mathbf{u})^T + \nabla \mathbf{u}]$$

Settings

Description	Value
Solid model	Isotropic
Force linear strains	On
Nearly incompressible material	Off
Specify	Young's modulus and Poisson's ratio
Calculate dissipated energy	Off
Young's modulus	From material
Poisson's ratio	From material
Density	From material

Used products

COMSOL Multiphysics

Shape functions

Name	Shape function	Unit	Description	Shape frame	Selection
u	Lagrange (Quadratic)	m	Displacement field, R component	Material	No domains
w	Lagrange (Quadratic)	m	Displacement field, Z component	Material	No domains

Axial Symmetry 1

Selection

Geometric entity level Boundary

Selection Boundaries 1–2

Used products

COMSOL Multiphysics

Shape functions

Constraint	Constraint force	Shape function	Selection
-u	-test(u)	Lagrange	Boundaries 1–2

Initial Values 1

Selection

Geometric entity level Domain

Selection Domains 1–3

Settings

Description	Value
Displacement field	{0, 0, 0}
Structural velocity field	{0, 0, 0}

Variables

Name	Expression	Unit	Selection
solid.uInitr	0	m	Domains 1–3
solid.uInitphi	0	m	Domains 1–3
solid.uInitz	0	m	Domains 1–3
solid.utInitr	0	m/s	Domains 1–3
solid.utInitphi	0	m/s	Domains 1–3
solid.utInitz	0	m/s	Domains 1–3

#### Pellet Domains

##### Selection

Geometric entity level Domain

Selection Domains 1–2

##### Equations

$$\mathbf{0} = \nabla \cdot \mathbf{F} \mathbf{S} + \mathbf{F}_V, \quad \mathbf{F} = \mathbf{I} + \nabla \mathbf{u}$$

$$\mathbf{S} = \mathbf{S}_{ad} + \mathbf{C} : \boldsymbol{\epsilon}_{el}, \quad \boldsymbol{\epsilon}_{el} = \boldsymbol{\epsilon} - \boldsymbol{\epsilon}_{inel}$$

$$\mathbf{S}_{ad} = \mathbf{S}_0 + \mathbf{S}_{ext} + \mathbf{S}_q$$

$$\boldsymbol{\epsilon}_{inel} = \boldsymbol{\epsilon}_0 + \boldsymbol{\epsilon}_{th} + \boldsymbol{\epsilon}_{hs} + \boldsymbol{\epsilon}_{pl} + \boldsymbol{\epsilon}_{cr}$$

$$\boldsymbol{\epsilon} = \frac{1}{2} \left[ (\nabla \mathbf{u})^T + \nabla \mathbf{u} + (\nabla \mathbf{u})^T \nabla \mathbf{u} \right]$$

##### Settings

Description	Value
Solid model	Isotropic
Force linear strains	Off
Nearly incompressible material	Off
Specify	Young's modulus and Poisson's ratio

Description	Value
Calculate dissipated energy	Off
Young's modulus	From material
Poisson's ratio	From material
Density	From material

Properties from material

Property	Material	Property group
Young's modulus	UO2	Basic
Poisson's ratio	UO2	Basic
Density	UO2	Basic

Variables

Name	Expression	Unit	Selection
solid.rho	material.rho	kg/m <sup>3</sup>	Domains 1–2
solid.Qh	0	W/m <sup>3</sup>	Domains 1–2
solid.gradUrR	uR	1	Domains 1–2
solid.gradUphiR	0	1	Domains 1–2
solid.gradUzR	wR	1	Domains 1–2
solid.gradUrPHI	0	1	Domains 1–2
solid.gradUphiPHI	if(abs(R)<0.001*h,uR,u/R)	1	Domains 1–2
solid.gradUzPHI	0	1	Domains 1–2
solid.gradUrZ	uZ	1	Domains 1–2
solid.gradUphiZ	0	1	Domains 1–2
solid.gradUzZ	wZ	1	Domains 1–2

Name	Expression	Unit	Selection
solid.FdrR	1+solid.gradUrR	1	Domains 1–2
solid.FdphiR	solid.gradUphiR	1	Domains 1–2
solid.FdzR	solid.gradUzR	1	Domains 1–2
solid.FdrPHI	solid.gradUrPHI	1	Domains 1–2
solid.FdphiPHI	1+solid.gradUphiPHI	1	Domains 1–2
solid.FdzPHI	solid.gradUzPHI	1	Domains 1–2
solid.FdrZ	solid.gradUrZ	1	Domains 1–2
solid.FdphiZ	solid.gradUphiZ	1	Domains 1–2
solid.FdzZ	1+solid.gradUzZ	1	Domains 1–2
solid.Fdlr1	solid.FdrR	1	Domains 1–2
solid.Fdlphi1	solid.FdphiR	1	Domains 1–2
solid.Fdlz1	solid.FdzR	1	Domains 1–2
solid.Fdlr2	solid.FdrPHI	1	Domains 1–2
solid.Fdlphi2	solid.FdphiPHI	1	Domains 1–2
solid.Fdlz2	solid.FdzPHI	1	Domains 1–2
solid.Fdlr3	solid.FdrZ	1	Domains 1–2
solid.Fdlphi3	solid.FdphiZ	1	Domains 1–2
solid.Fdlz3	solid.FdzZ	1	Domains 1–2
uRt	root.comp1.uRTIME- uRR*d(R, TIME)- uRZ*d(Z, TIME)	1/s	Domains 1–2
uZt	root.comp1.uZTIME- uZR*d(R, TIME)- uZZ*d(Z, TIME)	1/s	Domains 1–2
uRtt	d(root.comp1.uRTIME- uRR*d(R, TIME)- uRZ*d(Z, TIME), TIME) -d(root.comp1.uRTIME- uRR*d(R, TIME)-	1/s^2	Domains 1–2



Name	Expression	Unit	Selection
	$uRZ * d(Z, TIME), R) * d(R, TIME) -$ $d(\text{root.comp1.uRTIME} - uRR * d(R, TIME) - uRZ * d(Z, TIME), Z) * d(Z, TIME)$		
uZtt	$d(\text{root.comp1.uZTIME} - uZR * d(R, TIME) - uZZ * d(Z, TIME), TIME) -$ $d(\text{root.comp1.uZTIME} - uZR * d(R, TIME) - uZZ * d(Z, TIME), R) * d(R, TIME) -$ $d(\text{root.comp1.uZTIME} - uZR * d(R, TIME) - uZZ * d(Z, TIME), Z) * d(Z, TIME)$	1/s <sup>2</sup>	Domains 1–2
wRt	$\text{root.comp1.wRTIME} - wRR * d(R, TIME) - wRZ * d(Z, TIME)$	1/s	Domains 1–2
wZt	$\text{root.comp1.wZTIME} - wZR * d(R, TIME) - wZZ * d(Z, TIME)$	1/s	Domains 1–2
wRtt	$d(\text{root.comp1.wRTIME} - wRR * d(R, TIME) - wRZ * d(Z, TIME), TIME) -$ $d(\text{root.comp1.wRTIME} - wRR * d(R, TIME) - wRZ * d(Z, TIME), R) * d(R, TIME) -$ $d(\text{root.comp1.wRTIME} - wRR * d(R, TIME) - wRZ * d(Z, TIME), Z) * d(Z, TIME)$	1/s <sup>2</sup>	Domains 1–2
wZtt	$d(\text{root.comp1.wZTIME} - wZR * d(R, TIME) - wZZ * d(Z, TIME), TIME) -$ $d(\text{root.comp1.wZTIME} - wZR * d(R, TIME) - wZZ * d(Z, TIME), R) * d(R, TIME)$	1/s <sup>2</sup>	Domains 1–2

Name	Expression	Unit	Selection
	R,TIME)- d(root.comp1.wZTIME- wZR*d(R,TIME)- wZZ*d(Z,TIME),Z)*d(Z ,TIME)		
ut	root.comp1.uTIME- uR*d(R,TIME)- uZ*d(Z,TIME)	m/s	Domains 1–2
wt	root.comp1.wTIME- wR*d(R,TIME)- wZ*d(Z,TIME)	m/s	Domains 1–2
utt	d(root.comp1.uTIME- uR*d(R,TIME)- uZ*d(Z,TIME),TIME)- d(root.comp1.uTIME- uR*d(R,TIME)- uZ*d(Z,TIME),R)*d(R, TIME)- d(root.comp1.uTIME- uR*d(R,TIME)- uZ*d(Z,TIME),Z)*d(Z, TIME)	m/s^2	Domains 1–2
wtt	d(root.comp1.wTIME- wR*d(R,TIME)- wZ*d(Z,TIME),TIME)- d(root.comp1.wTIME- wR*d(R,TIME)- wZ*d(Z,TIME),R)*d(R, TIME)- d(root.comp1.wTIME- wR*d(R,TIME)- wZ*d(Z,TIME),Z)*d(Z, TIME)	m/s^2	Domains 1–2
solid.D11	solid.E*(1- solid.nu)/((1+solid.nu)*( 1-2*solid.nu))	Pa	Domains 1–2
solid.D12	solid.E*solid.nu/((1+soli d.nu)*(1-2*solid.nu))	Pa	Domains 1–2
solid.D13	solid.E*solid.nu/((1+soli	Pa	Domains 1–2

Name	Expression	Unit	Selection
	$d.nu*(1-2*solid.nu)$		
solid.D14	0	Pa	Domains 1–2
solid.D15	0	Pa	Domains 1–2
solid.D16	0	Pa	Domains 1–2
solid.D22	$solid.E*(1-solid.nu)/((1+solid.nu)*(1-2*solid.nu))$	Pa	Domains 1–2
solid.D23	$solid.E*solid.nu/((1+solid.nu)*(1-2*solid.nu))$	Pa	Domains 1–2
solid.D24	0	Pa	Domains 1–2
solid.D25	0	Pa	Domains 1–2
solid.D26	0	Pa	Domains 1–2
solid.D33	$solid.E*(1-solid.nu)/((1+solid.nu)*(1-2*solid.nu))$	Pa	Domains 1–2
solid.D34	0	Pa	Domains 1–2
solid.D35	0	Pa	Domains 1–2
solid.D36	0	Pa	Domains 1–2
solid.D44	$0.5*solid.E/(1+solid.nu)$	Pa	Domains 1–2
solid.D45	0	Pa	Domains 1–2
solid.D46	0	Pa	Domains 1–2
solid.D55	$0.5*solid.E/(1+solid.nu)$	Pa	Domains 1–2
solid.D56	0	Pa	Domains 1–2
solid.D66	$0.5*solid.E/(1+solid.nu)$	Pa	Domains 1–2
solid.K	$solid.E/(3*(1-2*solid.nu))$	N/m <sup>2</sup>	Domains 1–2
solid.Eequ	solid.E	Pa	Domains 1–2
solid.nuequ	solid.nu	1	Domains 1–2

Name	Expression	Unit	Selection
solid.Gequ	solid.G	N/m <sup>2</sup>	Domains 1–2
solid.cp	$\sqrt{(\text{solid.K}+4*\text{solid.G}/3)/\text{solid.rho}}$	m/s	Domains 1–2
solid.cs	$\sqrt{\text{solid.G}/\text{solid.rho}}$	m/s	Domains 1–2
solid.E	material.E	Pa	Domains 1–2
solid.nu	material.nu	1	Domains 1–2
solid.G	$0.5*\text{solid.E}/(1+\text{solid.nu})$	N/m <sup>2</sup>	Domains 1–2
solid.lambLame	$\text{solid.E}*\text{solid.nu}/((1+\text{solid.nu})*(1-2*\text{solid.nu}))$	N/m <sup>2</sup>	Domains 1–2
solid.muLame	$0.5*\text{solid.E}/(1+\text{solid.nu})$	N/m <sup>2</sup>	Domains 1–2
solid.Cgl11	solid.D11+solid.D12+solid.D13	Pa	Domains 1–2
solid.Cgl12	solid.D14+solid.D24+solid.D34	Pa	Domains 1–2
solid.Cgl13	solid.D16+solid.D26+solid.D36	Pa	Domains 1–2
solid.Cgl22	solid.D12+solid.D22+solid.D23	Pa	Domains 1–2
solid.Cgl23	solid.D15+solid.D25+solid.D35	Pa	Domains 1–2
solid.Cgl33	solid.D13+solid.D23+solid.D33	Pa	Domains 1–2
solid.eRR	uR	1	Domains 1–2
solid.eRPHI	0	1	Domains 1–2
solid.eRZ	$0.5*(uZ+wR)$	1	Domains 1–2
solid.ePHIPHI	if(abs(R)<0.001*h,uR,u/R)	1	Domains 1–2
solid.ePHIZ	0	1	Domains 1–2
solid.eZZ	wZ	1	Domains 1–2

Name	Expression	Unit	Selection
solid.el11	solid.eRR	1	Domains 1–2
solid.el12	solid.eRPHI	1	Domains 1–2
solid.el13	solid.eRZ	1	Domains 1–2
solid.el22	solid.ePHIPHI	1	Domains 1–2
solid.el23	solid.ePHIZ	1	Domains 1–2
solid.el33	solid.eZZ	1	Domains 1–2
solid.eel11	solid.el11-solid.eil11- solid.eiel11	1	Domains 1–2
solid.eel12	solid.el12-solid.eil12- solid.eiel12	1	Domains 1–2
solid.eel13	solid.el13-solid.eil13- solid.eiel13	1	Domains 1–2
solid.eel22	if(cracked_model_flag, min(solid.el22- solid.eil22- solid.eiel22,0),solid.el22 -solid.eil22-solid.eiel22)	1	Domains 1–2
solid.eel23	solid.el23-solid.eil23- solid.eiel23	1	Domains 1–2
solid.eel33	solid.el33-solid.eil33- solid.eiel33	1	Domains 1–2
solid.Cel11	1+2*solid.eel11	1	Domains 1–2
solid.Cel12	2*solid.eel12	1	Domains 1–2
solid.Cel13	2*solid.eel13	1	Domains 1–2
solid.Cel22	1+2*solid.eel22	1	Domains 1–2
solid.Cel23	2*solid.eel23	1	Domains 1–2
solid.Cel33	1+2*solid.eel33	1	Domains 1–2
solid.eil11	0	1	Domains 1–2
solid.eil12	0	1	Domains 1–2

Name	Expression	Unit	Selection
solid.eil13	0	1	Domains 1–2
solid.eil22	0	1	Domains 1–2
solid.eil23	0	1	Domains 1–2
solid.eil33	0	1	Domains 1–2
solid.eiel11	0	1	Domains 1–2
solid.eiel12	0	1	Domains 1–2
solid.eiel13	0	1	Domains 1–2
solid.eiel22	0	1	Domains 1–2
solid.eiel23	0	1	Domains 1–2
solid.eiel33	0	1	Domains 1–2
solid.evol	solid.eRR+solid.ePHIPH I+solid.eZZ	1	Domains 1–2
solid.J	solid.FdrR*solid.FdphiP HI*solid.FdzZ+solid.Fdr PHI*solid.FdphiZ*solid. FdzR+solid.FdrZ*solid. FdphiR*solid.FdzPHI- solid.FdrR*solid.FdphiZ *solid.FdzPHI- solid.FdrPHI*solid.Fdph iR*solid.FdzZ- solid.FdrZ*solid.FdphiP HI*solid.FdzR	1	Domains 1–2
solid.Ceil11	(solid.Cel22*solid.Cel33 - solid.Cel23^2)/(solid.Ce l11*solid.Cel22*solid.C el33+2*solid.Cel12*soli d.Cel23*solid.Cel13- solid.Cel11*solid.Cel23 ^2- solid.Cel12^2*solid.Cel 33- solid.Cel22*solid.Cel13 ^2)	1	Domains 1–2

Name	Expression	Unit	Selection
solid.Ceil12	$\frac{(\text{solid.Cel23} * \text{solid.Cel13} - \text{solid.Cel12} * \text{solid.Cel33})}{(\text{solid.Cel11} * \text{solid.Cel22} * \text{solid.Cel33} + 2 * \text{solid.Cel12} * \text{solid.Cel23} * \text{solid.Cel13} - \text{solid.Cel11} * \text{solid.Cel23}^2 - \text{solid.Cel12}^2 * \text{solid.Cel33} - \text{solid.Cel22} * \text{solid.Cel13}^2)}$	1	Domains 1–2
solid.Ceil13	$\frac{(\text{solid.Cel12} * \text{solid.Cel23} - \text{solid.Cel22} * \text{solid.Cel13})}{(\text{solid.Cel11} * \text{solid.Cel22} * \text{solid.Cel33} + 2 * \text{solid.Cel12} * \text{solid.Cel23} * \text{solid.Cel13} - \text{solid.Cel11} * \text{solid.Cel23}^2 - \text{solid.Cel12}^2 * \text{solid.Cel33} - \text{solid.Cel22} * \text{solid.Cel13}^2)}$	1	Domains 1–2
solid.Ceil22	$\frac{(\text{solid.Cel11} * \text{solid.Cel33} - \text{solid.Cel13}^2)}{(\text{solid.Cel11} * \text{solid.Cel22} * \text{solid.Cel33} + 2 * \text{solid.Cel12} * \text{solid.Cel23} * \text{solid.Cel13} - \text{solid.Cel11} * \text{solid.Cel23}^2 - \text{solid.Cel12}^2 * \text{solid.Cel33} - \text{solid.Cel22} * \text{solid.Cel13}^2)}$	1	Domains 1–2
solid.Ceil23	$\frac{(\text{solid.Cel12} * \text{solid.Cel13} - \text{solid.Cel11} * \text{solid.Cel23})}{(\text{solid.Cel11} * \text{solid.Cel22} * \text{solid.Cel33} + 2 * \text{solid.Cel12} * \text{solid.Cel23} * \text{solid.Cel13} - \text{solid.Cel11} * \text{solid.Cel23}^2 - \text{solid.Cel12}^2 * \text{solid.Cel33} - \text{solid.Cel22} * \text{solid.Cel13}^2)}$	1	Domains 1–2

Name	Expression	Unit	Selection
	Cel13- solid.Cel11*solid.Cel23 ^2- solid.Cel12^2*solid.Cel 33- solid.Cel22*solid.Cel13 ^2)		
solid.Ceil33	(solid.Cel11*solid.Cel22 - solid.Cel12^2)/(solid.Ce 111*solid.Cel22*solid.C el33+2*solid.Cel12*soli d.Cel23*solid.Cel13- solid.Cel11*solid.Cel23 ^2- solid.Cel12^2*solid.Cel 33- solid.Cel22*solid.Cel13 ^2)	1	Domains 1–2
solid.Jel	sqrt(solid.Cel11*solid.C el22*solid.Cel33+2*soli d.Cel12*solid.Cel23*soli d.Cel13- solid.Cel11*solid.Cel23 ^2- solid.Cel12^2*solid.Cel 33- solid.Cel22*solid.Cel13 ^2)	1	Domains 1–2
solid.eR	solid.eRR	1	Domains 1–2
solid.ePHI	solid.ePHIPHI	1	Domains 1–2
solid.eZ	solid.eZZ	1	Domains 1–2
solid.Sil11	0	N/m <sup>2</sup>	Domains 1–2
solid.Sil12	0	N/m <sup>2</sup>	Domains 1–2
solid.Sil13	0	N/m <sup>2</sup>	Domains 1–2
solid.Sil22	0	N/m <sup>2</sup>	Domains 1–2
solid.Sil23	0	N/m <sup>2</sup>	Domains 1–2



Name	Expression	Unit	Selection
solid.Sil33	0	N/m <sup>2</sup>	Domains 1–2
solid.SI11	solid.Sil11+solid.D11*solid.eel11+solid.D12*solid.eel22+solid.D13*solid.eel33+2*solid.D14*solid.eel12+2*solid.D15*solid.eel23+2*solid.D16*solid.eel13	N/m <sup>2</sup>	Domains 1–2
solid.SI12	solid.Sil12+solid.D14*solid.eel11+solid.D24*solid.eel22+solid.D34*solid.eel33+2*solid.D44*solid.eel12+2*solid.D45*solid.eel23+2*solid.D46*solid.eel13	N/m <sup>2</sup>	Domains 1–2
solid.SI13	solid.Sil13+solid.D16*solid.eel11+solid.D26*solid.eel22+solid.D36*solid.eel33+2*solid.D46*solid.eel12+2*solid.D56*solid.eel23+2*solid.D66*solid.eel13	N/m <sup>2</sup>	Domains 1–2
solid.SI22	solid.Sil22+solid.D12*solid.eel11+solid.D22*solid.eel22+solid.D23*solid.eel33+2*solid.D24*solid.eel12+2*solid.D25*solid.eel23+2*solid.D26*solid.eel13	N/m <sup>2</sup>	Domains 1–2
solid.SI23	solid.Sil23+solid.D15*solid.eel11+solid.D25*solid.eel22+solid.D35*solid.eel33+2*solid.D45*solid.eel12+2*solid.D55*solid.eel23+2*solid.D56*solid.eel13	N/m <sup>2</sup>	Domains 1–2
solid.SI33	solid.Sil33+solid.D13*solid.eel11+solid.D23*solid.eel22+solid.D33*solid.eel33+2*solid.D34*solid.eel12+2*solid.D35*solid.eel23+2*solid.D36*solid.eel13	N/m <sup>2</sup>	Domains 1–2

Name	Expression	Unit	Selection
	lid.eel23+2*solid.D36*solid.eel13		
solid.SRR	solid.SI11	N/m <sup>2</sup>	Domains 1–2
solid.SRPHI	solid.SI12	N/m <sup>2</sup>	Domains 1–2
solid.SRZ	solid.SI13	N/m <sup>2</sup>	Domains 1–2
solid.SPHIPHI	solid.SI22	N/m <sup>2</sup>	Domains 1–2
solid.SPHIZ	solid.SI23	N/m <sup>2</sup>	Domains 1–2
solid.SZZ	solid.SI33	N/m <sup>2</sup>	Domains 1–2
solid.SR	solid.SRR	N/m <sup>2</sup>	Domains 1–2
solid.SPHI	solid.SPHIPHI	N/m <sup>2</sup>	Domains 1–2
solid.SZ	solid.SZZ	N/m <sup>2</sup>	Domains 1–2
solid.u_ttR	d(root.comp1.uTIME-uR*d(R, TIME)-uZ*d(Z, TIME), TIME)-d(root.comp1.uTIME-uR*d(R, TIME)-uZ*d(Z, TIME), R)*d(R, TIME)-d(root.comp1.uTIME-uR*d(R, TIME)-uZ*d(Z, TIME), Z)*d(Z, TIME)	m/s <sup>2</sup>	Domains 1–2
solid.u_ttPHI	0	m/s <sup>2</sup>	Domains 1–2
solid.u_ttZ	d(root.comp1.wTIME-wR*d(R, TIME)-wZ*d(Z, TIME), TIME)-d(root.comp1.wTIME-wR*d(R, TIME)-wZ*d(Z, TIME), R)*d(R, TIME)-d(root.comp1.wTIME-wR*d(R, TIME)-wZ*d(Z, TIME), Z)*d(Z, TIME)	m/s <sup>2</sup>	Domains 1–2

Name	Expression	Unit	Selection
solid.u_tR	root.comp1.uTIME- uR*d(R,TIME)- uZ*d(Z,TIME)	m/s	Domains 1-2
solid.u_tPHI	0	m/s	Domains 1-2
solid.u_tZ	root.comp1.wTIME- wR*d(R,TIME)- wZ*d(Z,TIME)	m/s	Domains 1-2
solid.accR	solid.u_ttR	m/s^2	Domains 1-2
solid.accPHI	0	m/s^2	Domains 1-2
solid.accZ	solid.u_ttZ	m/s^2	Domains 1-2
solid.vel	sqrt(real(solid.u_tR)^2+real(solid.u_tPHI)^2+real(solid.u_tZ)^2)	m/s	Domains 1-2
solid.acc	sqrt(real(solid.accR)^2+real(solid.accPHI)^2+real(solid.accZ)^2)	m/s^2	Domains 1-2
solid.G0	solid.Gequ	N/m^2	Domains 1-2
solid.Ldr	d(solid.gradUrR,TIME)- d(solid.gradUrR,R)*d(R,TIME)- d(solid.gradUrR,Z)*d(Z,TIME)	1/s	Domains 1-2
solid.Ldrphi	0.5*(d(solid.gradUrPHI,TIME)- d(solid.gradUrPHI,R)*d(R,TIME)- d(solid.gradUrPHI,Z)*d(Z,TIME)+d(solid.gradUphiR,TIME)- d(solid.gradUphiR,R)*d(R,TIME)- d(solid.gradUphiR,Z)*d(Z,TIME))	1/s	Domains 1-2
solid.Ldrz	0.5*(d(solid.gradUrZ,TIME)- d(solid.gradUrZ,R)*d(R,TIME)-	1/s	Domains 1-2

Name	Expression	Unit	Selection
	$d(\text{solid.gradUrZ,Z}) * d(Z, \text{TIME}) + d(\text{solid.gradUzR}, \text{TIME}) - d(\text{solid.gradUzR,R}) * d(R, \text{TIME}) - d(\text{solid.gradUzR,Z}) * d(Z, \text{TIME}))$		
solid.Ldphi	$d(\text{solid.gradUphiPHI, TIME}) - d(\text{solid.gradUphiPHI,R}) * d(R, \text{TIME}) - d(\text{solid.gradUphiPHI,Z}) * d(Z, \text{TIME})$	1/s	Domains 1–2
solid.Ldphiz	$0.5 * (d(\text{solid.gradUphiZ}, \text{TIME}) - d(\text{solid.gradUphiZ,R}) * d(R, \text{TIME}) - d(\text{solid.gradUphiZ,Z}) * d(Z, \text{TIME}) + d(\text{solid.gradUzPHI, TIME}) - d(\text{solid.gradUzPHI,R}) * d(R, \text{TIME}) - d(\text{solid.gradUzPHI,Z}) * d(Z, \text{TIME}))$	1/s	Domains 1–2
solid.Ldz	$d(\text{solid.gradUzZ, TIME}) - d(\text{solid.gradUzZ,R}) * d(R, \text{TIME}) - d(\text{solid.gradUzZ,Z}) * d(Z, \text{TIME})$	1/s	Domains 1–2
solid.Lwr	0	1/s	Domains 1–2
solid.Lwrphi	$0.5 * (d(\text{solid.gradUrPHI, TIME}) - d(\text{solid.gradUrPHI,R}) * d(R, \text{TIME}) - d(\text{solid.gradUrPHI,Z}) * d(Z, \text{TIME}) - d(\text{solid.gradUphiR, TIME}) + d(\text{solid.gradUphiR,R}) * d(R, \text{TIME}) + d(\text{solid.gradUphiR,Z}) * d(Z, \text{TIME}))$	1/s	Domains 1–2

Name	Expression	Unit	Selection
solid.Lwrz	$0.5*(d(\text{solid.gradUrZ,TIME})-d(\text{solid.gradUrZ,R})*d(\text{R,TIME})-d(\text{solid.gradUrZ,Z})*d(\text{Z,TIME})-d(\text{solid.gradUzR,TIME})+d(\text{solid.gradUzR,R})*d(\text{R,TIME})+d(\text{solid.gradUzR,Z})*d(\text{Z,TIME}))$	1/s	Domains 1–2
solid.Lwphi	0	1/s	Domains 1–2
solid.Lwphiz	$0.5*(d(\text{solid.gradUphiZ,TIME})-d(\text{solid.gradUphiZ,R})*d(\text{R,TIME})-d(\text{solid.gradUphiZ,Z})*d(\text{Z,TIME})-d(\text{solid.gradUzPHI,TIME})+d(\text{solid.gradUzPHI,R})*d(\text{R,TIME})+d(\text{solid.gradUzPHI,Z})*d(\text{Z,TIME}))$	1/s	Domains 1–2
solid.Lwz	0	1/s	Domains 1–2
solid.Ws	$0.5*((\text{solid.SI11}+\text{solid.Sil11})*\text{solid.eel11}+2*(\text{solid.SI12}+\text{solid.Sil12})*\text{solid.eel12}+2*(\text{solid.SI13}+\text{solid.Sil13})*\text{solid.eel13}+(\text{solid.SI22}+\text{solid.Sil22})*\text{solid.eel22}+2*(\text{solid.SI23}+\text{solid.Sil23})*\text{solid.eel23}+(\text{solid.SI33}+\text{solid.Sil33})*\text{solid.eel33})$	J/m <sup>3</sup>	Domains 1–2
solid.Wh	$0.5*((\text{solid.SI11}+\text{solid.Sil11})*\text{solid.eel11}+2*(\text{solid.SI12}+\text{solid.Sil12})*\text{solid.eel12}+2*(\text{solid.SI13}+\text{solid.Sil13})*\text{solid.eel13}+(\text{solid.SI22}+\text{solid.Sil22})*\text{solid.eel22}+2*(\text{solid.SI23}+\text{solid.Sil23})*\text{solid.eel23}+(\text{solid.SI33}+\text{solid.Sil33})*\text{solid.eel33})$	J/m <sup>3</sup>	Domains 1–2

Name	Expression	Unit	Selection
	3)*solid.eel33)		
solid.disp	$\sqrt{\text{real}(u)^2 + \text{real}(w)^2}$	m	Domains 1–2
solid.PrR	solid.FdrR*solid.SR+solid.FdrPHI*solid.SRPHI+solid.FdrZ*solid.SRZ	N/m <sup>2</sup>	Domains 1–2
solid.PphiR	solid.FdphiR*solid.SR+solid.FdphiPHI*solid.SRPHI+solid.FdphiZ*solid.SRZ	N/m <sup>2</sup>	Domains 1–2
solid.PzR	solid.FdzR*solid.SR+solid.FdzPHI*solid.SRPHI+solid.FdzZ*solid.SRZ	N/m <sup>2</sup>	Domains 1–2
solid.PrPHI	solid.FdrR*solid.SRPHI+solid.FdrPHI*solid.SPHI+solid.FdrZ*solid.SPHIZ	N/m <sup>2</sup>	Domains 1–2
solid.PphiPHI	solid.FdphiR*solid.SRPHI+solid.FdphiPHI*solid.SPHI+solid.FdphiZ*solid.SPHIZ	N/m <sup>2</sup>	Domains 1–2
solid.PzPHI	solid.FdzR*solid.SRPHI+solid.FdzPHI*solid.SPHI+solid.FdzZ*solid.SPHIZ	N/m <sup>2</sup>	Domains 1–2
solid.PrZ	solid.FdrR*solid.SRZ+solid.FdrPHI*solid.SPHIZ+solid.FdrZ*solid.SZ	N/m <sup>2</sup>	Domains 1–2
solid.PphiZ	solid.FdphiR*solid.SRZ+solid.FdphiPHI*solid.SPHIZ+solid.FdphiZ*solid.SZ	N/m <sup>2</sup>	Domains 1–2
solid.PzZ	solid.FdzR*solid.SRZ+solid.FdzPHI*solid.SPHIZ+solid.FdzZ*solid.SZ	N/m <sup>2</sup>	Domains 1–2
solid.sr	solid.SR	N/m <sup>2</sup>	Domains 1–2

<b>Name</b>	<b>Expression</b>	<b>Unit</b>	<b>Selection</b>
solid.srphi	solid.SRPHI	N/m <sup>2</sup>	Domains 1–2
solid.srz	solid.SRZ	N/m <sup>2</sup>	Domains 1–2
solid.sphi	solid.SPFI	N/m <sup>2</sup>	Domains 1–2
solid.sphiz	solid.SPHIZ	N/m <sup>2</sup>	Domains 1–2
solid.sz	solid.SZ	N/m <sup>2</sup>	Domains 1–2
solid.sl11	solid.SI11	N/m <sup>2</sup>	Domains 1–2
solid.sl12	solid.SI12	N/m <sup>2</sup>	Domains 1–2
solid.sl13	solid.SI13	N/m <sup>2</sup>	Domains 1–2
solid.sl22	solid.SI22	N/m <sup>2</sup>	Domains 1–2
solid.sl23	solid.SI23	N/m <sup>2</sup>	Domains 1–2
solid.sl33	solid.SI33	N/m <sup>2</sup>	Domains 1–2
solid.sdevr	solid.sr- (solid.sr+solid.sphi+solid.sz)/3	N/m <sup>2</sup>	Domains 1–2
solid.sdevrphi	solid.srphi	N/m <sup>2</sup>	Domains 1–2
solid.sdevrz	solid.srz	N/m <sup>2</sup>	Domains 1–2
solid.sdevphi	solid.sphi- (solid.sr+solid.sphi+solid.sz)/3	N/m <sup>2</sup>	Domains 1–2
solid.sdevphiz	solid.sphiz	N/m <sup>2</sup>	Domains 1–2
solid.sdevz	solid.sz- (solid.sr+solid.sphi+solid.sz)/3	N/m <sup>2</sup>	Domains 1–2
solid.SdevR	solid.SR- (solid.SR+solid.SPFI+solid.SZ)/3	N/m <sup>2</sup>	Domains 1–2
solid.SdevRPHI	solid.SRPHI	N/m <sup>2</sup>	Domains 1–2
solid.SdevRZ	solid.SRZ	N/m <sup>2</sup>	Domains 1–2

Name	Expression	Unit	Selection
solid.SdevPHI	solid.SPHI- (solid.SR+solid.SPHI+s olid.SZ)/3	N/m <sup>2</sup>	Domains 1–2
solid.SdevPHIZ	solid.SP Hiz	N/m <sup>2</sup>	Domains 1–2
solid.SdevZ	solid.SZ- (solid.SR+solid.SP HI+s olid.SZ)/3	N/m <sup>2</sup>	Domains 1–2
solid.I1s	solid.sl11+solid.sl22+sol id.sl33	N/m <sup>2</sup>	Domains 1–2
solid.I2s	0.5*(solid.I1s <sup>2</sup> - solid.sl11 <sup>2</sup> - 2*solid.sl12 <sup>2</sup> - 2*solid.sl13 <sup>2</sup> - solid.sl22 <sup>2</sup> - 2*solid.sl23 <sup>2</sup> - solid.sl33 <sup>2</sup> )	kg <sup>2</sup> /(m <sup>2</sup> *s <sup>4</sup> )	Domains 1–2
solid.I3s	solid.sl11*solid.sl22*soli d.sl33+2*solid.sl12*soli d.sl23*solid.sl13- solid.sl11*solid.sl23 <sup>2</sup> - solid.sl12 <sup>2</sup> *solid.sl33- solid.sl22*solid.sl13 <sup>2</sup>	kg <sup>3</sup> /(m <sup>3</sup> *s <sup>6</sup> )	Domains 1–2
solid.II2s	0.5*((solid.sl11- (solid.sl11+solid.sl22+s olid.sl33)/3) <sup>2</sup> +2*solid.s l12 <sup>2</sup> +2*solid.sl13 <sup>2</sup> +(s olid.sl22- (solid.sl11+solid.sl22+s olid.sl33)/3) <sup>2</sup> +2*solid.s l23 <sup>2</sup> +(solid.sl33- (solid.sl11+solid.sl22+s olid.sl33)/3) <sup>2</sup> )	kg <sup>2</sup> /(m <sup>2</sup> *s <sup>4</sup> )	Domains 1–2
solid.II3s	(solid.sl11- (solid.sl11+solid.sl22+s olid.sl33)/3)*(solid.sl22- (solid.sl11+solid.sl22+s olid.sl33)/3)*(solid.sl33- (solid.sl11+solid.sl22+s olid.sl33)/3)+2*solid.sl1 2*solid.sl23*solid.sl13-	kg <sup>3</sup> /(m <sup>3</sup> *s <sup>6</sup> )	Domains 1–2



Name	Expression	Unit	Selection
	$\frac{(solid.sl11 - (solid.sl11 + solid.sl22 + solid.sl33)/3) * solid.sl23^2 - solid.sl12^2 * (solid.sl33 - (solid.sl11 + solid.sl22 + solid.sl33)/3) - (solid.sl11 + solid.sl22 + solid.sl33)/3 * solid.sl13^2}{2}$		
solid.thetaL	$\text{atan2}(\sqrt{\max(0, 14814814814814814 * solid.II2s^3 - solid.II3s^2, \text{eps})}, solid.II3s)/3$	rad	Domains 1–2
solid.eelvol	$solid.eel11 + solid.eel22 + solid.eel33$	1	Domains 1–2
solid.eeldev11	$solid.eel11 - (solid.eel11 + solid.eel22 + solid.eel33)/3$	1	Domains 1–2
solid.eeldev12	$solid.eel12$	1	Domains 1–2
solid.eeldev13	$solid.eel13$	1	Domains 1–2
solid.eeldev22	$solid.eel22 - (solid.eel11 + solid.eel22 + solid.eel33)/3$	1	Domains 1–2
solid.eeldev23	$solid.eel23$	1	Domains 1–2
solid.eeldev33	$solid.eel33 - (solid.eel11 + solid.eel22 + solid.eel33)/3$	1	Domains 1–2
solid.II2eel	$0.5 * ((solid.eel11 - (solid.eel11 + solid.eel22 + solid.eel33)/3)^2 + 2 * solid.eel12^2 + 2 * solid.eel13^2 + (solid.eel22 - (solid.eel11 + solid.eel22 + solid.eel33)/3)^2 + 2 * solid.eel23^2 + (solid.eel33 - (solid.eel11 + solid.eel22 + solid.eel33)/3)^2)$	1	Domains 1–2

Name	Expression	Unit	Selection
	+solid.eel33)/3)^2)		
solid.pm	- (solid.sl11+solid.sl22+solid.sl33)/3	N/m <sup>2</sup>	Domains 1–2
solid.curlUR	0	1	Domains 1–2
solid.curlUPHI	solid.gradUrZ- solid.gradUzR	1	Domains 1–2
solid.curlUZ	0	1	Domains 1–2
solid.mises	(3*solid.II2s)^0.5	N/m <sup>2</sup>	Domains 1–2
solid.tresca	solid.sp1-solid.sp3	N/m <sup>2</sup>	Domains 1–2
solid.Tar	solid.sr*solid.nr+solid.sr phi*solid.nphi+solid.srz *solid.nz	N/m <sup>2</sup>	Boundaries 1–7, 12–13
solid.Taphi	solid.srphi*solid.nr+soli d.sphi*solid.nphi+solid.s phiz*solid.nz	N/m <sup>2</sup>	Boundaries 1–7, 12–13
solid.Taz	solid.srz*solid.nr+solid.s phiz*solid.nphi+solid.sz *solid.nz	N/m <sup>2</sup>	Boundaries 1–7, 12–13
solid.Ws_tot	root.comp1.solid.lemm2. int7(2*solid.Ws*pi*R)	J	Global
solid.Wh_tot	root.comp1.solid.lemm2. int8(2*solid.Wh*pi*R)	J	Global
solid.RFr	reactf(u)	N	Domains 1–2
solid.RFphi	0	N	Domains 1–2
solid.RFz	reactf(w)	N	Domains 1–2
solid.RMr	- solid.RFz*solid.refpntph i-solid.RFphi*(z- solid.refpntz)	N*m	Domains 1–2
solid.RMphi	-solid.RFz*(r- solid.refpntr)+solid.RFr*	N*m	Domains 1–2

Name	Expression	Unit	Selection
	(z-solid.refpntz)		
solid.RMz	solid.RFphi*(r-solid.refpntr)+solid.RFr*solid.refpntphi	N*m	Domains 1–2

Shape functions

Name	Shape function	Unit	Description	Shape frame	Selection
u	Lagrange (Quadratic)	m	Displacement field, R component	Material	Domains 1–2
w	Lagrange (Quadratic)	m	Displacement field, Z component	Material	Domains 1–2

Weak expressions

Weak expression	Integration frame	Selection
2*(-solid.SI11*var(solid.el11,u)-2*solid.SI12*var(solid.el12,u)-2*solid.SI13*var(solid.el13,u)-solid.SI22*var(solid.el22,u)-2*solid.SI23*var(solid.el23,u)-solid.SI33*var(solid.el33,u))*pi*R	Material	Domains 1–2

Inelastic Strain

Selection

Geometric entity level Domain

Selection Domains 1–2

Equations

$$\epsilon_0 = \underline{\underline{\epsilon_0}}$$

$$S_0 = \underline{\underline{S_0}}$$

Variables

Name	Expression	Unit	Selection
solid.eil11	ne_strain_r_UO2	1	Domains 1-2
solid.eil12	0	1	Domains 1-2
solid.eil13	0	1	Domains 1-2
solid.eil22	ne_strain_phi_UO2	1	Domains 1-2
solid.eil23	0	1	Domains 1-2
solid.eil33	ne_strain_z_UO2	1	Domains 1-2
solid.Sil11	0	N/m^2	Domains 1-2
solid.Sil12	0	N/m^2	Domains 1-2
solid.Sil13	0	N/m^2	Domains 1-2
solid.Sil22	0	N/m^2	Domains 1-2
solid.Sil23	0	N/m^2	Domains 1-2
solid.Sil33	0	N/m^2	Domains 1-2

Sheath Domains

Selection

Geometric entity level Domain

Selection Domain 3

Equations

$$\underline{0} = \underline{\nabla} \cdot \underline{F S} + \underline{F V}, \quad \underline{F} = \underline{I} + \underline{\nabla} \underline{u}$$

$$\underline{S} = \underline{S}_{ad} + \underline{C} : \underline{\epsilon}_{el}, \quad \underline{\epsilon}_{el} = \underline{\epsilon} - \underline{\epsilon}_{inel}$$

$$\underline{S}_{ad} = \underline{S}_0 + \underline{S}_{ext} + \underline{S}_q$$

$$\underline{\epsilon}_{inel} = \underline{\epsilon}_0 + \underline{\epsilon}_{th} + \underline{\epsilon}_{hs} + \underline{\epsilon}_{pl} + \underline{\epsilon}_{cr}$$

$$\underline{\epsilon} = \frac{1}{2} \left[ (\underline{\nabla} \underline{u})^T + \underline{\nabla} \underline{u} + (\underline{\nabla} \underline{u})^T \underline{\nabla} \underline{u} \right]$$

## Settings

Description	Value
Solid model	Isotropic
Force linear strains	Off
Nearly incompressible material	Off
Specify	Young's modulus and Poisson's ratio
Calculate dissipated energy	Off
Young's modulus	From material
Poisson's ratio	From material
Density	From material

## Properties from material

Property	Material	Property group
Young's modulus	Zircaloy	Basic
Poisson's ratio	Zircaloy	Basic
Density	Zircaloy	Basic

## Variables

Name	Expression	Unit	Selection
solid.rho	material.rho	kg/m <sup>3</sup>	Domain 3
solid.Qh	0	W/m <sup>3</sup>	Domain 3
solid.gradUrR	uR	1	Domain 3
solid.gradUphiR	0	1	Domain 3
solid.gradUzR	wR	1	Domain 3
solid.gradUrPHI	0	1	Domain 3
solid.gradUphiPHI	if(abs(R)<0.001*h,uR,u/R)	1	Domain 3

Name	Expression	Unit	Selection
solid.gradUzPHI	0	1	Domain 3
solid.gradUrZ	uZ	1	Domain 3
solid.gradUphiZ	0	1	Domain 3
solid.gradUzZ	wZ	1	Domain 3
solid.FdrR	1+solid.gradUrR	1	Domain 3
solid.FdphiR	solid.gradUphiR	1	Domain 3
solid.FdzR	solid.gradUzR	1	Domain 3
solid.FdrPHI	solid.gradUrPHI	1	Domain 3
solid.FdphiPHI	1+solid.gradUphiPHI	1	Domain 3
solid.FdzPHI	solid.gradUzPHI	1	Domain 3
solid.FdrZ	solid.gradUrZ	1	Domain 3
solid.FdphiZ	solid.gradUphiZ	1	Domain 3
solid.FdzZ	1+solid.gradUzZ	1	Domain 3
solid.Fdlr1	solid.FdrR	1	Domain 3
solid.Fdlphi1	solid.FdphiR	1	Domain 3
solid.Fdlz1	solid.FdzR	1	Domain 3
solid.Fdlr2	solid.FdrPHI	1	Domain 3
solid.Fdlphi2	solid.FdphiPHI	1	Domain 3
solid.Fdlz2	solid.FdzPHI	1	Domain 3
solid.Fdlr3	solid.FdrZ	1	Domain 3
solid.Fdlphi3	solid.FdphiZ	1	Domain 3
solid.Fdlz3	solid.FdzZ	1	Domain 3
uRt	root.comp1.uRTIME-uRR*d(R,TIME)-uRZ*d(Z,TIME)	1/s	Domain 3
uZt	root.comp1.uZTIME-uZR*d(R,TIME)-uZZ*d(Z,TIME)	1/s	Domain 3
uRtt	d(root.comp1.uRTIME-uRR*d(R,TIME)-uRZ*d(Z,TIME),TIME)-d(root.comp1.uRTIME-	1/s^2	Domain 3

Name	Expression	Unit	Selection
	$uRR*d(R,TIME)-uRZ*d(Z,TIME),R)*d(R,TIME)-d(\text{root.comp1.uRTIME}-uRR*d(R,TIME)-uRZ*d(Z,TIME),Z)*d(Z,TIME)$		
uZtt	$d(\text{root.comp1.uZTIME}-uZR*d(R,TIME)-uZZ*d(Z,TIME),TIME)-d(\text{root.comp1.uZTIME}-uZR*d(R,TIME)-uZZ*d(Z,TIME),R)*d(R,TIME)-d(\text{root.comp1.uZTIME}-uZR*d(R,TIME)-uZZ*d(Z,TIME),Z)*d(Z,TIME)$	1/s <sup>2</sup>	Domain 3
wRt	$\text{root.comp1.wRTIME}-wRR*d(R,TIME)-wRZ*d(Z,TIME)$	1/s	Domain 3
wZt	$\text{root.comp1.wZTIME}-wZR*d(R,TIME)-wZZ*d(Z,TIME)$	1/s	Domain 3
wRtt	$d(\text{root.comp1.wRTIME}-wRR*d(R,TIME)-wRZ*d(Z,TIME),TIME)-d(\text{root.comp1.wRTIME}-wRR*d(R,TIME)-wRZ*d(Z,TIME),R)*d(R,TIME)-d(\text{root.comp1.wRTIME}-wRR*d(R,TIME)-wRZ*d(Z,TIME),Z)*d(Z,TIME)$	1/s <sup>2</sup>	Domain 3
wZtt	$d(\text{root.comp1.wZTIME}-wZR*d(R,TIME)-wZZ*d(Z,TIME),TIME)-d(\text{root.comp1.wZTIME}-wZR*d(R,TIME)-wZZ*d(Z,TIME),R)*d(R,TIME)-d(\text{root.comp1.wZTIME}-wZR*d(R,TIME)-wZZ*d(Z,TIME),Z)*d(Z,TIME)$	1/s <sup>2</sup>	Domain 3
ut	$\text{root.comp1.uTIME}-uR*d(R,TIME)-uZ*d(Z,TIME)$	m/s	Domain 3
wt	$\text{root.comp1.wTIME}-wR*d(R,TIME)-wZ*d(Z,TIME)$	m/s	Domain 3
utt	$d(\text{root.comp1.uTIME}-uR*d(R,TIME)-uZ*d(Z,TIME),TIME)-d(\text{root.comp1.uTIME}-uR*d(R,TIME)-uZ*d(Z,TIME),R)*d(R,TIME)-d(\text{root.comp1.uTIME}-uR*d(R,TIME)-uZ*d(Z,TIME),Z)*d(Z,TIME)$	m/s <sup>2</sup>	Domain 3
wtt	$d(\text{root.comp1.wTIME}-wR*d(R,TIME)-wZ*d(Z,TIME),TIME)-d(\text{root.comp1.wTIME}-wR*d(R,TIME)-wZ*d(Z,TIME),R)*d(R,TIME)-d(\text{root.comp1.wTIME}-wR*d(R,TIME)-wZ*d(Z,TIME),Z)*d(Z,TIME)$	m/s <sup>2</sup>	Domain 3
solid.D11	$\text{solid.E}*(1-\text{solid.nu})/((1+\text{solid.nu})*(1-2*\text{solid.nu}))$	Pa	Domain 3
solid.D12	$\text{solid.E}*\text{solid.nu}/((1+\text{solid.nu})*(1-2*\text{solid.nu}))$	Pa	Domain 3
solid.D13	$\text{solid.E}*\text{solid.nu}/((1+\text{solid.nu})*(1-2*\text{solid.nu}))$	Pa	Domain 3

Name	Expression	Unit	Selection
solid.D14	0	Pa	Domain 3
solid.D15	0	Pa	Domain 3
solid.D16	0	Pa	Domain 3
solid.D22	$\text{solid.E} \cdot (1 - \text{solid.nu}) / ((1 + \text{solid.nu}) \cdot (1 - 2 \cdot \text{solid.nu}))$	Pa	Domain 3
solid.D23	$\text{solid.E} \cdot \text{solid.nu} / ((1 + \text{solid.nu}) \cdot (1 - 2 \cdot \text{solid.nu}))$	Pa	Domain 3
solid.D24	0	Pa	Domain 3
solid.D25	0	Pa	Domain 3
solid.D26	0	Pa	Domain 3
solid.D33	$\text{solid.E} \cdot (1 - \text{solid.nu}) / ((1 + \text{solid.nu}) \cdot (1 - 2 \cdot \text{solid.nu}))$	Pa	Domain 3
solid.D34	0	Pa	Domain 3
solid.D35	0	Pa	Domain 3
solid.D36	0	Pa	Domain 3
solid.D44	$0.5 \cdot \text{solid.E} / (1 + \text{solid.nu})$	Pa	Domain 3
solid.D45	0	Pa	Domain 3
solid.D46	0	Pa	Domain 3
solid.D55	$0.5 \cdot \text{solid.E} / (1 + \text{solid.nu})$	Pa	Domain 3
solid.D56	0	Pa	Domain 3
solid.D66	$0.5 \cdot \text{solid.E} / (1 + \text{solid.nu})$	Pa	Domain 3
solid.K	$\text{solid.E} / (3 \cdot (1 - 2 \cdot \text{solid.nu}))$	N/m <sup>2</sup>	Domain 3
solid.Eequ	solid.E	Pa	Domain 3
solid.nuequ	solid.nu	1	Domain 3
solid.Gequ	solid.G	N/m <sup>2</sup>	Domain 3
solid.cp	$\sqrt{(\text{solid.K} + 4 \cdot \text{solid.G} / 3) / \text{solid.rho}}$	m/s	Domain 3
solid.cs	$\sqrt{\text{solid.G} / \text{solid.rho}}$	m/s	Domain 3
solid.E	material.E	Pa	Domain 3



Name	Expression	Unit	Selection
solid.nu	material.nu	1	Domain 3
solid.G	$0.5 * \text{solid.E} / (1 + \text{solid.nu})$	N/m <sup>2</sup>	Domain 3
solid.lambLame	$\text{solid.E} * \text{solid.nu} / ((1 + \text{solid.nu}) * (1 - 2 * \text{solid.nu}))$	N/m <sup>2</sup>	Domain 3
solid.muLame	$0.5 * \text{solid.E} / (1 + \text{solid.nu})$	N/m <sup>2</sup>	Domain 3
solid.Cgl11	solid.D11+solid.D12+solid.D13	Pa	Domain 3
solid.Cgl12	solid.D14+solid.D24+solid.D34	Pa	Domain 3
solid.Cgl13	solid.D16+solid.D26+solid.D36	Pa	Domain 3
solid.Cgl22	solid.D12+solid.D22+solid.D23	Pa	Domain 3
solid.Cgl23	solid.D15+solid.D25+solid.D35	Pa	Domain 3
solid.Cgl33	solid.D13+solid.D23+solid.D33	Pa	Domain 3
solid.eRR	uR	1	Domain 3
solid.eRPHI	0	1	Domain 3
solid.eRZ	$0.5 * (uZ + wR)$	1	Domain 3
solid.ePHIPHI	if(abs(R)<0.001*h,uR,u/R)	1	Domain 3
solid.ePHIZ	0	1	Domain 3
solid.eZZ	wZ	1	Domain 3
solid.el11	solid.eRR	1	Domain 3
solid.el12	solid.eRPHI	1	Domain 3
solid.el13	solid.eRZ	1	Domain 3
solid.el22	solid.ePHIPHI	1	Domain 3
solid.el23	solid.ePHIZ	1	Domain 3
solid.el33	solid.eZZ	1	Domain 3
solid.eel11	solid.el11-solid.eil11-solid.eiel11	1	Domain 3
solid.eel12	solid.el12-solid.eil12-solid.eiel12	1	Domain 3
solid.eel13	solid.el13-solid.eil13-solid.eiel13	1	Domain 3

Name	Expression	Unit	Selection
solid.eel22	solid.el22-solid.eil22-solid.eiel22	1	Domain 3
solid.eel23	solid.el23-solid.eil23-solid.eiel23	1	Domain 3
solid.eel33	solid.el33-solid.eil33-solid.eiel33	1	Domain 3
solid.Cel11	1+2*solid.eel11	1	Domain 3
solid.Cel12	2*solid.eel12	1	Domain 3
solid.Cel13	2*solid.eel13	1	Domain 3
solid.Cel22	1+2*solid.eel22	1	Domain 3
solid.Cel23	2*solid.eel23	1	Domain 3
solid.Cel33	1+2*solid.eel33	1	Domain 3
solid.eil11	0	1	Domain 3
solid.eil12	0	1	Domain 3
solid.eil13	0	1	Domain 3
solid.eil22	0	1	Domain 3
solid.eil23	0	1	Domain 3
solid.eil33	0	1	Domain 3
solid.eiel11	0	1	Domain 3
solid.eiel12	0	1	Domain 3
solid.eiel13	0	1	Domain 3
solid.eiel22	0	1	Domain 3
solid.eiel23	0	1	Domain 3
solid.eiel33	0	1	Domain 3
solid.evol	solid.eRR+solid.ePHIPHI+solid.eZZ	1	Domain 3
solid.J	solid.FdrR*solid.FdphiPHI*solid.FdzZ+solid.FdrPHI*solid.FdphiZ*solid.FdzR+solid.FdrZ*solid.FdphiR*solid.FdzPHI-solid.FdrR*solid.FdphiZ*solid.FdzPHI-solid.FdrPHI*solid.FdphiR*solid.FdzZ-solid.FdrZ*solid.FdphiPHI*solid.FdzR	1	Domain 3

Name	Expression	Unit	Selection
solid.Ceil11	$(\text{solid.Cel22} * \text{solid.Cel33} - \text{solid.Cel23}^2) / (\text{solid.Cel11} * \text{solid.Cel22} * \text{solid.Cel33} + 2 * \text{solid.Cel12} * \text{solid.Cel23} * \text{solid.Cel13} - \text{solid.Cel11} * \text{solid.Cel23}^2 - \text{solid.Cel12}^2 * \text{solid.Cel33} - \text{solid.Cel22} * \text{solid.Cel13}^2)$	1	Domain 3
solid.Ceil12	$(\text{solid.Cel23} * \text{solid.Cel13} - \text{solid.Cel12} * \text{solid.Cel33}) / (\text{solid.Cel11} * \text{solid.Cel22} * \text{solid.Cel33} + 2 * \text{solid.Cel12} * \text{solid.Cel23} * \text{solid.Cel13} - \text{solid.Cel11} * \text{solid.Cel23}^2 - \text{solid.Cel12}^2 * \text{solid.Cel33} - \text{solid.Cel22} * \text{solid.Cel13}^2)$	1	Domain 3
solid.Ceil13	$(\text{solid.Cel12} * \text{solid.Cel23} - \text{solid.Cel22} * \text{solid.Cel13}) / (\text{solid.Cel11} * \text{solid.Cel22} * \text{solid.Cel33} + 2 * \text{solid.Cel12} * \text{solid.Cel23} * \text{solid.Cel13} - \text{solid.Cel11} * \text{solid.Cel23}^2 - \text{solid.Cel12}^2 * \text{solid.Cel33} - \text{solid.Cel22} * \text{solid.Cel13}^2)$	1	Domain 3
solid.Ceil22	$(\text{solid.Cel11} * \text{solid.Cel33} - \text{solid.Cel13}^2) / (\text{solid.Cel11} * \text{solid.Cel22} * \text{solid.Cel33} + 2 * \text{solid.Cel12} * \text{solid.Cel23} * \text{solid.Cel13} - \text{solid.Cel11} * \text{solid.Cel23}^2 - \text{solid.Cel12}^2 * \text{solid.Cel33} - \text{solid.Cel22} * \text{solid.Cel13}^2)$	1	Domain 3
solid.Ceil23	$(\text{solid.Cel12} * \text{solid.Cel13} - \text{solid.Cel11} * \text{solid.Cel23}) / (\text{solid.Cel11} * \text{solid.Cel22} * \text{solid.Cel33} + 2 * \text{solid.Cel12} * \text{solid.Cel23} * \text{solid.Cel13} - \text{solid.Cel11} * \text{solid.Cel23}^2 - \text{solid.Cel12}^2 * \text{solid.Cel33} - \text{solid.Cel22} * \text{solid.Cel13}^2)$	1	Domain 3
solid.Ceil33	$(\text{solid.Cel11} * \text{solid.Cel22} - \text{solid.Cel12}^2) / (\text{solid.Cel11} * \text{solid.Cel22} * \text{solid.Cel33} + 2 * \text{solid.Cel12} * \text{solid.Cel23} * \text{solid.Cel13} - \text{solid.Cel11} * \text{solid.Cel23}^2 - \text{solid.Cel12}^2 * \text{solid.Cel33} - \text{solid.Cel22} * \text{solid.Cel13}^2)$	1	Domain 3
solid.Jel	$\sqrt{(\text{solid.Cel11} * \text{solid.Cel22} * \text{solid.Cel33} + 2 * \text{solid.Cel12} * \text{solid.Cel23} * \text{solid.Cel13} - \text{solid.Cel11} * \text{solid.Cel23}^2 - \text{solid.Cel12}^2 * \text{solid.Cel33} - \text{solid.Cel22} * \text{solid.Cel13}^2)}$	1	Domain 3
solid.eR	solid.eRR	1	Domain 3
solid.ePHI	solid.ePHIPHI	1	Domain 3
solid.eZ	solid.eZZ	1	Domain 3
solid.Sil11	0	N/m <sup>2</sup>	Domain 3

Name	Expression	Unit	Selection
solid.Sil12	0	N/m <sup>2</sup>	Domain 3
solid.Sil13	0	N/m <sup>2</sup>	Domain 3
solid.Sil22	0	N/m <sup>2</sup>	Domain 3
solid.Sil23	0	N/m <sup>2</sup>	Domain 3
solid.Sil33	0	N/m <sup>2</sup>	Domain 3
solid.SI11	solid.Sil11+solid.D11*solid.eel11+solid.D12*solid.eel22+solid.D13*solid.eel33+2*solid.D14*solid.eel12+2*solid.D15*solid.eel23+2*solid.D16*solid.eel13	N/m <sup>2</sup>	Domain 3
solid.SI12	solid.Sil12+solid.D14*solid.eel11+solid.D24*solid.eel22+solid.D34*solid.eel33+2*solid.D44*solid.eel12+2*solid.D45*solid.eel23+2*solid.D46*solid.eel13	N/m <sup>2</sup>	Domain 3
solid.SI13	solid.Sil13+solid.D16*solid.eel11+solid.D26*solid.eel22+solid.D36*solid.eel33+2*solid.D46*solid.eel12+2*solid.D56*solid.eel23+2*solid.D66*solid.eel13	N/m <sup>2</sup>	Domain 3
solid.SI22	solid.Sil22+solid.D12*solid.eel11+solid.D22*solid.eel22+solid.D23*solid.eel33+2*solid.D24*solid.eel12+2*solid.D25*solid.eel23+2*solid.D26*solid.eel13	N/m <sup>2</sup>	Domain 3
solid.SI23	solid.Sil23+solid.D15*solid.eel11+solid.D25*solid.eel22+solid.D35*solid.eel33+2*solid.D45*solid.eel12+2*solid.D55*solid.eel23+2*solid.D56*solid.eel13	N/m <sup>2</sup>	Domain 3
solid.SI33	solid.Sil33+solid.D13*solid.eel11+solid.D23*solid.eel22+solid.D33*solid.eel33+2*solid.D34*solid.eel12+2*solid.D35*solid.eel23+2*solid.D36*solid.eel13	N/m <sup>2</sup>	Domain 3
solid.SRR	solid.SI11	N/m <sup>2</sup>	Domain 3
solid.SRPHI	solid.SI12	N/m <sup>2</sup>	Domain 3
solid.SRZ	solid.SI13	N/m <sup>2</sup>	Domain 3
solid.SPHIPHI	solid.SI22	N/m <sup>2</sup>	Domain 3
solid.SPHIZ	solid.SI23	N/m <sup>2</sup>	Domain 3
solid.SZZ	solid.SI33	N/m <sup>2</sup>	Domain 3
solid.SR	solid.SRR	N/m <sup>2</sup>	Domain 3

Name	Expression	Unit	Selection
solid.SPFI	solid.SPFI PHI	N/m <sup>2</sup>	Domain 3
solid.SZ	solid.SZZ	N/m <sup>2</sup>	Domain 3
solid.u_ttR	d(root.comp1.uTIME-uR*d(R, TIME)- uZ*d(Z, TIME), TIME)-d(root.comp1.uTIME- uR*d(R, TIME)-uZ*d(Z, TIME), R)*d(R, TIME)- d(root.comp1.uTIME-uR*d(R, TIME)- uZ*d(Z, TIME), Z)*d(Z, TIME)	m/s <sup>2</sup>	Domain 3
solid.u_ttPHI	0	m/s <sup>2</sup>	Domain 3
solid.u_ttZ	d(root.comp1.wTIME-wR*d(R, TIME)- wZ*d(Z, TIME), TIME)-d(root.comp1.wTIME- wR*d(R, TIME)-wZ*d(Z, TIME), R)*d(R, TIME)- d(root.comp1.wTIME-wR*d(R, TIME)- wZ*d(Z, TIME), Z)*d(Z, TIME)	m/s <sup>2</sup>	Domain 3
solid.u_tR	root.comp1.uTIME-uR*d(R, TIME)-uZ*d(Z, TIME)	m/s	Domain 3
solid.u_tPHI	0	m/s	Domain 3
solid.u_tZ	root.comp1.wTIME-wR*d(R, TIME)-wZ*d(Z, TIME)	m/s	Domain 3
solid.accR	solid.u_ttR	m/s <sup>2</sup>	Domain 3
solid.accPHI	0	m/s <sup>2</sup>	Domain 3
solid.accZ	solid.u_ttZ	m/s <sup>2</sup>	Domain 3
solid.vel	sqrt(real(solid.u_tR)^2+real(solid.u_tPHI)^2+real(solid.u_t Z)^2)	m/s	Domain 3
solid.acc	sqrt(real(solid.accR)^2+real(solid.accPHI)^2+real(solid.acc Z)^2)	m/s <sup>2</sup>	Domain 3
solid.G0	solid.Gequ	N/m <sup>2</sup>	Domain 3
solid.Ldr	d(solid.gradUrR, TIME)-d(solid.gradUrR, R)*d(R, TIME)- d(solid.gradUrR, Z)*d(Z, TIME)	1/s	Domain 3
solid.Ldrphi	0.5*(d(solid.gradUrPHI, TIME)- d(solid.gradUrPHI, R)*d(R, TIME)- d(solid.gradUrPHI, Z)*d(Z, TIME)+d(solid.gradUphiR, TIM E)-d(solid.gradUphiR, R)*d(R, TIME)- d(solid.gradUphiR, Z)*d(Z, TIME))	1/s	Domain 3
solid.Ldrz	0.5*(d(solid.gradUrZ, TIME)- d(solid.gradUrZ, R)*d(R, TIME)-	1/s	Domain 3

Name	Expression	Unit	Selection
	$d(\text{solid.gradUrZ,Z}) * d(Z, \text{TIME}) + d(\text{solid.gradUzR, TIME}) - d(\text{solid.gradUzR,R}) * d(R, \text{TIME}) - d(\text{solid.gradUzR,Z}) * d(Z, \text{TIME})$		
solid.Ldphi	$d(\text{solid.gradUphiPHI, TIME}) - d(\text{solid.gradUphiPHI,R}) * d(R, \text{TIME}) - d(\text{solid.gradUphiPHI,Z}) * d(Z, \text{TIME})$	1/s	Domain 3
solid.Ldphiz	$0.5 * (d(\text{solid.gradUphiZ, TIME}) - d(\text{solid.gradUphiZ,R}) * d(R, \text{TIME}) - d(\text{solid.gradUphiZ,Z}) * d(Z, \text{TIME}) + d(\text{solid.gradUzPHI, TIME}) - d(\text{solid.gradUzPHI,R}) * d(R, \text{TIME}) - d(\text{solid.gradUzPHI,Z}) * d(Z, \text{TIME}))$	1/s	Domain 3
solid.Ldz	$d(\text{solid.gradUzZ, TIME}) - d(\text{solid.gradUzZ,R}) * d(R, \text{TIME}) - d(\text{solid.gradUzZ,Z}) * d(Z, \text{TIME})$	1/s	Domain 3
solid.Lwr	0	1/s	Domain 3
solid.Lwrphi	$0.5 * (d(\text{solid.gradUrPHI, TIME}) - d(\text{solid.gradUrPHI,R}) * d(R, \text{TIME}) - d(\text{solid.gradUrPHI,Z}) * d(Z, \text{TIME}) - d(\text{solid.gradUphiR, TIME}) + d(\text{solid.gradUphiR,R}) * d(R, \text{TIME}) + d(\text{solid.gradUphiR,Z}) * d(Z, \text{TIME}))$	1/s	Domain 3
solid.Lwrz	$0.5 * (d(\text{solid.gradUrZ, TIME}) - d(\text{solid.gradUrZ,R}) * d(R, \text{TIME}) - d(\text{solid.gradUrZ,Z}) * d(Z, \text{TIME}) - d(\text{solid.gradUzR, TIME}) + d(\text{solid.gradUzR,R}) * d(R, \text{TIME}) + d(\text{solid.gradUzR,Z}) * d(Z, \text{TIME}))$	1/s	Domain 3
solid.Lwphi	0	1/s	Domain 3
solid.Lwphiz	$0.5 * (d(\text{solid.gradUphiZ, TIME}) - d(\text{solid.gradUphiZ,R}) * d(R, \text{TIME}) - d(\text{solid.gradUphiZ,Z}) * d(Z, \text{TIME}) - d(\text{solid.gradUzPHI, TIME}) + d(\text{solid.gradUzPHI,R}) * d(R, \text{TIME}) + d(\text{solid.gradUzPHI,Z}) * d(Z, \text{TIME}))$	1/s	Domain 3
solid.Lwz	0	1/s	Domain 3
solid.Ws	$0.5 * ((\text{solid.S111} + \text{solid.Sil11}) * \text{solid.eel11} + 2 * (\text{solid.S112} + \text{solid.Sil12}) * \text{solid.eel12} + 2 * (\text{solid.S113} + \text{solid.Sil13}) * \text{solid.eel13} + (\text{solid.S122} + \text{solid.Sil22}) * \text{solid.eel22} + 2 * (\text{solid.S123} + \text{solid.Sil23}) * \text{solid.eel23} + (\text{solid.S133} + \text{solid.Sil33}) * \text{solid.eel33})$	J/m <sup>3</sup>	Domain 3
solid.Wh	$0.5 * ((\text{solid.S111} + \text{solid.Sil11}) * \text{solid.eel11} + 2 * (\text{solid.S112} + \text{solid.Sil12}) * \text{solid.eel12} + 2 * (\text{solid.S113} + \text{solid.Sil13}) * \text{solid.eel13} + (\text{solid.S122} + \text{solid.Sil22}) * \text{solid.eel22} + 2 * (\text{solid.S123} + \text{solid.Sil23}) * \text{solid.eel23} + (\text{solid.S133} + \text{solid.Sil33}) * \text{solid.eel33})$	J/m <sup>3</sup>	Domain 3

Name	Expression	Unit	Selection
	$13+(\text{solid.SI22}+\text{solid.Sil22})*\text{solid.eel22}+2*(\text{solid.SI23}+\text{solid.Sil23})*\text{solid.eel23}+(\text{solid.SI33}+\text{solid.Sil33})*\text{solid.eel33}$		
solid.disp	$\text{sqrt}(\text{real}(u)^2+\text{real}(w)^2)$	M	Domain 3
solid.PrR	$\text{solid.FdrR}*\text{solid.SR}+\text{solid.FdrPHI}*\text{solid.SRPHI}+\text{solid.FdrZ}*\text{solid.SRZ}$	N/m <sup>2</sup>	Domain 3
solid.PphiR	$\text{solid.FdphiR}*\text{solid.SR}+\text{solid.FdphiPHI}*\text{solid.SRPHI}+\text{solid.FdphiZ}*\text{solid.SRZ}$	N/m <sup>2</sup>	Domain 3
solid.PzR	$\text{solid.FdzR}*\text{solid.SR}+\text{solid.FdzPHI}*\text{solid.SRPHI}+\text{solid.FdzZ}*\text{solid.SRZ}$	N/m <sup>2</sup>	Domain 3
solid.PrPHI	$\text{solid.FdrR}*\text{solid.SRPHI}+\text{solid.FdrPHI}*\text{solid.SPHI}+\text{solid.FdrZ}*\text{solid.SPHIZ}$	N/m <sup>2</sup>	Domain 3
solid.PphiPHI	$\text{solid.FdphiR}*\text{solid.SRPHI}+\text{solid.FdphiPHI}*\text{solid.SPHI}+\text{solid.FdphiZ}*\text{solid.SPHIZ}$	N/m <sup>2</sup>	Domain 3
solid.PzPHI	$\text{solid.FdzR}*\text{solid.SRPHI}+\text{solid.FdzPHI}*\text{solid.SPHI}+\text{solid.FdzZ}*\text{solid.SPHIZ}$	N/m <sup>2</sup>	Domain 3
solid.PrZ	$\text{solid.FdrR}*\text{solid.SRZ}+\text{solid.FdrPHI}*\text{solid.SPHIZ}+\text{solid.FdrZ}*\text{solid.SZ}$	N/m <sup>2</sup>	Domain 3
solid.PphiZ	$\text{solid.FdphiR}*\text{solid.SRZ}+\text{solid.FdphiPHI}*\text{solid.SPHIZ}+\text{solid.FdphiZ}*\text{solid.SZ}$	N/m <sup>2</sup>	Domain 3
solid.PzZ	$\text{solid.FdzR}*\text{solid.SRZ}+\text{solid.FdzPHI}*\text{solid.SPHIZ}+\text{solid.FdzZ}*\text{solid.SZ}$	N/m <sup>2</sup>	Domain 3
solid.sr	solid.SR	N/m <sup>2</sup>	Domain 3
solid.srphi	solid.SRPHI	N/m <sup>2</sup>	Domain 3
solid.srz	solid.SRZ	N/m <sup>2</sup>	Domain 3
solid.sphi	solid.SPHI	N/m <sup>2</sup>	Domain 3
solid.sphiz	solid.SPHIZ	N/m <sup>2</sup>	Domain 3
solid.sz	solid.SZ	N/m <sup>2</sup>	Domain 3
solid.sl11	solid.SI11	N/m <sup>2</sup>	Domain 3
solid.sl12	solid.SI12	N/m <sup>2</sup>	Domain 3

Name	Expression	Unit	Selection
solid.sl13	solid.Sl13	N/m <sup>2</sup>	Domain 3
solid.sl22	solid.Sl22	N/m <sup>2</sup>	Domain 3
solid.sl23	solid.Sl23	N/m <sup>2</sup>	Domain 3
solid.sl33	solid.Sl33	N/m <sup>2</sup>	Domain 3
solid.sdevr	solid.sr-(solid.sr+solid.sphi+solid.sz)/3	N/m <sup>2</sup>	Domain 3
solid.sdevrphi	solid.srphi	N/m <sup>2</sup>	Domain 3
solid.sdevrz	solid.srz	N/m <sup>2</sup>	Domain 3
solid.sdevphi	solid.sphi-(solid.sr+solid.sphi+solid.sz)/3	N/m <sup>2</sup>	Domain 3
solid.sdevphiz	solid.sphiz	N/m <sup>2</sup>	Domain 3
solid.sdevz	solid.sz-(solid.sr+solid.sphi+solid.sz)/3	N/m <sup>2</sup>	Domain 3
solid.SdevR	solid.SR-(solid.SR+solid.SPHI+solid.SZ)/3	N/m <sup>2</sup>	Domain 3
solid.SdevRPHI	solid.SRPHI	N/m <sup>2</sup>	Domain 3
solid.SdevRZ	solid.SRZ	N/m <sup>2</sup>	Domain 3
solid.SdevPHI	solid.SPHI-(solid.SR+solid.SPHI+solid.SZ)/3	N/m <sup>2</sup>	Domain 3
solid.SdevPHIZ	solid.SPHIZ	N/m <sup>2</sup>	Domain 3
solid.SdevZ	solid.SZ-(solid.SR+solid.SPHI+solid.SZ)/3	N/m <sup>2</sup>	Domain 3
solid.I1s	solid.sl11+solid.sl22+solid.sl33	N/m <sup>2</sup>	Domain 3
solid.I2s	0.5*(solid.I1s <sup>2</sup> -solid.sl11 <sup>2</sup> -2*solid.sl12 <sup>2</sup> - 2*solid.sl13 <sup>2</sup> -solid.sl22 <sup>2</sup> -2*solid.sl23 <sup>2</sup> -solid.sl33 <sup>2</sup> )	kg <sup>2</sup> /(m <sup>2</sup> *s <sup>4</sup> )	Domain 3
solid.I3s	solid.sl11*solid.sl22*solid.sl33+2*solid.sl12*solid.sl23*solid.sl13-solid.sl11*solid.sl23 <sup>2</sup> -solid.sl12 <sup>2</sup> *solid.sl33-solid.sl22*solid.sl13 <sup>2</sup>	kg <sup>3</sup> /(m <sup>3</sup> *s <sup>6</sup> )	Domain 3
solid.II2s	0.5*((solid.sl11-(solid.sl11+solid.sl22+solid.sl33)/3) <sup>2</sup> +2*solid.sl12 <sup>2</sup> +2*solid.sl13 <sup>2</sup> +2*(solid.sl11+solid.sl22+solid.sl33)/3) <sup>2</sup> +2*solid.sl23 <sup>2</sup> +2*(solid.sl11+solid.sl22+solid.sl33)/3) <sup>2</sup>	kg <sup>2</sup> /(m <sup>2</sup> *s <sup>4</sup> )	Domain 3
solid.II3s	(solid.sl11-(solid.sl11+solid.sl22+solid.sl33)/3)*(solid.sl22-(solid.sl11+solid.sl22+solid.sl33)/3)*(solid.sl33-	kg <sup>3</sup> /(m <sup>3</sup> *s <sup>6</sup> )	Domain 3



Name	Expression	Unit	Selection
	$(\text{solid.sl11}+\text{solid.sl22}+\text{solid.sl33})/3+2*\text{solid.sl12}*\text{solid.sl23}*\text{solid.sl13}-(\text{solid.sl11}-(\text{solid.sl11}+\text{solid.sl22}+\text{solid.sl33})/3)*\text{solid.sl23}^2-\text{solid.sl12}^2*(\text{solid.sl33}-(\text{solid.sl11}+\text{solid.sl22}+\text{solid.sl33})/3)-(\text{solid.sl22}-(\text{solid.sl11}+\text{solid.sl22}+\text{solid.sl33})/3)*\text{solid.sl13}^2$	6)	
solid.thetaL	$\text{atan2}(\text{sqrt}(\max(0.14814814814814814* \text{solid.II2s}^3-\text{solid.II3s}^2, \text{eps})), \text{solid.II3s})/3$	Rad	Domain 3
solid.eelvol	$\text{solid.eel11}+\text{solid.eel22}+\text{solid.eel33}$	1	Domain 3
solid.eeldev11	$\text{solid.eel11}-(\text{solid.eel11}+\text{solid.eel22}+\text{solid.eel33})/3$	1	Domain 3
solid.eeldev12	$\text{solid.eel12}$	1	Domain 3
solid.eeldev13	$\text{solid.eel13}$	1	Domain 3
solid.eeldev22	$\text{solid.eel22}-(\text{solid.eel11}+\text{solid.eel22}+\text{solid.eel33})/3$	1	Domain 3
solid.eeldev23	$\text{solid.eel23}$	1	Domain 3
solid.eeldev33	$\text{solid.eel33}-(\text{solid.eel11}+\text{solid.eel22}+\text{solid.eel33})/3$	1	Domain 3
solid.II2eel	$0.5*((\text{solid.eel11}-(\text{solid.eel11}+\text{solid.eel22}+\text{solid.eel33})/3)^2+2*\text{solid.eel12}^2+2*\text{solid.eel13}^2+(\text{solid.eel22}-(\text{solid.eel11}+\text{solid.eel22}+\text{solid.eel33})/3)^2+2*\text{solid.eel23}^2+(\text{solid.eel33}-(\text{solid.eel11}+\text{solid.eel22}+\text{solid.eel33})/3)^2)$	1	Domain 3
solid.pm	$-(\text{solid.sl11}+\text{solid.sl22}+\text{solid.sl33})/3$	N/m <sup>2</sup>	Domain 3
solid.curlUR	0	1	Domain 3
solid.curlUPHI	$\text{solid.gradUrZ}-\text{solid.gradUzR}$	1	Domain 3
solid.curlUZ	0	1	Domain 3
solid.mises	$(3*\text{solid.II2s})^{0.5}$	N/m <sup>2</sup>	Domain 3
solid.tresca	$\text{solid.sp1}-\text{solid.sp3}$	N/m <sup>2</sup>	Domain 3
solid.Tar	$\text{solid.sr}*\text{solid.nr}+\text{solid.srphi}*\text{solid.nphi}+\text{solid.srz}*\text{solid.nz}$	N/m <sup>2</sup>	Boundaries 8–11
solid.Taphi	$\text{solid.srphi}*\text{solid.nr}+\text{solid.sphi}*\text{solid.nphi}+\text{solid.sphiz}*\text{solid.nz}$	N/m <sup>2</sup>	Boundaries 8–11
solid.Taz	$\text{solid.srz}*\text{solid.nr}+\text{solid.sphiz}*\text{solid.nphi}+\text{solid.sz}*\text{solid.nz}$	N/m <sup>2</sup>	Boundaries 8–11

Name	Expression	Unit	Selection
solid.Ws_tot	root.comp1.solid.lemm3.int10(2*solid.Ws*pi*R)	J	Global
solid.Wh_tot	root.comp1.solid.lemm3.int11(2*solid.Wh*pi*R)	J	Global
solid.RFr	reacf(u)	N	Domain 3
solid.RFphi	0	N	Domain 3
solid.RFz	reacf(w)	N	Domain 3
solid.RMr	-solid.RFz*solid.refpntphi-solid.RFphi*(z-solid.refpntz)	N*m	Domain 3
solid.RMphi	-solid.RFz*(r-solid.refpntr)+solid.RFr*(z-solid.refpntz)	N*m	Domain 3
solid.RMz	solid.RFphi*(r-solid.refpntr)+solid.RFr*solid.refpntphi	N*m	Domain 3

#### Shape functions

Name	Shape function	Unit	Description	Shape frame	Selection
u	Lagrange (Quadratic)	m	Displacement field, R component	Material	Domain 3
w	Lagrange (Quadratic)	m	Displacement field, Z component	Material	Domain 3

#### Weak expressions

Weak expression	Integration frame	Selection
$2*(-\text{solid.SI11}*\text{var}(\text{solid.el11},u)-2*\text{solid.SI12}*\text{var}(\text{solid.el12},u)-2*\text{solid.SI13}*\text{var}(\text{solid.el13},u)-\text{solid.SI22}*\text{var}(\text{solid.el22},u)-2*\text{solid.SI23}*\text{var}(\text{solid.el23},u)-\text{solid.SI33}*\text{var}(\text{solid.el33},u))*\pi*R$	Material	Domain 3

#### Inelastic Strain

##### Selection

Geometric entity level Domain

Selection Domain 3

Equations

$$\epsilon_0 = \epsilon_0$$

$$S_0 = S_0$$

Variables

Name	Expression	Unit	Selection
solid.eil11	ne_strain_r_Zir	1	Domain 3
solid.eil12	0	1	Domain 3
solid.eil13	0	1	Domain 3
solid.eil22	ne_strain_phi_Zir	1	Domain 3
solid.eil23	0	1	Domain 3
solid.eil33	ne_strain_z_Zir	1	Domain 3
solid.Sil11	0	N/m <sup>2</sup>	Domain 3
solid.Sil12	0	N/m <sup>2</sup>	Domain 3
solid.Sil13	0	N/m <sup>2</sup>	Domain 3
solid.Sil22	0	N/m <sup>2</sup>	Domain 3
solid.Sil23	0	N/m <sup>2</sup>	Domain 3
solid.Sil33	0	N/m <sup>2</sup>	Domain 3

Coolant Pressure

Selection

Geometric entity level    Boundary

Selection                      Boundary 11

Equations

$$S \cdot n = F_A$$

$$F_A = -p n$$

Settings

Description	Value
Load type	Pressure
Pressure	coolant_pressure

Variables

Name	Expression	Unit	Selection
solid.FperArear	-solid.bnd11.fPress*solid.nr	N/m <sup>2</sup>	Boundary 11
solid.FperAreaphi	- solid.bnd11.fPress*solid.nphi	N/m <sup>2</sup>	Boundary 11
solid.FperAreaz	-solid.bnd11.fPress*solid.nz	N/m <sup>2</sup>	Boundary 11
solid.bnd11.FollowerPressure	coolant_pressure	Pa	Boundary 11
solid.bnd11.ur	u	m	Boundary 11
solid.bnd11.uphi	0	m	Boundary 11
solid.bnd11.uz	w	m	Boundary 11
solid.bnd11.fPress	solid.bnd11.FollowerPressure	Pa	Boundary 11

Weak expressions

Weak expression	Integration frame	Selection
2*solid.bnd11.fPress*dvol_spatial*(- solid.nr*test(solid.bnd11.ur)-solid.nphi*test(solid.bnd11.uphi)- solid.nz*test(solid.bnd11.uz))*r*pi*R/(dvol*R)	Material	Boundary 11

Sheath Internal Pressure

Selection

Geometric entity level    Boundary

Selection                      Boundary 8

Equations

$$\mathbf{S} \cdot \mathbf{n} = \mathbf{F}_A$$

$$\mathbf{F}_A = -p \mathbf{n}$$

Settings

Description	Value
Load type	Pressure
Pressure	P_contact_sheath + P_gas

Variables

Name	Expression	Unit	Selection
solid.FperArear	-solid.bndl2.fPress*solid.nr	N/m^2	Boundary 8
solid.FperAreaphi	-solid.bndl2.fPress*solid.nphi	N/m^2	Boundary 8
solid.FperAreaz	-solid.bndl2.fPress*solid.nz	N/m^2	Boundary 8
solid.bndl2.FollowerPressure	P_contact_sheath+P_gas	Pa	Boundary 8
solid.bndl2.ur	u	m	Boundary 8
solid.bndl2.uphi	0	m	Boundary 8
solid.bndl2.uz	w	m	Boundary 8
solid.bndl2.fPress	solid.bndl2.FollowerPressure	Pa	Boundary 8

Weak expressions

Weak expression	Integration frame	Selection
2*solid.bndl2.fPress*dvol_spatial*(-solid.nr*test(solid.bndl2.ur)-solid.nphi*test(solid.bndl2.uphi)-solid.nz*test(solid.bndl2.uz))*r*pi*R/(dvol*R)	Material	Boundary 8

## Pellet Contact Pressure

Selection

Geometric entity level    Boundary

Selection                      Boundaries 6–7

Equations

$$\mathbf{S} \cdot \mathbf{n} = \mathbf{F}_A$$

$$\mathbf{F}_A = -p \mathbf{n}$$

Settings

Description	Value
Load type	Pressure
Pressure	sheath(P_contact_sheath)

Variables

Name	Expression	Unit	Selection
solid.FperArear	-solid.bndl4.fPress*solid.nr	N/m <sup>2</sup>	Boundaries 6–7
solid.FperAreaphi	-solid.bndl4.fPress*solid.nphi	N/m <sup>2</sup>	Boundaries 6–7
solid.FperAreaz	-solid.bndl4.fPress*solid.nz	N/m <sup>2</sup>	Boundaries 6–7
solid.bndl4.FollowerPressure	sheath(P_contact_sheath)	Pa	Boundaries 6–7
solid.bndl4.ur	u	m	Boundaries 6–7
solid.bndl4.uphi	0	m	Boundaries 6–7
solid.bndl4.uz	w	m	Boundaries 6–7
solid.bndl4.fPress	solid.bndl4.FollowerPressure	Pa	Boundaries 6–7

Weak expressions

Weak expression	Integration frame	Selection
$2 * \text{solid.bndl4.fPress} * \text{dvol\_spatial} * (-\text{solid.nr} * \text{test}(\text{solid.bndl4.ur}) - \text{solid.nphi} * \text{test}(\text{solid.bndl4.uphi}) - \text{solid.nz} * \text{test}(\text{solid.bndl4.uz})) * r * \pi * R / (\text{dvol} * R)$	Material	Boundaries 6–7

Pellet Gas Pressure

Selection

Geometric entity level    Boundary

Selection                    Boundaries 4–7, 12–13

Equations

$$\mathbf{S} \cdot \mathbf{n} = \mathbf{F}_A$$

$$\mathbf{F}_A = -p \mathbf{n}$$

Settings

Description	Value
Load type	Pressure
Pressure	P_gas

Variables

Name	Expression	Unit	Selection
solid.FperArear	-solid.bndl5.fPress*solid.nr	N/m <sup>2</sup>	Boundaries 4–7, 12–13
solid.FperAreaphi	- solid.bndl5.fPress*solid.nphi	N/m <sup>2</sup>	Boundaries 4–7, 12–13
solid.FperAreaz	-solid.bndl5.fPress*solid.nz	N/m <sup>2</sup>	Boundaries 4–7, 12–13
solid.bndl5.FollowerPressure	P_gas	Pa	Boundaries 4–7, 12–13
solid.bndl5.ur	u	m	Boundaries 4–7, 12–13

Name	Expression	Unit	Selection
solid.bndl5.uphi	0	m	Boundaries 4–7, 12–13
solid.bndl5.uz	w	m	Boundaries 4–7, 12–13
solid.bndl5.fPress	solid.bndl5.FollowerPressure	Pa	Boundaries 4–7, 12–13

Weak expressions

Weak expression	Integration frame	Selection
$2 * \text{solid.bndl5.fPress} * \text{dvol\_spatial} * (-\text{solid.nr} * \text{test}(\text{solid.bndl5.ur}) - \text{solid.nphi} * \text{test}(\text{solid.bndl5.uphi}) - \text{solid.nz} * \text{test}(\text{solid.bndl5.uz})) * r * \pi * R / (\text{dvol} * R)$	Material	Boundaries 4–7, 12–13

Sheath Bottom Axial

Selection

Geometric entity level    Boundary

Selection                    Boundary 9

Equations

$$w = u_{0z}$$

Settings

Description	Value
Notation	Standard notation
Prescribed in r direction	Off
Prescribed in phi direction	Off
Prescribed in z direction	On
Displacement constraint, r component	0
Displacement constraint, phi component	0



Description	Value
Displacement constraint, z component	0
Apply reaction terms on	Individual dependent variables
Use weak constraints	Off
Constraint method	Elemental

#### Variables

Name	Expression	Unit	Selection
solid.disp1.U01	0	m	Boundary 9
solid.disp1.U02	0	m	Boundary 9
solid.disp1.U03	0	m	Boundary 9
solid.disp1.usr	u	m	Boundary 9
solid.disp1.usphi	0	m	Boundary 9
solid.disp1.usz	w	m	Boundary 9
solid.disp1.ur	solid.disp1.usr	m	Boundary 9
solid.disp1.uphi	solid.disp1.usphi	m	Boundary 9
solid.disp1.uz	solid.disp1.usz	m	Boundary 9

#### Shape functions

Constraint	Constraint force	Shape function	Selection
0	-test(u)	Lagrange (Quadratic)	Boundary 9
0	0		Boundary 9
-solid.disp1.uz+solid.disp1.U03	-test(w)	Lagrange (Quadratic)	Boundary 9

#### Sheath Top Axial (Penalty Method)

#### Selection

Geometric entity level Boundary

Selection Boundary 10

Equations

$$\mathbf{S} \cdot \mathbf{n} = \mathbf{F}_A$$

Settings

Description	Value
Load type	Load defined as force per unit area
Load	User defined
Load	{0, 0, axial_contact_pressure_sheath}

Variables

Name	Expression	Unit	Selection
solid.FperArear	solid.bndl3.FAr	N/m^2	Boundary 10
solid.FperAreaphi	0	N/m^2	Boundary 10
solid.FperAreaz	solid.bndl3.FAz	N/m^2	Boundary 10
solid.bndl3.ur	u	m	Boundary 10
solid.bndl3.uphi	0	m	Boundary 10
solid.bndl3.uz	w	m	Boundary 10
solid.bndl3.FperArear	0	N/m^2	Boundary 10
solid.bndl3.FperAreaphi	0	N/m^2	Boundary 10
solid.bndl3.FperAreaz	axial_contact_pressure_sheath	N/m^2	Boundary 10
solid.bndl3.FAr	solid.bndl3.FperArear	N/m^2	Boundary 10
solid.bndl3.FAphi	0	N/m^2	Boundary 10
solid.bndl3.FAz	solid.bndl3.FperAreaz	N/m^2	Boundary 10

Weak expressions

Weak expression	Integration frame	Selection
$2*(\text{solid.bndl3.FAr}*test(\text{solid.bndl3.ur})+\text{solid.bndl3.FAphi}*test(\text{solid.bndl3.uphi})+\text{solid.bndl3.FAz}*test(\text{solid.bndl3.uz}))*\pi*R$	Material	Boundary 10

Sheath Top&Bot Radial BC

Selection

Geometric entity level    Boundary

Selection                      Boundaries 9–10

Equations

$$u_{dst} = u_{src}$$

Settings

Description	Value
Type of periodicity	User defined
Periodic in u	On
Periodic in v	On
Periodic in w	Off
Type of periodicity	{Continuity, Continuity, Continuity}
Apply reaction terms on	All physics (symmetric)
Use weak constraints	Off
Constraint method	Elemental

Variables

Name	Expression	Unit	Description	Selection
solid.pc1.sign_u	-1		Sign in constraint for u	Boundary 10
solid.pc1.sign_v	0		Sign in constraint for v	Boundary 10
solid.pc1.sign_w	-1		Sign in constraint for w	Boundary 10

Shape functions

Constraint	Constraint force	Shape function	Selection
if(root.comp1.solid.incontact_pc1, u+solid.pc1.sign_u*solid.src2dst_pc1(u),0)	if(root.comp1.solid.incontact_pc1, test(u+solid.pc1.sign_u*solid.src2dst_pc1(u)),0)	Lagrange (Quadratic)	Boundary 10
if(root.comp1.solid.incontact_pc1, solid.pc1.sign_v*solid.src2dst_pc1(0),0)	if(root.comp1.solid.incontact_pc1, test(solid.pc1.sign_v*solid.src2dst_pc1(0)),0)		Boundary 10
0	0	Lagrange (Quadratic)	Boundary 10

Pellet Hole

Selection

Geometric entity level Boundary

Selection Boundaries 1–2

Settings

Description	Value
Apply reaction terms on	User defined
Constraint expression	u - if(R>1e-5[m], nojac(ne_strain_phi_UO2*R), 0)
Constraint force expression	test(u)
Shape function type	Lagrange
Element order	Quadratic

Description	Value
Frame	Material
Constraint method	Elemental

Shape functions

Constraint	Constraint force	Shape function	Selection
u-if(R>1.0E-5[m],nojac(ne_strain_phi_UO2*R),0)	test(u)	Lagrange (Quadratic)	Boundaries 1–2

Pellet Axial Constraint

Selection

Geometric entity level Point

Selection Point 1

Equations

$$w = u_{0z}$$

Settings

Description	Value
Notation	Standard notation
Prescribed in r direction	Off
Prescribed in phi direction	Off
Prescribed in z direction	On
Displacement constraint, r component	0
Displacement constraint, phi component	0
Displacement constraint, z component	0
Apply reaction terms on	Individual dependent variables

Description	Value
Use weak constraints	Off
Constraint method	Elemental

#### Variables

Name	Expression	Unit	Selection
solid.disp2.U01	0	M	Point 1
solid.disp2.U02	0	M	Point 1
solid.disp2.U03	0	M	Point 1
solid.disp2.usr	u	M	Point 1
solid.disp2.usphi	0	M	Point 1
solid.disp2.usz	w	M	Point 1
solid.disp2.ur	solid.disp2.usr	M	Point 1
solid.disp2.uphi	solid.disp2.usphi	M	Point 1
solid.disp2.uz	solid.disp2.usz	M	Point 1

#### Shape functions

Constraint	Constraint force	Shape function	Selection
0	-test(u)	Lagrange (Quadratic)	Point 1
0	0		Point 1
-solid.disp2.uz+solid.disp2.U03	-test(w)	Lagrange (Quadratic)	Point 1

#### Global Equations 1

#### Selection

Geometric entity level Entire model

## Settings

Description	Value
Name	pellet_stack_axial_displacement
f(u,ut,utt,t)	pellet_stack_axial_displacement - nojac(bot_land_point(w)) - nojac(pellet_bot_surface_max(-z)/2)
Initial value (u_0)	0
Initial value (u_t0)	0
Description	
Value type when using splitting of complex variables	Complex
Dependent variable quantity	Length (m)
Source term quantity	Length (m)

## Shape functions

Name	Shape function	Unit	Description	Shape frame	Selection
pellet_stack_axial_displacement	ODE	m	State variable pellet_stack_axial_displacement		Global

## Heat Transfer in Solids

### Selection

Geometric entity level    Domain

Selection                    Domains 1–3

### Equations

$$\rho c_p \frac{\partial T}{\partial t} + \rho c_p \mathbf{u} \cdot \nabla T + \nabla \cdot \mathbf{q} = Q + Q_{\text{ted}}$$

$$\mathbf{q} = -k\nabla T$$

#### Settings

Description	Value
Temperature	Linear
Compute boundary fluxes	On
Apply smoothing to boundary fluxes	On
Value type when using splitting of complex variables	Real
Heat transfer in porous media	Off
Streamline diffusion	On
Crosswind diffusion	On
Isotropic diffusion	Off
Enable conversions between material and spatial frames	On

#### Variables

Name	Expression	Unit	Selection
ht.q0	0	W/m <sup>2</sup>	Boundaries 3–13
ht.Tu	T	K	Boundaries 3–13
ht.Td	T	K	Boundaries 3–13
ht.opaqueLayer	1		Boundaries 3–13
ht.Tvar	T	K	Domains 1–3
ht.Tvar	T	K	Boundaries 1–13
ht.Tvar	T	K	Points 1–12
ht.addContinuityWeak	1		Boundaries 1–13
ht.isConductiveLayer	1		Domains 1–3
ht.d	1	1	Domains 1–3



Name	Expression	Unit	Selection
ht.F_mat11	spatial.F11	1	Domains 1–3
ht.F_mat21	0	1	Domains 1–3
ht.F_mat31	spatial.F31	1	Domains 1–3
ht.F_mat12	0	1	Domains 1–3
ht.F_mat22	0	1	Domains 1–3
ht.F_mat32	0	1	Domains 1–3
ht.F_mat13	spatial.F13	1	Domains 1–3
ht.F_mat23	0	1	Domains 1–3
ht.F_mat33	spatial.F33	1	Domains 1–3
ht.invF_mat11	spatial.invF11	1	Domains 1–3
ht.invF_mat21	0	1	Domains 1–3
ht.invF_mat31	spatial.invF31	1	Domains 1–3
ht.invF_mat12	0	1	Domains 1–3
ht.invF_mat22	0	1	Domains 1–3
ht.invF_mat32	0	1	Domains 1–3
ht.invF_mat13	spatial.invF13	1	Domains 1–3
ht.invF_mat23	0	1	Domains 1–3
ht.invF_mat33	spatial.invF33	1	Domains 1–3
ht.Ftang_mat11	dtang(r,R)	1	Boundaries 1–13
ht.Ftang_mat21	0	1	Boundaries 1–13
ht.Ftang_mat31	dtang(r,Z)	1	Boundaries 1–13
ht.Ftang_mat12	0	1	Boundaries 1–13
ht.Ftang_mat22	0	1	Boundaries 1–13
ht.Ftang_mat32	0	1	Boundaries 1–13
ht.Ftang_mat13	dtang(z,R)	1	Boundaries 1–13

Name	Expression	Unit	Selection
ht.Ftang_mat23	0	1	Boundaries 1–13
ht.Ftang_mat33	dtang(z,Z)	1	Boundaries 1–13
ht.detInvF	if(r>0.001/sqrt(sqrt(emetric2)),spatial. detInvF*R/r,spatial.detInvF)	1	Domains 1–3
ht.detInvF	if(r>0.001/sqrt(sqrt(mean(emetric2))),s patial.detInvF*R/r,spatial.detInvF)	1	Boundaries 1–13
ht.detInvF	if(r>0.001/sqrt(sqrt(mean(emetric2))),s patial.detInvF*R/r,spatial.detInvF)	1	Points 1–12
ht.nr	nr	1	Boundary 3
ht.nphi	0	1	Boundary 3
ht.nz	nz	1	Boundary 3
ht.nr	dnr	1	Boundaries 1–2, 4–13
ht.nphi	0	1	Boundaries 1–2, 4–13
ht.nz	dnz	1	Boundaries 1–2, 4–13
ht.nrmesh	root.nrmesh	1	Boundary 3
ht.nphimesh	0	1	Boundary 3
ht.nzmesh	root.nzmesh	1	Boundary 3
ht.nrmesh	root.dnrmesh	1	Boundaries 1–2, 4–13
ht.nphimesh	0	1	Boundaries 1–2, 4–13
ht.nzmesh	root.dnzmesh	1	Boundaries 1–2, 4–13
ht.dnr	dnr	1	Boundaries 1–13
ht.dnphi	0	1	Boundaries 1–13
ht.dnz	dnz	1	Boundaries 1–13
ht.unr	unr	1	Boundaries 1–13
ht.unphi	0	1	Boundaries 1–13
ht.unz	unz	1	Boundaries 1–13

Name	Expression	Unit	Selection
ht.dEiInt	ht.intDom((d(ht.rho*ht.Ei,TIME)- d(ht.rho*ht.Ei,r)*d(r,TIME)- d(ht.rho*ht.Ei,z)*d(z,TIME))*ht.varInt Spa)	W	Global
ht.dEi0Int	ht.intDom((d(ht.rho*ht.Ei0,TIME)- d(ht.rho*ht.Ei0,r)*d(r,TIME)- d(ht.rho*ht.Ei0,z)*d(z,TIME))*ht.varI ntSpa)	W	Global
ht.ntfluxInt	ht.intExtBnd(ht.ntflux*ht.varIntSpa)	W	Global
ht.ntefluxInt	ht.intExtBnd(ht.nteflux*ht.varIntSpa)	W	Global
ht.QInt	ht.intDom(ht.Qtot*ht.varIntSpa)- ht.intIntBnd((ht.ndflux_u+ht.ndflux_d) *ht.varIntSpa)	W	Global
ht.WnsInt	0	W	Global
ht.WInt	0	W	Global

### Heat Transfer in Solids 1

Selection

Geometric entity level Domain

Selection No domains

Equations

$$\rho C_p \frac{\partial T}{\partial t} + \rho C_p \mathbf{u} \cdot \nabla T + \nabla \cdot \mathbf{q} = Q + Q_{ted}$$

$$\mathbf{q} = -k \nabla T$$

Settings

Description	Value
Thermal conductivity	From material
Density	From material

Description	Value
Heat capacity at constant pressure	From material

#### Variables

Name	Expression	Unit	Selection
ht.ntrflux_u	up(ht.trfluxr)*ht.unr+up(ht.trfluxphi)*ht.unphi+up(ht.trfluxz)*ht.unz	W/m <sup>2</sup>	Boundary 3
ht.ntrflux_d	down(ht.trfluxr)*ht.dnr+down(ht.trfluxphi)*ht.dnphi+down(ht.trfluxz)*ht.dnz	W/m <sup>2</sup>	Boundary 3
ht.ncflux_u	up(ht.cfluxr)*ht.unr+up(ht.cfluxphi)*ht.unphi+up(ht.cfluxz)*ht.unz	W/m <sup>2</sup>	Boundary 3
ht.ncflux_d	down(ht.cfluxr)*ht.dnr+down(ht.cfluxphi)*ht.dnphi+down(ht.cfluxz)*ht.dnz	W/m <sup>2</sup>	Boundary 3
ht.ndflux	if(r>0.001/sqrt(sqrt(mean(emetric2))),0.25*(uflux_spatial(T)-dflux_spatial(T))/(pi*r),NaN)/ht.d	W/m <sup>2</sup>	Boundary 3
ht.ndflux_u	if(r>0.001/sqrt(sqrt(mean(emetric2))),-0.5*uflux_spatial(T)/(pi*r),NaN)/ht.d	W/m <sup>2</sup>	Boundary 3
ht.ndflux_d	if(r>0.001/sqrt(sqrt(mean(emetric2))),-0.5*dflux_spatial(T)/(pi*r),NaN)/ht.d	W/m <sup>2</sup>	Boundary 3
ht.ntflux_u	ht.ndflux_u+ht.ntrflux_u+ht.ncflux_u	W/m <sup>2</sup>	Boundary 3
ht.ntflux_d	ht.ndflux_d+ht.ntrflux_d+ht.ncflux_d	W/m <sup>2</sup>	Boundary 3
ht.nteflux_u	up(ht.tefluxr)*ht.unr+up(ht.tefluxphi)*ht.unphi+up(ht.tefluxz)*ht.unz-up(ht.dfluxr)*ht.unr-up(ht.dfluxphi)*ht.unphi-up(ht.dfluxz)*ht.unz+ht.ndflux_u	W/m <sup>2</sup>	Boundary 3
ht.nteflux_d	down(ht.tefluxr)*ht.dnr+down(ht.tefluxphi)*ht.dnphi+down(ht.tefluxz)*ht.dnz-down(ht.dfluxr)*ht.dnr-down(ht.dfluxphi)*ht.dnphi-down(ht.dfluxz)*ht.dnz+ht.ndflux_d	W/m <sup>2</sup>	Boundary 3

#### Shape functions

Name	Shape function	Unit	Description	Shape frame	Selection
------	----------------	------	-------------	-------------	-----------

Name	Shape function	Unit	Description	Shape frame	Selection
T	Lagrange (Linear)	K	Temperature	Spatial	No domains

Axial Symmetry 1

Selection

Geometric entity level Boundary

Selection Boundaries 1-2

Thermal Insulation 1

Selection

Geometric entity level Boundary

Selection No boundaries

Equations

$$-\mathbf{n} \cdot \mathbf{q} = 0$$

Initial Values 1

Selection

Geometric entity level Domain

Selection No domains

Settings

Description	Value
Temperature	coolant_temperature

Fission Heating

Selection

Geometric entity level Domain

Selection Domains 1–2

Equations



Settings

Description	Value
Heat source	General source
Heat source	User defined
Heat source	heating_power_density
Frame type	Material

Variables

Name	Expression	Unit	Selection
ht.Q	ht.hs1.Q	W/m <sup>3</sup>	Domains 1–2
ht.Qtot	ht.hs1.Q	W/m <sup>3</sup>	Domains 1–2
ht.hs1.Q	heating_power_density*ht.detInvF	W/m <sup>3</sup>	Domains 1–2

Weak expressions

Weak expression	Integration frame	Selection
$2*ht.hs1.Q*test(T)*ht.d*pi*r$	Spatial	Domains 1–2

Pellet Outside Boundary Heat Flux

Selection

Geometric entity level Boundary

Selection No boundaries

Equations

$$-\mathbf{n} \cdot \mathbf{q} = q_0$$

Settings

Description	Value
Heat flux	General inward heat flux
Inward heat flux	-sheath(ht.hf2.q0)
Frame type	Spatial

Sheath Inside Boundary Heat Flux

Selection

Geometric entity level Boundary

Selection No boundaries

Equations

$$-\mathbf{n} \cdot \mathbf{q} = q_0$$

Settings

Description	Value
Heat flux	General inward heat flux
Inward heat flux	if(z<=top_land_point(z), (pellet(T) - T)*nojac(gap_conductance_sheath), 0)
Frame type	Spatial

Sheath Outside Surface Heat Flux

Selection

Geometric entity level Boundary

Selection No boundaries

Equations

$$-\mathbf{n} \cdot \mathbf{q} = q_0$$

Settings

Description	Value
Heat flux	General inward heat flux
Inward heat flux	-Zircaloy_to_coolant_conductivity*(T - coolant_temperature) + heat_flux_from_oxidation
Frame type	Spatial

Cool Down (Simple Properties)

Selection

Geometric entity level Domain

Selection Domains 1-3

Equations

$$\rho C_p \frac{\partial T}{\partial t} + \rho C_p \mathbf{u} \cdot \nabla T + \nabla \cdot \mathbf{q} = Q + Q_{\text{ted}}$$

$$\mathbf{q} = -k \nabla T$$

Settings

Description	Value
Thermal conductivity	User defined
Thermal conductivity	{{1, 0, 0}, {0, 1, 0}, {0, 0, 1}}
Density	User defined
Density	1
Heat capacity at constant pressure	User defined



Description	Value
-------------	-------

Heat capacity at constant pressure 1

Variables

Name	Expression	Unit	Selection
domflux.Tr	$-ht.k\_effrr*Tr-ht.k\_effrz*Tz$	W/m <sup>2</sup>	Domains 1–3
domflux.Tz	$-ht.k\_effzr*Tr-ht.k\_effzz*Tz$	W/m <sup>2</sup>	Domains 1–3
ht.WnsInt	$ht.solid2.intDom(ht.pA*(d(ht.ur,r)+if(abs(r)<0.001*h,d(ht.ur,r),ht.ur/r)+d(ht.uz,z))*ht.solid2.varIntSpa)$	W	Global
Trt	$root.comp1.TrTIME-Trr*d(r,TIME)-Trz*d(z,TIME)$	K/(m*s)	Domains 1–3
Tzt	$root.comp1.TzTIME-Tzr*d(r,TIME)-Tzz*d(z,TIME)$	K/(m*s)	Domains 1–3
Trtt	$d(root.comp1.TrTIME-Trr*d(r,TIME)-Trz*d(z,TIME),TIME)-d(root.comp1.TrTIME-Trr*d(r,TIME)-Trz*d(z,TIME),r)*d(r,TIME)-d(root.comp1.TrTIME-Trr*d(r,TIME)-Trz*d(z,TIME),z)*d(z,TIME)$	K/(m*s <sup>2</sup> )	Domains 1–3
Tztt	$d(root.comp1.TzTIME-Tzr*d(r,TIME)-Tzz*d(z,TIME),TIME)-d(root.comp1.TzTIME-Tzr*d(r,TIME)-Tzz*d(z,TIME),r)*d(r,TIME)-d(root.comp1.TzTIME-Tzr*d(r,TIME)-Tzz*d(z,TIME),z)*d(z,TIME)$	K/(m*s <sup>2</sup> )	Domains 1–3
Tt	$root.comp1.TTIME-Tr*d(r,TIME)-Tz*d(z,TIME)$	K/s	Domains 1–3
Ttt	$d(root.comp1.TTIME-Tr*d(r,TIME)-Tz*d(z,TIME),TIME)-d(root.comp1.TTIME-Tr*d(r,TIME)-Tz*d(z,TIME),r)*d(r,TIME)-d(root.comp1.TTIME-Tr*d(r,TIME)-Tz*d(z,TIME),z)*d(z,TIME)$	K/s <sup>2</sup>	Domains 1–3
ht.krr	$(ht.F\_mat11^2+ht.F\_mat21^2+ht.F\_mat31^2)*ht.detInvF$	W/(m*K)	Domains 1–3

Name	Expression	Unit	Selection
ht.kphir	0	W/(m*K)	Domains 1-3
ht.kzr	$(ht.F\_mat13*ht.F\_mat11+ht.F\_mat23*ht.F\_mat21+ht.F\_mat33*ht.F\_mat31)*ht.detInvF$	W/(m*K)	Domains 1-3
ht.krphi	0	W/(m*K)	Domains 1-3
ht.khiphi	0	W/(m*K)	Domains 1-3
ht.kzphi	0	W/(m*K)	Domains 1-3
ht.krz	$(ht.F\_mat11*ht.F\_mat13+ht.F\_mat21*ht.F\_mat23+ht.F\_mat31*ht.F\_mat33)*ht.detInvF$	W/(m*K)	Domains 1-3
ht.kphiz	0	W/(m*K)	Domains 1-3
ht.kzz	$(ht.F\_mat13^2+ht.F\_mat23^2+ht.F\_mat33^2)*ht.detInvF$	W/(m*K)	Domains 1-3
ht.rho	ht.detInvF	kg/m <sup>3</sup>	Domains 1-3
ht.Cp	1	J/(kg*K)	Domains 1-3
ht.alphap	$-d(ht.rho,T)/(ht.rho+eps)$	1/K	Domains 1-3
ht.pA	model.input.minput_pressure	Pa	Domains 1-3
ht.gradTmag	$\sqrt{ht.gradTr^2+ht.gradTphi^2+ht.gradTz^2}$	K/m	Domains 1-3
ht.kmean	$0.5*(ht.k\_effir+ht.k\_effzz)$	W/(m*K)	Domains 1-3
ht.Q	0	W/m <sup>3</sup>	Domains 1-3
ht.qs	0	W/(m <sup>3</sup> *K)	Domains 1-3
ht.Qmet	0	W/m <sup>3</sup>	Domains 1-3
ht.Qtot	0	W/m <sup>3</sup>	Domains 1-3
ht.rhoInt	subst(ht.rho,root.comp1.ht.solid2.minput_pressure,ht.pA)	kg/m <sup>3</sup>	Domains 1-3
ht.CpInt	subst(ht.Cp,root.comp1.ht.solid2.minput_pressure,ht.pA)	J/(kg*K)	Domains 1-3
ht.gammaInt	subst(ht.gamma,root.comp1.ht.solid2.minput_pressure,ht.pA)	1	Domains 1-3
ht.TRef	298.15[K]	K	Domains 1-3

Name	Expression	Unit	Selection
ht.pRef	ht.solid2.pRef	Pa	Domains 1–3
ht.HRef	0	J/kg	Domains 1–3
ht.DeltaH	integrate(subst(ht.CpInt,ht.pA,ht.pRef),T,ht.T Ref,T)	J/kg	Domains 1–3
ht.H	ht.HRef+ht.DeltaH	J/kg	Domains 1–3
ht.H0	ht.H	J/kg	Domains 1–3
ht.Ei	ht.H	J/kg	Domains 1–3
ht.Ei0	ht.Ei	J/kg	Domains 1–3
ht.Qbtot	0	W/m <sup>2</sup>	Boundaries 3– 13
ht.k_effrr	ht.krr	W/(m*K)	Domains 1–3
ht.k_effphir	ht.kphir	W/(m*K)	Domains 1–3
ht.k_effzr	ht.kzr	W/(m*K)	Domains 1–3
ht.k_effrphi	ht.krphi	W/(m*K)	Domains 1–3
ht.k_effphiphi	ht.kphiphi	W/(m*K)	Domains 1–3
ht.k_effzphi	ht.kzphi	W/(m*K)	Domains 1–3
ht.k_effrz	ht.krz	W/(m*K)	Domains 1–3
ht.k_effphiz	ht.kphiz	W/(m*K)	Domains 1–3
ht.k_effzz	ht.kzz	W/(m*K)	Domains 1–3
ht.C_eff	ht.rho*ht.Cp	J/(m <sup>3</sup> *K)	Domains 1–3
ht.ur	0	m/s	Domains 1–3
ht.uphi	0	m/s	Domains 1–3
ht.uz	0	m/s	Domains 1–3
ht.gradTr	Tr	K/m	Domains 1–3
ht.gradTphi	0	K/m	Domains 1–3
ht.gradTz	Tz	K/m	Domains 1–3

Name	Expression	Unit	Selection
ht.Qltot	0	W/m	Points 4–12
ht.alphaTdrr	$ht.k\_effrr/ht.C\_eff$	$m^2/s$	Domains 1–3
ht.alphaTdphir	$ht.k\_effphir/ht.C\_eff$	$m^2/s$	Domains 1–3
ht.alphaTdzz	$ht.k\_effzz/ht.C\_eff$	$m^2/s$	Domains 1–3
ht.alphaTdrphi	$ht.k\_effrphi/ht.C\_eff$	$m^2/s$	Domains 1–3
ht.alphaTdphiphi	$ht.k\_effphiphi/ht.C\_eff$	$m^2/s$	Domains 1–3
ht.alphaTdzhphi	$ht.k\_effzhphi/ht.C\_eff$	$m^2/s$	Domains 1–3
ht.alphaTdrz	$ht.k\_effrz/ht.C\_eff$	$m^2/s$	Domains 1–3
ht.alphaTdphiz	$ht.k\_effphiz/ht.C\_eff$	$m^2/s$	Domains 1–3
ht.alphaTdzz	$ht.k\_effzz/ht.C\_eff$	$m^2/s$	Domains 1–3
ht.alphaTdMean	$ht.kmean/ht.C\_eff$	$m^2/s$	Domains 1–3
ht.dfluxr	$-ht.k\_effrr*Tr-ht.k\_effrz*Tz$	$W/m^2$	Domains 1–3
ht.dfluxphi	$-ht.k\_effphir*Tr-ht.k\_effphiz*Tz$	$W/m^2$	Domains 1–3
ht.dfluxz	$-ht.k\_effzr*Tr-ht.k\_effzz*Tz$	$W/m^2$	Domains 1–3
ht.dfluxMag	$\sqrt{ht.dfluxr^2+ht.dfluxphi^2+ht.dfluxz^2}$	$W/m^2$	Domains 1–3
ht.trlfluxr	0	$W/m^2$	Domains 1–3
ht.trlfluxphi	0	$W/m^2$	Domains 1–3
ht.trlfluxz	0	$W/m^2$	Domains 1–3
ht.trlfluxMag	$\sqrt{ht.trlfluxr^2+ht.trlfluxphi^2+ht.trlfluxz^2}$	$W/m^2$	Domains 1–3
ht.cfluxr	0	$W/m^2$	Domains 1–3
ht.cfluxphi	0	$W/m^2$	Domains 1–3
ht.cfluxz	0	$W/m^2$	Domains 1–3
ht.cfluxMag	$\sqrt{ht.cfluxr^2+ht.cfluxphi^2+ht.cfluxz^2}$	$W/m^2$	Domains 1–3
ht.tfluxr	$ht.dfluxr+ht.trlfluxr+ht.cfluxr$	$W/m^2$	Domains 1–3
ht.tfluxphi	$ht.dfluxphi+ht.trlfluxphi+ht.cfluxphi$	$W/m^2$	Domains 1–3

Name	Expression	Unit	Selection
ht.tfluxz	ht.dfluxz+ht.trlfluxz+ht.cfluxz	W/m <sup>2</sup>	Domains 1–3
ht.tfluxMag	$\sqrt{\text{ht.tfluxr}^2+\text{ht.tfluxphi}^2+\text{ht.tfluxz}^2}$	W/m <sup>2</sup>	Domains 1–3
ht.tefluxr	ht.dfluxr	W/m <sup>2</sup>	Domains 1–3
ht.tefluxphi	ht.dfluxphi	W/m <sup>2</sup>	Domains 1–3
ht.tefluxz	ht.dfluxz	W/m <sup>2</sup>	Domains 1–3
ht.tefluxMag	$\sqrt{\text{ht.tefluxr}^2+\text{ht.tefluxphi}^2+\text{ht.tefluxz}^2}$	W/m <sup>2</sup>	Domains 1–3
ht.rflux	0	W/m <sup>2</sup>	Boundaries 3–13
ht.chflux	0	W/m <sup>2</sup>	Boundaries 3–13
ht.ntrlflux	$\text{mean}(\text{ht.trlfluxr})*\text{ht.nr}+\text{mean}(\text{ht.trlfluxphi})*\text{ht.nphi}+\text{mean}(\text{ht.trlfluxz})*\text{ht.nz}$	W/m <sup>2</sup>	Boundaries 3–13
ht.ntrlflux_u	$\text{up}(\text{ht.trlfluxr})*\text{ht.unr}+\text{up}(\text{ht.trlfluxphi})*\text{ht.unphi}+\text{up}(\text{ht.trlfluxz})*\text{ht.unz}$	W/m <sup>2</sup>	Boundary 3
ht.ntrlflux_d	$\text{down}(\text{ht.trlfluxr})*\text{ht.dnr}+\text{down}(\text{ht.trlfluxphi})*\text{ht.dnphi}+\text{down}(\text{ht.trlfluxz})*\text{ht.dnz}$	W/m <sup>2</sup>	Boundary 3
ht.ncflux	$\text{mean}(\text{ht.cfluxr})*\text{ht.nr}+\text{mean}(\text{ht.cfluxphi})*\text{ht.nphi}+\text{mean}(\text{ht.cfluxz})*\text{ht.nz}$	W/m <sup>2</sup>	Boundaries 3–13
ht.ncflux_u	$\text{up}(\text{ht.cfluxr})*\text{ht.unr}+\text{up}(\text{ht.cfluxphi})*\text{ht.unphi}+\text{up}(\text{ht.cfluxz})*\text{ht.unz}$	W/m <sup>2</sup>	Boundary 3
ht.ncflux_d	$\text{down}(\text{ht.cfluxr})*\text{ht.dnr}+\text{down}(\text{ht.cfluxphi})*\text{ht.dnphi}+\text{down}(\text{ht.cfluxz})*\text{ht.dnz}$	W/m <sup>2</sup>	Boundary 3
ht.ndflux	$\text{if}(r>0.001/\sqrt{\text{mean}(\text{emetric2})}),-0.5*\text{dflux\_spatial}(T)/(\text{pi}*r),\text{NaN})/\text{ht.d}$	W/m <sup>2</sup>	Boundaries 1–2, 4–13
ht.ndflux	$\text{if}(r>0.001/\sqrt{\text{mean}(\text{emetric2})}),0.25*(\text{uflux\_spatial}(T)-\text{dflux\_spatial}(T))/(\text{pi}*r),\text{NaN})/\text{ht.d}$	W/m <sup>2</sup>	Boundary 3
ht.ndflux_u	$\text{if}(r>0.001/\sqrt{\text{mean}(\text{emetric2})}),-0.5*\text{uflux\_spatial}(T)/(\text{pi}*r),\text{NaN})/\text{ht.d}$	W/m <sup>2</sup>	Boundary 3
ht.ndflux_d	$\text{if}(r>0.001/\sqrt{\text{mean}(\text{emetric2})}),-0.5*\text{dflux\_spatial}(T)/(\text{pi}*r),\text{NaN})/\text{ht.d}$	W/m <sup>2</sup>	Boundary 3

Name	Expression	Unit	Selection
ht.ntflux	ht.ndflux+ht.ntrflflux+ht.ncflux	W/m <sup>2</sup>	Boundaries 3–13
ht.ntflux_u	ht.ndflux_u+ht.ntrflflux_u+ht.ncflux_u	W/m <sup>2</sup>	Boundary 3
ht.ntflux_d	ht.ndflux_d+ht.ntrflflux_d+ht.ncflux_d	W/m <sup>2</sup>	Boundary 3
ht.nteflux	mean(ht.tefluxr)*ht.nr+mean(ht.tefluxphi)*ht.nphi+mean(ht.tefluxz)*ht.nz-mean(ht.dfluxr)*ht.nr-mean(ht.dfluxphi)*ht.nphi-mean(ht.dfluxz)*ht.nz+ht.ndflux	W/m <sup>2</sup>	Boundaries 3–13
ht.nteflux_u	up(ht.tefluxr)*ht.unr+up(ht.tefluxphi)*ht.unphi+up(ht.tefluxz)*ht.unz-up(ht.dfluxr)*ht.unr-up(ht.dfluxphi)*ht.unphi-up(ht.dfluxz)*ht.unz+ht.ndflux_u	W/m <sup>2</sup>	Boundary 3
ht.nteflux_d	down(ht.tefluxr)*ht.dnr+down(ht.tefluxphi)*ht.dnphi+down(ht.tefluxz)*ht.dnz-down(ht.dfluxr)*ht.dnr-down(ht.dfluxphi)*ht.dnphi-down(ht.dfluxz)*ht.dnz+ht.ndflux_d	W/m <sup>2</sup>	Boundary 3
ht.gamma	1	1	Domains 1–3
ht.helem	h_spatial	m	Domains 1–3
ht.res_T	-ht.k_effrr*Trr-ht.k_effrz*Trz-ht.k_effphi*phi*if(abs(r)<0.001*h,Trr,Tr/r)-ht.k_effzr*Tzr-ht.k_effzz*Tzz-(ht.qs+ht.qs_oop)*T+ht.rho*ht.Cp*(ht.ur*Tr+ht.uz*Tz)-ht.Q-ht.Qoop	W/m <sup>3</sup>	Domains 1–3
ht.solid2.pRef	model.input.pRef	Pa	Domains 1–3
ht.solid2.dEiInt	ht.solid2.intDom((d(ht.rho*ht.Ei,TIME)-d(ht.rho*ht.Ei,r)*d(r,TIME)-d(ht.rho*ht.Ei,z)*d(z,TIME))*ht.solid2.varInt Spa)	W	Global
ht.solid2.dEi0Int	ht.solid2.intDom((d(ht.rho*ht.Ei0,TIME)-d(ht.rho*ht.Ei0,r)*d(r,TIME)-d(ht.rho*ht.Ei0,z)*d(z,TIME))*ht.solid2.varInt Spa)	W	Global
ht.solid2.ntfluxInt	ht.solid2.intExtBnd(ht.ntflux*ht.solid2.varInt Spa)+ht.solid2.intExtBndUp(ht.ntflux_u*ht.solid2.varInt Spa)	W	Global

Name	Expression	Unit	Selection
	$d2.varIntSpa)+ht.solid2.intExtBndDown(ht.ntflux\_d*ht.solid2.varIntSpa)$		
ht.solid2.ntefluxInt	$ht.solid2.intExtBnd(ht.nteflux*ht.solid2.varIntSpa)+ht.solid2.intExtBndUp(ht.nteflux\_u*ht.solid2.varIntSpa)+ht.solid2.intExtBndDown(ht.nteflux\_d*ht.solid2.varIntSpa)$	W	Global
ht.solid2.QInt	$ht.solid2.intDom(ht.Qtot*ht.solid2.varIntSpa)-ht.solid2.intIntBnd((ht.ndflux\_u+ht.ndflux\_d)*ht.solid2.varIntSpa)$	W	Global
ht.solid2.WnsInt	$ht.solid2.intDom(ht.pA*(d(ht.ur,r)+if(abs(r)<0.001*h,d(ht.ur,r),ht.ur/r)+d(ht.uz,z))*ht.solid2.varIntSpa)$	W	Global
ht.solid2.WInt	0	W	Global

#### Shape functions

Name	Shape function	Unit	Description	Shape frame	Selection
T	Lagrange (Linear)	K	Temperature	Spatial	Domains 1–3

#### Weak expressions

Weak expression	Integration frame	Selection
$2*(-(ht.k\_effr*Tr+ht.k\_effz*Tz)*test(Tr)-(ht.k\_effzr*Tr+ht.k\_effzz*Tz)*test(Tz))*ht.d*pi*r$	Spatial	Domains 1–3
$-2*ht.rho*ht.Cp*(ht.ur*Tr+ht.uz*Tz)*test(T)*ht.d*pi*r$	Spatial	Domains 1–3
$2*ht.streamline*pi*r$	Spatial	Domains 1–3

#### Cool Down Temp

##### Selection

Geometric entity level Domain

Selection Domains 1–3

Settings

Description	Value
Temperature	298.15[K]

Variables

Name	Expression	Unit	Description	Selection
ht.Tinit	298.15[K]	K	Temperature	Domains 1–3

Temperature 1

Selection

Geometric entity level	Boundary
Selection	Boundaries 3–13

Equations

$$T = T_0$$

Settings

Description	Value
Temperature	298.15[K]
	Classic constraints
Apply reaction terms on	All physics (symmetric)
Use weak constraints	Off
Constraint method	Elemental

Variables

Name	Expression	Unit	Selection
------	------------	------	-----------



Name	Expression	Unit	Selection
ht.T0	298.15[K]	K	Boundaries 3–13
ht.temp1.ntfluxInt	ht.temp1.intExtBnd(ht.ntflux*ht.temp1.varIntSpa)	W	Global
ht.temp1.ntefluxInt	ht.temp1.intExtBnd(ht.nteflux*ht.temp1.varIntSpa)	W	Global
ht.temp1.ntfluxInt_u	ht.temp1.intIntBnd(ht.ntflux_u*ht.temp1.varIntSpa)	W	Global
ht.temp1.ntefluxInt_u	ht.temp1.intIntBnd(ht.nteflux_u*ht.temp1.varIntSpa)	W	Global
ht.temp1.ntfluxInt_d	ht.temp1.intIntBnd(ht.ntflux_d*ht.temp1.varIntSpa)	W	Global
ht.temp1.ntefluxInt_d	ht.temp1.intIntBnd(ht.nteflux_d*ht.temp1.varIntSpa)	W	Global
ht.temp1.Tave	if(ht.temp1.intBnd(ht.temp1.varIntSpa*ht.rho*ht.Cp*(ht.ur*ht.nr+ht.uphi*ht.nphi+ht.uz*ht.nz))==0,ht.temp1.intBnd(ht.temp1.varIntSpa*T)/ht.temp1.intBnd(ht.temp1.varIntSpa),ht.temp1.intBnd(ht.temp1.varIntSpa*ht.rho*ht.Cp*T*(ht.ur*ht.nr+ht.uphi*ht.nphi+ht.uz*ht.nz))/ht.temp1.intBnd(ht.temp1.varIntSpa*ht.rho*ht.Cp*(ht.ur*ht.nr+ht.uphi*ht.nphi+ht.uz*ht.nz)))	K	Global

#### Shape functions

Constraint	Constraint force	Shape function	Selection
ht.T0-ht.Tvar	test(ht.T0-ht.Tvar)	Lagrange (Linear)	Boundaries 3–13

#### Burnup

#### Selection

Geometric entity level Domain

Selection Domains 1–2

## Settings

Description	Value
Shape function type	Lagrange
Element order	Linear
Value type when using splitting of complex variables	Real
Frame	Material
Dependent variable quantity	Dimensionless (1)
Source term quantity	None
Unit	1/s

## Variables

Name	Expression	Unit	Description	Selection
dode.nR	nR		Normal vector, R component	Boundaries 1–7, 12–13
dode.nPHI	root.nPHI		Normal vector, PHI component	Boundaries 1–7, 12–13
dode.nZ	nZ		Normal vector, Z component	Boundaries 1–7, 12–13
dode.nRmesh	root.nRmesh		Normal vector (mesh), R component	Boundaries 1–7, 12–13
dode.nPHImesh	root.nPHImesh		Normal vector (mesh), PHI component	Boundaries 1–7, 12–13
dode.nZmesh	root.nZmesh		Normal vector (mesh), Z component	Boundaries 1–7, 12–13

## Distributed ODE 1

### Selection

Geometric entity level    Domain

Selection                    Domains 1–2

Equations

$$e_s \frac{\partial^2 \text{burnup}_{\text{local}}}{\partial t^2} + d_s \frac{\partial \text{burnup}_{\text{local}}}{\partial t} = f$$

Settings

Description	Value
Source term	burnup_time_derivative
Damping or mass coefficient	1
Mass coefficient	0

Variables

Name	Expression	Unit	Description	Selection
burnup_localt	d(burnup_local,TIME)	1/s	Dependent variable burnup_local, first time derivative	Domains 1–2
burnup_localtt	d(burnup_localt,TIME)	1/s^2	Dependent variable burnup_local, second time derivative	Domains 1–2

Shape functions

Name	Shape function	Unit	Description	Shape frame	Selection
burnup_local	Lagrange (Linear)	1	Dependent variable burnup_local	Material	Domains 1–2

Initial Values 1

Selection

Geometric entity level Domain

Selection Domains 1–2

Settings

Description	Value
Initial value for burnup_local	0.00001
Initial time derivative of burnup_local	burnup_time_derivative

Avg Burnup

Selection

Geometric entity level Entire model

Settings

Description	Value
Name	burnup_avg
f(u,ut,utt,t)	burnup_avg - pellet_int_matframe(burnup_local*R)/pellet_int_matframe(R)
Initial value (u_0)	0.00001
Initial value (u_t0)	0
Description	
Value type when using splitting of complex variables	Complex
Dependent variable quantity	Dimensionless (1)
Source term quantity	None
Unit	1

Shape functions

Name	Shape function	Unit	Description	Shape frame	Selection
burnup_avg	ODE	1	State variable burnup_avg		Global

Desnification Fraction

Selection

Geometric entity level Domain

Selection Domains 1–2

Settings

Description	Value
Shape function type	Lagrange
Element order	Linear
Value type when using splitting of complex variables	Real
Frame	Material
Dependent variable quantity	Dimensionless (1)
Source term quantity	None
Unit	1/s

Variables

Name	Expression	Unit	Description	Selection
dode2.nR	nR		Normal vector, R component	Boundaries 1–7, 12–13
dode2.nPHI	root.nPHI		Normal vector, PHI component	Boundaries 1–7, 12–13
dode2.nZ	nZ		Normal vector, Z component	Boundaries 1–7, 12–13
dode2.nRmesh	root.nRmesh		Normal vector (mesh), R component	Boundaries 1–7, 12–13
dode2.nPHImesh	root.nPHImesh		Normal vector (mesh),	Boundaries 1–7, 12–13

Name	Expression	Unit	Description	Selection
			PHI component	
dode2.nZmesh	root.nZmesh		Normal vector (mesh), Z component	Boundaries 1–7, 12–13

Distributed ODE 1

Selection

Geometric entity level Domain

Selection Domains 1–2

Equations

$$e_s \frac{\partial^2 \text{densification\_fraction}}{\partial t^2} + d_s \frac{\partial \text{densification\_fraction}}{\partial t} = f$$

Settings

Description	Value
Source term	densification_fraction_derivative
Damping or mass coefficient	1
Mass coefficient	0

Variables

Name	Expression	Unit	Description	Selection
densification_fractiont	d(densification_fraction,TIME)	1/s	Dependent variable densification_fraction, first time derivative	Domains 1–2
densification_fractiontt	d(densification_fractiont,TIME)	1/s^2	Dependent variable densification_fraction, second	Domains 1–2

Name	Expression	Unit	Description	Selection
			time derivative	

Shape functions

Name	Shape function	Unit	Description	Shape frame	Selection
densification_fraction	Lagrange (Linear)	1	Dependent variable densification_fraction	Material	Domains 1–2

Initial Values 1

Selection

Geometric entity level Domain

Selection Domains 1–2

Settings

Description	Value
Initial value for densification_fraction	0
Initial time derivative of densification_fraction	densification_fraction_derivative

Gaseous Fission Product Swelling

Selection

Geometric entity level Domain

Selection Domains 1–2

Settings

Description	Value
Shape function type	Lagrange

Description	Value
Element order	Linear
Value type when using splitting of complex variables	Real
Frame	Material
Dependent variable quantity	Dimensionless (1)
Source term quantity	None
Unit	1/s

Variables

Name	Expression	Unit	Selection
dode3.nR	nR		Boundaries 1–7, 12–13
dode3.nPHI	root.nPHI		Boundaries 1–7, 12–13
dode3.nZ	nZ		Boundaries 1–7, 12–13
dode3.nRmesh	root.nRmesh		Boundaries 1–7, 12–13
dode3.nPHImesh	root.nPHImesh		Boundaries 1–7, 12–13
dode3.nZmesh	root.nZmesh		Boundaries 1–7, 12–13

Distributed ODE 1

Selection

Geometric entity level Domain

Selection Domains 1–2

Equations

$$e_s \frac{\partial^2 gas_{fps}}{\partial t^2} + d_s \frac{\partial gas_{fps}}{\partial t} = f$$

Settings



Description	Value
Source term	gas_fps_time_derivative*time_ramp(t[1/s] - 2.5)
Damping or mass coefficient	1
Mass coefficient	0

Variables

Name	Expression	Unit	Description	Selection
gas_fpst	d(gas_fps,TIME)	1/s	Dependent variable gas_fps, first time derivative	Domains 1–2
gas_fpstt	d(gas_fpst,TIME)	1/s <sup>2</sup>	Dependent variable gas_fps, second time derivative	Domains 1–2

Shape functions

Name	Shape function	Unit	Description	Shape frame	Selection
gas_fps	Lagrange (Linear)	1	Dependent variable gas_fps	Material	Domains 1–2

Initial Values 1

Selection

Geometric entity level Domain

Selection Domains 1–2

Settings

Description	Value
Initial value for gas_fps	0
Initial time derivative of gas_fps	0

UO2 Grain Diameter

## Selection

Geometric entity level Domain

Selection Domains 1–2

## Settings

Description	Value
Shape function type	Lagrange
Element order	Linear
Value type when using splitting of complex variables	Real
Frame	Material
Dependent variable quantity	Length (m)
Source term quantity	Velocity field (m/s)

## Variables

Name	Expression	Unit	Selection
dode4.nR	nR		Boundaries 1–7, 12–13
dode4.nPHI	root.nPHI		Boundaries 1–7, 12–13
dode4.nZ	nZ		Boundaries 1–7, 12–13
dode4.nRmesh	root.nRmesh		Boundaries 1–7, 12–13
dode4.nPHImesh	root.nPHImesh		Boundaries 1–7, 12–13
dode4.nZmesh	root.nZmesh		Boundaries 1–7, 12–13

## Distributed ODE 1

### Selection

Geometric entity level Domain

Selection Domains 1–2

Equations

$$e_s \frac{\partial^2 \text{UO2\_grain\_diameter}}{\partial t^2} + d_s \frac{\partial \text{UO2\_grain\_diameter}}{\partial t} = f$$

Settings

Description	Value
Source term	UO2_grain_diameter_growth_rate
Damping or mass coefficient	1
Mass coefficient	0

Variables

Name	Expression	Unit	Description	Selection
UO2_grain_diametert	d(UO2_grain_diameter, TIME)	m/s	Dependent variable UO2_grain_diameter, first time derivative	Domains 1–2
UO2_grain_diametertt	d(UO2_grain_diameter t, TIME)	m/s^2	Dependent variable UO2_grain_diameter, second time derivative	Domains 1–2

Shape functions

Name	Shape function	Unit	Description	Shape frame	Selection
UO2_grain_diameter	Lagrange (Linear)	m	Dependent variable UO2_grain_diameter	Material	Domains 1–2

Initial Values 1

Selection

Geometric entity level Domain

Selection Domains 1–2

Settings

Description	Value
Initial value for UO2_grain_diameter	UO2_grain_diameter_int
Initial time derivative of UO2_grain_diameter	0

Fission Gas Release

Selection

Geometric entity level Domain

Selection Domains 1–2

Settings

Description	Value
Shape function type	Lagrange
Element order	Linear
Value type when using splitting of complex variables	Real
Frame	Material
Dependent variable quantity	None
Unit	1/m <sup>3</sup>
Source term quantity	None
Unit	1/m <sup>3</sup> /s

Variables

Name	Expression	Unit	Selection
dode5.nR	nR		Boundaries 1–7, 12–13
dode5.nPHI	root.nPHI		Boundaries 1–7, 12–13

Name	Expression	Unit	Selection
dode5.nZ	nZ		Boundaries 1–7, 12–13
dode5.nRmesh	root.nRmesh		Boundaries 1–7, 12–13
dode5.nPHImesh	root.nPHImesh		Boundaries 1–7, 12–13
dode5.nZmesh	root.nZmesh		Boundaries 1–7, 12–13

#### Grain Boundary Fission Gas Concentration

Selection

Geometric entity level Domain

Selection Domains 1–2

Equations

$$e_s \frac{\partial^2 \mathbf{u}}{\partial t^2} + d_s \frac{\partial \mathbf{u}}{\partial t} = \mathbf{f}$$

$$\mathbf{u} = [fg_{gb}, fg_{gb, cumulative}]^T$$

Settings

Description	Value
Source term	{(fg_rate_to_gb - fg_rate_to_element)*time_ramp(t[1/s] - 2.5), fg_rate_to_gb*time_ramp(t[1/s] - 2.5)}
Damping or mass coefficient	{{1, 0}, {0, 1}}
Mass coefficient	{{0, 0}, {0, 0}}

Variables

Name	Expression	Unit	Description	Selection
fg_gbt	d(fg_gb, TIME)	1/(m <sup>3</sup> *s)	Dependent variable fg_gb, first time derivative	Domains 1–2

Name	Expression	Unit	Description	Selection
fg_gbtt	d(fg_gbt,TIME)	1/(m <sup>3</sup> *s <sup>2</sup> )	Dependent variable fg_gb, second time derivative	Domains 1–2
fg_gb_cumulativet	d(fg_gb_cumulative, TIME)	1/(m <sup>3</sup> *s)	Dependent variable fg_gb_cumulative, first time derivative	Domains 1–2
fg_gb_cumulativett	d(fg_gb_cumulativet, TIME)	1/(m <sup>3</sup> *s <sup>2</sup> )	Dependent variable fg_gb_cumulative, second time derivative	Domains 1–2

#### Shape functions

Name	Shape function	Unit	Description	Selection
fg_gb	Lagrange (Linear)	1/m <sup>3</sup>	Dependent variable fg_gb	Domains 1–2
fg_gb_cumulative	Lagrange (Linear)	1/m <sup>3</sup>	Dependent variable fg_gb_cumulative	Domains 1–2

#### Initial Values 1

##### Selection

Geometric entity level Domain

Selection Domains 1–2

#### Settings

Description	Value
Initial value for fg_gb	0
Initial time derivative of fg_gb	0
Initial value for fg_gb_cumulative	0

Description	Value
Initial time derivative of fg_gb_cumulative	0

Fission Gas Released to Element

Selection

Geometric entity level Entire model

Settings

Description	Value
Name	m_fg_element
f(u,ut,utt,t)	m_fg_element - nojac(2*pi*pellet_int_matframe((fg_gb_cumulative-fg_gb)*R)/6.022e23[1/mol]*num_pellets/num_pellets_model)
Initial value (u_0)	0
Initial value (u_t0)	0
Description	
Value type when using splitting of complex variables	Complex
Dependent variable quantity	None
Unit	Mol
Source term quantity	None
Unit	Mol

Shape functions

Name	Shape function	Unit	Description	Shape frame	Selection
m_fg_element	ODE	mol	State variable m_fg_element		Global

### Weak Contribution 1

Selection

Geometric entity level    Boundary

Selection                    Boundary 3; Extra dimension: ad1 {Domain 1}

Settings

Description	Value
Weak expression	$(\text{root.compl.u1 TIME}-1)*\text{test}(u1) - 1*d(u1, r1)*\text{test}(d(u1, r1))$
Use automatic quadrature settings	On

Weak expressions

Weak expression	Integration frame	Selection
$2*((-1+\text{root.compl.u1 TIME})*\text{test}(u1)-d(u1,r1)*\text{test}(d(u1,r1)))*\pi*R$	Material	Boundary 3; Extra dimension: ad1 {Domain 1}

### Auxiliary Dependent Variable 1

Selection

Geometric entity level    Boundary

Selection                    Boundary 3; Extra dimension: ad1 {Domain 1}

Settings

Description	Value
Field variable name	u1
Initial value	0



Description	Value
Initial time derivative	0
Shape function type	Lagrange
Element order	Quadratic
Frame	Spatial
Value type when using splitting of complex variables	Complex

#### Shape functions

Name	Shape function	Unit	Description	Shape frame	Selection
u1	Lagrange (Quadratic)		Auxiliary dependent variable u1	Spatial	Boundary 3; Extra dimension: ad1 {Domain 1}

#### Pointwise Constraint 1

##### Selection

Geometric entity level    Boundary

Selection                      No boundaries ; Extra dimension: ad1 {Boundary 2}

#### Settings

Description	Value
Apply reaction terms on	All physics (symmetric)
Constraint expression	u1 - 0
Constraint method	Elemental
Shape function type	Lagrange
Element order	Quadratic
Frame	Spatial

Internal Gas Pressure

Global Equations 1

Selection

Geometric entity level Entire model

Settings

Description	Value
Name	P_gas_calc
f(u,ut,utt,t)	P_gas_calc - m_gas_element*8.314[J/K/mol]/nojac(inv_T_int_total)
Initial value (u_0)	0
Initial value (u_t0)	0
Description	
Value type when using splitting of complex variables	Complex
Dependent variable quantity	Pressure (Pa)
Source term quantity	Pressure (Pa)

Shape functions

Name	Shape function	Unit	Description	Shape frame	Selection
P_gas_calc	ODE	Pa	State variable P_gas_calc		Global

Low-Temperature Creep

Selection

Geometric entity level Domain

Selection Domain 3

## Settings

Description	Value
Shape function type	Lagrange
Element order	Linear
Value type when using splitting of complex variables	Real
Frame	Material
Dependent variable quantity	Dimensionless (1)
Source term quantity	None
Unit	1/s

## Variables

Name	Expression	Unit	Description	Selection
dode7.nR	nR		Normal vector, R component	Boundaries 8–11
dode7.nPHI	root.nPHI		Normal vector, PHI component	Boundaries 8–11
dode7.nZ	nZ		Normal vector, Z component	Boundaries 8–11
dode7.nRmesh	root.nRmesh		Normal vector (mesh), R component	Boundaries 8–11
dode7.nPHImesh	root.nPHImesh		Normal vector (mesh), PHI component	Boundaries 8–11
dode7.nZmesh	root.nZmesh		Normal vector (mesh), Z component	Boundaries 8–11

## Distributed ODE 1

### Selection

Geometric entity level    Domain

Selection                    Domain 3

Equations

$$e_s \frac{\partial^2 \text{low\_temp\_creep}}{\partial t^2} + d_s \frac{\partial \text{low\_temp\_creep}}{\partial t} = f$$

Settings

Description	Value
Source term	low_temp_creep_rate
Damping or mass coefficient	1
Mass coefficient	0

Variables

Name	Expression	Unit	Description	Selection
low_temp_creep	d(low_temp_creep, TIME)	1/s	Dependent variable low_temp_creep, first time derivative	Domain 3
low_temp_creep	d(d(low_temp_creep, TIME), TIME)	1/s^2	Dependent variable low_temp_creep, second time derivative	Domain 3

Shape functions

Name	Shape function	Unit	Description	Shape frame	Selection
low_temp_creep	Lagrange (Linear)	1	Dependent variable low_temp_creep	Material	Domain 3

Initial Values 1

Selection

Geometric entity level Domain

Selection Domain 3

### Settings

Description	Value
Initial value for low_temp_creep	0
Initial time derivative of low_temp_creep	0

### Sheath Internal Stress

Used products

COMSOL Multiphysics

### Selection

Geometric entity level Domain

Selection Domain 3

### Settings

Description	Value
Shape function type	Lagrange
Element order	Linear
Value type when using splitting of complex variables	Real
Frame	Material
Dependent variable quantity	Pressure (Pa)
Source term quantity	None
Unit	Pa/s

### Variables

Name	Expression	Unit	Description	Selection
------	------------	------	-------------	-----------

Name	Expression	Unit	Description	Selection
dode8.nR	nR		Normal vector, R component	Boundaries 8–11
dode8.nPHI	root.nPHI		Normal vector, PHI component	Boundaries 8–11
dode8.nZ	nZ		Normal vector, Z component	Boundaries 8–11
dode8.nRmesh	root.nRmesh		Normal vector (mesh), R component	Boundaries 8–11
dode8.nPHImesh	root.nPHImesh		Normal vector (mesh), PHI component	Boundaries 8–11
dode8.nZmesh	root.nZmesh		Normal vector (mesh), Z component	Boundaries 8–11

Distributed ODE 1

Selection

Geometric entity level Domain

Selection Domain 3

Equations

$$e_s \frac{\partial^2 \text{stress}_{rt,ef}}{\partial t^2} + d_s \frac{\partial \text{stress}_{rt,ef}}{\partial t} = f$$

Settings

Description	Value
Source term	stress_int_ref_derivative*time_ramp(t[1/s] - 2)
Damping or mass coefficient	1
Mass coefficient	0

Variables

Name	Expression	Unit	Description	Selection
stress_int_ref	d(stress_int_ref,TIME)	Pa/s	Dependent variable stress_int_ref, first time derivative	Domain 3
stress_int_ref	d(stress_int_ref,TIME)	Pa/s <sup>2</sup>	Dependent variable stress_int_ref, second time derivative	Domain 3

#### Shape functions

Name	Shape function	Unit	Description	Shape frame	Selection
stress_int_ref	Lagrange (Linear)	Pa	Dependent variable stress_int_ref	Material	Domain 3

#### Initial Values 1

Selection

Geometric entity level Domain

Selection Domain 3

#### Settings

Description	Value
Initial value for stress_int_ref	stress_int_initial
Initial time derivative of stress_int_ref	0

Sheath Alpha Phase Fraction

Used products

COMSOL Multiphysics

Selection

Geometric entity level    Domain  
 Selection                    Domain 3

Settings

Description	Value
Shape function type	Lagrange
Element order	Linear
Value type when using splitting of complex variables	Real
Frame	Material
Dependent variable quantity	Dimensionless (1)
Source term quantity	None
Unit	1/s

Variables

Name	Expression	Unit	Description	Selection
dode9.nR	nR		Normal vector, R component	Boundaries 8–11
dode9.nPHI	root.nPHI		Normal vector, PHI component	Boundaries 8–11
dode9.nZ	nZ		Normal vector, Z component	Boundaries 8–11
dode9.nRmesh	root.nRmesh		Normal vector (mesh), R component	Boundaries 8–11
dode9.nPHImesh	root.nPHImesh		Normal vector (mesh), PHI component	Boundaries 8–11
dode9.nZmesh	root.nZmesh		Normal vector (mesh), Z component	Boundaries 8–11

Distributed ODE 1



Selection

Geometric entity level Domain

Selection Domain 3

Equations

$$e_s \frac{\partial^2 \text{Zir\_}j\text{pha\_phase}}{\partial t^2} + d_s \frac{\partial \text{Zir\_}j\text{pha\_phase}}{\partial t} = f$$

Settings

Description	Value
Source term	alpha_frac_rate
Damping or mass coefficient	1
Mass coefficient	0

Variables

Name	Expression	Unit	Description	Selection
Zir_alpha_phaset	d(Zir_alpha_phase,TIME )	1/s	Dependent variable Zir_alpha_phase, first time derivative	Domain 3
Zir_alpha_phasett	d(Zir_alpha_phaset,TIM E)	1/s^2	Dependent variable Zir_alpha_phase, second time derivative	Domain 3

Shape functions

Name	Shape function	Unit	Description	Shape frame	Selection
Zir_alpha_phase	Lagrange (Linear)	1	Dependent variable Zir_alpha_phase	Material	Domain 3

Initial Values 1

Selection

Geometric entity level Domain

Selection Domain 3

#### Settings

Description	Value
Initial value for Zir_alpha_phase	1
Initial time derivative of Zir_alpha_phase	0

#### Sheath Recrystallized Fraction

Selection

Geometric entity level Domain

Selection Domain 3

#### Settings

Description	Value
Shape function type	Lagrange
Element order	Linear
Value type when using splitting of complex variables	Real
Frame	Material
Dependent variable quantity	Dimensionless (1)
Source term quantity	None
Unit	1/s

#### Variables

Name	Expression	Unit	Selection
dode10.nR	nR		Boundaries 8–11

Name	Expression	Unit	Selection
dode10.nPHI	root.nPHI		Boundaries 8–11
dode10.nZ	nZ		Boundaries 8–11
dode10.nRmesh	root.nRmesh		Boundaries 8–11
dode10.nPHImesh	root.nPHImesh		Boundaries 8–11
dode10.nZmesh	root.nZmesh		Boundaries 8–11

Distributed ODE 1

Selection

Geometric entity level Domain

Selection Domain 3

Equations

$$e_s \frac{\partial^2 \text{URCvolfrac}}{\partial t^2} + d_s \frac{\partial \text{URCvolfrac}}{\partial t} = f$$

Settings

Description	Value
Source term	-recrystallization_rate
Damping or mass coefficient	1
Mass coefficient	0

Variables

Name	Expression	Unit	Description	Selection
URCvolfrac	d(URCvolfrac,TIME)	1/s	Dependent variable URCvolfrac, first time derivative	Domain 3
URCvolfrac <sup>2</sup>	d(URCvolfrac <sup>2</sup> ,TIME)	1/s <sup>2</sup>	Dependent variable URCvolfrac, second time	Domain 3

Name	Expression	Unit	Description	Selection
			derivative	

Shape functions

Name	Shape function	Unit	Description	Shape frame	Selection
URCvolfrac	Lagrange (Linear)	1	Dependent variable URCvolfrac	Material	Domain 3

Initial Values 1

Selection

Geometric entity level Domain

Selection Domain 3

Settings

Description	Value
Initial value for URCvolfrac	1
Initial time derivative of URCvolfrac	0

Sheath Creep

Selection

Geometric entity level Domain

Selection Domain 3

Settings

Description	Value
Shape function type	Lagrange

Description	Value
Element order	Linear
Value type when using splitting of complex variables	Real
Frame	Material
Dependent variable quantity	Dimensionless (1)
Source term quantity	None
Unit	1/s

#### Variables

Name	Expression	Unit	Description	Selection
dode6.nR	nR		Normal vector, R component	Boundaries 8–11
dode6.nPHI	root.nPHI		Normal vector, PHI component	Boundaries 8–11
dode6.nZ	nZ		Normal vector, Z component	Boundaries 8–11
dode6.nRmesh	root.nRmesh		Normal vector (mesh), R component	Boundaries 8–11
dode6.nPHImesh	root.nPHImesh		Normal vector (mesh), PHI component	Boundaries 8–11
dode6.nZmesh	root.nZmesh		Normal vector (mesh), Z component	Boundaries 8–11

#### Distributed ODE 1

##### Selection

Geometric entity level    Domain

Selection                    Domain 3

#### Equations

$$e_{\alpha} \frac{\partial^2 \mathbf{u}}{\partial t^2} + d_{\alpha} \frac{\partial \mathbf{u}}{\partial t} = \mathbf{f}$$

$$\mathbf{u} = [\text{creep}_r, \text{creep}_{\phi}, \text{creep}_z]^T$$

Settings

Description	Value
Source term	{creep_rate_r*time_ramp(t[1/s] - 2), creep_rate_phi*time_ramp(t[1/s] - 2), creep_rate_z*time_ramp(t[1/s] - 2)}
Damping or mass coefficient	{{1, 0, 0}, {0, 1, 0}, {0, 0, 1}}
Mass coefficient	{{0, 0, 0}, {0, 0, 0}, {0, 0, 0}}

Variables

Name	Expression	Unit	Description	Selection
creep_rt	d(creep_r,TIME)	1/s	Dependent variable creep_r, first time derivative	Domain 3
creep_rtt	d(creep_rt,TIME)	1/s^2	Dependent variable creep_r, second time derivative	Domain 3
creep_phit	d(creep_phi,TIME)	1/s	Dependent variable creep_phi, first time derivative	Domain 3
creep_phitt	d(creep_phit,TIME)	1/s^2	Dependent variable creep_phi, second time derivative	Domain 3
creep_zt	d(creep_z,TIME)	1/s	Dependent variable creep_z, first time derivative	Domain 3
creep_ztt	d(creep_zt,TIME)	1/s^2	Dependent variable creep_z, second time derivative	Domain 3

Shape functions

Name	Shape function	Unit	Description	Shape frame	Selection
------	----------------	------	-------------	-------------	-----------

Name	Shape function	Unit	Description	Shape frame	Selection
creep_r	Lagrange (Linear)	1	Dependent variable creep_r	Material	Domain 3
creep_phi	Lagrange (Linear)	1	Dependent variable creep_phi	Material	Domain 3
creep_z	Lagrange (Linear)	1	Dependent variable creep_z	Material	Domain 3

#### Initial Values 1

##### Selection

Geometric entity level Domain

Selection Domain 3

##### Settings

Description	Value
Initial value for creep_r	0
Initial time derivative of creep_r	0
Initial value for creep_phi	0
Initial time derivative of creep_phi	0
Initial value for creep_z	0
Initial time derivative of creep_z	0

#### Sheath Oxidation

##### Selection

Geometric entity level Boundary

Selection Boundary 11

Settings

Description	Value
Shape function type	Lagrange
Element order	Linear
Value type when using splitting of complex variables	Real
Frame	Material
Dependent variable quantity	Length (m)
Source term quantity	Velocity field (m/s)

Distributed ODE 1

Selection

Geometric entity level    Boundary

Selection                    Boundary 11

Equations

$$e_s \frac{\partial^2 \mathbf{u}}{\partial t^2} + d_s \frac{\partial \mathbf{u}}{\partial t} = \mathbf{f}$$

$$\mathbf{u} = [\text{zir\_outside\_oxided\_thickness}, \text{alpha\_zirconium\_thickness}]^T$$

Settings

Description	Value
Source term	{zir_outside_oxided_thickness_growth_rate, alpha_zirconium_thickness_growth_rate}
Damping or mass coefficient	{{1, 0}, {0, 1}}
Mass coefficient	{{0, 0}, {0, 0}}

Variables



Name	Expression	Unit	Description	Selection
zir_outside_oxidized_thickness	$d(\text{zir\_outside\_oxidized\_thickness}, \text{TIME})$	m/s	Dependent variable zir_outside_oxidized_thickness, first time derivative	Boundary 11
zir_outside_oxidized_thickness	$d(\text{zir\_outside\_oxidized\_thickness}, \text{TIME})$	m/s <sup>2</sup>	Dependent variable zir_outside_oxidized_thickness, second time derivative	Boundary 11
alpha_zirconium_thickness	$d(\text{alpha\_zirconium\_thickness}, \text{TIME})$	m/s	Dependent variable alpha_zirconium_thickness, first time derivative	Boundary 11
alpha_zirconium_thickness	$d(\text{alpha\_zirconium\_thickness}, \text{TIME})$	m/s <sup>2</sup>	Dependent variable alpha_zirconium_thickness, second time derivative	Boundary 11

#### Shape functions

Name	Shape function	Unit	Description	Shape frame	Selection
zir_outside_oxidized_thickness	Lagrange (Linear)	m	Dependent variable zir_outside_oxidized_thickness	Material	Boundary 11
alpha_zirconium_thickness	Lagrange (Linear)	m	Dependent variable alpha_zirconium_thickness	Material	Boundary 11

#### Initial Values 1

##### Selection

Geometric entity level    Boundary

Selection                    Boundary 11

#### Settings

Description	Value
Initial value for zir_outside_oxidized_thickness	zir_outside_oxidized_thickness_initial
Initial time derivative of zir_outside_oxidized_thickness	0
Initial value for alpha_zirconium_thickness	alpha_zirconium_thickness_initial
Initial time derivative of alpha_zirconium_thickness	0

#### Deformed Geometry

##### Selection

Geometric entity level    Domain

Selection                    Domain 3

##### Settings

Description	Value
Geometry frame coordinates	{Rg, PHIg, Zg}
Geometry shape order	1

#### Variables

Name	Expression	Unit	Selection
dg.nRg	nRg		Boundaries 8–11
dg.nPHIg	root.nPHIg		Boundaries 8–11
dg.nZg	nZg		Boundaries 8–11
dg.nRgmesh	root.nRgmesh		Boundaries 8–11
dg.nPHIgmesh	root.nPHIgmesh		Boundaries 8–11
dg.nZgmesh	root.nZgmesh		Boundaries 8–11
dg.nR	nR		Boundaries 8–11
dg.nPHI	root.nPHI		Boundaries 8–11

Name	Expression	Unit	Selection
dg.nZ	nZ		Boundaries 8–11
dg.nRmesh	root.nRmesh		Boundaries 8–11
dg.nPHImesh	root.nPHImesh		Boundaries 8–11
dg.nZmesh	root.nZmesh		Boundaries 8–11
dg.relVol	$(d(R,root.xi1)*d(Z,root.xi2)-d(R,root.xi2)*d(Z,root.xi1))/dvol\_geometry$	1	Domain 3
dg.relVolMin	dg.minOp(dg.relVol)	1	Global
dg.relVolMax	dg.maxOp(dg.relVol)	1	Global
dg.minqual	dg.minOp(qual)		Global
dg.FRRg_mesh	d(R,Rg)	1	Domain 3
dg.FPHIRg_mesh	0	1	Domain 3
dg.FZRg_mesh	d(Z,Rg)	1	Domain 3
dg.FRPHIg_mesh	0	1	Domain 3
dg.FPHIPHIg_mesh	1	1	Domain 3
dg.FZPHIg_mesh	0	1	Domain 3
dg.FRZg_mesh	d(R,Zg)	1	Domain 3
dg.FPHIZg_mesh	0	1	Domain 3
dg.FZZg_mesh	d(Z,Zg)	1	Domain 3
dg.J_mesh	$dg.FRRg\_mesh*dg.FPHIPHIg\_mesh*dg.FZZg\_mesh+dg.FRPHIg\_mesh*dg.FPHIZg\_mesh*dg.FZRg\_mesh+dg.FRZg\_mesh*dg.FPHIRg\_mesh*dg.FZPHIg\_mesh-dg.FRRg\_mesh*dg.FPHIZg\_mesh*dg.FZPHIg\_mesh-dg.FRPHIg\_mesh*dg.FPHIRg\_mesh*dg.FZZg\_mesh-dg.FRZg\_mesh*dg.FPHIPHIg\_mesh*dg.FZRg\_mesh$	1	Domain 3
dg.IIiso	$-1.5+0.5*(dg.FRRg\_mesh^2+dg.FPHIRg\_mesh^2+dg.FZRg\_mesh^2)$	1	Domain 3

Name	Expression	Unit	Selection
	$g\_mesh^2 + dg.FRPg\_mesh^2 + dg.FPHIPg\_mesh^2 + dg.FZPHg\_mesh^2 + dg.FRZg\_mesh^2 + dg.FPHZg\_mesh^2 + dg.FZZg\_mesh^2 * dg.J\_mesh^{(-2/3)}$		
dg.IIisoMax	dg.maxOp(dg.IIiso)	1	Global
dg.PRRg_mesh	d(dg.FRRg_mesh, TIME)	1/s	Domain 3
dg.PPHIRg_mesh	d(dg.FPHIRg_mesh, TIME)	1/s	Domain 3
dg.PZRg_mesh	d(dg.FZRg_mesh, TIME)	1/s	Domain 3
dg.PRPg_mesh	d(dg.FRPg_mesh, TIME)	1/s	Domain 3
dg.PPHIPg_mesh	d(dg.FPHIPg_mesh, TIME)	1/s	Domain 3
dg.PZPHg_mesh	d(dg.FZPHg_mesh, TIME)	1/s	Domain 3
dg.PRZg_mesh	d(dg.FRZg_mesh, TIME)	1/s	Domain 3
dg.PPHZg_mesh	d(dg.FPHZg_mesh, TIME)	1/s	Domain 3
dg.PZZg_mesh	d(dg.FZZg_mesh, TIME)	1/s	Domain 3
dg.PRRg_test	test(dg.FRRg_mesh)	1	Domain 3
dg.PPHIRg_test	test(dg.FPHIRg_mesh)	1	Domain 3
dg.PZRg_test	test(dg.FZRg_mesh)	1	Domain 3
dg.PRPg_test	test(dg.FRPg_mesh)	1	Domain 3
dg.PPHIPg_test	test(dg.FPHIPg_mesh)	1	Domain 3
dg.PZPHg_test	test(dg.FZPHg_mesh)	1	Domain 3
dg.PRZg_test	test(dg.FRZg_mesh)	1	Domain 3
dg.PPHZg_test	test(dg.FPHZg_mesh)	1	Domain 3
dg.PZZg_test	test(dg.FZZg_mesh)	1	Domain 3

Name	Expression	Unit	Selection
dg.G_mesh	1	1	Domain 3
Rt	d(R,TIME)	m/s	Global
PHIt	0	m/s	Global
Zt	d(Z,TIME)	m/s	Global

#### Fixed Mesh 1

##### Selection

Geometric entity level Domain

Selection No domains

#### Prescribed Mesh Displacement 1

##### Selection

Geometric entity level Boundary

Selection Boundaries 9–10

#### Settings

Description	Value
Prescribed # displacement	{Off, On}
Use weak constraints	Off

#### Variables

Name	Expression	Unit	Description	Selection
dg.R_free	R	m	Coordinate, R component	Boundaries 9–10
dg.Z_free	Z	m	Coordinate, Z component	Boundaries 9–10

Shape functions

Constraint	Constraint force	Shape function	Selection
0	test(-dg.R_free)	Lagrange (Linear)	Boundaries 9–10
0	0		Boundaries 9–10
Zg-dg.Z_free	test(-dg.Z_free)	Lagrange (Linear)	Boundaries 9–10

Prescribed Mesh Displacement 2

Selection

Geometric entity level    Boundary

Selection                    Boundary 11

Settings

Description	Value
Prescribed # displacement	{On, On}
Prescribed mesh displacement	{nojac(-sheath_thickness_lost), 0}
Use weak constraints	Off

Variables

Name	Expression	Unit	Description	Selection
dg.R_free	R	m	Coordinate, R component	Boundary 11
dg.Z_free	Z	m	Coordinate, Z component	Boundary 11

Shape functions

Constraint	Constraint force	Shape function	Selection
Rg-dg.R_free+nojac(-sheath_thickness_lost)	test(-dg.R_free)	Lagrange (Linear)	Boundary 11

Constraint	Constraint force	Shape function	Selection
0	0		Boundary 11
Zg-dg.Z_free	test(-dg.Z_free)	Lagrange (Linear)	Boundary 11

Prescribed Mesh Displacement 3

Selection

Geometric entity level Boundary

Selection Boundary 8

Settings

Description	Value
Prescribed # displacement	{On, On}
Prescribed mesh displacement	{0, 0}
Use weak constraints	Off

Variables

Name	Expression	Unit	Description	Selection
dg.R_free	R	m	Coordinate, R component	Boundary 8
dg.Z_free	Z	m	Coordinate, Z component	Boundary 8

Shape functions

Constraint	Constraint force	Shape function	Selection
Rg-dg.R_free	test(-dg.R_free)	Lagrange (Linear)	Boundary 8
0	0		Boundary 8
Zg-dg.Z_free	test(-dg.Z_free)	Lagrange (Linear)	Boundary 8

Free Deformation 1

Selection

Geometric entity level Domain

Selection Domain 3

Settings

Description	Value
Initial mesh displacement	{0, 0}

Shape functions

Name	Shape function	Unit	Description	Shape frame	Selection
R	Lagrange (Linear)	m	Material coordinate R	Geometry	Domain 3
Z	Lagrange (Linear)	m	Material coordinate Z	Geometry	Domain 3

Weak expressions

Weak expression	Integration frame	Selection
if(dg.relVol<0,NaN*test(R),-RRg*test(RRg)-RZg*test(RZg)-ZRg*test(ZRg)-ZZg*test(ZZg))	Geometry	Domain 3

Selection

Geometric entity level Domain

Selection Domains 1–3

Equations

Settings



Description	Value
Element order	Quadratic

Axial Symmetry 1

Selection

Geometric entity level Boundary

Selection Boundaries 1–2

Discrete States 1

Selection

Geometric entity level Entire model

Settings

Description	Value
Discrete state	m_gas_extra_fill
Initial value for discrete state	0[mol]
Description of discrete state	0

Shape functions

Name	Shape function	Unit	Description	Shape frame	Selection
m_gas_extra_fill	ODE		0		Global

Explicit Event 1

Selection

Geometric entity level Entire model

### Settings

Description	Value
Start of event	gas_pressure_set_time
Period of event	9e99
Variable	m_gas_extra_fill
Expression	gas_pressure_set_value/R_const*inv_T_int_total - m_gas_element

### Stop Conditions Events

#### Selection

Geometric entity level Domain

Selection Domains 1–3

### Equations

### Settings

Description	Value
Element order	Quadratic

### Axial Symmetry 1

#### Selection

Geometric entity level Boundary

Selection Boundaries 1–2

### Indicator States 1

#### Selection

Geometric entity level Entire model

### Settings

Description	Value
Indicator state	burnup_stop
Indicator expression	burnup_avg - burnup_max
Initial value for indicator state	0
Description of indicator state	0

### Shape functions

Name	Shape function	Unit	Description	Shape frame	Selection
burnup_stop	ODE		0		Global

### Burnup Stop Event

#### Selection

Geometric entity level Entire model

### Settings

Description	Value
Condition	burnup_stop>0

### Time-Step Storing

### Global Equations 1

#### Selection

Geometric entity level Entire model

## Settings

Description	Value
Name	solver_time_steps
f(u,ut,utt,t)	solver_time_steps - timestep
Initial value (u_0)	0
Initial value (u_t0)	0
Description	
Value type when using splitting of complex variables	Complex
Dependent variable quantity	Time (s)
Source term quantity	Time (s)

## Shape functions

Name	Shape function	Unit	Description	Shape frame	Selection
solver_time_steps	ODE	s	State variable		Global

## Mesh 1

### Mesh statistics

Description	Value
Minimum element quality	0.4529
Average element quality	0.7917
Quadrilateral elements	536
Edge elements	192
Vertex elements	12

## Size (size)

## Settings

Description	Value
Maximum element size	0.00125
Minimum element size	5.58E-6
Curvature factor	0.3
Maximum element growth rate	1.3

Mapped 1 (map1)

Selection

Geometric entity level Domain

Selection Domains 1–2

Settings

Description	Value
Adjust evenly distributed edge mesh	On

Distribution 2 (dis2)

Selection

Geometric entity level Boundary

Selection Boundaries 6–7

Settings

Description	Value
Distribution properties	Predefined distribution type
Number of elements	$\text{floor}(\text{mesh\_nodes\_pellet\_axial}/2)$
Reverse direction	On

### Distribution 3 (dis3)

Selection

Geometric entity level    Boundary

Selection                    Boundaries 12–13

Settings

<b>Description</b>	<b>Value</b>
Distribution properties	Predefined distribution type
Number of elements	mesh_nodes_pellet_dish
Element ratio	1.5

### Distribution 4 (dis4)

Selection

Geometric entity level    Boundary

Selection                    Boundaries 4–5

Settings

<b>Description</b>	<b>Value</b>
Distribution properties	Predefined distribution type
Number of elements	mesh_nodes_pellet_chamfer

### Mapped 2 (map2)

Selection

Geometric entity level    Domain

Selection                    Domain 3

Settings

Description	Value
Adjust evenly distributed edge mesh	On

Distribution 1 (dis1)

Selection

Geometric entity level    Boundary

Selection                    Boundary 10

Settings

Description	Value
Number of elements	mesh_nodes_sheath_radial

Distribution 2 (dis2)

Selection

Geometric entity level    Boundary

Selection                    Boundary 9

Settings

Description	Value
Number of elements	mesh_nodes_sheath_radial

Distribution 3 (dis3)

Selection

Geometric entity level    Boundary

Selection                    Boundary 8

Settings

Description	Value
Number of elements	mesh_nodes_sheath_axial*num_pellets_model

Mapped 3 (map3)

Selection

Geometric entity level Domain

Selection No domains

Settings

Description	Value
Adjust evenly distributed edge mesh	On

Distribution 1 (dis1)

Selection

Geometric entity level Boundary

Selection No boundaries

Settings

Description	Value
Number of elements	1

Free Triangular 1 (ftri1)

Selection

Geometric entity level Domain



Selection                      No domains

Size 1 (size1)

Selection

Geometric entity level    Domain

Selection                      No domains

Settings

Description	Value
Minimum element size	0.00156
Minimum element size	Off
Curvature factor	Off
Resolution of narrow regions	0.9
Resolution of narrow regions	Off
Maximum element growth rate	2
Maximum element growth rate	Off
Predefined size	Extremely coarse
Custom element size	Custom

Component 2

Date    Feb 20, 2014 10:37:58 AM

Component settings

Unit system                      SI

Geometry shape order    automatic

## Geometry 2

### Units

Length unit    m

Angular unit    deg

### Geometry statistics

Description	Value
Space dimension	2
Number of domains	1
Number of boundaries	4
Number of vertices	4

## Rectangle 1 (r1)

### Position

Description	Value
Position	{pellet_hole_radius, 0}

### Layers

### Size

Description	Value
Width	pellet_radius - pellet_hole_radius
Height	1

## Array 1 (arr1)

### Settings

Description	Value
-------------	-------

Description	Value
Size	num_pellets_model
Array type	Linear
Size	num_pellets_model
Displacement	{2*pellet_radius, 0}

Form Assembly (fin)

Settings

Description	Value
Action	Form an assembly
Create pairs	Off

Fission Gas Grain Boundary

Used products

COMSOL Multiphysics

Selection

Geometric entity level Domain

Selection Domain 1

Settings

Description	Value
Shape function type	Lagrange
Element order	Quadratic
Compute boundary fluxes	On
Apply smoothing to boundary fluxes	On

Description	Value
Value type when using splitting of complex variables	Complex
Dependent variable quantity	None
Unit	1/m <sup>3</sup>
Source term quantity	None
Unit	1/m <sup>3</sup> /s

Variables

Name	Expression	Unit	Description	Selection
c.nx	nx		Normal vector, x component	Boundaries 1–4
c.ny	ny		Normal vector, y component	Boundaries 1–4
c.nz	nz		Normal vector, z component	Boundaries 1–4
c.nxmesh	root.nxmesh		Normal vector (mesh), x component	Boundaries 1–4
c.nymesh	root.nymesh		Normal vector (mesh), y component	Boundaries 1–4
c.nzmesh	root.nzmesh		Normal vector (mesh), z component	Boundaries 1–4

Coefficient Form PDE 1

Selection

Geometric entity level Domain

Selection Domain 1

Equations

$$e_a \frac{\partial^2 g_f \text{rain}_c \text{onc}}{\partial t^2} + d_a \frac{\partial g_f \text{rain}_c \text{onc}}{\partial t} + \nabla \cdot (-c \nabla g_f \text{rain}_c \text{onc} - d g_f \text{rain}_c \text{onc} + \gamma) + \beta \cdot \nabla g_f \text{rain}_c \text{onc} + a g_f \text{rain}_c \text{onc} = f$$

$$\nabla = \left[ \frac{\partial}{\partial x}, \frac{\partial}{\partial y} \right]$$

Settings

Description	Value
Diffusion coefficient	$\{\{0, 0\}, \{0, (y[1/m])^2 * \text{nojac}(\text{comp1.pellet\_mid}(\text{fg\_diff\_coeff}))\}\}$
Absorption coefficient	0
Source term	$(y[1/m])^2 * \text{fg\_yeild} * \text{nojac}(\text{comp1.pellet\_mid}((\text{UO2\_grain\_radius}[1/m])^2 * \text{fission\_rate\_density}))$
Mass coefficient	0
Damping or mass coefficient	$(y[1/m])^2 * \text{nojac}(\text{comp1.pellet\_mid}((\text{UO2\_grain\_radius}[1/m])^2))$
Conservative flux convection coefficient	$\{0, 0\}$
Convection coefficient	$\{0, 0\}$
Conservative flux source	$\{0, 0\}$

#### Variables

Name	Expression	Unit	Description	Selection
domflux.fg_g rain_concx	0		Domain flux, x component	Domain 1
domflux.fg_g rain_concy	$-(y[1/m])^2 * \text{nojac}(\text{comp1.pellet\_mid}(\text{fg\_diff\_coeff})) * \text{fg\_grain\_concy}$	$1/(m^2*s)$	Domain flux, y component	Domain 1

#### Shape functions

Name	Shape function	Unit	Description	Shape frame	Selection
fg_grain_conc	Lagrange (Quadratic)	$1/m^3$	Dependent variable fg_grain_conc	Material	Domain 1

Zero Flux 1

Selection

Geometric entity level Boundary

Selection Boundaries 1–2, 4

Equations

$$-\mathbf{n} \cdot (-c \nabla fg_{\text{grain\_conc}} - af g_{\text{grain\_conc}} + \gamma) = 0$$

$$\nabla = \left[ \frac{\partial}{\partial x}, \frac{\partial}{\partial y} \right]$$

Initial Values 1

Selection

Geometric entity level Domain

Selection Domain 1

Settings

Description	Value
Initial value for fg_grain_conc	0
Initial time derivative of fg_grain_conc	0

Dirichlet Boundary Condition 1

Selection

Geometric entity level Boundary

Selection Boundary 3

Equations

$$fg_{\text{rain\_conc}} = r$$

$$g_{\text{reaction}} = -\mu$$

Settings

Description	Value
-------------	-------

Description	Value
Value on boundary	0
Prescribed value of fg_grain_conc	On
Apply reaction terms on	Individual dependent variables
Use weak constraints	Off
Constraint method	Elemental

Shape functions

Constraint	Constraint force	Shape function	Selection
-fg_grain_conc	-test(fg_grain_conc)	Lagrange (Quadratic)	Boundary 3

Mesh 2

Mesh statistics

Description	Value
Minimum element quality	0.005225
Average element quality	0.1332
Quadrilateral elements	312
Edge elements	76
Vertex elements	4

Size (size)

Settings

Description	Value
Maximum element size	0.067
Minimum element size	3.0E-4
Curvature factor	0.3

Description	Value
Maximum element growth rate	1.3

Edge 1 (edg1)

Selection

Geometric entity level    Boundary

Selection                      Boundaries 1, 4

Size 1 (size1)

Selection

Geometric entity level    Point

Selection                      Points 2, 4

Settings

Description	Value
Maximum element size	1e-3
Minimum element size	3.0E-4
Minimum element size	Off
Curvature factor	0.3
Curvature factor	Off
Resolution of narrow regions	Off
Maximum element growth rate	1.3
Maximum element growth rate	Off
Custom element size	Custom

Mapped 1 (map1)



Selection

Geometric entity level Domain

Selection Remaining

Settings

Description	Value
Adjust evenly distributed edge mesh	On

Distribution 1 (dis1)

Selection

Geometric entity level Boundary

Selection Boundary 3

Settings

Description	Value
Distribution properties	Predefined distribution type
Number of elements	mesh_nodes_pellet_dish + mesh_nodes_pellet_chamfer
Element ratio	5.5
Reverse direction	On

## **Appendix E: Using MPM-FAST**

This Appendix will focus on providing enough background on COMSOL's Graphical User Interface (GUI) to enable the reader to run different power histories, pellet materials and collect the modelled results. Section AE.1 will focus on the parameters and variables that inform the model of the pellet and element initial conditions as well as providing the model with an element's power history. Section AE.2 will focus on extracting the modelled results from COMSOL.

This will be far from a comprehensive discussion of COMSOL's capabilities. As this does not describe the implementation of the materials models or how COMSOL, only the Windows version uses the command ribbon, these instructions can be applied to these builds. The central column of the GUI provides the data about the portion of the model selected as well as the space for the user to edit the model to meet their needs. The right column reports on the work that the model has done. The column is split into two fields: the upper field displays graphics (in the case of Figure 31 it displays the geometry of the pellet and sheath of the intermediate element from ADA), the lower field has tabs that provide text information about the functioning of the model. To edit the physical

phenomena, it is recommended that only the parameters, variables and data manipulation describe below be undertaken by the reader.

The example used in this section is for the intermediate element from bundle ADA from the BDL-422 experiment. Figure 31 below displays the default view of MPM-FAST with the COMSOL 4.4 GUI. There are two methods of navigating through the components of a COMSOL model: 1) tab menus, and command ribbon along the upper portion of the GUI similar to other Microsoft Office software GUIs, 2) below the command ribbon the screen is segregated into three columns, the left column contains a series of drop menus that allow access to all the components of a COMSOL model. The instructions below will be based on navigating the model by selecting the specific portions of the model from the left column of the COMSOL GUI.

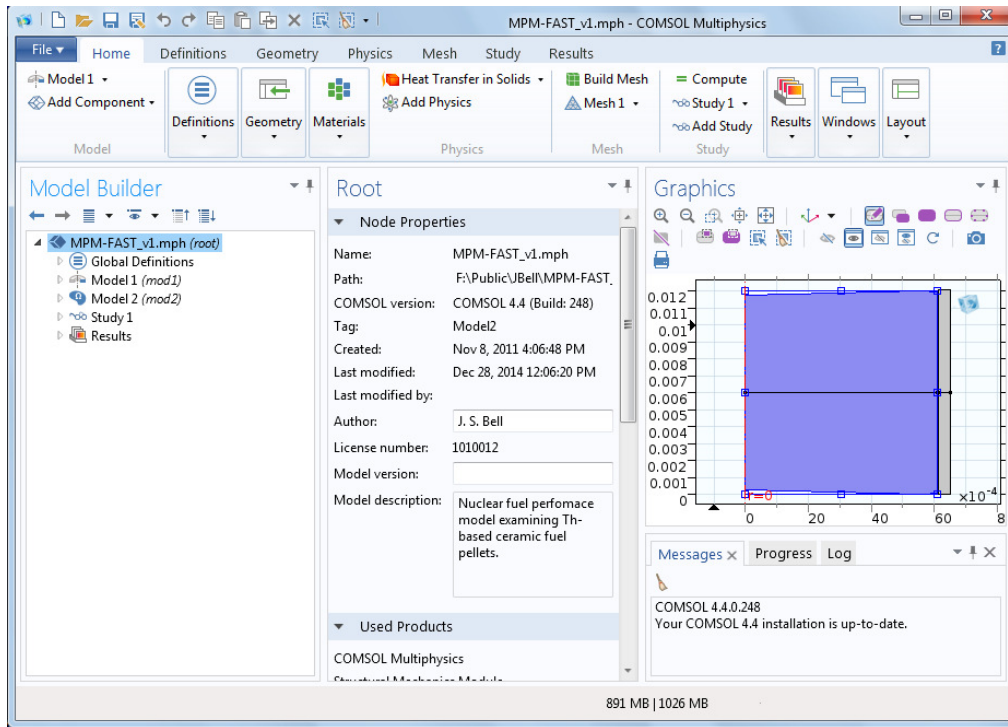


Figure 31: Default view of the MPM-FAST using the Windows version of COMSOL Multiphysics 4.4.

## AE.1 Input

Element and pellet manufacturing data is inputted into the model as Global Parameters. This is accomplished by expanding the “Global Definitions” drop menu, which is the first in the list within the left column in Figure 31. To expand a drop menu select it with the mouse and left-click it. Global Parameter can then be edited by selecting Parameters (first in the list); this is displayed in Figure 32.

Once Parameters is selected the second column in the GUI will display a four column table, first column establishes the name of the parameter, second column is where the value (or expression) of the parameter is set (the square parenthesis [] sets units or dimensions of the parameter), the third column repeats the value of the parameter but in SI units, and the final column allows for further descriptions, notes or comments. The table is not edited directly; there are three text fields, for establishing the name, expression and descriptions.

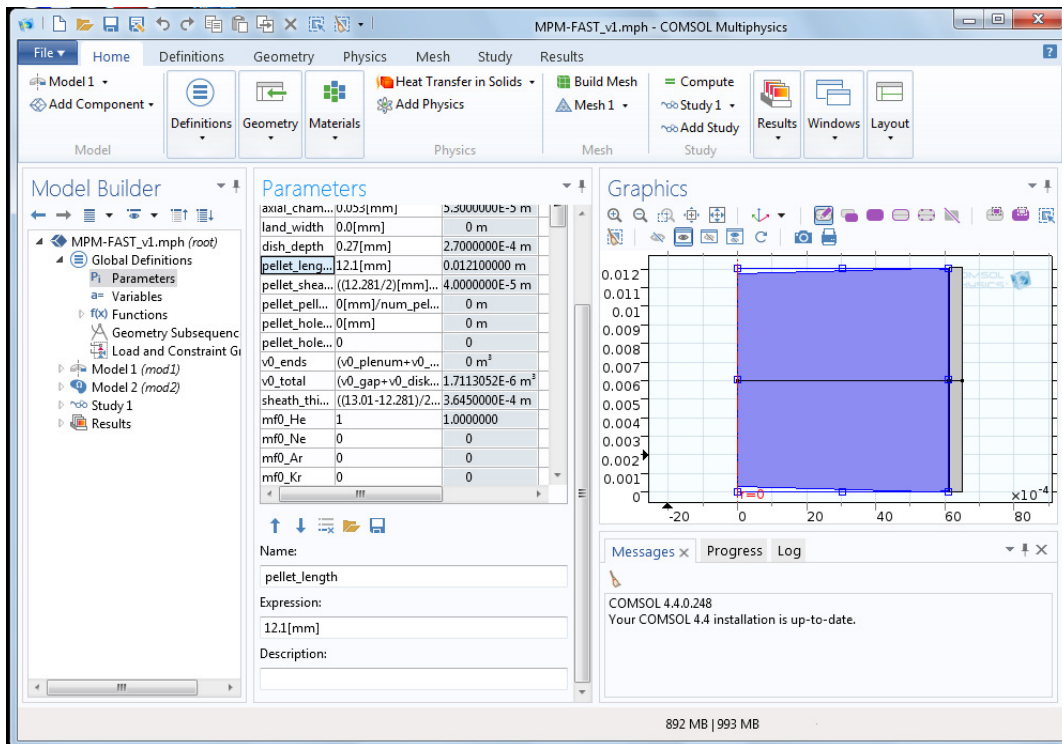


Figure 32: Global Definitions drop menu expanded, presenting the parameter table

The Parameters table from Figure 32 does not display all the input information. There are 89 input parameters, 90 if you include the parameter “peripheral\_tc\_location” which is a remnant of a previous iteration of the model and no longer in affects the model. All the remaining parameters are listed in a series of tables based on what aspect of the model it controls. Input parameters used to generate the model geometry of the pellet and sheath are given in Table 39.

Table 39: Parameters that establish the MPM-FAST's geometry.

<b>Parameter</b>
pellet_radius
radial_chamfer
axial_chamfer
land_width
dish_depth
pellet_length
pellet_sheath_gap
pellet_pellet_gap
pellet_hole_radius
sheath_thickness
sheath_internal_radius
sheath_length_initial
num_dishes
num_chamfers

Table 40 presents the parameters where additional pellet and sheath fabrication data is entered. Since FAST was developed for UO<sub>2</sub> not all of MPM-FAST's parameter names for pellet based values have been edited to be more general, which is the case for the pellet properties being named UO<sub>2</sub> below. Pellet, sheath, root means squared (RMS) roughness contribute to the heat transfer calculation in the pellet-to-sheath gap. "pellet\_mat" is the parameter that enables the user to select pellet material to be modelled; by assigning a value of: 1 MPM-FAST will model UO<sub>2</sub>, 2 for (Th,U)O<sub>2</sub>, and 3 for (Th,Pu)O<sub>2</sub>. "s\_dev" is for the stoichiometric deviation of oxygen in the pellet material.

Table 40: Parameters that describe the initial values for various physical aspects of the fuel pellet and sheath.

<b>Parameters</b>
UO <sub>2</sub> _pore_fraction_initial
UO <sub>2</sub> _roughness
s_dev
UO <sub>2</sub> _grain_diameter_int
rho_UO <sub>2</sub> _theory
pellet_solid_volume
pellet_mat
RMS_surf_roughness
Zir_roughness

Table 41 lists the parameters that establish how fine the mesh is applied to the pellet and sheath. The model is currently using the mesh settings that were recommended by Prudil for the modelling of UO<sub>2</sub> fuel.

Table 41: Parameters that control the finite-element mesh.

<b>Parameters</b>
mesh_nodes_pellet_dish
mesh_nodes_pellet_chamfer
mesh_nodes_pellet_axial
mesh_nodes_sheath_radial
mesh_nodes_sheath_axial

Table 42 contains the parameters that control time dependent solver.

“t\_max” and “burnup\_max” are the model’s stop conditions. While attempting to model the power histories from DME-221 and BDL-422, “t\_max” is set artificially high and relies on the exit burnup of the fuel set as “burnup\_max” as the stop condition. In Prudil’s work, it was found that establishing shorter time steps within the first 10 seconds of the irradiation time prevented convergence issues from the transient conditions of the fuel starting up.

Table 42: Solver control variables.

<b>Parameters</b>
t_max
burnup_max
timestep_range1_start
timestep_range1_size
timestep_range1_end
timestep_range2_start
timestep_range2_size
timestep_range2_end
max_time_step



Within Table 43 are the parameters that provide initial guesses and tolerance values to several of the non-linear equations in MPM-FAST, as well as “pellet\_hoop\_stress\_enabled\_flag” which enables or disables the pellet cracking model. It is recommended that these parameters remain unchanged.

Table 43: Initial guesses or tolerance values for non-linear calculations.

<b>Parameters</b>
contact_error_tol
coolant_pressure_parm
coolant_temperature_parm
sheath_coolant_ht_coef_parm
gas_pressure_forced_parm
T_ends_parm
fg_release_damping_constant
contact_penalty_factor
contact_pressure_est
pellet_hoop_stress_enabled_flag
creep_r
creep_z

Any parameter that relates to the initial internal free volume of the element is given in Table 44. Most of these volumes are calculated from the input of the geometry variables, with the exception of: “num\_pellets”, “v0\_plenum”, “v0\_C\_insert”, and “pellet\_hole\_free\_vol\_fraction”. “pellet\_hole\_free\_vol\_fraction” is to take into account an instrumented pellet and the amount of volume the instrument takes up in relation to the hole,

“v0\_C\_insert” is volume around the carbon insert disk associated with a tri-lobe plenum from BDL-422, “v0\_plenum” is the volume of the plenum, and “num\_pellets” is the number of pellets in the fuel stack.

Table 44: Initial values for the internal element volume displayed in Figure 5.

<b>Parameters</b>
v0_gap
v0_chamfer
v0_disk
v0_dish
v0_pellet_hole
v0_pellet
v0_plenum
v0_C_insert
v0_ends
v0_total
num_pellets
dish_radius
vol_ratio
pellet_hole_free_vol_fraction

In order to determine the initial partial pressure of the gas’s components, the total initial temperature “T0\_fill”, pressure “P0\_fill” and the mole fraction of each of the components (variables beginning with “mf0”), “T\_geom\_ref” is a reference temperature, and “m0\_gas\_element” is the initial moles of fill gas within the element. Table 45 displays these variables that enable the user to input the initial composition of the element fill gas. In its default mode (which is the

same gas model as ELESTRES), only “mf0\_He” and “mf0\_Ar” are available for use.

Table 45: Parameters to determine the initial mole fractions of fill gas, temperature and pressure.

<b>Parameters</b>
mf0_He
mf0_Ne
mf0_Ar
mf0_Kr
mf0_Xe
mf0_N2
mf0_O2
P0_fill
T0_fill
m0_gas_element
T_geom_ref

Table 46 contains the parameters that initiate the burnup calculation and pertain to fission. These include “M\_HEU” molar mass of heavy enriched uranium, “M\_Th” molar mass of thorium, “M\_O” molar mass of oxygen, “M\_m” molar mass of metal atoms within the fuel, “M\_mO2” is the molar mass of the ceramic dioxide, “wPer\_U” is the weight percent of uranium in the fuel, and the last parameter that isn’t named for exactly what it is, is “U235\_percent”. As mentioned in the discussion on the flux depression model (Section 3.5.1), in context of Th-based fuel without uranium this parameter represents the initial fissile content.

Table 46: Energy of fission, initial values for the mass, atomic weight and atom percent of pellet materials for burnup calculation.

<b>Parameters</b>
energy_per_fission
mass_UO2
mass_U
num_neutron_per_fission
M_HEU
M_Th
M_O
M_m
wPer_U
M_mO2
U235_percent

Each of the parameters in Table 47 enables MPM-FAST to determine how much stable fission gas is produced. It is recommended that these remain unchanged from their current values.

Table 47: Parameters that enable the model to determine the production of stable fission gas during irradiation.

<b>Parameters</b>
Percent_fission_gas_yield_UO2
Percent_fission_gas_yield_Th
Xe_to_Kr_UO2
Xe_to_Kr_Th

Once the manufacturing data and solver settings are provided to the model, the power history of the element is then required to ensure the model is representative of the fuel's irradiation. Figure 33 shows the drop down menu where a power history can be established as a global function in MPM-FAST.

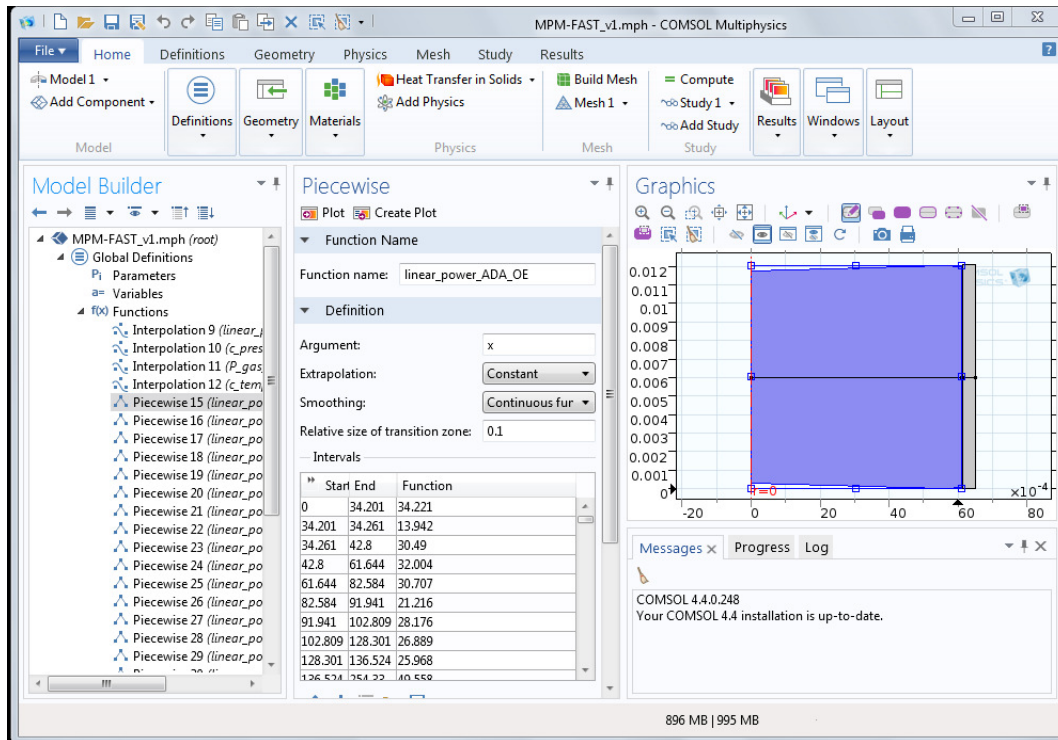


Figure 33: Global Definitions drop menu and Functions expanded, presenting the power history for one of the elements from BDL-422.

There is an additional step required to inform MPM-FAST the history to be used. Figure 34 displays the GUI of MPM-FAST in the process of editing this parameter within the model. The parameter is named “linear\_power”, it can be found by expanding the “Model 1” drop menu as well as the “Definitions” and “Variables” sub drop menus. “linear\_power” is then found within “Input Parameter Switches” table that appears in the second column of the GUI when it is selected. “linear\_power” is the first variable within the table, it is

important to note that if the user is going to run a power history pre-loaded in the model, MPM-FAST needs the user to select independent variable for the power history function. This is accomplished by inputting the name of the pre-loaded power history followed by the appropriate independent variable in round parenthesis and then the units of the dependent variable in square parenthesis. For example, the run used in the figures of the GUI is “linear\_power\_ADA\_IE(burnup\_avg)[kW/m]”, the independent variable is the average burnup of the pellet and the dependent variable is in  $\text{kW m}^{-1}$ . All of the loaded power histories in MPM-FAST are setup to be implemented in this fashion. However it is possible to load power histories that are time dependant with the only difference indicating that the independent variable is time, or conversely you can enter a constant vale in this field.

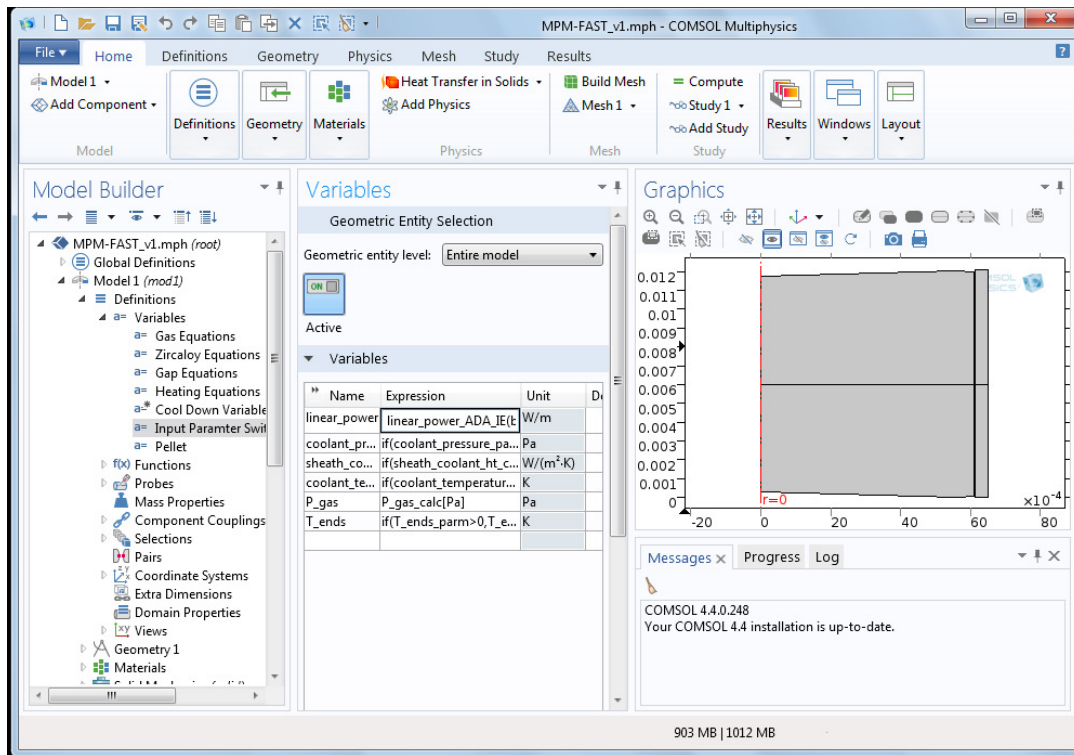


Figure 34 Model 1, Definitions, and Variables drop menus expanded, presenting the table for Input Parameter Switches table.

Having established the power history and entered the manufacturing data for the element, it is now time for the model to begin its fuel performance calculation. There are two ways of initiating the calculation. In the command ribbon there is a button labeled compute, in addition the compute button is displayed in the second column of the GUI when the “Study” drop menu is expanded. Both locations are circled in a Figure 35 below.



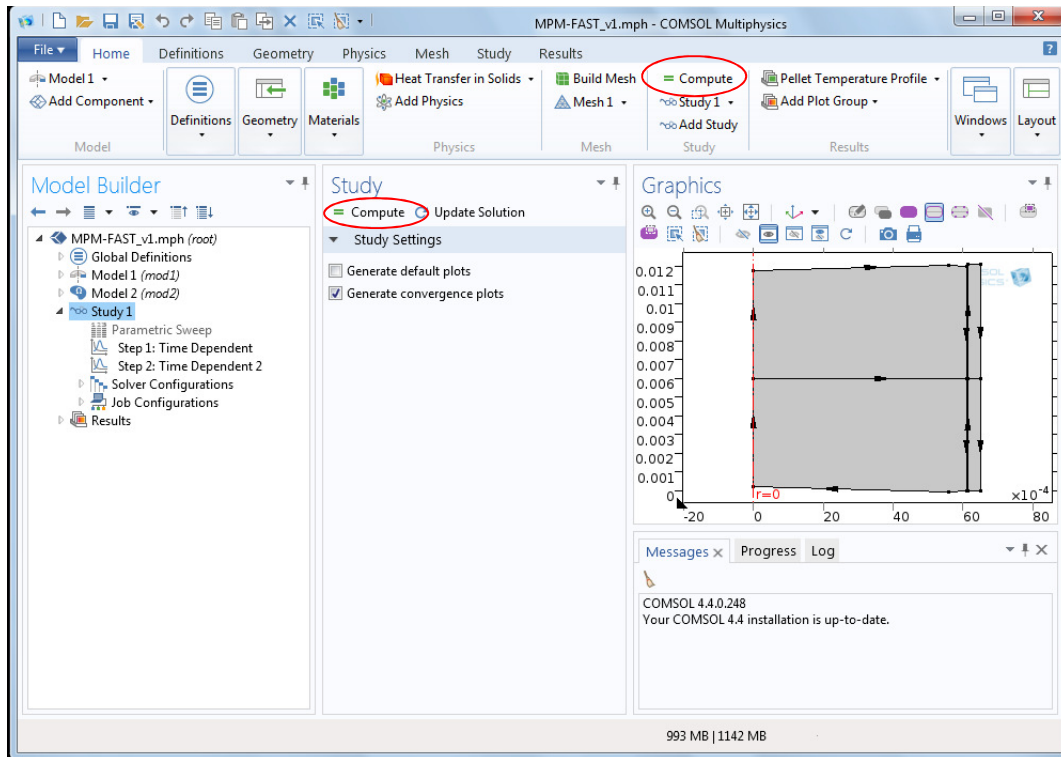


Figure 35: Study 1 drop menu expanded.

Once the calculation is initiated, all actions in the command ribbon and the left and middle column will be frozen out. In the right hand column of the GUI several tabs will be initiated in the upper and lower windows as shown in Figure 36 below. The tabs in the upper partition of the left column display graphs for the convergence of each computational step for both the time dependent and non-linear solvers. The other tabs display the last view of the model geometry examined, and a graph showing the relative burnup of the fuel model compared to the exit burnup entered in the input parameters. In the lower portion of the left

column will contain four tabs: the “Progress” tab updates on the completion of each solver step, the “Messages” will also display how many degrees of freedom in the model once initiated as well as how much time the computation took to be complete when finished, “Log” lists each solver step when it is initiated with a time stamp indicating the length of time in seconds the model has calculated the fuel to be irradiated for, and the final tab “Probe Table 20” updates the relative burnup step displayed.

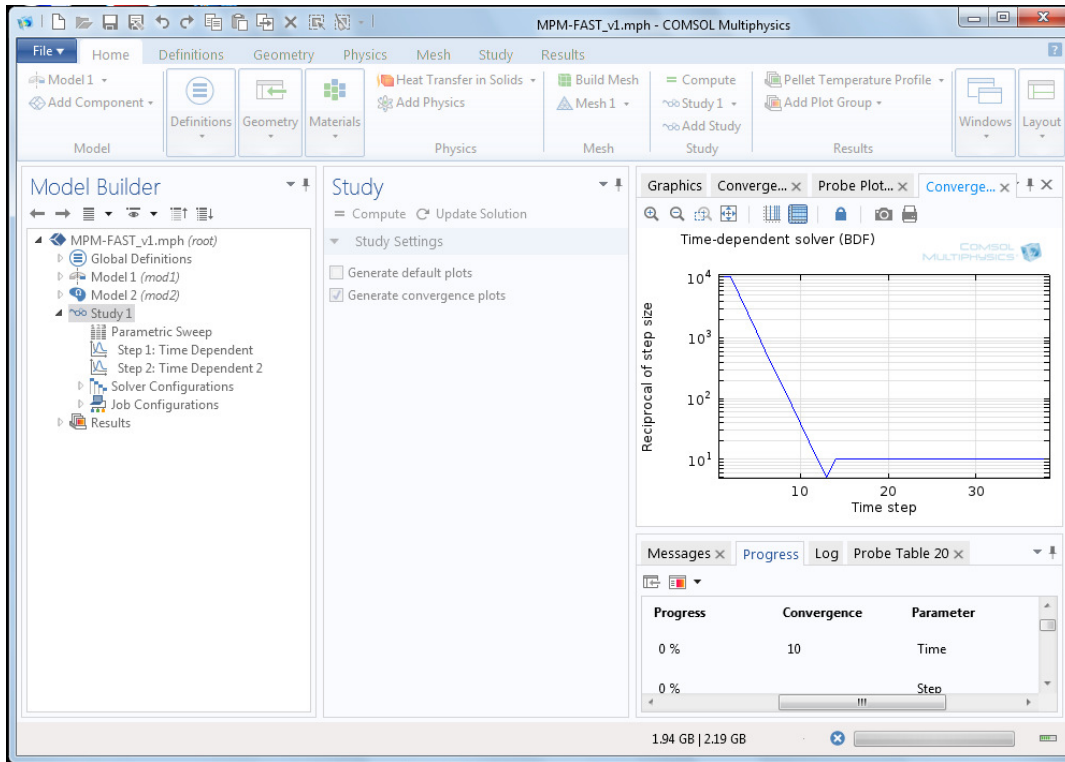


Figure 36: GUI during a calculation, most functions are locked, with access to the progress of the calculation available via the various tab in the left most column of the GUI.

## AE.2 Post Processing

Once the calculation is complete, the “Progress” tab will close and the “Message” tab will open in the bottom portion of the left most column of the GUI as seen in Figure 37. All the remaining functional component of the COMSOL will be unlocked. In order to access the results of the computation, the “Results” drop menu in the right column needs to be expanded. Within the drop menu is the sub menu “Derived Variables”. Listed within this sub menu are a series of calculations of interest to CNL they are: sheath strain at the mid-pellet “Mid Pellet Strain”, the maximum displacement calculated to the sheath “Ridge Height”, sheath strain in the region of pellet to pellet contact “Max Strain”, “Pellet-to-Pellet Interface Contact Pressure”, average “Pellet-to-Sheath contact Pressure”, the number of “Stable Fission Gas Fission Products” produced, “Fission Gas Released to Free Volume”, “Fission Gas Accumulated on Grain Boundary”, “Fission Gas Still Within Fuel Grains”, and the “Average Fuel-to-Sheath Heat Transfer Coefficient”.

Once the user selects the variable from the list, to have the model report its values throughout the irradiation, select and left click the “Evaluate” button in the top right of the centre column (circled in Figure 37). The model will generate a table at the bottom of the right most column; the table will consist of two columns

with the irradiation time stamp and the value of the variable at that point in the model. By right clicking on this table, the model will present options for coping the data that will allow it to be pasted in as text in most other programs (It will be properly be copied with the same format into Excel).

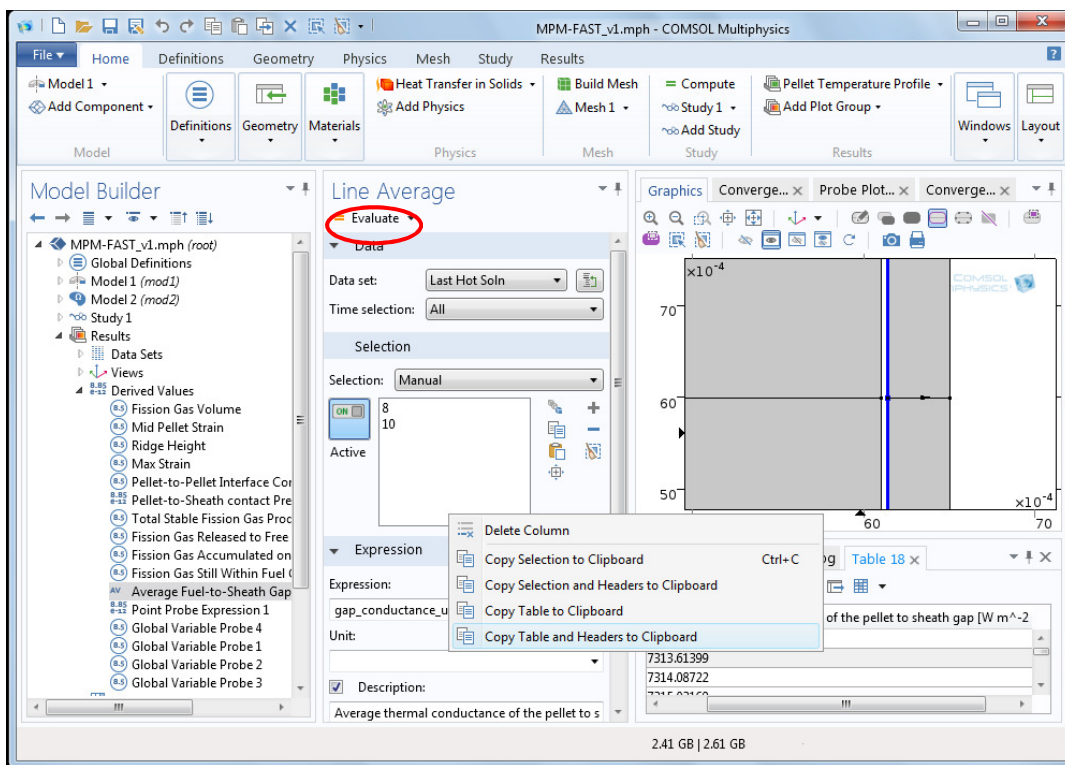


Figure 37: Displays the GUI where the data from the calculation of the average fuel-to-sheath heat transfer coefficient.

Another request made of CNL was to be able to view the radial mid-plane temperature profile of the pellet, as well as the radial grain size profile. These can

also be accessed from the “Results” drop menu as seen below in Figure 38; they are labelled “Pellet Temperature Profile” and “Pellet Grain Size Profile” respectively (circled in left column of Figure 38. When either are of these selected “Line Graph 1” will drop below, by left clicking on “Line Graph 1” with the mouse will open the options for generating the one dimensional plot in the middle column. In the middle column under the light blue banner labelled “Data” there is a drop list next to the text “Data set:” ensure that the “Last Hot Soln” is selected. Under this there is another drop down list next to the text “Time selection:” pick the option “From list”, below a list of all the time steps the model calculated will appear, select however many desired. It is important to ensure a small number of these times from the list, as the default selection will attempt to plot all the profiles from each time step on the same graph (this will freeze COMSOL until it generates the graph and take a long time). Having selected the desired time to take the profile from, left click on the “Plot” button in the top right of the center column (as labelled with the arrow in Figure 38. The plot will then be displayed in the upper portion of the right column.

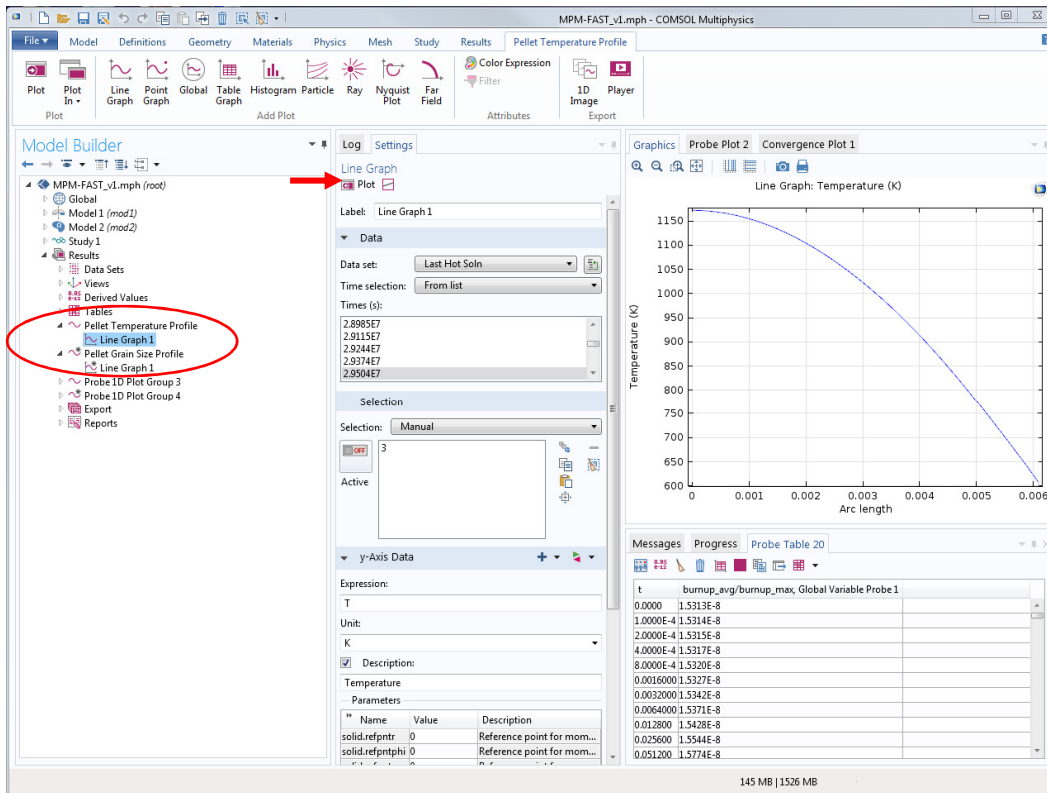


Figure 38: Expansion of the Results drop menu with the pellet temperature profile selected.